

THERMOCHEMICAL INVESTIGATIONS ON Bi-Fe-O AND Bi-Cr-O SYSTEMS

By

MEERA A.V

CHEM02201004002

**Indira Gandhi Centre for Atomic Research,
Kalpakkam, Tamil Nadu, India**

*A thesis submitted to the
Board of Studies in Chemical Sciences
In partial fulfillment of requirements
for the Degree of*

DOCTOR OF PHILOSOPHY

of

HOMI BHABHA NATIONAL INSTITUTE



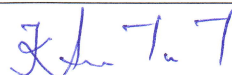
May, 2017

Homi Bhabha National Institute

Recommendations of the Viva Voce Committee

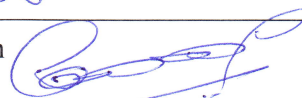
As members of the Viva Voce Committee, we certify that we have read the dissertation prepared by Meera A.V entitled "Thermochemical investigations on Bi-Fe-O and Bi-Cr-O systems" and recommend that it may be accepted as fulfilling the thesis requirement for the award of Degree of Doctor of Philosophy.

Chairman - Dr. K. Ananthasivan



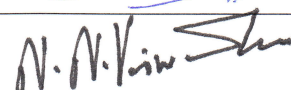
Date: 30/1/18

Guide / Convener - Dr. T. Gnanasekaran



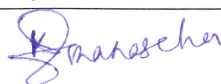
Date: 30/1/18

Examiner - Dr. N. N. Viswanathan



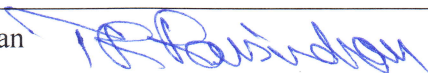
Date: 30/1/18

Member 1 - Dr. K.I. Gnanasekar



Date: 30/1/2018

Member 2 - Dr. T.R. Ravindran



Date: 30.1.2018

Member 3 - Dr. Rajesh Ganesan



Date: 30/01/18

Final approval and acceptance of this thesis is contingent upon the candidate's submission of the final copies of the thesis to HBNI.

I/We hereby certify that I/we have read this thesis prepared under my/our direction and recommend that it may be accepted as fulfilling the thesis requirement.

Date: 30/1/19
Place: Kalpakam



Dr. T. Gnanasekaran
(Guide)

STATEMENT BY AUTHOR

This dissertation has been submitted in partial fulfillment of requirements for an advanced degree at Homi Bhabha National Institute (HBNI) and is deposited in the Library to be made available to borrowers under rules of the HBNI.

Brief quotations from this dissertation are allowable without special permission, provided that accurate acknowledgement of source is made. Requests for permission for extended quotation from or reproduction of this manuscript in whole or in part may be granted by the Competent Authority of HBNI when in his or her judgment the proposed use of the material is in the interests of scholarship. In all other instances, however, permission must be obtained from the author.

Meera A.V

DECLARATION

I, hereby declare that the investigation presented in the thesis has been carried out by me. The work is original and has not been submitted earlier as a whole or in part for a degree / diploma at this or any other Institution / University.

Meera A.V

List of Publications arising from the thesis

I. Published:

1. Partial phase diagram of Bi-Fe-O system and the standard molar Gibbs energy of formation of $\text{Bi}_2\text{Fe}_4\text{O}_9$, A.V. Meera, Rajesh Ganesan, T. Gnanasekaran, J. Alloys Compd., **2017**, 692, 841-847.
2. Studies on the phase diagram of Bi-Cr-O system, A.V. Meera, Joysurya Basu, Rajesh Ganesan, T. Gnanasekaran, J. Nucl. Mater., **2017**, 487, 174-185.
3. Determination of the standard molar enthalpies of formation and heat capacities of $\text{Bi}_{25}\text{FeO}_{39}$ (s) and $\text{Bi}_2\text{Fe}_4\text{O}_9$ (s) by calorimetry, A.V. Meera, G. Jogeswararao, R. Venkata Krishnan, Rajesh Ganesan, K. Ananthasivan, T. Gnanasekaran, J. Chem. Thermodyn., **2018**, 118, 283-291.

II. Communicated:

1. Standard molar Gibbs energy of formation of ' $\text{Bi}_{22}\text{Cr}_{18}\text{O}_{60}$ ' and ' $\text{Bi}_{38}\text{CrO}_{60}$ ', A.V. Meera, Rajesh Ganesan, T. Gnanasekaran, Communicated to Thermochimica Acta.

III. Manuscripts under preparation:

1. Studies on thermodynamic stability of BiFeO_3 , A.V. Meera, Rajesh Ganesan, T. Gnanasekaran.

IV. Conference presentations:

1. "Phase diagram studies on Bi-Fe-O system", A.V. Meera, R. Ganesan, T. Gnanasekaran, Fourth Interdisciplinary Symposium on Materials Chemistry (ISMC) held at Bhabha Atomic Research Centre, Mumbai on 11-15 December 2012.
2. "Phase diagram studies on Bi-Fe-O" system, A.V. Meera, R. Ganesan, T. Gnanasekaran, International Conference on Materials and Characterization Techniques (ICMCT) held at Vellore Institute of Technology, Vellore on 10-12 March 2014.

3. "Phase diagram investigation on Bi-Fe-O system", A.V. Meera, R. Ganesan, T. Gnanasekaran, Nuclear Materials Conference, NUMAT-2014 held at Florida, USA on 27-31 October 2014.
4. "Phase diagram studies on Bi-Cr-O system", A.V. Meera, R. Ganesan, T. Gnanasekaran, Nuclear Materials Conference, NUMAT-2014 held at Florida, USA on 27-31 October 2014.
5. "Phase diagram and thermochemical studies on Bi-Fe-O and Bi-Cr-O systems", A.V. Meera, Rajesh Ganesan, T. Gnanasekaran, DAE-BRNS Theme meeting on Chemistry in Nuclear Technology (CHEMNUT) held at Indira Gandhi Centre for Atomic Research, Kalpakkam on 30-31 July 2015.
6. "Phase diagram and thermodynamic studies on Pb-M-O and Bi-M-O (M: Fe, Cr, Mo) ternary systems", A.V Meera, P.M Aiswarya, S.K Sahu, R Ganesan, T. Gnanasekaran, Proceedings of the DAE-BRNS fifth Interdisciplinary Symposium on Materials Chemistry held at Bhabha Atomic Research Centre, Mumbai on 9-13 December 2014.

Meera A.V

*Dedicated to
my family,
friends
and
teachers*

ACKNOWLEDGEMENTS

I take this opportunity to thank all those who supported and helped me to complete my PhD.

First of all, I would like to express my sincere gratitude to my research supervisor, Dr. T Gnanasekaran, for giving me the opportunity to work with him and for introducing me to a wonderful area like experimental thermodynamics. His passion to science, honesty and enthusiasm inspired me deeply and helped me to develop interest in research. I am very grateful for his efforts to improve my scientific knowledge, experimental skills and writing skills. I am also indebted to him for patiently going through the various versions of my thesis and journal papers and for his critical comments.

I am immensely indebted to my technical advisor, Dr. Rajesh Ganesan who helped me endlessly in each and every stages of my PhD life. He was always available for clarifying doubts and for helping in doing the experiments. He taught me how to do research in a systematic and disciplined way. Without him my PhD would not have been successful.

I thank my Doctoral committee chairman, Dr. K. Ananthasivan, former chairman Dr. K. Nagarajan and members, Dr. K. I. Gnanasekar and Dr. T. R. Ravindran for their time to time evaluation and valuable suggestions.

I would like to thank Dr. U. Kamachi Mudali, Director, MC & MFCG, Dr. A. K. Badhuri, Director, IGCAR and former director Dr. P.R. Vasudeva Rao for the excellent research facilities I enjoyed at IGCAR. I thank Dr. S. Anthonysamy, Dean of Chemical Science and the former Dean, Dr. V. Ganesan for the pleasant academic and research atmosphere. I acknowledge DAE/IGCAR for financial support. I would like to thank Dr. M. Saibaba and GSO for providing me a pleasant stay at research scholar's enclave.

My sincere thanks to Dr. Joysurya Basu for his efforts to elucidate the structure of the new compound which was identified during this work. His expertise and dedication has been vital in this project. I thank Mr. G. Jogeswara Rao, Dr. R.

Venkatkrishnan and Dr. K. Ananthasivan for their help in the solution calorimetry experiments and for fruitful scientific discussions.

The inspiration, help and suggestions received from Dr. K. I. Gnanasekar and Dr. V. Jayaraman have been invaluable in my PhD life. I am grateful to them for all the helps and for the precious time they dedicated to me. I am also thankful to Dr. R. Sridharan for his valuable suggestions and support. I sincerely acknowledge Dr. K.S. Viswanathan for his wonderful spectroscopy classes which helped me to understand the basics.

Special thanks to Dr. E. Prabhu, Mrs. P.C. Clinsha and Mr. Sajal Ghosh for their selfless support, valuable suggestions and fruitful scientific discussions. They helped me a lot in carrying out the experiments at all point of time.

I sincerely anknowledge Dr. R. Sudha, Dr. Arup Dasgupta, Mr. Pradyumna Kumar Parida, Dr. Shamima Hussain, Dr. R. Priya and Mr. Sai Kumaran for characterizing my samples using SEM and EDS. My sincere thanks to Mr. Raja Madhavan for characterizing my samples by XRD. I am grateful to Mr. A. Sree Rama Murthy for doing XPS for my sample. My sincere gratitude to Mr. Nair Afijith Ravindranath for doing BET analysis for my samples. I am grateful to Dr. S. Vijayalakshmi, Mrs. S. Annapoorani and Mrs. R. Uma Maheswari for analyzing my samples using AAS and ICP-OES.

I am thankful to Mr. K. Haridas of Central Glass Blowing Facility for vacuum sealing of my samples. I am also thankful to Mr. N. Eswaran and his team in workshop and Mr. Khaja Mohideen for their help and support in constructing the experimental setup. I am also thankful to Mr. K.A.S. Kutty for his neat drafting work. My sincere thanks to Mr. Henson Raj and Mr. G. Vijayaraghavan of Quality Control Division for their relentless support for helium leak testing.

I thank all the LMCS and NCSS members for the pleasant academic and friendly atmosphere I enjoyed in the group. I would like to thank, Mr. S. Shyamkumar, Mr. C. V. Vishnu Vardhan, Mrs. P.R. Reshmi, Mr. Sanjit Kumar Parida, Mr. S. Nagaraj, Mrs. M. Nalini, Mrs. T. Muthu Ambika, Mr. Kishore Naick, Mr. M. Venkatesh, Mr. Sandeep Swamy, Mr. I. Lakshmi Gandan, Dr. Souman Das,

Mr. Ravindra Babu, Mr. Jose Joseph and Ms. Veena for their valuable suggestions, help, support, consideration and love.

Words cannot express my sincere gratitude to my best friends, Aiswarya, Soja and Rasmi who were always with me along my PhD life. Their friendly advice, soothing words, being at the needful moments helped me to overcome the obstacles I faced and continue my work. Thanks for making me smile in my miserable situations. Without them I cannot imagine my life in Kalpakkam. Thank you for the wonderful moments you have given to me. I am also thankful to Mrs. Sumala, Soja's mother for the motherly affection and kind support.

I thank my senior Dr. Sulata Kumari Sahu for her valuable advices. With her help only I started my research career. Special thanks to her for sending the scientific articles which were not available in IGCAR.

I would never forget the memorable companionship of my friends and batch mates, especially my previous roommate Rasmi C.K, Rajni chechi, Priyada chechi, Assa chechi and family, Saji chechi, Sabeena, Kamali, Suresh, Benedict, Kalyan, Devidas, Avinash, Anbu, Leona, Mahavishnu, Prema, Sanjay, Gopi, Preethi, Sivadasan, Saswath and his wife Uma, Parvathy, Nithin, Radhikesh and Irshad. Special thanks to Mr. Liju Krishnan whose friendship always made me happy. I am thankful to my friends, Prajitha K.P and Savithri N.G for introducing me to IGCAR.

I sincerely acknowledge my teachers in the Chemistry department of Newman college for their blessings and encouragement. I am grateful to Mr. Maria Starwin for his coaching classes which helped me a lot in understanding the subject.

Special thanks to Mr. Ajith Kumar and family who made my life in Kalpakkam comfortable. I am so grateful to them for considering me like a family member. I am also thankful to Mrs. Reshmi and family for their love, concern and support during my stay in Kalpakkam.

My research and life at IGCAR was possible due to the endless support from my family. First of all I thank my parents Mr. Venugopal and Mrs. Valsala who have never said 'No' to any of my ambitions. I am so grateful to them for giving me the freedom to select a career of my choice. Special thanks to my brother Mr.

Harikrishnan who always made me happy, supported me and encouraged me. Their unconditional support and love was my motivation to continue the work during my difficult times. I am so grateful to my husband, Mr. Amarnath whose love, support and companionship made me hopeful and cheerful. I am obliged to my mother in law and sister in laws for the helps and support they extended to me. I extend my gratitude to all my family members for their love and encouragement.

Meera A.V

CONTENTS

	Page No.
SYNOPSIS	xvi
LIST OF FIGURES	xxviii
LIST OF TABLES	xxxii
CHAPTER 1 INTRODUCTION	1
1.1 Heavy liquid metal coolants	1
1.2 Phase diagram of lead-bismuth system and lead bismuth eutectic alloy	3
1.3 LBE – Compatibility problems with structural steel	4
1.4 Strategies to mitigate corrosion in lead and LBE systems	7
1.4.1 Development of new structural steels for use in heavy liquid metal coolant systems	7
1.4.2 Formation of protective coatings on the steel surface	8
1.5 Thermodynamic basis of the role of oxygen in mitigation of corrosion	12
1.6 Aim of this work	15
1.7 References	16
CHAPTER 2 EXPERIMENTAL METHODS	21
2.1 Preparation of compounds	21
2.1.1 Solid state reaction between oxides	21
2.1.2 Coprecipitation and calcination of hydroxides	22
2.2 Phase equilibration studies	23
2.3 Techniques for materials characterization	24
2.3.1 X-ray Diffraction (XRD)	24
2.3.1.1 Generation of X-rays and general experimental methods	24
2.3.1.2 Powder diffraction method	26
2.3.1.3 Source of background radiation in XRD	28
2.3.2 Electron microscopy	29
2.3.2.1 Scanning Electron Microscopy (SEM)	29
2.3.2.2 Transmission Electron Microscopy (TEM)	30
2.3.2.2.1 Modes of operation	31
2.3.2.2.2 Sample preparation for TEM	33

2.4 Simultaneous Thermogravimetry (TG) and Differential Thermal Analysis (DTA)	33
2.5 Oxygen potential measurements employing solid oxide electrolytes	34
2.5.1 Defect structure and conduction mechanism in oxide based solid electrolytes	36
2.5.1.1 Pure MO_2 based electrolyte	36
2.5.1.2 Doped ThO_2	37
2.5.2 Electrolytic Domain	38
2.5.3 Application of solid electrolytes for emf measurements	39
2.6 Calorimetric techniques	41
2.6.1 Isoperibol calorimeter	41
2.6.2 Differential Scanning Calorimetry (DSC)	49
2.6.2.1 Heat flux DSC	49
2.6.2.2 Power compensation DSC	50
2.6.2.3 Calibration of DSC	51
2.6.2.3.1 Temperature calibration	52
2.6.2.3.2 Heat calibration	52
2.6.2.3.3 Heat flow rate calibration	52
2.6.2.4 Heat capacity measurement using DSC	52
2.7 Pseudo-isopiestic equilibrations of samples under controlled oxygen partial pressures	56
2.8 References	59

CHAPTER 3 THERMOCHEMICAL STUDIES ON Bi-Fe-O SYSTEM	62
3.1 Introduction	62
3.2 Literature survey	62
3.2.1 Fe-O system	62
3.2.2 Bi-Fe System	63
3.2.3 Bi-O System	64
3.2.4 Bi_2O_3 - Fe_2O_3 system	65
3.3 Experimental	73
3.3.1 Materials	73
3.3.2 Preparation of ternary oxides	74
3.3.3 Equilibration studies	74

3.3.4	Oxygen potential measurements using yttria stabilized zirconia solid electrolyte	82
3.3.5	Investigations on thermal stability of BiFeO_3	87
3.3.5.1	DTA and DSC studies with BiFeO_3	87
3.3.5.2	Equilibration of BiFeO_3 in vacuum and air at different temperatures	88
3.3.5.3	Equilibration of samples containing BiFeO_3 with liquid Bi	91
3.3.6	Determination of standard enthalpy of formation of bismuth ferrites by acid solution calorimetry	92
3.3.7	Heat capacity measurements using differential scanning calorimetry	93
3.4	Results and discussion	94
3.4.1	Preparation of ternary compounds	94
3.4.1.1	Solid state reaction between oxides	94
3.4.1.2	Reaction between precursors prepared through solution route	94
3.4.2	Studies involving equilibration of Bi_2O_3 and Fe_2O_3	96
3.4.3	Studies with samples of composition within the section bound by Bi, Fe and $\text{Bi}_2\text{Fe}_4\text{O}_9$	96
3.4.3.1	Long term equilibration of samples in the temperature range of 773 to 1023 K	96
3.4.3.2	Gibbs energy of formation of $\text{Bi}_2\text{Fe}_4\text{O}_9$ from emf measurements	97
3.4.3.3	Standard enthalpy of formation of $\text{Bi}_2\text{Fe}_4\text{O}_9$ from acid solution calorimetry experiments	103
3.4.3.4	Measurement of heat capacity of $\text{Bi}_2\text{Fe}_4\text{O}_9$ using differential scanning calorimetry	110
3.4.3.5	Deviation of measured C_p values from the estimates by the Neumann-Kopp rule (NKR)	114
3.4.3.6	Internal consistency of the measured thermodynamic data	117
3.4.4	Studies with samples of composition within the section bound by Bi, $\text{Bi}_2\text{Fe}_4\text{O}_9$ and Bi_2O_3	119
3.4.4.1	Long term equilibration of samples in the temperature range of 773 to 1023 K	119
3.4.4.2	Experiments to determine the temperature range of stability of BiFeO_3	120

3.4.4.2.1	DTA and DSC experiments with BiFeO_3	120
3.4.4.2.2	Equilibration of BiFeO_3 in vacuum and air at different temperatures	120
3.4.4.2.3	Equilibration of samples containing BiFeO_3 with liquid Bi	124
3.4.4.3	Emf measurements	129
3.4.4.4	Standard enthalpy of formation of $\text{Bi}_{25}\text{FeO}_{39}$	134
3.4.4.5	Heat capacity measurement of $\text{Bi}_{25}\text{FeO}_{39}$ using differential scanning calorimetry	137
3.4.4.6	Deviation of measured C_p values from the estimates by the Neumann-Kopp rule (NKR)	139
3.5	References	141
CHAPTER 4 THERMOCHEMICAL STUDIES ON Bi-Cr-O		
	SYSTEM	146
4.1	Introduction	146
4.2	Literature survey	146
4.2.1	Cr-O system	146
4.2.2	Bi-Cr system	151
4.2.3	Studies on Bi_2O_3 - CrO_3 pseudo-binary system	151
4.2.4	Studies on Bi_2O_3 - Cr_2O_3 pseudo-binary system	158
4.3	Experimental	159
4.3.1	Materials	159
4.3.2	Preparation of ternary compounds	160
4.3.3	Phase equilibration studies	161
4.3.3.1	Equilibrations of mixtures of Bi_2O_3 and Cr_2O_3 in air	161
4.3.3.2	Equilibrations of mixtures of Bi_2O_3 and Cr_2O_3 in vacuum	162
4.3.3.2.1	Characterization by Transmission Electron Microscopy (TEM)	163
4.3.3.3	Pseudo-isopiestic equilibrations of samples under controlled oxygen partial pressures	164
4.3.3.4	Additional equilibration studies	167
4.3.4	Emf measurements	171
4.4	Results and discussion	172

4.4.1	Preparation of ternary compounds	172
4.4.2	Phase equilibration results	173
4.4.2.1	Equilibrations of mixtures of Bi_2O_3 and Cr_2O_3 in air	173
4.4.2.2	Equilibrations of mixtures of Bi_2O_3 and Cr_2O_3 in vacuum	174
4.4.2.2.1	TEM analysis	177
4.4.2.3	Pseudo-isopiestic equilibrations of samples under controlled oxygen partial pressures	181
4.4.2.4	Additional equilibration studies	181
4.4.3	Oxygen potential measurements in liquid Bi	186
4.5	References	190
CHAPTER 5 SUMMARY AND CONCLUSIONS		195
5.1	Prediction of the nature of passive oxide layer on steel-liquid Bi interface	198
5.2	References	206
CHAPTER 6 SCOPE FOR FUTURE STUDIES		208
6.1	References	209

SYNOPSIS

Liquid lead and lead-bismuth eutectic (LBE) alloy are considered as candidate coolants for the fourth generation nuclear reactors and both a spallation neutron target as well as coolant in accelerator driven systems (ADS) because of their favorable thermal, physical and chemical properties [1]. These properties include high boiling and low melting temperatures, high thermal conductivity, low viscosity, low neutron capture cross section and moderation, and high spallation neutron yield. On the basis of their low chemical reactivity with water and air compared to those of liquid sodium, they are also considered as a secondary circuit coolant to be used in the fast breeder reactors (FBRs). However, chemical interaction of these liquid metals with structural steels is a critical issue. They are highly corrosive to steels because of the relatively high solubility of alloying components of steels in them [2]. Past work has shown the unsuitability of austenitic stainless steels containing nickel owing to high solubility of nickel. Attempts have been made to minimize the corrosion by adopting different approaches: (i) using ferritic steels containing optimum amounts of Cr, Mo, Si, C and N, (ii) surface alloying of steel with Si and Al [3, 4], (iii) by adding corrosion inhibitors such as Ti and Zr to the liquid alloys which leads to the formation of passive nitride and carbide layers on the surface of the steels [5, 6]. Current approach in different laboratories for the reduction of this corrosion focuses on insitu formation of a passive oxide layer on the steel surface by control of dissolved oxygen concentration in the liquid metal. It has been observed that when the dissolved oxygen concentration is below 10^{-7} at% in the coolant, the corrosion is mainly determined by the solubility of the alloying components of steel in the liquid metal. The corrosion rate has been observed to decrease significantly with increase in

oxygen content and it reached a minimum when the oxygen concentration range was 10^{-7} at% by forming a protective oxide film on the steel surface [7]. Further increase in oxygen concentration led to enhancement of the corrosion rate, indicating instability of the protective oxide film at higher oxygen levels.

To understand the composition and thermochemical stability of the protective oxide film formed over the structural steels, a detailed knowledge on the phase diagrams of Pb-M-O and Bi-M-O systems (M= alloying components of steels) as well as the thermochemical data on ternary oxygen compounds formed in these systems are essential. Iron and chromium being the major alloying elements of candidate structural steels, a detailed study on Pb-M-O and Bi-M-O (M= Fe, Cr) systems are required. Sulata et al. [8-13] studied Pb-Fe-O and Pb-Cr-O systems and reported the thermochemical properties of the ternary compounds present in these systems. In the present thesis work, studies on Bi-Fe-O and Bi-Cr-O systems have been carried out.

The objectives set for the present thesis work are

- 1) Determination of ternary phase diagrams of Bi-Fe-O and Bi-Cr-O systems.
- 2) Measurement of thermochemical data viz., Gibbs energy of formation, enthalpy of formation and the heat capacity of the ternary compounds in these systems which are stable in liquid bismuth.

2. Organization of the thesis

The thesis is divided into six chapters. Chapter 1 contains the introduction to the present work. Experimental methods and techniques used in the present study are described in Chapter 2. Chapter 3 describes studies carried out on Bi-Fe-O ternary system and Chapter 4 describes the studies conducted on Bi-Cr-O ternary system.

Chapter 5 provides the summary of the results and conclusions drawn from the present work and Chapter 6 recommends the investigations to be carried out in future.

Chapter 1

In this chapter, physical and chemical properties of various reactor coolants are compared and factors leading to the choice of heavy liquid metals as coolants for a nuclear reactor are briefly discussed. Characteristics of liquid Pb and LBE alloy favoring their choice as coolant cum spallation target in ADS and also as a secondary circuit coolant in fast breeder reactors are presented and compared with other coolants. The compatibility problems of LBE with the structural steel are then summarized in light of the solubility of alloying elements of steels in LBE. Different approaches adopted to minimize this corrosion are then discussed which include: 1) development of new structural steel material which is compatible with LBE and 2) forming protective coatings over the steel surface by adding inhibitors or by controlling the oxygen concentration in the coolant so as to form a passive oxide layer. In the first approach, addition of different elements such as Cr, Mo, Si, C, N, Ti and V in optimum concentrations to ferritic steels is recommended as a solution to minimize corrosion. Surface alloying of steels with Si and Al is also discussed in the view of reducing corrosion. In the second approach, various methods adopted to form protective coatings over the steel surface such as adding inhibitors, predeposition of protective ceramic coatings etc. are discussed. The disadvantages of these coatings are then described and the formation of a protective oxide layer by maintaining optimum oxygen concentration in the coolant is described as the current approach. The thermodynamic basis of the role of dissolved oxygen in imparting corrosion

resistance and thereby the need of the present study on the phase diagrams of Bi-M-O (M: Fe, Cr) systems is brought out.

Chapter 2

This chapter describes the experimental techniques and methods used in the preparation and characterization of compounds in Bi-Fe-O and Bi-Cr-O systems and in the measurement of their thermochemical data. Experimental procedures adopted for equilibration to establish phase diagrams, construction and operation of emf cells, calorimetry etc. are described. Theoretical details of the oxide-solid electrolytes and their application are also discussed. Salient features of X-ray diffraction (XRD), thermogravimetry and differential thermal analysis (TG/DTA), differential scanning calorimetry, scanning electron microscopy and transmission electron microscopy and their application in the present work are also briefly described in this chapter.

Chapter 3

In this chapter, a detailed review of the available literature data in Bi-Fe-O system is presented first and the need for a comprehensive work on this system is discussed. The details of the experiments carried out in this work on Bi-Fe-O system and the phase diagram deduced from the results and the relevant thermochemical data are then described in this chapter.

The literature indicates that only three ternary compounds exist in the Bi_2O_3 - Fe_2O_3 system viz, $\text{Bi}_2\text{Fe}_4\text{O}_9$, BiFeO_3 and $\text{Bi}_{25}\text{FeO}_{39}$. All these compounds decompose peritectically but there is disagreement in the measured values of the peritectic decomposition temperatures cited in the literature. No studies have so far been

reported in the literature on the ternary phase diagram of Bi-Fe-O system. The thermochemical data on these ternary compounds are also limited.

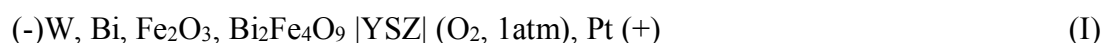
Ternary compounds of this system were prepared by the solid-state reaction of Bi_2O_3 and Fe_2O_3 in air as well as by co-precipitating the hydroxides followed by heating them in air at appropriate temperatures for prolonged periods. The products were characterized by XRD. It is to be pointed out that the preparation of BiFeO_3 always resulted in a mixture of BiFeO_3 (major phase) and $\text{Bi}_{25}\text{FeO}_{39}$ (minor phase). Phase fields in this system were identified by equilibrating mixtures made out of different ternary and binary oxides of this system in sealed ampoules at elevated temperatures for prolonged periods. The resultant products were identified by XRD. Based on the results of these experiments, the following phase fields have been identified in the composition region bound by Bi, Fe and $\text{Bi}_2\text{Fe}_4\text{O}_9$:

Temperature range 773 to 853 K: (1) Bi-Fe- Fe_3O_4 , (2) Bi- Fe_3O_4 - Fe_2O_3 , (3) Bi- Fe_2O_3 - $\text{Bi}_2\text{Fe}_4\text{O}_9$

Temperature range 853 to 1023 K: (1) Bi-Fe-FeO, (2) Bi-FeO- Fe_3O_4 , (3) Bi- Fe_3O_4 - Fe_2O_3 , (4) Bi- Fe_2O_3 - $\text{Bi}_2\text{Fe}_4\text{O}_9$

Experiments were also carried out to establish the phase fields in the composition region bound by Bi, $\text{Bi}_2\text{Fe}_4\text{O}_9$ and Bi_2O_3 . Results of these equilibrations clearly showed the existence of the phase field, Bi- $\text{Bi}_{25}\text{FeO}_{39}$ - Bi_2O_3 in the temperature range 773 to 1023 K. Experiments were carried out to determine the temperature range over which BiFeO_3 is stable by equilibrating BiFeO_3 at different temperatures and by equilibrating phase mixtures of Bi, $\text{Bi}_2\text{Fe}_4\text{O}_9$, BiFeO_3 and Bi, BiFeO_3 , $\text{Bi}_{25}\text{FeO}_{39}$ in liquid Bi. The results of these experiments showed that BiFeO_3 is metastable at low temperatures and becomes thermodynamically stable only around

940 K. Since the temperature above which BiFeO_3 becomes thermodynamically stable could not be established, the exact temperature at which the two phase fields that contain BiFeO_3 as a coexisting phase appear could not be ascertained. Hence, the phase fields that exist in the composition region bound by Bi, $\text{Bi}_2\text{Fe}_4\text{O}_9$ and Bi_2O_3 could not be established. Based on these results, the partial phase diagram of Bi-Fe-O system, in the temperature range of 773 to 1023 K has been constructed. Standard molar Gibbs energy of formation of the $\text{Bi}_2\text{Fe}_4\text{O}_9$ was determined by measuring the equilibrium oxygen partial pressures over the relevant phase fields by using a solid oxide electrolyte based emf cell. The following galvanic cell was constructed and used for determination of the Gibbs energy of formation $\text{Bi}_2\text{Fe}_4\text{O}_9$:



Based on the data obtained from this emf cell, standard molar Gibbs energy of formation of $\text{Bi}_2\text{Fe}_4\text{O}_9$ was deduced and is given by eqn. (1):

$$\Delta_f G_m^o < \text{Bi}_2\text{Fe}_4\text{O}_9 > \pm 0.6 \text{ kJ} = -2196.2 + 0.7679 (T / \text{K}) \quad (T: 799-1023 \text{ K}) \quad (1)$$

Heat capacities of $\text{Bi}_{25}\text{FeO}_{39}$ and $\text{Bi}_2\text{Fe}_4\text{O}_9$ were measured by using differential scanning calorimetry. The temperature dependence of their heat capacities was found to be:

$$C_p < \text{Bi}_{25}\text{FeO}_{39} > (\text{J K}^{-1} \text{ mol}^{-1}) \pm 49.9 = 1529.9 + 200.6 \times 10^{-3} T - 21.6 \times 10^6 T^{-2} \quad (T / \text{K}: 308-818) \quad (2)$$

$$C_p < \text{Bi}_2\text{Fe}_4\text{O}_9 > (\text{J K}^{-1} \text{ mol}^{-1}) \pm 11 = 395.5 - 23.0 \times 10^{-3} T - 7.6 \times 10^6 T^{-2} \quad (T / \text{K}: 313-773) \quad (3)$$

Molar heat capacities of these compounds have also been estimated using the Neumann-Kopp rule (NKR) and the deviation in the measured C_p values from the estimated values is also discussed.

The standard molar enthalpies of formation, $\Delta_f H_m^0(298.15 \text{ K})$ of $\text{Bi}_{25}\text{FeO}_{39}$ (s) and $\text{Bi}_2\text{Fe}_4\text{O}_9$ (s) were also determined using an isoperibol acid solution calorimeter. The enthalpies of solution of the pure compounds, viz., $\text{Bi}_{25}\text{FeO}_{39}$ (s) and $\text{Bi}_2\text{Fe}_4\text{O}_9$ (s) as well as the starting materials viz., Bi_2O_3 and Fe_2O_3 in HCl (8.38 mol kg^{-1}) at 298.15 K were measured. By using the values of the standard molar enthalpies of formation of Bi_2O_3 (s) and Fe_2O_3 (s) from the literature [14], the standard molar enthalpies of formation of $\text{Bi}_{25}\text{FeO}_{39}$ (s) and $\text{Bi}_2\text{Fe}_4\text{O}_9$ (s) were determined as $-7540.7 \pm 256.7 \text{ kJ mol}^{-1}$ and $-2170.8 \pm 28.6 \text{ kJ mol}^{-1}$, respectively. The internal consistency of the experimentally determined thermochemical properties of $\text{Bi}_2\text{Fe}_4\text{O}_9$, viz. Gibbs energy, enthalpy of formation and heat capacity, has also been evaluated.

Chapter 4

A detailed review of the data reported in the literature on Bi-Cr-O system is presented first and the need for a comprehensive work on this system is then discussed. The experiments carried out to deduce the phase diagram and to measure the thermo-chemical properties of the ternary oxides of this system are then described.

Nine ternary compounds have been reported so far in the Bi-Cr-O system. Among these eight of them lie on the Bi_2O_3 - CrO_3 pseudo binary line, viz. $\text{Bi}_{38}\text{CrO}_{60}$, $\text{Bi}_{14}\text{CrO}_{24}$, $\text{Bi}_8\text{CrO}_{15}$, $\text{Bi}_{31}\text{Cr}_5\text{O}_{61.5}$, $\text{Bi}_{10}\text{Cr}_2\text{O}_{21}$, $\text{Bi}_6\text{Cr}_2\text{O}_{15}$, Bi_2CrO_6 , and $\text{Bi}_2\text{Cr}_4\text{O}_{15}$ and

one lies on the $\text{Bi}_2\text{O}_3\text{-Cr}_2\text{O}_3$ pseudo-binary line, viz. BiCrO_3 . The compound, BiCrO_3 has been reported to be stable only under high pressure.

Ternary compounds of this system were prepared by the solid-state reaction of Bi_2O_3 and Cr_2O_3 . These compounds were characterized by XRD. Phase fields in this system were identified by equilibrating mixtures made out of ternary and binary oxides in different ratios, held in sealed ampoules at elevated temperatures for prolonged periods. The resulting products were also identified by XRD. These data show the existence of only six compounds at 1023 K, namely $\text{Bi}_{38}\text{CrO}_{60}$, $\text{Bi}_{14}\text{CrO}_{24}$, $\text{Bi}_{31}\text{Cr}_5\text{O}_{61.5}$, $\text{Bi}_{10}\text{Cr}_2\text{O}_{21}$, $\text{Bi}_6\text{Cr}_2\text{O}_{15}$ and Bi_2CrO_6 and only four compounds at 773 K, namely $\text{Bi}_{38}\text{CrO}_{60}$, $\text{Bi}_{14}\text{CrO}_{24}$, $\text{Bi}_{31}\text{Cr}_5\text{O}_{61.5}$ and $\text{Bi}_6\text{Cr}_2\text{O}_{15}$ on the $\text{Bi}_2\text{O}_3\text{-Cr}_2\text{O}_3$ pseudo-binary. Preparation of $\text{Bi}_{38}\text{CrO}_{60}$ and equilibration studies show that the Bi to Cr ratio in $\text{Bi}_{38}\text{CrO}_{60}$ is not exactly 38 and it might be less than that, but in the present work, the composition of this compound is assumed to be ' $\text{Bi}_{38}\text{CrO}_{60}$ '. The existence of a new compound with the composition, $\text{Bi}_{22}\text{Cr}_{18}\text{O}_{60}$ falling on the line connecting Bi_2O_3 and Cr_2O_3 at 1023 K was also identified. This compound has been characterized by XRD, SEM and TEM. Structural analysis of this phase by TEM indicated that Cr could exist in different oxidation states in this phase and hence the latter might exhibit oxygen nonstoichiometry. In the absence of quantitative data in support of this phenomenon, the composition of the new phase was also assumed to be ' $\text{Bi}_{22}\text{Cr}_{18}\text{O}_{60}$ '. Based on the results of all these equilibration studies, presence of the following phase fields and lines connecting the phases could be identified at 773 K: 1) Bi-Cr- Cr_2O_3 , 2) Bi- $\text{Bi}_2\text{O}_3\text{-Cr}_2\text{O}_3$, 3) $\text{Bi}_2\text{O}_3\text{-'Bi}_{38}\text{CrO}_{60}\text{'-Cr}_2\text{O}_3$, 4) ' $\text{Bi}_{38}\text{CrO}_{60}\text{'-Cr}_2\text{O}_3\text{-Bi}_{14}\text{CrO}_{24}$, 5) ' $\text{Bi}_{38}\text{CrO}_{60}\text{'-Cr}_2\text{O}_3$, 6) $\text{Bi}_{31}\text{Cr}_5\text{O}_{61.5}\text{-Cr}_2\text{O}_3$, 7) $\text{Bi}_6\text{Cr}_2\text{O}_{15}\text{-Cr}_2\text{O}_3$. The phase fields and lines identified at 1023 K are 1) Bi-Cr- Cr_2O_3 , 2) Bi-' $\text{Bi}_{22}\text{Cr}_{18}\text{O}_{60}\text{'-Cr}_2\text{O}_3$, 3) Bi-' $\text{Bi}_{22}\text{Cr}_{18}\text{O}_{60}\text{'-Bi}_{38}\text{CrO}_{60}\text{'}$, 4)

'Bi₃₈CrO₆₀'-'Bi₂₂Cr₁₈O₆₀'-Cr₂O₃, 5) 'Bi₃₈CrO₆₀'-Bi₁₄CrO₂₄-Cr₂O₃, 6) Bi₃₁Cr₅O_{61.5}-Bi₁₀Cr₂O₂₁-Cr₂O₃, 7) Bi₁₀Cr₂O₂₁-Cr₂O₃-Bi₆Cr₂O₁₅, 8) Bi₁₄CrO₂₄-Cr₂O₃, 9) Bi₃₁Cr₅O_{61.5}-Cr₂O₃, 10) Bi₁₀Cr₂O₂₁-Cr₂O₃. Using these data, the partial phase diagram of the Bi-Cr-O system has been constructed.

Equilibrium oxygen potentials in the Bi-Cr₂O₃-Bi₂₂Cr₁₈O₆₀ phase field were measured by employing the following emf cell based on solid oxide electrolyte in the temperature range 929 to 1025 K:



From the measured oxygen potentials, the Gibbs energy of formation of 'Bi₂₂Cr₁₈O₆₀' and 'Bi₃₈CrO₆₀' could be deduced.

Chapter 5

Summary and conclusions deduced from the present work are given in this chapter.

Bi-Fe-O ternary phase diagram shows that on increasing the dissolved oxygen concentration in liquid bismuth in equilibrium with iron metal, iron oxides would precipitate first as the coexisting phases. With further increase in oxygen concentration, Bi₂Fe₄O₉ would appear as the first ternary compound stable in liquid bismuth.

The phase diagram of Bi-Cr-O system at 773 K shows that on increasing the dissolved oxygen concentration in liquid bismuth in equilibrium with chromium, Cr₂O₃ would precipitate first as the coexisting phase. With further increase in the oxygen concentration, Bi would co-exist with Cr₂O₃ and Bi₂O₃. No ternary compounds would be stable in liquid Bi at 773 K. At 1023 K, on increasing the

dissolved oxygen concentration in bismuth which is in equilibrium with chromium metal the first phase which would appear would be Cr_2O_3 . With further increase in oxygen concentration, $\text{Bi}_{22}\text{Cr}_{18}\text{O}_{60}$ would appear as the ternary compound that would be stable in liquid bismuth. When the oxygen concentration is further increased, $\text{Bi}_{38}\text{CrO}_{60}$ would appear (when $\text{Bi/Cr} > 1$, in the system). Further increase in dissolved oxygen would lead to the disappearance of ' $\text{Bi}_{22}\text{Cr}_{18}\text{O}_{60}$ ' and the appearance of Bi_2O_3 .

Based on the thermochemical data on Bi-M-O (M: Fe, Cr) systems obtained from the present work and the data reported in the literature on Pb-M-O (M: Fe, Cr) systems [8-13], the nature of the passive oxide layer that would be formed over the ferritic structural steel in LBE systems is discussed.

Chapter 6

In this Chapter, scope for the future studies is discussed.

In Bi-Fe-O ternary system, Gibbs energies of formation of BiFeO_3 and $\text{Bi}_{25}\text{FeO}_{39}$ need to be determined. In Bi-Cr-O system, Gibbs energies of formation of the ternary compounds, namely $\text{Bi}_{14}\text{CrO}_{24}$, $\text{Bi}_{31}\text{Cr}_5\text{O}_{61.5}$, $\text{Bi}_{10}\text{Cr}_2\text{O}_{21}$, $\text{Bi}_6\text{Cr}_2\text{O}_{15}$, Bi_2CrO_6 , their enthalpies of formation and heat capacities need to be measured.

Mo containing steels such as 9Cr-1Mo steel are being considered as the structural material for LBE. Similarly, steels surface alloyed with Si and Al is also found to be promising candidates as structural material [3, 4]. Hence, the studies on A-Mo-O, A-Si-O and A-Al-O systems (where A = Pb, Bi) are suggested for future investigations.

References

1. B.F. Gromov (Ed), Heavy Liquid Metal Coolants in Nuclear Technology (HLMC 98), Vols.1&2, SSC RF-IPPE, Obninsk, 1999.
2. S. Gossé, Thermodynamic assessment of solubility and activity of iron, chromium, and nickel in lead bismuth eutectic, *J. Nucl. Mater.* 449 (2014) 122–131.
3. L. Ruiguo, F. Jun, and F. Zhongchao, Microstructure and properties of laser surface alloying 304 stainless steel with Si, *Chin. J. Met.Sci. Technol.* 8 (1992) 335-338.
4. A. Weisenburger, A. Jianu, W. An, R. Fetzer, M. D. Giacco, A. Heinzl, G. Muller, V.G. Markov, A.D. Kasthanov, Creep, creep-rupture tests of Al-surface alloyed T-91 steel in liquid lead bismuth at 500 and 550°C, *J. Nucl. Mater.* 431 (2012) 77-84.
5. O.F. Kammerer, J.R. Weeks, J. Sadofsky, W.E. Miller, D.H. Gurinsky, Zirconium and titanium inhibit corrosion and mass transfer of steels by liquid heavy metals, *Trans. AIME*, 212 (1958) 20-25.
6. J.R. Weeks, Lead, bismuth, tin and their alloys as nuclear coolants, *Nucl. Eng. Des.* 15 (1971) 363-372.
7. I.V. Gorynin, G.P. Karzov, V.G. Markov, V.A. Yakovlev, Structural materials for atomic reactors with liquid metal heat - transfer agents in the form of lead or lead-bismuth alloy, *Met. Sci. Heat Treat.* 41 (1999) 384-388.
8. S.K. Sahu, R. Ganesan, T. Gnanasekaran, Studies on phase diagram of Pb–Cr–O system, *J. Nucl. Mater.* 376 (2008) 366-370.

9. S.K. Sahu, R. Ganesan, T. Gnanasekaran, Standard molar Gibbs free energy of formation of Pb_5CrO_8 (s), Pb_2CrO_5 (s), and PbCrO_4 (s), *J. Chem. Thermodyn.* 42 (2010) 1–7.
10. S.K. Sahu, R. Ganesan, T. G. Srinivasan, T. Gnanasekaran, The standard molar enthalpies of formation of Pb_2CrO_5 (s) and Pb_5CrO_8 (s) by acid solution calorimetry, *J. Chem. Thermodyn.* 43 (2011) 750–753.
11. S.K. Sahu, M. Sahu, R.S. Srinivasa, T. Gnanasekaran, Determination of heat capacities of PbCrO_4 (s), Pb_2CrO_5 (s), and Pb_5CrO_8 (s), *Monatsh. Chem.* 143 (2012) 1207–1214.
12. S.K. Sahu, R. Ganesan, T. Gnanasekaran, Studies on the phase diagram of Pb–Fe–O system and standard molar Gibbs energy of formation of ‘ $\text{PbFe}_5\text{O}_{8.5}$ ’ and $\text{Pb}_2\text{Fe}_2\text{O}_5$, *J. Nucl. Mater.* 426 (2012) 214–222.
13. S.K. Sahu, R. Ganesan, T. Gnanasekaran, The standard molar enthalpies of formation of $\text{Pb}_2\text{Fe}_2\text{O}_5$ (s) and $\text{PbFe}_5\text{O}_{8.5}$ (s) by acid solution calorimetry, *J. Chem. Thermodyn.* 56 (2013) 57–59.
14. O. Kubaschewski, C.B. Alcock, *Metallurgical Thermochemistry*, fifth ed., Pergamon, Oxford, 1979.

LIST OF FIGURES

<i>Figure No.</i>	<i>Figure Caption</i>	<i>Page No.</i>
1.1	Schematics of Accelerator Driven System	3
1.2	Binary phase diagram of Pb-Bi system	4
1.3	Solubility of major alloying elements of steels in Pb, Bi and LBE	6
	I) Below 742 K, precipitation of Bi_3Ni on saturation	
	II) Above 742 K, precipitation of BiNi on saturation	
1.4	Corrosion behavior of steels in flowing liquid lead after 3000 h at 823 K	10
1.5	Oxygen potentials of various metal/metal oxide equilibria	13
2.1	Schematic representation of (a) diffraction and (b) image modes in TEM	32
2.2	Fluorite structure	35
2.3	Schematic representation of the variation of electrical conductivity of ThO_2 and ThO_2 (Y_2O_3) solid solutions with oxygen pressure at constant temperature	38
2.4	Electrolytic domain boundaries of calcia stabilized zirconia and yttria-doped thoria	39
2.5	Temperature-time curve for exothermic dissolution process in isoperibol calorimeter, (a) initial temperature higher than the temperature of the outer jacket (T_o), (b) T_o is between the initial and final temperatures, (c) final temperature below T_o	44
2.6	Schematics of solution calorimeter	45
2.7	A typical plot showing the method by which temperature change was determined as given in ref. 12. T_1 and T_2 represent the initial and final temperatures, respectively as shown in Fig. 2.7 a. T_{c1} and T_{c2} are the initial and final temperatures, respectively after correction as shown in Fig. 2.7 b. ΔT_c is the corrected temperature change.	48
2.8	Heat flux DSC	50
2.9	Power compensation DSC	51
2.10	Three step procedure for measuring the heat capacity of a sample	55
2.11	Typical DSC run for blank, sample and reference	55

2.12	Schematic diagram of the pseudo-isopiestic equilibration setup in a gradient furnace	58
3.1	Partial phase diagram of Fe-O system	63
3.2	Phase diagram of Bi-Fe system	64
3.3	Phase diagram of Bi-O system	65
3.4	Bi ₂ O ₃ -Fe ₂ O ₃ pseudo-binary phase diagram	69
3.5	Compositions of samples taken for equilibration (□) in the Bi ₂ O ₃ -Fe ₂ O ₃ pseudo-binary line	75
3.6	Cu tube sealed under argon atmosphere with sample inside	77
3.7	Compositions of samples taken for equilibration (5 to 16) as given in Tables 3.3 and 3.4 and possible phase fields (dotted lines) of Bi-Fe-O system	79
3.8	Compositions of samples taken for equilibration (17 to 28) as given in Tables 3.5 and 3.6 and possible phase fields (dotted lines) of Bi-Fe-O system	79
3.9	Schematic of the emf cell	83
3.10	Photograph of the emf cell used	84
3.11	Schematic of the experimental setup used for equilibrating BiFeO ₃ at different temperatures	89
3.12	XRD patterns of prepared compounds are overlapped with their PCPDF patterns (■). (a) Bi ₂₅ FeO ₃₉ , (b) BiFeO ₃ and (c) Bi ₂ Fe ₄ O ₉ . Small shift of XRD pattern from the PCPDF patterns is due to the instrumental shift.	95
3.13	Variation of emf with temperature for cell – I	99
3.14	Comparison of the measured $\Delta_f G_m^\circ$ Bi ₂ Fe ₄ O ₉ in this work with that of the data derived by Phapale et al. [15]	102
3.15	A typical plot of dissolution of KCl in double distilled water	104
3.16	A typical plot of dissolution of TRIS in 0.1 mol kg ⁻¹ HCl	105
3.17	A typical plot of dissolution of Bi ₂ O ₃ in 8.38 mol kg ⁻¹ HCl	108
3.18	A typical plot of dissolution of Fe ₂ O ₃ in 8.38 mol kg ⁻¹ HCl	108
3.19	A typical plot of dissolution of Bi ₂ Fe ₄ O ₉ in 8.38 mol kg ⁻¹ HCl	109
3.20	Comparison of molar heat capacity of Bi ₂ O ₃ measured in this work with the data reported by Knacke et al. [34]	111

3.21	Molar heat capacity of $\text{Bi}_2\text{Fe}_4\text{O}_9$. C_p^{NKR} is the molar heat capacity calculated using Neumann-Kopp rule and $C_p^{NKR,corr}$ is after correcting for magnetic contribution.	113
3.22	XRD patterns obtained after equilibrating BiFeO_3 at different temperatures in vacuum for 480 h	121
3.23	XRD patterns obtained after equilibrating BiFeO_3 at different temperatures in air for 480 h	122
3.24	XRD patterns of the products formed after equilibration of Bi, $\text{Bi}_2\text{Fe}_4\text{O}_9$, BiFeO_3 mixture in liq. Bi (a) at 873 K and (b) at 1023 K for 480 h	125
3.25	XRD patterns of the products formed after equilibration of Bi, BiFeO_3 , $\text{Bi}_{25}\text{FeO}_{39}$ mixture in liq. Bi (a) at 873 K and (b) at 1023 K for 480 h	125
3.26	Isothermal cross section of the ternary phase diagram of Bi-Fe-O system at 773 K	128
3.27	Isothermal cross section of the ternary phase diagram of Bi-Fe-O system at 1023 K	128
3.28	Variation of emf with temperature for cells II, III, IV – a and IV – b	133
3.29	A typical plot of dissolution of $\text{Bi}_{25}\text{FeO}_{39}$ in $8.38 \text{ mol kg}^{-1} \text{ HCl}$	136
3.30	Molar heat capacity of $\text{Bi}_{25}\text{FeO}_{39}$. C_p^{NKR} is the molar heat capacity calculated using Neumann-Kopp rule and $C_p^{NKR,corr}$ is after correcting for magnetic contribution.	139
4.1	Partial phase diagram of Cr-O system	147
4.2	Literature data on the Gibbs energy of formation of Cr_2O_3	149
4.3	Measured equilibrium oxygen pressures of Cr/ Cr_2O_3 system and the electrolytic domain boundaries of calcia stabilized zirconia and yttria-doped thoria solid electrolytes	
	i) Measurements using CSZ based cells	
	(a) Tretjakow and Schmalzried [6]	
	(b) Pugliese and Fitterer [7]	
	(c) Davies and Smeltzer [8]	
	ii) Measurements using YDT based cells	
	(d) Mazandarany and Pehlke [9]	

	(e) Jacob [10]	
	(f) Holzheid and O'Neill [11]	150
4.4	Phase diagram of Bi-Cr system	151
4.5	Schematic diagram of the pseudo-isopiestic equilibration setup in a gradient furnace	166
4.6	Compositions chosen for equilibration at 773 K as given in Table 4.7	168
4.7	Compositions chosen for equilibration at 1023 K as given in Table 4.8	169
4.8	XRD patterns of the samples of compositions with $\text{Bi}_2\text{O}_3\text{:Cr}_2\text{O}_3$ molar ratios of 1.9:1, 1.5:1, 1.2:1 and 1:1.5 after equilibration at 1023 K. $\text{Cu K}\alpha \lambda = 1.54184 \text{ \AA}$.	175
4.9	SEM image of ' $\text{Bi}_{22}\text{Cr}_{18}\text{O}_{60}$ '	175
4.10	XRD pattern of ' $\text{Bi}_{22}\text{Cr}_{18}\text{O}_{60}$ '; $\text{Cu K}\alpha \lambda = 1.54184 \text{ \AA}$	176
4.11	Low magnification (a) and high resolution (b) phase contrast TEM image of ' $\text{Bi}_{22}\text{Cr}_{18}\text{O}_{60}$ '	178
4.12	Electron diffraction patterns of ' $\text{Bi}_{22}\text{Cr}_{18}\text{O}_{60}$ ' and their analysis	178
4.13	(a) Ternary phase diagram of Bi-Cr-O system at 773 K (b) enlarged portion of phase diagram	184
4.14	(a) Ternary phase diagram of Bi-Cr-O system at 1023 K (b) enlarged portion of phase diagram	185
4.15	Variation of measured oxygen potential with temperature	188
5.1 a	Oxygen potentials in liquid Bi containing different oxygen concentrations and with different chemical equilibria for SS-304	204
5.1 b	Oxygen potentials in liquid Bi containing different oxygen concentrations and with different chemical equilibria for 9Cr-1Mo steel	204
5.2 a	Oxygen potentials in LBE containing different oxygen concentrations and with different chemical equilibria for SS-304	205
5.2 b	Oxygen potentials in LBE containing different oxygen concentrations and with different chemical equilibria for 9Cr-1Mo steel	205

LIST OF TABLES

<i>Table No.</i>	<i>Table Caption</i>	<i>Page No</i>
1.1	Thermophysical properties of liquid metal coolants compared with water	2
1.2	Solubility of major alloying elements of steel in Pb, Bi and LBE	6
1.3	Diffusivity of oxygen	14
1.4	Standard Gibbs energy of dissolution of oxygen	14
1.5	Solubility of oxygen	14
3.1	Literature data on $\text{Bi}_2\text{O}_3\text{-Fe}_2\text{O}_3$ system	66
3.2	Details of equilibration of samples with composition falling on $\text{Bi}_2\text{O}_3\text{-Fe}_2\text{O}_3$ pseudo-binary line	76
3.3	Details of equilibration of samples with compositions in the section bound by Bi, Fe and $\text{Bi}_2\text{Fe}_4\text{O}_9$ at 1023 K	80
3.4	Details of equilibration of samples with compositions in the section bound by Bi, Fe and $\text{Bi}_2\text{Fe}_4\text{O}_9$ at 773 K	80
3.5	Details of equilibration of samples with compositions in the section bound by Bi, $\text{Bi}_2\text{Fe}_4\text{O}_9$ and Bi_2O_3 at 1023 K	81
3.6	Details of equilibration of samples with compositions in the section bound by Bi, $\text{Bi}_2\text{Fe}_4\text{O}_9$ and Bi_2O_3 at 773 K	81
3.7	Phases formed after equilibration of BiFeO_3 (containing small amount of $\text{Bi}_{25}\text{FeO}_{39}$) in vacuum for 480 h	90
3.8	Phases formed after equilibration of BiFeO_3 (containing small amount of $\text{Bi}_{25}\text{FeO}_{39}$) in air for 480 h	90
3.9	Results of equilibration of Bi, $\text{Bi}_2\text{Fe}_4\text{O}_9$, BiFeO_3 and Bi, BiFeO_3 , $\text{Bi}_{25}\text{FeO}_{39}$ mixtures in liquid Bi	91
3.10	Emf output of cell - I as a function of temperature	99
3.11	Calculation of Gibbs energy of formation of Fe_2O_3	101
3.12	Experimentally determined values of enthalpies of dissolution (ΔH) and molar enthalpies of dissolution ($\Delta_{\text{sol}}H_{\text{m}}$) of KCl in double distilled water (mass of solvent = 300 ± 0.01 g) at 298.15 K* and 0.1 M Pa pressure. ^a	104

3.13	Experimentally determined values of enthalpies of dissolution (ΔH) and molar enthalpies of dissolution ($\Delta_{\text{sol}}H_{\text{m}}$) of TRIS in 0.1 mol kg^{-1} HCl (mass of solvent = $298.53 \pm 0.01 \text{ g}$) at 298.15 K^* and 0.1 M Pa pressure. ^a	105
3.14	Experimentally determined values of enthalpies of dissolution (ΔH) and molar enthalpies of dissolution ($\Delta_{\text{sol}}H_{\text{m}}$) of $\text{Bi}_2\text{Fe}_4\text{O}_9$, Bi_2O_3 and Fe_2O_3 in $8.38 \pm 0.01 \text{ mol kg}^{-1}$ HCl (mass of solvent = $327.15 \pm 0.01 \text{ g}$) at 298.15 K^* and 0.1 M Pa pressure. ^a	107
3.15	Reaction scheme for calculating the standard molar enthalpy of formation of $\text{Bi}_2\text{Fe}_4\text{O}_9$	109
3.16	Measured heat capacity (C_p) values of Bi_2O_3 are compared with heat capacity values reported by Knacke et al. [34] at 0.1 M Pa pressure. ^a	111
3.17	Measured and fitted heat capacity (C_p) values of $\text{Bi}_2\text{Fe}_4\text{O}_9$ are compared with heat capacity values computed through Neumann-Kopp rule using C_p of Fe_2O_3 and Bi_2O_3 from [34] (C_p^{NKR}) and using C_p of Fe_2O_3 from [37] incorporating correction for magnetic contribution and C_p of Bi_2O_3 from [34] ($C_p^{\text{NKR,corr}}$) at 0.1 M Pa pressure. ^a	112
3.18	Unit cell volumes of $\text{Bi}_2\text{Fe}_4\text{O}_9$	116
3.19	Details of emf measurements	130
3.20	Output of cell II as a function of temperature	131
3.21	Output of cell III as a function of temperature	132
3.22	Output of cell IV – a as a function of temperature	132
3.23	Output of cell IV – b as a function of temperature	133
3.24	Experimentally determined values of enthalpies of dissolution (ΔH) and molar enthalpies of dissolution ($\Delta_{\text{sol}}H_{\text{m}}$) of $\text{Bi}_{25}\text{FeO}_{39}$ in $8.38 \pm 0.01 \text{ mol kg}^{-1}$ HCl (mass of solvent = $327.15 \pm 0.01 \text{ g}$) at 298.15 K^* and 0.1 M Pa pressure. ^a	135
3.25	Reaction scheme for calculating the standard molar enthalpy of formation of $\text{Bi}_{25}\text{FeO}_{39}$	136

3.26	Measured and fitted heat capacity (C_p) values of $\text{Bi}_{25}\text{FeO}_{39}$ are compared with heat capacity values computed through Neumann-Kopp rule using C_p of Fe_2O_3 and Bi_2O_3 from [34] (C_p^{NKR}) and using C_p of Fe_2O_3 from [37] incorporating correction for magnetic contribution and C_p of Bi_2O_3 from [34] ($C_p^{NKR,corr}$) at 0.1 M Pa pressure. ^a	138
3.27	Unit cell volumes of $\text{Bi}_{25}\text{FeO}_{39}$	140
4.1	Literature data on the Gibbs energy of formation of Cr_2O_3	149
4.2	Literature data on $\text{Bi}_2\text{O}_3\text{--CrO}_3$ and $\text{Bi}_2\text{O}_3\text{--Cr}_2\text{O}_3$ pseudo-binary systems	152
4.3	Experimental details adopted for the preparation of the ternary compounds	161
4.4	Results of equilibrations of mixtures of Bi_2O_3 and Cr_2O_3 in air	162
4.5	Results of equilibrations of mixtures of Bi_2O_3 and Cr_2O_3 in vacuum	163
4.6	Results of pseudo-isopiestic experiments	166
4.7	Results of the equilibration experiments carried out at 773 K	170
4.8	Results of the equilibration experiments carried out at 1023 K	170
4.9	Peak positions and relative intensity of the lines of the XRD pattern of ‘ $\text{Bi}_{22}\text{Cr}_{18}\text{O}_{60}$ ’	176
4.10	Output of emf cell as a function of temperature	187
5.1	Composition of SS-304 and 9Cr-1Mo steel	200

Chapter 1

INTRODUCTION

1.1 Heavy liquid metal coolants

Coolants with high heat capacities and thermal conductivities are required for heat removal in high energy density systems such as Fast Breeder Reactors (FBRs). Liquid metals with high heat transfer coefficients are promising candidates for these applications. These candidates are characterized by low melting point, high boiling point, high thermal conductivity, low vapour pressure, high radiation and thermal stability, low neutron absorption cross section, etc. The liquid metal coolant which has been extensively studied and used for this application is sodium. It possesses superior physical properties, compatible with the structural materials compared to other liquid metals and is less expensive. In current generation of fast breeder reactors, liquid sodium is the coolant used in the primary and secondary coolant circuits. Heat from sodium of the secondary circuit is used to generate high pressure steam at the steam generator to run the turbine and produce electrical energy. In case of a material failure at the steam generator, high-pressure and high temperature steam can leak into sodium in the secondary circuit and result in violent sodium-water chemical reaction. Due to the corrosive nature of NaOH formed, the leak can propagate leading to shut down of the reactor which is expensive. Though innovative steam generator designs and sensitive steam leak detection techniques are being evolved, alternate coolants such as lead and lead - bismuth eutectic (LBE), which are chemically less reactive towards water / steam and air, are being considered for their use in the secondary circuit of the fast reactor [1]. Thermophysical properties of Na,

Pb and LBE are compared with those of water in Table 1.1 [2, 3]. Selected properties are compared at 773 K, typical operating temperature of fast reactor. Pb and LBE have been considered as possible alternative coolants at least at the steam generator of the FBRs. LBE had been successfully used as a coolant in submarine nuclear reactors in Russia since 1950's [4].

Table 1.1 Thermophysical properties of liquid metal coolants compared with water [2, 3]

Property	Coolant			
	Sodium	Pb	LBE	H ₂ O
Melting Point (K)	371	600.6	398	273
Boiling Point (K)	1155	2021	1927	373
Density (kg m ⁻³) at 773 K	832	10452	10066	990 (at 323 K)
Thermal conductivity (W K ⁻¹ m ⁻¹) at 773 K	140	17.70	14.41	0.67 (at 323 K)
Specific heat (J kg ⁻¹ K ⁻¹) at 773 K	1264	144.82	141.05	1.339 (at 323K)
Vapour pressure (Pa) at 773 K	5.51×10 ²	2.12×10 ⁻³	2.61×10 ⁻³	101325 Pa (at 373 K)
Viscosity (Pa s) at 773 K	2.36×10 ⁻⁴	1.81×10 ⁻³	1.31×10 ⁻³	0.89 (at 298K)
Surface tension (N m ⁻¹) at 773 K	0.1563	0.4386	0.3867	71.99 (at 298K)

Recently, LBE gained renewed interest as a coolant and spallation target in Accelerator Driven Systems (ADS). ADS have been attracting worldwide attention because of their potential to burn long lived radioisotopes present in nuclear waste with simultaneous energy production [5-7]. Minor actinides (Np, Am and Cm) are generated in the nuclear reactors by neutron absorption processes and form a significant part of the nuclear waste. Because of their long half lives, these minor actinides pose major problem for their safe disposal. By using them along with U, Pu and Th as fuels, they can be incinerated in ADS to produce short lived radioactive or inactive products while generating energy.

The schematics of an ADS system is shown in Fig. 1.1 [8]. ADS consists of three main parts, namely, (i) an accelerator for producing high energy protons, (ii) a spallation target and (iii) a sub critical core where fission reaction takes place and produces thermal energy. High energy protons are generated in the accelerator and injected onto the heavy metal target viz., Pb or LBE. These heavy metal atoms undergo spallation producing 15 to 20 high energy neutrons per spallation event. These high energy neutrons enter the sub-critical core containing (U, Pu) based fuel with minor actinides resulting in their transmutation to produce stable nucleide or those with low half lives.

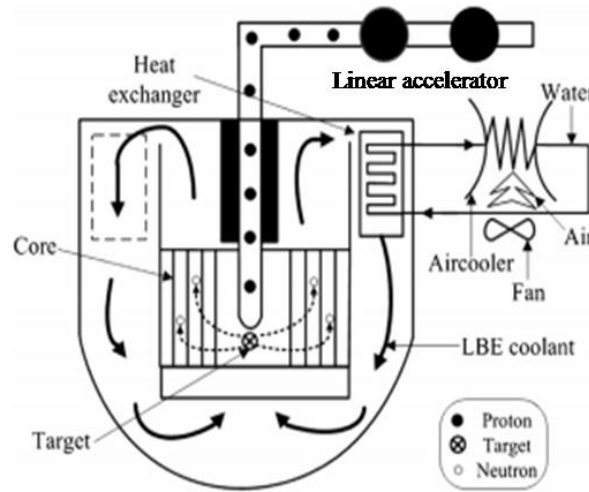


Fig. 1.1 Schematics of Accelerator Driven System [8]

1.2 Phase diagram of lead-bismuth system and lead bismuth eutectic alloy

The phase diagram of Pb-Bi binary system is shown in Fig. 1.2 [9]. Lead melts at 600.5 K while bismuth melts at 544.4 K. The maximum terminal solid solubility of Bi in Pb is 22 at% (at 460 K) whereas corresponding value of Pb in Bi is estimated to be ~ 0.5 at%. This system has no intermetallic compound with a definite composition. When solid Pb is saturated with Bi, ϵ phase having a wide non-stoichiometry precipitates and this phase is stable above 227 K. Bismuth content of this ϵ phase is \sim

27.5 at% at 227 K which increases to 40 at% at 398.5 K. It decomposes peritectically at 460 K. Above the melting point of lead, both metals are mutually soluble at all compositions. They form a eutectic with 55 at% Bi at 398.5 K. They have low vapour pressures which can be represented by the following expressions [10]:

$$\text{For Pb} \quad \log (P/\text{Pa}) = 9.7656 - 9544.8/T \quad (T: 820-1250 \text{ K}) \quad (1.1)$$

$$\text{For Bi} \quad \log (P/\text{Pa}) = 10.2523 - 9572.1/T \quad (T: 790-1350 \text{ K}) \quad (1.2)$$

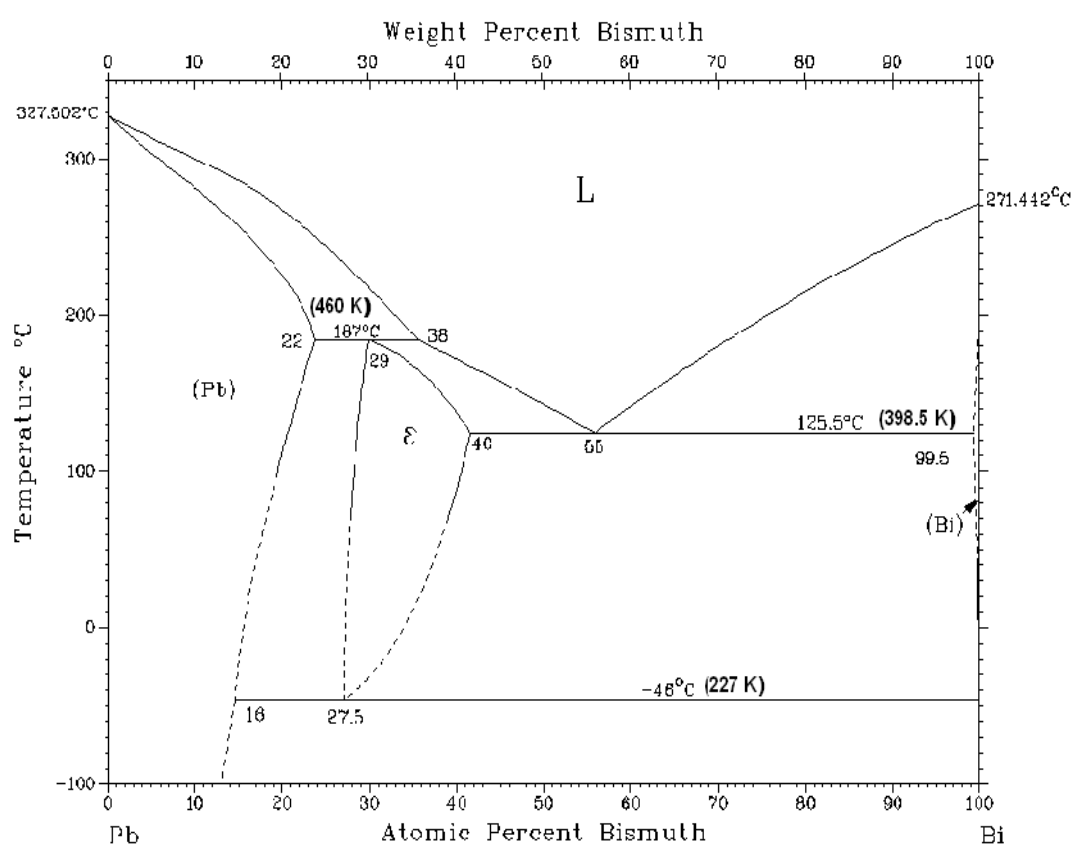


Fig. 1.2 Binary phase diagram of Pb-Bi system [9]

1.3 LBE – Compatibility problems with structural steel

Solubility of major alloying elements of steel, viz., Fe, Cr and Ni in Pb, Bi and LBE are shown in Table 1.2 and in Fig. 1.3 [9, 11-15]. Of all the components of steels, nickel has very high solubility in Pb, Bi and LBE. The solubility of iron and

chromium are approximately 2 to 3 orders lower than that of Ni. This high solubility leads to the selective depletion of nickel when nickel containing steels are used as structural material. Ni stabilizes the austenitic phase in 18-8 type stainless steels and the selective removal of Ni would lead to the transformation of austenitic phase to ferritic phase on the surface. If high Ni-Cr-Fe super alloys are used, the selective dissolution of Ni would result in relative increase in chromium content in the surface leading to precipitation of the brittle sigma phase. These phenomena would affect their mechanical properties including their capability to withstand thermal cycles. As solubility is temperature dependent, material will be transported from high temperature regions where the solubility is high to low temperature regions. This would be of serious concern at the heat exchangers and steam generators which are thin walled and are subjected to high temperature gradients. Precipitation at low temperature sections could lead to clogging of piping and also reduce the heat transfer characteristics. Relatively high solubility in liquid metals coupled with high flow velocities ($5-10 \text{ m s}^{-1}$) over long periods of time can lead to heavy corrosion and mass transfer phenomenon.

Table 1.2 Solubility of major alloying elements of steel in Pb, Bi and LBE [9, 11-15]

Metal	log(at%) in Pb	log(at%) in Bi	log(at%) in LBE
Fe	1.68 - 3006/T [9] ^a (T: 800-1300 K)	2.75 - 3980/T [9] (T: 973-1173 K)	0.5719 – 4398.6 / T [15] (T: 399-1173 K)
Cr	4.30 – 6720/T [11] (T: 1173-1473 K)	2.94 - 3610/T [13] (T: 658-901 K)	-0.2757 – 3056.1 / T [15] (T: 399-1173 K)
Ni	2.89 – 2189/T [12] (T: 773-1073 K)	1.06 – 618/T [14] (T: 755-1283 K)	2.8717 – 2932.9 / T (T: 528-742 K) 0.2871 – 1006.3 / T (T: 742-1173 K) [15]

^a Using the data from figure given in the reference.

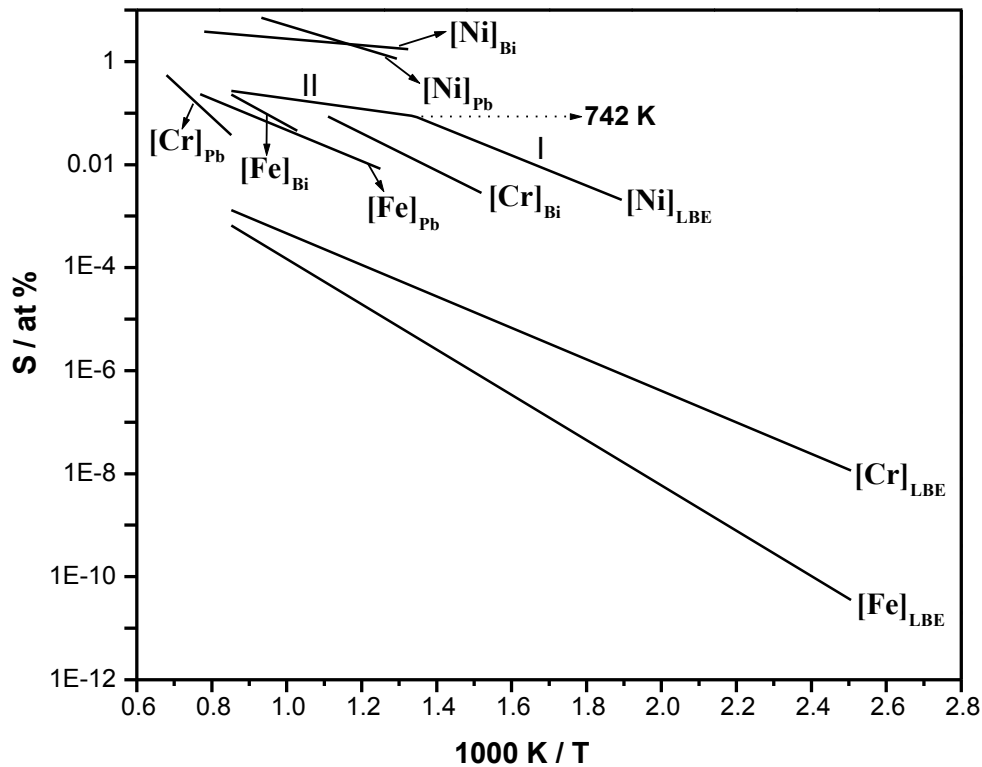


Fig.1.3 Solubility of major alloying elements of steels in Pb, Bi and LBE [9, 11-15].

I) Below 742 K, precipitation of Bi_3Ni on saturation

II) above 742 K, precipitation of BiNi on saturation

1.4 Strategies to mitigate corrosion in lead and LBE systems

Corrosion of structural steel in a circuit using Pb or LBE can be minimized by one of the following methods:

- 1) Developing and using new structural steel materials which are compatible with LBE
- 2) Forming protective coatings over the steel surface by adding inhibitors or by controlling oxygen in the coolant so as to form a passive oxide layer

1.4.1 Development of new structural steels for use in heavy liquid metal coolant systems

Because of high solubility of Ni in LBE, nickel free ferritic steels with appropriate concentrations of Cr, Mo, Si, etc are examined as potential candidates for LBE service. Cygan [16, 17] tested compatibility of several steel alloys with LBE and found the low-carbon steels to be useful container material for temperatures up to ~723 K. In the 1960s, Romano et al. [18] investigated materials for loops containing liquid Pb and LBE, and operating at temperatures up to 923 K. According to these authors, Croloy 1-1/4 (Fe-0.15C-1.25Cr-0.5Mo) showed no signs of corrosion in the temperature range of 573 to 773 K and up to 10000 h. Studies have shown that addition of Si, Ti, Mo and V to stainless steel could improve its corrosion resistance. Addition of these metals to the bulk of stainless steel can affect the mechanical properties of stainless steel. For example, Si addition is known to improve the corrosion resistance of stainless steel but addition of 1.5 to 2 wt% Si led to embrittlement and decreased its resistance to radiation damage [19]. Surface alloying of these stainless steels is considered as a better option to improve their corrosion resistance without affecting their mechanical properties. Ruiguo et al. [20] added Si

(11 wt%) to the surface of 304 stainless steel by laser melting to modify the corrosion and wear resistance. The authors found the surface alloyed steel had better corrosion resistance than 304 stainless steel. Abraham et al. [21] studied the behavior of two iron based alloys, namely AISI S-5 containing 2 wt% Si mild steel and HT-9 steel in molten lead-bismuth under a temperature gradient (823 to ~ 623-698 K) for 4500 h. The test showed that the AISI S-5 alloy was attacked by the molten lead-bismuth while HT-9 steel was not attacked. The latter was protected by a stable adherent FeCr_2O_4 - type spinel layer showing its suitability for structural material for LBE systems. A recent review by Park et al [22] on potential structural materials for LBE suggests three candidates: i) Croloy 2-1/4 steel (Fe-2.25Cr-1Mo), ii) modified 9Cr-1Mo steel (Fe-0.1C-9Cr-1Mo-0.5Mn-0.4Si-0.2V-0.08Nb-<0.2Ni) and iii) HT-9 steel (Fe-12Cr-1Mo-0.2C-0.4Si-0.5Ni-0.5Mn-0.3V-0.5W-0.02P-0.01S) on the basis of material compatibility and proton irradiation tests. According to these authors, these materials may be used only if LBE is completely deoxidized and treated with Zr or Mg inhibitors (discussed in the next section). Long term corrosion studies with these steels are being carried out in different laboratories in the world.

1.4.2 Formation of protective coatings on the steel surface

Inhibitors such as Zr or Ti are very effective in reducing the corrosion of steel by forming carbide or nitride films on the steel surface. When these inhibitors are added to the liquid metal, they react with nitrogen and carbon present in the steel to form inert and adherent layers of ZrN, TiN, or TiN + TiC [23, 24]. These insoluble films formed on the steel surface change the rate determining step of corrosion of the structural steel from liquid phase diffusion of dissolving atoms to the diffusion of dissolving atoms through the protective film. However, it is difficult to maintain the

integrity of these films on the surfaces since scrape and cuts take place during handling and installation. Since these coatings have no self healing ability, a fracture or spallation of the coating would lead to direct dissolution attack of the uncovered part of the steel by lead or LBE. The films can further lift, spall and flake during operation due to factors like differential thermal expansion [25]. Hence, inhibitors must remain in the coolant to ensure restoration of the film in the spalled areas. On the other hand, if the inhibitors are used in ADS, the products formed during the spallation reaction may react with the inhibitors in the coolant and lead to formation of undesirable products. Pre-deposition of protective ceramic coatings over the structural steels also helps in reducing corrosion. Coating of structural materials for LBE service with nitride or alumina films were reported in the literature [25]. However, providing a uniform coating on the surfaces of complex components is a challenging task.

The other way to reduce corrosion is by the in situ formation of a protective oxide layer over the structural steels by controlling the oxygen concentration in the liquid metal coolant [25]. Gorynin et al. [19] studied the corrosion behavior of two different austenitic steels namely, 15Cr-11Ni-3Si-MoNb and 16Cr-11Ni-3Mo in a loop with liquid lead at 823 K as a function of oxygen concentration. Corrosion rates observed after 3000 h are shown in Fig. 1.4. At oxygen concentration below $\sim 10^{-7}$ at% in lead, corrosion rate is determined by the solubility of the alloying components in liquid lead. The corrosion rate decreases steeply with increasing oxygen content. Above $\sim 10^{-6}$ at% of oxygen concentration, an oxide layer is formed on the steel surface and this protects the steel from dissolution of its alloying components. Further increase of oxygen concentration leads to the formation of lead oxide or a ternary

oxide depending on temperature. Gorynin et al. [19] studied the composition of the passive oxide layer formed over steels using X-ray diffraction (XRD) and microscopic spectral analysis and found that the external layer is made of Fe_3O_4 and the internal layer contains a mixed oxide $\text{FeO} \cdot \text{SiO}_2$ and $(\text{Fe}, \text{Cr})_3\text{O}_4$. According to them, for long term operations, Si steels with proper oxygen concentration in the coolant is required. They suggested a new austenitic steel with composition, 15Cr-11Ni-3Si-MoTi for the shell and internal structures and a martensitic steel of composition, 9Cr-1.5Ni-1.5Si-MoV for the piping system of the steam generator.

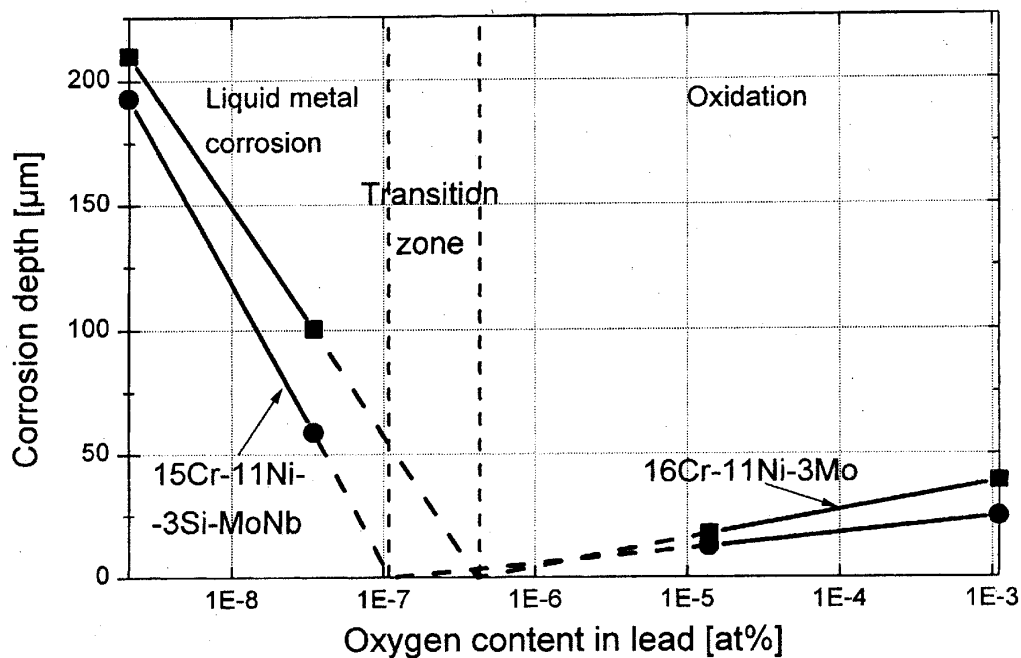


Fig. 1.4 Corrosion behavior of steels in flowing liquid lead after 3000 h at 823 K [19]

The type of protective oxide layer formed in the case of surface alloyed steel and steels without surface alloying are found to be different. Surface alloyed steels, develop an oxide layer of the surface alloying element on its surface and which will act as the protective oxide layer. Muller et al. [26] alloyed Al onto the surface of steel by pulsed intense electron beams and found the formation of a stable alumina surface film under low levels of oxygen in liquid lead. Weisenburger et al. [27] studied the

creep behavior of unmodified and Al- surface alloyed T-91 steel in LBE and found that surface alloying of steel with Al is a promising option to reduce corrosion. They observed that the alumina film formed on the surface of steel is very effective in preventing the dissolution of alloying components without influencing the mechanical properties of the base material.

Rivai et al. [28] carried out corrosion tests of several types of materials such as Al - Fe coated steels, high chromium steels, refractory metals and ceramics in LBE and liquid lead at 973 K. Oxygen concentrations in LBE and lead were 5×10^{-6} and 4.5×10^{-7} wt%, respectively. They found that a thin and stable oxide layer was formed over the Al-Fe coated steel and protected it from the attack by LBE and lead. High chromium steels were incompatible with lead alloys at 973 K. On the other hand, refractory metals such as molybdenum and tungsten, and ceramics such as SiC and Ti_3SiC_2 exhibited high corrosion resistance to liquid lead at 973 K. Short et al. [29] studied the corrosion behavior of F-91 and Fe-12Cr-2Si in static LBE at low (873 to 888 K) and high (973 to 988 K) temperatures while the oxygen potentials in LBE were maintained below as well as above those required for the formation of iron oxides. They observed that Fe-12Cr-2Si formed a protective oxide layer containing Cr, Si and Fe at both oxygen potentials. They also observed that F-91 steel underwent continuous internal oxidation and selective liquid metal dissolution of chromium at high and low oxygen potentials. Recently, Roy et al [30] studied the oxidation behavior of various austenitic stainless steels and Ni rich alloys in static LBE at 793 K with dissolved oxygen content maintained between 10^{-9} and 5×10^{-4} wt%. Their studies showed that Si and Al rich austenitic stainless steels exhibited improved corrosion resistance by forming adherent spinel oxide layer if the dissolved oxygen

concentration in LBE is sufficient for its formation. The results also showed that 18Cr-15Ni-3.7Si, 21Cr-11Ni-1.6Si and 14Cr-25Ni-3.5Al steels to be promising candidate materials.

1.5 Thermodynamic basis of the role of oxygen in mitigation of corrosion

Formation of the protective oxide layer over the structural steels and its stability are determined by thermochemical characteristics of the oxide formed. Fig. 1.5 shows the Ellingham plot for oxides of steel components along with those for Al_2O_3 , SiO_2 , PbO and Bi_2O_3 . It can be seen from the plot that the oxides of steel components and oxides of Al and Si are more stable than the oxides of lead and bismuth. Hence, at oxygen potentials lower than that required to form PbO and Bi_2O_3 in the liquid metal coolant, either the oxides of the alloying elements of the steel or the ternary oxides of Pb-M-O or Bi-M-O systems (where M = alloying elements in steels) could be formed at the steel-liquid metal interface. In the case of steels which were surface alloyed with aluminium, the protective oxide formed would be Al_2O_3 . Surface alloying with Si, leads to the formation of SiO_2 layer on the surface of the steel. In the case of steels which are not surface alloyed, the protective oxide formed would be either the oxides of the alloying elements of the steel or the ternary oxides of Pb-M-O or Bi-M-O systems (where M = alloying elements in steels). The nature and extent of formation of the oxide layer on structural steels would depend on the thermochemistry of oxygen in the coolant interface. The thermophysical and chemical properties viz., diffusivity, activity and solubility of oxygen in Pb and LBE have been determined by Ganesan et al [31] and the corresponding expressions are given in Tables 1.3 to 1.5. From the data on solubility and Gibbs energy of formation of PbO and Bi_2O_3 , the oxygen potentials in

the liquid metal at different oxygen levels can be calculated. The oxide film formed above a threshold value of oxygen potential in liquid metal effectively separates the steel surface from the liquid metal. Direct dissolution of the components of steel is significantly reduced since the diffusion coefficients of the alloying components of steel through this oxide layer are generally very low.

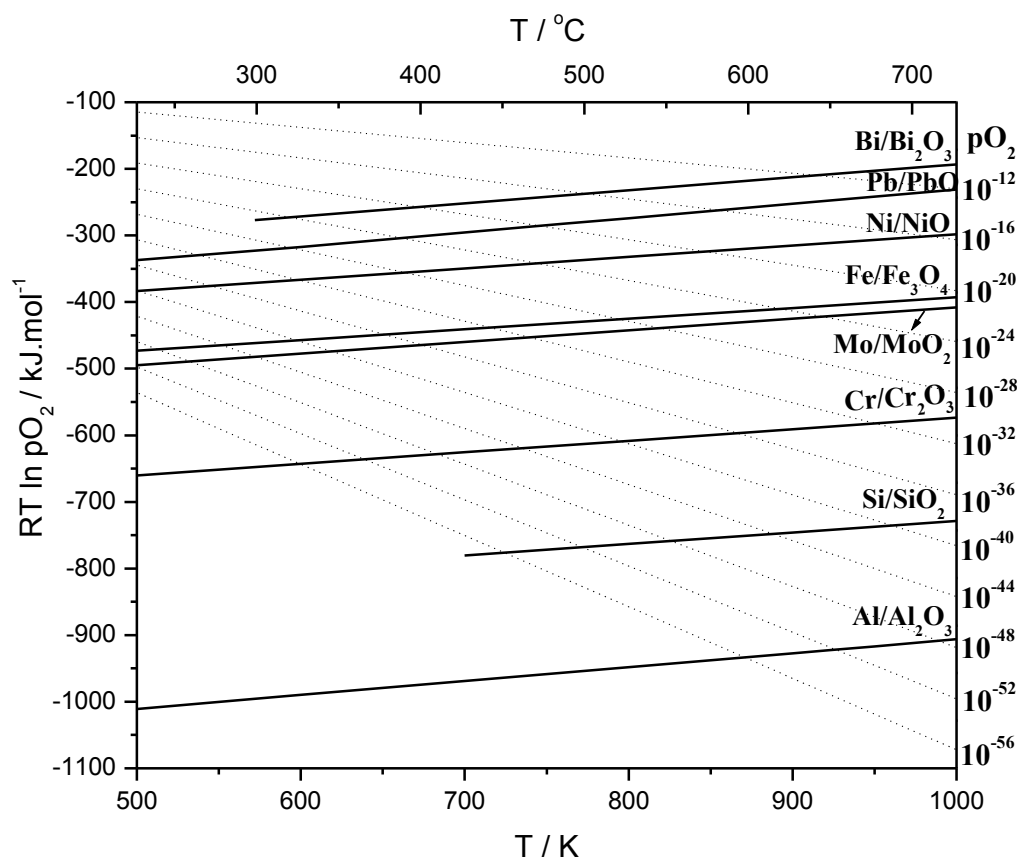


Fig. 1.5 Oxygen potentials of various metal/metal oxide equilibria

Table 1.3 Diffusivity of oxygen [31]

Diffusivity of oxygen	Temperature range
Pb: $\log (D_O^{Pb} / \text{cm}^2 \text{s}^{-1}) = -2.554 - 2384/T$	(T: 818-1061 K)
LBE: $\log (D_O^{LBE} / \text{cm}^2 \text{s}^{-1}) = -0.813 - 3612/T$	(T: 811-980 K)

Table 1.4 Standard Gibbs energy of dissolution of oxygen [31]

Standard Gibbs energy of dissolution of oxygen	Temperature range
Pb: $G_{O(Pb)}^{XS} = -121349 + 16.906T \text{ J (g atom)}^{-1}$	(T: 815-1090 K)
LBE: $G_{O(LBE)}^{XS} = -127389 + 27.938T \text{ J (g atom)}^{-1}$	(T: 812-1012 K)

Table 1.5 Solubility of oxygen [31]

Solubility of oxygen	Temperature range
Pb: $\log (S/\text{at}\% \text{O}) = -5100 / T + 4.32$	(T: 815-1090 K)
LBE: $\log (S/\text{at}\% \text{O}) = -4287 / T + 3.53$	(T: 812-1012 K)

To understand the formation and stability of the passive oxide layer on the steel surfaces, a detailed study on the interaction of Pb and Bi with the structural components of steel in the presence of oxygen is required. This in turn requires a complete knowledge of phase diagrams of Pb-M-O and Bi-M-O (where M = alloying components of steel) systems and the thermochemical data of the relevant ternary oxygen compounds of these systems. As seen earlier, because of the high solubility of Ni in lead and LBE, nickel free ferritic steels with proper concentrations of Mo, Mn, V, Si etc are recommended for use as structural material. Since iron and chromium are the major alloying elements of structural steels, knowledge on interaction of lead and bismuth with iron and chromium in steels is essential. Sahu et al. [32-37] established the phase diagrams of Pb-Fe-O and Pb-Cr-O systems and measured the thermochemical properties of the ternary compounds present in these systems. According to their data, Fe_3O_4 only would be formed at low oxygen concentrations

that are generally maintained in Pb-steel systems ($\sim 0.01\text{ppm}$). If the oxygen concentration in liquid lead is increased, PbO would precipitate at temperatures below 900 K. 'PbFe₅O_{8.5}' would be formed at high oxygen concentrations and above 900 K only. They also reported that no lead chromates would be stable in liquid lead. Interaction of Bi with the structural components of steel in presence of oxygen has not been studied. Even though, several investigations on pseudo-binary phase diagrams of Bi₂O₃-Fe₂O₃ and Bi₂O₃-CrO₃ systems have been reported in literature, studies on the ternary Bi-Fe-O and Bi-Cr-O phase diagrams have not been reported. Thermochemical data available for the binary systems are also limited. In this thesis work, detailed studies on the Bi-Fe-O and Bi-Cr-O systems have been carried out to establish the ternary phase diagrams and determine the thermochemical properties of the ternary compounds present in these systems.

1.6 Aim of this work

In the present thesis, a systematic work in the following has been carried out:

- 1) Determination of ternary phase diagrams (isothermal cross sections) of Bi-Fe-O and Bi-Cr-O systems
- 2) Measurement of thermochemical data such as Gibbs energy of formation, enthalpy of formation and the heat capacity of the ternary compounds present in the Bi-Fe-O and Bi-Cr-O systems by employing solid oxide electrolyte based emf cells, solution calorimetry and differential scanning calorimetry.

In this thesis, experimental methods and techniques used in the present study are described in Chapter 2. Chapter 3 describes the studies carried out on Bi-Fe-O ternary system and Chapter 4 describes the studies conducted on Bi-Cr-O ternary system. Chapter 5 provides the summary of the results and conclusions.

1.7 References

- 1) S. Athmalingam, Choice of coolant for secondary circuit of LMFBRs in: B.F. Gromov (Ed. in chief), Proceedings of the Heavy Liquid Metal Coolants in Nuclear Technology (HLMC-98), Vol. 2, SSC RF-IPPE, Obninsk (1999) 361-365.
- 2) Handbook on lead-bismuth eutectic alloy and lead Properties, materials compatibility, thermalhydraulics and technologies, OECD, NEA, 2015.
- 3) V. Sobolev, Database of thermophysical properties of liquid metal coolants for GEN-IV, Scientific report of the Belgian nuclear research centre, SCK•CEN-BLG-1069, 2011.
- 4) B.F. Gromov, G.I. Toshinsky, V.V. Checkunov, Y.I. Orlov, Y.S. Belomytsev, I.N. Gorelov, A.G. Karabash, M.P. Leonchuk, D.V. Pankratov, Y.G. Pashkin, Designing the reactor installation with lead-bismuth coolant for nuclear submarines. The brief history. Summarized operation results in: B.F. Gromov (Ed. in chief), Proceedings of the Heavy Liquid Metal Coolants in Nuclear Technology (HLMC-98), Vol. 1, SSC RF-IPPE, Obninsk (1999) 14-17.
- 5) Accelerator-driven systems (ADS) and fast reactors (FR) in advanced nuclear fuel cycles – A comparative study, Nuclear Energy Agency, Organization for Economic Cooperation and Development, NEA-3109, France, 2002.

- 6) Proceedings of the IAEA Technical meeting on review of national programmes on fast reactors and Accelerator Systems (ADS), 22-26 April, Karlsruhe, 2002.
- 7) Status of accelerator driven systems-Research and technology development, IAEA - TECDOC-1766, Vienna, 2015.
- 8) S. Yan, H. Fang, P. Wang, C. Sun, F. Zhao, H. Huang, Y. Wu, Modeling and control strategy of the China accelerator driven subcritical reactor, Progress in Nuclear Energy 71 (2014) 179-187.
- 9) T.B. Massalski (Ed. in chief), Binary alloys phase diagrams, The materials information society, Materials Park, 1990.
- 10) C.B. Alcock, V.P. Itkin, M.K. Horrigan, Vapour pressure equations for the metallic elements: 298-2500 K, Can. Metall. Quart. 23 (1984) 309.
- 11) M. Venkatraman, J.P. Neumann, The Cr-Pb (chromium-lead) system, Bull. Alloy Phase Diagr. 9 (1988) 155-157.
- 12) P. Nash, The Ni-Pb (nickel-lead) system, Bull. Alloy Phase Diagr. 8 (1987) 264-268.
- 13) M. Venkatraman, J.P. Neumann, The Bi-Cr (bismuth- chromium) system, Bull. Alloy Phase Diagr. 9 (1988) 271-273.
- 14) P. Nash, The Bi-Ni (bismuth-nickel) system, Bull. Alloy Phase Diagr. 6 (1985) 345-347.
- 15) S. Gossé, Thermodynamic assessment of solubility and activity of iron, chromium, and nickel in lead bismuth eutectic, J. Nucl. Mater. 449 (2014) 122–131.

- 16) R. Cygan, Circulation of lead-bismuth eutectic at intermediate temperatures, North American Aviation Report NAA-SR-253, 1953.
- 17) R. Cygan, Lead-bismuth eutectic thermal convection loop, North American Aviation Report NAA-SR-1060, 1954.
- 18) A.J. Romano, C.J. Klumet, D.H. Gurinsky, The Investigation of Container Materials for Bi and Pb alloys, Part I, Thermal Convection Loops, Brookhaven National Laboratory Report BNL-811 (1963).
- 19) I.V. Gorynin, G.P. Karzov, V.G. Markov, V.A. Yakovlev, Structural materials for atomic reactors with liquid metal heat - transfer agents in the form of lead or lead-bismuth alloy, *Met. Sci. Heat Treat.* 41 (1999) 384-388.
- 20) L. Ruiguo, F. Jun, F. Zhongchao, Microstructure and properties of laser surface alloying 304 stainless steel with Si, *Chin. J. Met. Sci. Technol.*, 8 (1992) 335-338.
- 21) D.P. Abraham, L. Leibowitz, V.A. Maroni, S.M. Mc Deavitt, A.G. Raraz, Corrosion of structural materials by lead based reactor coolants, in: IAEA-TECDOC-1356, Emerging nuclear energy and transmutation systems: Core physics and engineering aspects, International Atomic Energy Agency, Vienna (2003) 329–339.
- 22) J.J. Park, D.P. Butt, C.A. Beard, Review of liquid metal corrosion issues for potential containment materials for liquid lead and lead–bismuth eutectic spallation targets as a neutron source, *Nucl. Engg. Des.* 196 (2000) 315-325.

- 23) O.F. Kammerer, J.R. Weeks, J. Sadofsky, W.E. Miller, D.H. Gurinsky, Zirconium and titanium inhibit corrosion and mass transfer of steels by liquid heavy metals, *Trans. AIME*, 212 (1958) 20-25.
- 24) J.R. Weeks, Lead, bismuth, tin and their alloys as nuclear coolants, *Nucl. Eng. Des.* 15 (1971) 363-372.
- 25) N. Li, Active control of oxygen in molten lead–bismuth eutectic systems to prevent steel corrosion and coolant contamination, *J. Nucl. Mater.* 300 (2002) 73-81.
- 26) G. Muller, V. Engelko, A. Weisenburger, A. Heinzl, Surface alloying by pulsed intense electron beams, *Vacuum* 77 (2005) 469-474.
- 27) A. Weisenburger, A. Jianu, W. An, R. Fetzer, M.D. Giacco, A. Heinzl, G. Muller, V.G. Markov, A.D. Kasthanov, Creep, creep-rupture tests of Al-surface alloyed T-91 steel in liquid lead bismuth at 500 and 550°C, *J. Nucl. Mater.* 431 (2012) 77-84.
- 28) A.K. Rivai, M. Takahashi, Corrosion investigations of Al-Fe coated steels, refractory metals and ceramics in lead alloys at 700°C, *J. Nucl. Mater.* 398 (2010) 146-152.
- 29) M.P. Short, R.G. Ballinger, H.E. Hanninen, Corrosion resistance of alloys F91 and Fe-12Cr-2Si in lead bismuth eutectic up to 715°C, *J. Nucl. Mater.* 434 (2013) 259-281.
- 30) M. Roy, L. Martinelli, K. Ginestar, J. Favergeon, G. Moulin, Dissolution and oxidation behavior of various austenitic steels and Ni rich alloys in lead-bismuth eutectic at 520°C, *J. Nucl. Mater.* 468 (2016) 153-163.

- 31) R. Ganesan, T. Gnanasekaram, R.S. Srinivasa, Diffusivity, activity and solubility of oxygen in liquid lead and lead-bismuth eutectic alloy by electrochemical methods, *J. Nucl. Mater.* 349 (2006) 133-149.
- 32) S.K. Sahu, R. Ganesan, T. Gnanasekaran, Studies on phase diagram of Pb–Cr–O system, *J. Nucl. Mater.* 376 (2008) 366-370.
- 33) S.K. Sahu, R. Ganesan, T. Gnanasekaran, Standard molar Gibbs free energy of formation of Pb_5CrO_8 (s), Pb_2CrO_5 (s), and PbCrO_4 (s), *J. Chem. Thermodyn.* 42 (2010) 1–7.
- 34) S.K. Sahu, R. Ganesan, T.G. Srinivasan, T. Gnanasekaran, The standard molar enthalpies of formation of Pb_2CrO_5 (s) and Pb_5CrO_8 (s) by acid solution calorimetry, *J. Chem. Thermodyn.* 43 (2011) 750-753.
- 35) S.K. Sahu, M. Sahu, R.S. Srinivasa, T. Gnanasekaran, Determination of heat capacities of PbCrO_4 (s), Pb_2CrO_5 (s), and Pb_5CrO_8 (s), *Monatsh. Chem.* 143 (2012) 1207–1214.
- 36) S.K. Sahu, R. Ganesan, T. Gnanasekaran, Studies on the phase diagram of Pb–Fe–O system and standard molar Gibbs energy of formation of ‘ $\text{PbFe}_5\text{O}_{8.5}$ ’ and $\text{Pb}_2\text{Fe}_2\text{O}_5$, *J. Nucl. Mater.* 426 (2012) 214-222.
- 37) S.K. Sahu, R. Ganesan, T. Gnanasekaran, The standard molar enthalpies of formation of $\text{Pb}_2\text{Fe}_2\text{O}_5$ (s) and $\text{PbFe}_5\text{O}_{8.5}$ (s) by acid solution calorimetry, *J. Chem. Thermodyn.* 56 (2013) 57–59.

Chapter 2

EXPERIMENTAL METHODS

This chapter discusses details of all the experimental methods employed in this thesis work: (a) preparation of the compounds by different methods, (b) various kinds of equilibration studies, (c) structural and compositional characterization by X-ray Diffraction (XRD), Scanning Electron Microscopy (SEM) and Transmission Electron Microscopy (TEM) and (d) thermal characterization by Thermo Gravimetry and Differential Thermal Analysis (TG-DTA). This chapter also describes the details of oxygen pressure measurements using solid oxide electrolyte based emf cells, heat capacity measurements using DSC, enthalpy measurements using isoperibol solution calorimeter and isopiestic experiments at high oxygen pressures to identify the coexisting phases.

2.1 Preparation of compounds

Ternary compounds of Bi-Fe-O and Bi-Cr-O systems were prepared by two different methods, namely 1) solid state reaction between oxides and 2) coprecipitation and calcination of hydroxides.

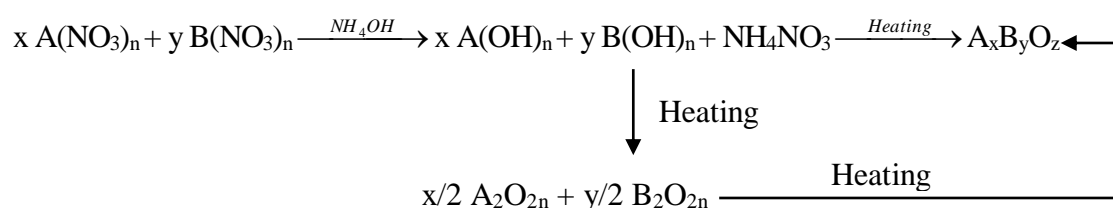
2.1.1 Solid state reaction between oxides [1]

This method involves compacting homogeneous mixtures of the constituent oxides and heating the compacts at a particular temperature for a prolonged duration. The product forms initially at the interface between the particles of the reactants. For further reaction, the reactants need to be transported to the interface by diffusion. Since diffusion of species in the solids is slower compared to that in the liquids and

gases, it is necessary to heat the reactant oxides to high temperatures to facilitate the reaction to take place. Compaction and pelletization of the reactant mixture will also help to bring the reactants into intimate contact. Because of the accumulation of the products at the interface, a diffusion barrier develops and hinders further reaction. Hence, one or two intermediate grindings are required to break the diffusion barrier and to push the reaction to completion. Homogeneous mixing of the reactants is very important for solid state reactions. Usually this is carried out by manually mixing the reactants in a mortar and pestle or by mechanical mixing with a ball mill.

2.1.2 Coprecipitation and calcination of hydroxides [1]

This method involves the preparation of a homogeneous solution of appropriate composition of the nitrates or chlorides of the reactant metals. This is followed by quantitative coprecipitation of the metals as their hydroxides. The coprecipitated hydroxides are then heated to form the ternary compound either directly or through intermediate formation of oxides. This can be represented as:



Compared to the solid state reaction method, molecular level mixing of the reactants is achieved in the solution route which results in the increased homogeneity of the mixture of hydroxides. This enables the formation of the compound at temperatures lower than those required for the solid state reaction between oxides and results in the product with fine particle size. Obviously this method would apply to metal hydroxides having very low solubility products.

2.2 Phase equilibration studies [2]

Phase equilibration is a simple method employed to find out the phases that coexist in a system at a particular temperature. This involves preparing a homogeneous mixture of appropriate quantities of the oxides, ternary compounds and elemental metals to obtain a sample of desired composition. The mixture is compacted into pellets and heated in suitable containers under appropriate environment for a prolonged period of time followed by quenching in ice cold water or in liquid nitrogen. Quenching the samples after equilibration helps to preserve the phases that co-exist at the equilibration temperature at ambient conditions. It is preferable to heat the samples under inert gas environment or in vacuum by placing them in low volume and closed containers so that the composition of the samples remain constant throughout the equilibration. To confirm the attainment of equilibrium, samples can be quenched after a period of time, ground and characterized by XRD. The samples can be compacted again into pellets and equilibrated under the same experimental conditions. The presence of identical phases after two successive long term equilibrations would prove the attainment of equilibrium. Additional way of confirming the attainment of equilibrium is to equilibrate samples with combination of different oxides and ternary compounds but having the same overall composition. If the final phases after the long term equilibrations are same in all these samples, the attainment of equilibrium and the coexistence of the phases would be confirmed. In this present work, phase equilibration studies were carried out to establish the isothermal cross sections of the ternary Bi-Fe-O and Bi-Cr-O systems.

2.3 Techniques for materials characterization

2.3.1 X-ray Diffraction (XRD) [1, 3, 4]

X-ray diffraction is the most important and widely used technique for the characterization of materials and for the determination of their crystal structures. Diffraction is essentially a scattering phenomenon where the atoms or ions in a crystal scatter the characteristic X-rays (generated from a source) that fall upon it and obey the following condition:

$$n\lambda = 2d\sin\theta \quad (2.1)$$

where λ is the wavelength of X-ray used, d is the interplanar spacing in the crystal, θ is the angle of incidence of the X-rays and n is the order of reflection. This is known as Bragg's law of diffraction. An X-ray diffraction equipment consists of an X-ray source, sample holder and a detector.

2.3.1.1 Generation of X-rays and general experimental methods

X-rays are produced when high energy charged particles such as electrons generated by a hot filament collide a target material. Electrons emitted from the hot filament are accelerated by application of some tens of thousands of voltage to the target material. During the collision, the electrons are decelerated and the energy lost by the electrons is converted to electromagnetic radiation. All the electrons would not decelerate in identical manner. Velocity of some of the electrons reduces to zero in one impact and release all their energy at once giving X-rays of high energy (low wavelength). Other electrons lose their energy after multiple collisions until all of the kinetic energy is released as X-rays of low energy (high wavelength). This results in the emission of a mixture of different wavelengths called 'white radiation' or

continuous spectrum from the target. When the accelerating voltage is increased beyond a certain critical value, electrons with high energy strike the metal target and electrons from the inner shell of the target atoms are knocked out creating a vacant orbital. Subsequently, electrons from the outer shells occupy the inner vacant orbitals with simultaneous emission of characteristic X-rays. These characteristic X-rays are superimposed upon the continuous spectrum. For copper, the $2p \longrightarrow 1s$ transition gives X-rays of wavelength 1.54184 \AA called K_α and $3p \longrightarrow 1s$ transition gives X-rays of wavelength 1.3922 \AA called K_β . The K_α transition occurs much more frequently than K_β transition and this intense K_α radiation is used in diffraction experiments. In order to separate the white and K_β radiations from K_α , a Ni filter is used in the XRD instruments. The K_α radiation is, in fact, a doublet with $K_{\alpha 1} = 1.54056 \text{ \AA}$ and $K_{\alpha 2} = 1.54433 \text{ \AA}$ because of the two possible spin states of the $2p$ electron which makes the transition relative to the spin of the vacant $1s$ orbital. In some X-ray instruments, $K_{\alpha 1}$ and $K_{\alpha 2}$ radiations are not resolved and the weighted average of these two i.e., 1.54184 \AA is used. In other instruments, $K_{\alpha 1}$ and $K_{\alpha 2}$ radiations are resolved using a monochromator (graphite or germanium) which filters $K_{\alpha 2}$ and passes only $K_{\alpha 1}$ radiation through it. Though copper, cobalt, molybdenum etc are used as target metals, target with copper K_α radiation having a wavelength of 1.54184 \AA is generally used for diffraction experiments.

An arbitrary setting of a single crystal in a beam of X-rays will not produce any diffracted beams. For this to occur, λ or θ should be varied continuously during the experiment. Depending upon the ways these quantities are varied three main diffraction methods exist. They are 1) Laue method 2) Rotating single crystal method and 3) Powder method. In Laue method, with θ fixed, λ will be varied. In the other

two methods, with fixed λ value, θ would be varied. Since λ is fixed in most of the instruments, Laue method is not used as widely as the single crystal and powder methods. While single crystal method is used for finding the space group and for the determination of crystal structure, powder technique is used for the qualitative identification of crystalline phases or compounds. In this work, powder method was used and a brief description of this technique is given below.

2.3.1.2 Powder diffraction method

In this method, a monochromatic beam of X-rays is made to fall on a finely divided sample held in a suitable holder. Sample in the form of powder enables random arrangement of the crystals and lattice planes in all possible orientations. Among the randomly oriented lattice planes, some planes will be exactly oriented at Bragg angle θ to the incident beam and these planes will diffract X-rays. The diffracted beams will be detected by a detector and sent to a multi channel pulse height analyzer and the output is fed to a data acquisition system.

The most commonly used detectors for powder X-ray diffraction are scintillation and gas filled detectors. Scintillation detectors work on the ability of X-rays to cause certain substances to fluoresce visible light. When X-ray photon collides with a scintillator which is usually a sodium iodide crystal activated with a small amount of thallium, the latter produces photons in the blue region of the visible spectrum. These photons enter into a photomultiplier tube where these photons are absorbed by a photocathode (which is a light sensitive material) and electrons are ejected. These electrons are multiplied by electrodes known as metal channel dynodes. The number of electrons ejected by the photocathode is proportional to the number of visible photons which strike it, which in turn is proportional to the energy

of the X-ray photon. Gas filled detectors work on the principle that X-ray photons can ionize inert gas atoms such as argon or xenon into an electron (e^-) and ion (e.g. Ar^+) pair. Since the ionization energy required to eject an outer electron is low compared to the energy of the X-ray photon, one X-ray photon can produce several hundreds of ion pairs. It consists of a cylindrical metal shell filled with an inert gas which acts as the cathode and a metal wire which acts as anode. A constant potential difference say, 200 V is maintained between cathode and anode. When X-ray photons enter the cylinder, they ionize the inert gas producing photoelectrons and positive ions. Under the influence of the electric field, the photoelectrons move towards the anode metal wire and ions move towards the cathode shell. All the electrons and ions will be collected at the electrodes and this results in a small constant current which is a measure of the X-ray intensity. In the same instrument, if the voltage is increased to 1000 V, due to the high electric field, multiple ionization takes place which results in the ionization of a large number of atoms (10^3 to 10^5 times larger than in normal case) by the absorption of a single X-ray photon. As a result of this, an avalanche of electrons hits the metal wire and causes a detectable current in the external circuit. For converting the Ar^+ ions back to Ar atoms, a quenching gas such as methane (CH_4) is mixed with the inert gas (e.g. 90% Ar : 10% CH_4). Position sensitive detectors (PSDs) are a special kind of gas filled detectors where the anode wire is long and curved and is connected to a multi channel analyzer (MCA). When X-ray beams which are diffracted at particular 2θ angles from the specimen enter the side window of the cathode shell at particular points, it causes pulse formation at those points. The pulses then travel to the two ends of the wire, and the position at which the pulse originates may be determined by comparing the amplitude or the arrival time of the pulses at the ends of the anode. The pulses are stored in the MCA according to the pulse position

on the wire. This enables PSDs to record data over whole range of scattering angles, which can be useful where speed of acquisition is crucial.

Each crystalline phase has a characteristic X-ray diffraction pattern which can be used as a fingerprint for its identification. The powder diffraction patterns of almost all elements and compounds have been collected as Powder Diffraction Files (PDF) and maintained by Joint Committee of Powder Diffraction Standards (JCPDS). An unknown phase can be identified by comparing its powder XRD pattern with these Powder Diffraction Files. Powder method can also be used for studying solid solution formation, determination of crystallite size, study of crystal distortions by stress, measurements of thermal expansion coefficients, determination of high temperature phase transitions (by high temperature XRD), etc.

2.3.1.3 Source of background radiation in XRD

The main source of background radiation in XRD is the fluorescence of the sample. Fluorescence occurs when the incident beam (emitted from the target) knocks out electrons from the inner shell of the atoms in the sample. Then the electrons from the outer shell drop down to occupy empty levels in the inner shells and while doing so they emit their excess energy as X-ray. For example, the ionization potentials of 1s electron in nickel, cobalt and iron correspond to 1.4880, 1.6081 and 1.7433 Å and therefore Cu - K_{α} radiation with a wavelength of 1.54184 Å may ionize 1s electron in cobalt and iron but not in nickel. So samples containing cobalt and iron fluoresce strongly in Cu - K_{α} radiation. If the fluorescent radiation is weak, it can be absorbed by using a secondary monochromator (graphite monochromator) between the sample and the detector. If it is strong, it is better to change the primary beam ie, instead of Cu - K_{α} , Mo - K_{α} or Fe - K_{α} can be used.

In the present work, the phase characterization of all samples was carried out by X-ray powder diffractometer (M/s. Inel, France) with Cu - K α and with a position sensitive detector.

2.3.2 Electron microscopy

The smallest size of an object that can be examined through an optical microscope is limited by the wavelength of the visible light (0.4-0.7 μ m). For viewing sub micrometre-sized particles, it is essential to use electron microscopy. An electron microscope uses electrons instead of visible light and their low and variable wavelength makes it possible to get a resolution which is several thousand times better than that is achievable with a light microscope. Electron microscopes are of two types i.e., 1) Scanning Electron Microscope (SEM) where electrons reflected off from the surface of the sample are analyzed and 2) Transmission Electron Microscope (TEM) where electrons that pass through the sample are analyzed. While SEM is used to study the surface morphology of the samples, by using TEM, details on crystal structure and imaging of dislocations, tiny precipitates, grain boundaries and other defect structures in solids can be obtained.

2.3.2.1 Scanning Electron Microscopy (SEM) [1, 5 - 7]

In a scanning electron microscope, the surface of a sample is scanned using an accelerated beam of electrons from an electron gun. When electrons interact with the sample, several phenomena like absorption, secondary electron emission, backscattering, X-ray emission, auger electron emission, diffraction etc can happen. In SEM, the low energy secondary electrons emitted from the near surface layers ($\approx 50\text{\AA}$) of the sample and high energy electrons backscattered from some depth in the sample

and have energy close to the impinging electrons are measured to build up an image of the sample. As secondary electrons are emitted from the near surface of the sample, secondary electron imaging is more sensitive to surface topography. Backscattered electrons have the advantage that they are sensitive to the atomic number of the nuclei they scatter from and as a result heavier elements which backscatter more efficiently appear as bright and lighter elements appear as dark in backscattered image. This helps to distinguish the phases in the sample. Most of the scanning electron microscopes have an additional facility called EDS (Energy Dispersive X-ray Analysis) for measuring the energy of X-rays generated from the sample due to electron interaction. These X-rays are characteristic emission spectra of the elements present in the sample. By scanning the energy and intensity of the emitted X-rays, it is possible to identify the elements in the sample and their composition.

In this work, the elemental composition of the sample, ' $\text{Bi}_{22}\text{Cr}_{18}\text{O}_{60}$ ' was studied using SEM-EDS (M/s. Philips, Netherlands, Model No. XL30).

2.3.2.2 Transmission Electron Microscopy (TEM) [7, 8]

TEM is a high resolution tool compared to SEM and enables the measurement of sizes of nanoparticles, grains, crystallites and atomic arrangements in a material. It also enables detection of low quantities of new phases which cannot be detected by XRD. In TEM, a beam of accelerated electrons is transmitted through an ultra-thin specimen. While passing through the specimen, the electron beam interacts with the specimen and as a result, an image is formed. This image is magnified and focussed onto an imaging device. The main components of a TEM are: a) illumination system composed of an electron gun and condenser lenses which produce a fine electron beam, b) an objective lens which produces the diffraction pattern and an initial magnified

image of the specimen, c) a magnification system to produce the final image and d) a sample chamber

2.3.2.2.1 Modes of operation

TEM can be operated in two basic modes: diffraction mode and image mode. Schematic representations of image and diffraction modes are presented in Fig. 2.1. In the conventional mode i.e., image mode, TEM is operated to form images by bright field, dark field or lattice image (phase) contrast. A bright field or dark field image is formed when only direct (diffracted) beam is used for image formation. This is achieved with the help of an objective aperture, which prevents the passage of all other beams to the recording system. A lattice fringe (phase contrast) is formed by the interference of at least two beams in the image plane of the objective lens. During the image-forming process, all the beams through the objective aperture are made to recombine such that, their phases and amplitudes are preserved. In the diffraction mode, the objective lens produces a diffraction pattern of the specimen in its back focal plane. The first image is rotated 180° against the diffraction pattern. Then the diffraction pattern and the first image are magnified using intermediate and projector lenses. The diffraction pattern contains electrons from the whole area of the specimen which was illuminated by the beam. Such a pattern is not very useful. Also, the direct beam is sometimes so intense that it will damage the viewing screen or saturate the CCD camera. Hence, in order to get diffraction pattern from a specific area of the specimen and to reduce the intensity of the direct beam, an aperture can be inserted above the specimen which would only permit electrons that pass through it to hit the specimen. It is called selected area electron diffraction (SAED). Different substances will give different diffraction patterns. For example, a single crystal generates a spot

pattern, a poly-crystalline material produces a ring pattern and an amorphous or glassy material generates a series of diffuse halos in the diffraction pattern.

Scanning transmission electron microscopy (STEM) which is an advanced version of TEM combines the scanning ability of SEM with the high resolution achieved in TEM. In STEM, the probe used is very small (10 - 15 nm) compared to TEM. STEM can be used to study the energy losses of the transmitted electrons which is called electron energy loss spectroscopy (EELS) or to investigate the X-rays emitted from the specimens (by electron diffraction spectroscopy) to determine the chemical composition of the specimen.

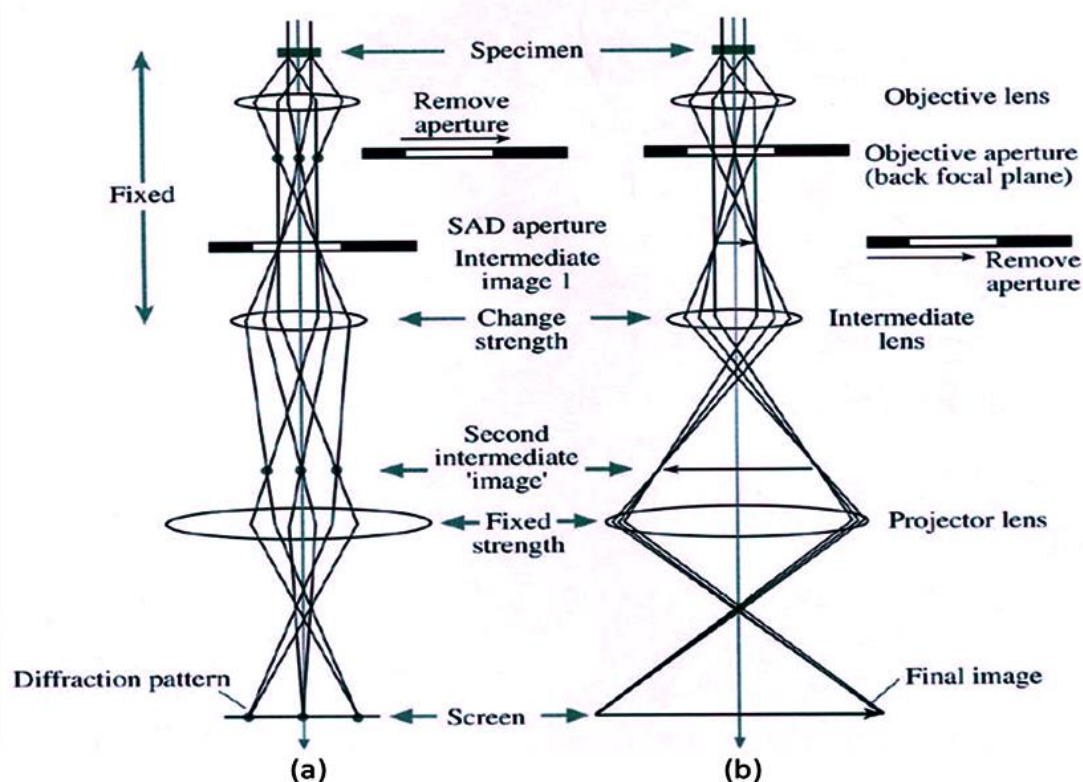


Fig. 2.1 Schematic representation of (a) diffraction and (b) image modes in TEM

2.3.2.2.2 Sample preparation for TEM

Since electrons have to be transmitted through the sample, the thickness of the sample should be of the order of hundreds of nanometers only. When the sample thickness is high, electrons will be completely absorbed by the sample. Sample preparation for TEM is a complex process which includes several processes like chemical thinning, electropolishing, ion beam thinning etc.

In this work, structure and composition of the sample, ' $\text{Bi}_{22}\text{Cr}_{18}\text{O}_{60}$ ' was studied using transmission electron microscope (Tecnai G2 F30) operated at 300 kV.

2.4 Simultaneous Thermogravimetry (TG) and Differential Thermal Analysis (DTA) [1]

Thermogravimetry is a technique for measuring the weight change of a sample as a function of temperature or time. DTA measures the temperature difference between the sample and an inert reference when they are subjected to identical heating or cooling cycles and is used to detect physical or chemical processes in the sample with absorption or release of heat energy. Usually, TG and DTA are coupled in a single instrument and this enables the simultaneous determination of thermogravimetry and differential thermal analysis of samples.

In a typical TG / DTA experiment, a few milligrams of the sample is taken in a suitable crucible and is subjected to a predetermined temperature programme. From the weight change of the sample, it is possible to find out the various processes like decomposition, oxidation, reduction and removal of water of crystallization that occur in the sample. Temperature of the sample and reference would be the same until a thermal event occurs in the sample. During a thermal event, the sample temperature either lags behind or leads the reference temperature which gives rise to endothermic

or exothermic peak in DTA. The area under the DTA peak can be used to determine the enthalpy change of the process by proper calibration. When an evolved gas analyzer (EGA) is attached to a TG-DTA, qualitative information about the chemical nature of evolved gases from the sample can be obtained and correlated with the measured weight loss and thermal event of the sample.

In the present study, TG/DTA system (SETSYS Evolution 16/18 model, M/s Setaram, France) was used for checking the thermal stability of BiFeO₃.

2.5 Oxygen potential measurements employing solid oxide electrolytes [9, 10]

Solid electrolytes are those solids with high conductivity and this conductivity is mainly due to ions. The total conductivity of an ionic solid is given by

$$\sigma_T = \sigma_{i+} + \sigma_{e+} + \sigma_h \quad (2.2)$$

where σ_i , σ_e and σ_h represent conductivities due to ions, electrons and holes, respectively. The electronic / hole conductivity in solid electrolytes is very small and their contribution to the total conductivity would be negligible. For a solid electrolyte to be useful, the transport number of the ion of interest, defined as the ratio of ionic conductivity to total electrical conductivity (σ_i / σ_T), should be greater than 0.99. The ionic conductivity of solid electrolytes is as high as $10^{-1} - 10^{-4} \text{ ohm}^{-1} \text{ cm}^{-1}$ at the chosen operating temperature. Ionic conductivity in solid electrolytes arises due to the specific features of its crystal structure and the presence of defects. These defects can be due to vacancies, interstitials, schottky defects, frenkel defects, impurities etc. The temperature dependence of the conductivity of electrolytes can be represented by the general expression as given below:

$$\sigma = A \exp (-E_a / kT) \quad (2.3)$$

where σ is the ionic conductivity, A is the pre-exponential factor, k is Boltzmann constant and E_a is the activation energy for ionic transport. Both activation energy and pre-exponential factor depend upon the oxide system under consideration.

Most of the solid electrolytes which exhibit predominant oxide ion conduction possess either fluorite or distorted fluorite structure. The fluorite structure is shown in Fig. 2.2. It can be described as a face centered cubic arrangement of cations with anions occupying all the tetrahedral sites. In fluorite structure, each metal cation is surrounded by 8 oxygen anions and each oxygen anion is tetrahedrally coordinated by four metal cations. It is important to note that large octahedral voids are vacant in this structure and this kind of open structure permits oxide ion movement from one lattice position to another with low activation energy (~ 1 eV).

Doped- ThO_2 and stabilized- ZrO_2 are the commonly used solid oxide electrolytes. While ZrO_2 -based electrolytes with high conductivity can be used in high oxygen partial pressure range, ThO_2 -based electrolytes with greater thermodynamic stability are suitable for use in low oxygen pressure ranges.

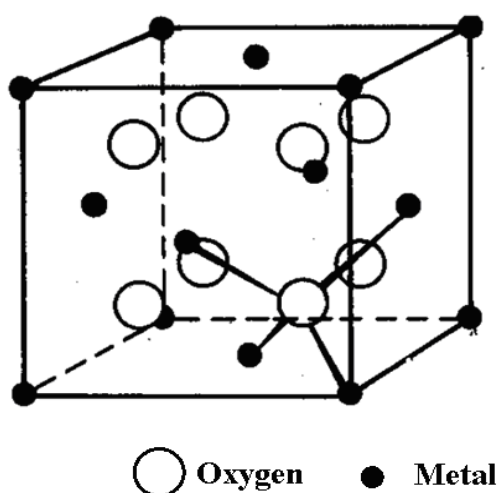


Fig. 2.2 Fluorite structure

2.5.1 Defect structure and conduction mechanism in oxide based solid electrolytes

2.5.1.1 Pure MO₂ based electrolyte

The defect equilibria and conduction mechanism in fluorite type oxides can be described by taking ThO₂ as an example. Studies have shown that the ionic defects occurring in fluorite type structures are essentially interstitial anions and anionic vacancies. Hence, the predominant ionic defects in thoria are oxygen vacancies and oxygen interstitials.

Considering only fully ionized defects, the formation of an anionic Frenkel defect in ThO₂ can be written as:



When the concentration of oxygen anions is large compared to the number of defects, the equilibrium constant for the above reaction can be written as:

$$K_1 = [V_o^{\bullet\bullet}] [O_i''] \quad (2.5)$$

Any variation in the oxygen pressure in equilibrium with ThO₂ changes the concentration of ionic and electronic defects. At high oxygen pressures, there will be an equilibrium between oxygen in the surrounding atmosphere and interstitial oxide ions in the solid which will lead to positive hole conduction in the electrolyte, i.e.,



The equilibrium constant of the above reaction can be written as:

$$K_2 = [O_i''] * p^2 * p_{O_2}^{-1/2} \quad (2.7)$$

where p represents the number of positive holes per unit volume. If $[O_i'']$ is large and constant, equation (2.7) becomes:

$$p \propto p_{O_2}^{1/4} \quad (2.8)$$

which indicates a $p_{O_2}^{1/4}$ dependence of the hole conductivity.

At low oxygen pressures, oxygen vacancies are formed which are electrically compensated by electrons dissociated from vacant oxygen sites.



The equilibrium constant for the above reaction can be written as:

$$K_3 = [V_o''] * n^2 * p_{O_2}^{1/2} \quad (2.10)$$

If $[V_o'']$ is large and constant, equation (2.10) becomes:

$$n \propto p_{O_2}^{-1/4} \quad (2.11)$$

which indicates a $p_{O_2}^{-1/4}$ dependence of conductivity due to electrons.

2.5.1.2 Doped ThO₂

When ThO₂ is doped with Y₂O₃, addition of two yttrium ions creates one oxygen vacancy. It can be represented as:



At a fixed oxygen pressure, increase in oxygen vacancy concentration results in decrease in the concentration of oxygen interstitials (eq. 2.5), increase in the electron hole concentration (eq. 2.7) and decrease in the electron concentration (eq.

2.10). The effects of Y_2O_3 additions on the electrical conductivity of ThO_2 are schematically shown in Fig. 2.3. From the figure, it is clear that the ionic conductivity (σ_{ion}) and electron hole conductivity (σ_h) increase and electron conductivity decreases with increasing Y_2O_3 content.

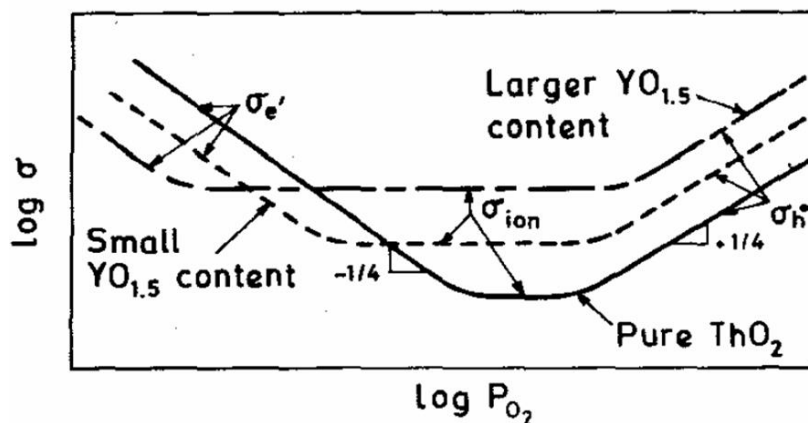


Fig. 2.3 Schematic representation of the variation of electrical conductivity of ThO_2 and $ThO_2 (Y_2O_3)$ solid solutions with oxygen pressure at constant temperature

2.5.2 Electrolytic Domain

The temperature and oxygen pressure regions within which the electronic and hole contributions to the total electrical conductivity of a solid electrolyte are less than 1% is called the electrolytic domains of the solid electrolyte. The electrolytic domain of ZrO_2 (15 mol% CaO) and ThO_2 (15 mol% $YO_{1.5}$) electrolytes are shown in Fig. 2.4 [10]. The upper and lower boundary lines are known as upper electrolytic domain boundary (UEDB) and lower electrolytic domain boundary (LEDB), respectively. Within these domain boundaries, the fraction of the ionic conductivity is greater than 0.99 at all temperatures and oxygen pressures. For example, the electrolytic domain of ThO_2 (15 mol% $YO_{1.5}$) is between $\sim 10^{-7}$ and 10^{-24} atm of p_{O_2} at 1273 K. At oxygen pressures above $\sim 10^{-6}$ atm, hole conduction is greater than 1% and at oxygen pressures below $\sim 10^{-24}$ atm, electronic conductivity becomes greater than

1%. For ZrO_2 (15 mol % CaO), electrolytic domain boundaries are between 10^4 and 10^{-18} atm at 1273 K.

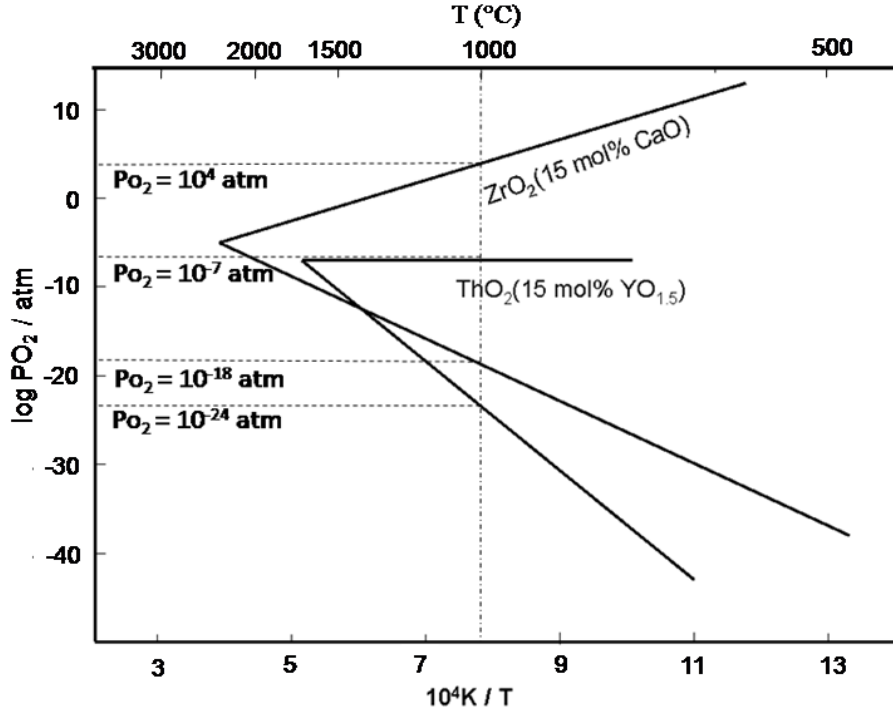
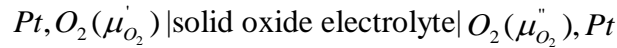


Fig. 2.4 Electrolytic domain boundaries of calcia stabilized zirconia and yttria-doped thoria (reproduced from ref. [10])

2.5.3 Application of solid electrolytes for emf measurements

A galvanic cell employing oxide ion conducting solid electrolyte can be represented as follows:



The quantities μ'_{O_2} and μ''_{O_2} represent the chemical potentials of oxygen at the two electrodes and are determined by appropriate electrode reactions. Under thermodynamic equilibrium at the electrode-electrolyte interfaces, the emf, E of the cell is given by

$$E(\text{volts}) = \left(\frac{1}{4F}\right) \int_{\mu_{O_2}'}^{\mu_{O_2}''} t_{ion} d\mu_{O_2} \quad (2.13)$$

where 4 represents the number of electrons involved in the transport of one oxygen molecule, F is the faraday constant and t_{ion} is the transport number of the oxide ions in the solid electrolyte. When $\mu_{O_2}' < \mu_{O_2}''$ and $t_{ion} \sim 1$,

$$E(\text{Volts}) = \left(\frac{1}{4F}\right) \int_{\mu_{O_2}'}^{\mu_{O_2}''} d\mu_{O_2} = \frac{RT}{4F} \ln \frac{P_{O_2}''}{P_{O_2}'} \quad (2.14)$$

While selecting a solid electrolyte for emf measurements, the following criteria need to be taken into consideration:

- 1) The oxygen partial pressure range of the system under study should fall within the electrolytic domain boundaries of the electrolyte used.
- 2) The solid electrolyte should be chemically compatible with the electrode materials at the temperature range of measurements.
- 3) The solid electrolyte should possess high ionic conductivity and meet the criterion of $t_{ion} \geq 0.99$

In the present work, the Gibbs energies of formation of $\text{Bi}_2\text{Fe}_4\text{O}_9$, ' $\text{Bi}_{22}\text{Cr}_{18}\text{O}_{60}$ ' and ' $\text{Bi}_{38}\text{CrO}_{60}$ ' were determined by emf technique using yttria stabilized zirconia based emf cells. This technique was also used to measure the equilibrium oxygen potentials of the mixtures of i) Bi, $\text{Bi}_2\text{Fe}_4\text{O}_9$, BiFeO_3 ii) Bi, $\text{Bi}_2\text{Fe}_4\text{O}_9$, $\text{Bi}_{25}\text{FeO}_{39}$ and iii) Bi, BiFeO_3 , $\text{Bi}_{25}\text{FeO}_{39}$ in liquid bismuth.

2.6 Calorimetric techniques

Calorimetry is the technique used to measure the heat changes associated with a chemical reaction or a physical process. This heat change can be used to derive the thermochemical properties of compounds. Calorimetry can be classified into two types i.e., reaction calorimetry and non-reaction calorimetry. In reaction calorimetry, heat change associated with a chemical reaction is measured whereas in non-reaction calorimetry, heat change associated with a physical change is measured. Calorimetric measurements can be carried out under constant volume and constant pressure conditions. While the heat measured under constant volume gives the change in the internal energy of the system, heat measured under constant pressure gives the change in the enthalpy of the system.

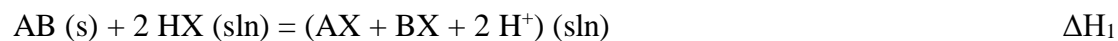
Based on the temperature of the calorimeter (T_C) and that of the surroundings (T_S) calorimeters can be classified into different types: (a) isothermal calorimeter in which $T_C = T_S$ and is a constant; (b) adiabatic calorimeter in which $T_C = T_S$ but they are varying which means there is no heat transfer across the boundary; (c) a constant heat flow calorimeter where $T_C - T_S$ is maintained constant and (d) isoperibol calorimeter in which temperature of the surrounding is held at constant temperature ($T_S = \text{constant}$) and T_C is measured.

In the present work, an isoperibol calorimeter was employed to measure the heat of dissolution of compounds and deduce their standard enthalpies of formation.

2.6.1 Isoperibol calorimeter [11 - 16]

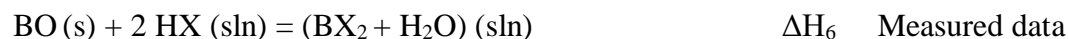
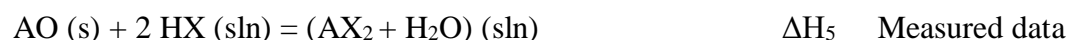
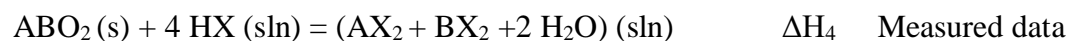
The basic experiment involves determining the enthalpy of dissolution of a substance AB by dissolving in a specified solvent, say HX taken in a calorimetric

vessel. Corresponding amount of pure elements A and B are also dissolved in a separate experiment in the same solvent such that the final solution in both cases is identical. The standard enthalpy of formation of AB can be calculated as:



$\Delta H_1 - (\Delta H_2 + \Delta H_3)$ will give the standard molar enthalpy of formation of the compound AB from elements i.e., $\text{A (s)} + \text{B (s)} = \text{AB (s)}$ (standard enthalpy of formation of elements is taken as zero).

Similarly, consider the determination of enthalpy of formation of the ternary oxide ABO_2 . This can be obtained by measuring the heat of dissolution of ABO_2 and those of the constituent oxides AO and BO in the same solvent (say, HX, where X is a halogen) and using the values of standard enthalpy of formation of AO and BO from literature.

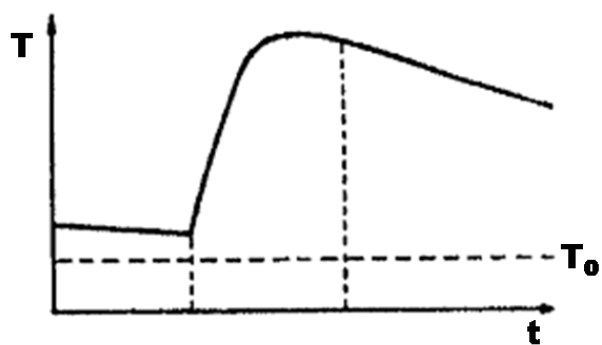


$(\Delta H_5 + \Delta H_6 + \Delta H_7 + \Delta H_8) - \Delta H_4$ will give the standard molar enthalpy of formation of the compound ABO_2 from elements i.e., $\text{A (s)} + \text{B (s)} + \text{O}_2 (\text{g}) = \text{ABO}_2 (\text{s})$.

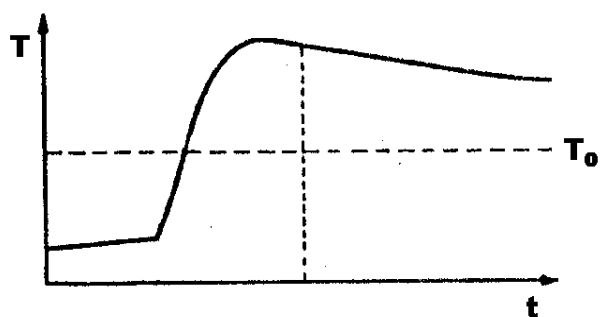
Selection of calorimetric solvent is very important in isoperibol solution calorimetry. It should dissolve the solute in a reasonable time (within ~ 10 minutes) and it should have low vapour pressure. It should also give moderate heats of dissolution for solutes so that the error in the measurement of ΔT is low. Liquid metals can also be used as solvents in calorimetry. Use of mercury as a solvent for alloys such as lead with tin, bismuth and zinc and of zinc with tin and mercury were reported in the literature [14]. During the dissolution of the sample, the temperature in the calorimeter rises or falls until the reaction is completed. From the temperature change and the value of energy equivalent of the calorimeter (which can be determined by carrying out an electrical calibration before and after the sample dissolution), the enthalpy of reaction can be calculated. The heat leak occurs during thermal equilibration and during the reaction process can be corrected by applying Newton's law of cooling:

$$\frac{dT_C}{dt} = k (T_C - T_S) \quad (2.15)$$

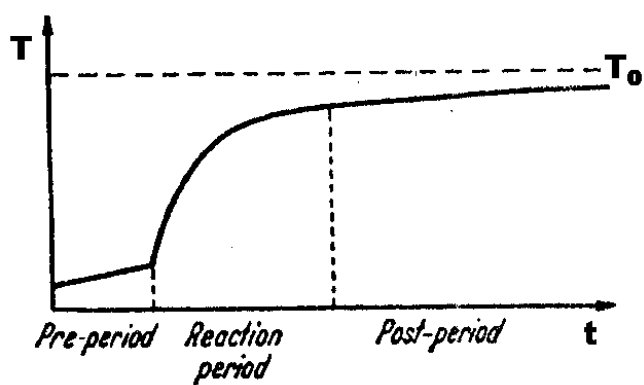
where t is the time and k is the constant. The error due to this correction is made small by designing the calorimeter in such a way that the proportionality constant is small. The cooling constant can be made as small as possible by silvering the inner walls of the double walled Dewar and by sealing the evacuated annular gap between them. The typical temperature-time curve obtained for an exothermic process is shown in Fig.2.5. The type of curve depends upon the initial temperature of the inner vessel relative to that of the outer jacket (T_o), which is shown in the diagram as a dotted line. The schematics of the experimental setup used in the present work is shown in Fig. 2.6 [15].



(a)



(b)



(c)

Fig. 2.5 Temperature-time curve for exothermic dissolution process in isoperibol calorimeter, (a) initial temperature higher than the temperature of the outer jacket (T_0), (b) T_0 is between the initial and final temperatures, (c) final temperature below T_0

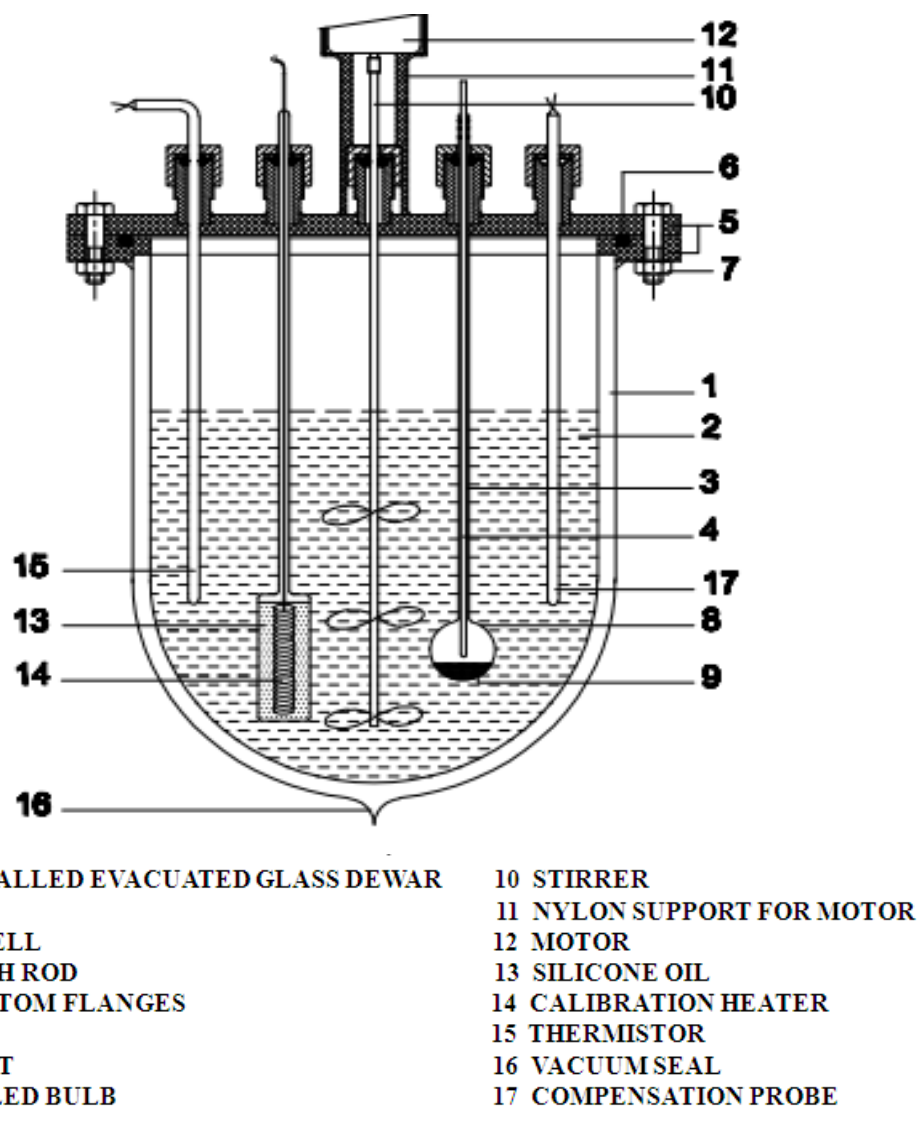
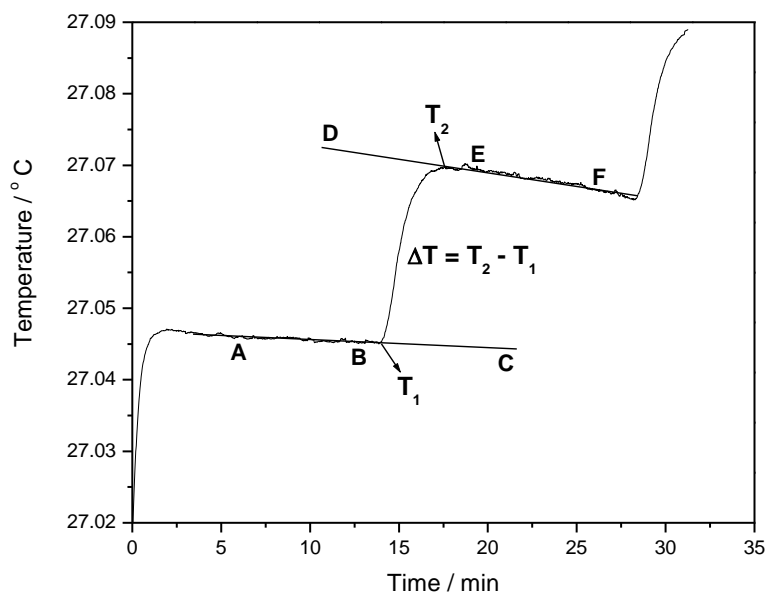


Fig. 2.6 Schematics of solution calorimeter [15]

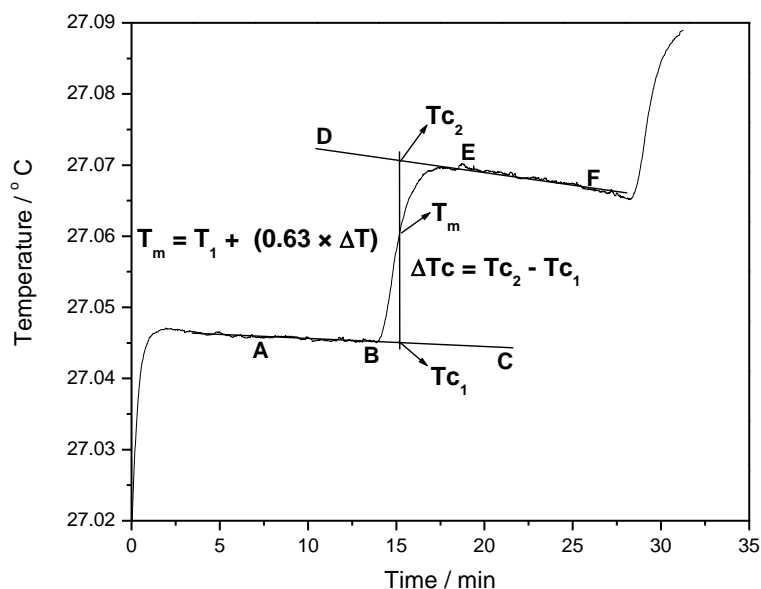
The main constituent of the isoperibol calorimeter is the vessel in which the reaction of interest takes place. It was made up of a double walled glass Dewar of 0.3 dm³ capacity with an evacuated interspace. The top of the vessel was fitted with an annular Perspex flange having an O-ring groove. It also had a mating top-cover flange with leak tight fittings for introducing a stirrer, a sample bulb, a heater enclosure and a thermistor. The Dewar with all the fittings was kept immersed into a water bath that maintained the temperature within ± 0.01 K so as to minimize the exchange of heat

with the surroundings. The sample was taken inside a small glass tube provided with a thin walled bulb at the bottom. The glass tube had a glass push rod, which was sealed to the inner wall of the sample tube using a set of O-rings. This arrangement enabled isolation of sample from surroundings. A stirrer made up of PTFE, enabled uniform stirring of the calorimetric fluid in the Dewar. The stirrer was driven by a motor so that the frictional heat generated by the stirring was constant both during the experiment as well as during the calibrations. The calorimeter was calibrated by electrical as well as by chemical methods. A PTFE coated resistance wire with very low temperature coefficient of resistance (KARMA) was used as a calibration heater such that the change of resistance would be negligible during the calibration. The resistance of the heater was $14.3\ \Omega$. The heater was enclosed in a glass bulb (≈ 0.2 mm wall thickness) to avoid any possible interaction with the solvent. Silicone oil, which is inert and has low heat capacity and low vapour pressure was filled in the bulb to immerse the heater and this design enabled fast conduction of heat from the heater to the calorimetric fluid. The temperature of the calorimetric fluid was measured using a thermistor (M/s. PARR Instruments Company, USA) connected to a data acquisition system, interfaced to a personal computer and was recorded as a function of time. The electrical calibration was performed by applying a constant current using a stable power source, for a known period of time. The current and duration of its passage for the calibration were decided by the time taken for the sample to dissolve completely under the experimental conditions and the weight of the sample taken for each experiment. The current was measured across a precision resistor ($1.000\ \Omega$) of suitable current rating, connected in series. Chemical calibration was carried out by measuring the heats of dissolution of KCl (SRM 1655, M/s NIST, USA) and TRIS (M/s Merck, UK) in double distilled water and $0.1\ \text{mol kg}^{-1}$ HCl,

respectively. The sample for calibration was weighed accurately and taken inside the sample tube. 0.300 dm³ of double distilled water was transferred into the calorimetric vessel and equilibrated at the bath temperature. The calorimeter was fitted with its flange and all the components were allowed to equilibrate at the bath temperature with the stirrer rotating at a constant speed. When the temperature of the calorimeter is in equilibrium with the surrounding water bath, a steady temperature signal was obtained. After a steady signal had been obtained from the control unit, the bulb was broken, the sample was allowed to dissolve in the solvent and the calorimeter signal was recorded. The system was calibrated electrically in situ before and after each of this calibration experiment. The temperature change, ΔT , during electrical calibration as well as during chemical calibration was corrected for heat exchange between calorimeter and surroundings by the method given in ref. 12 and was used for the evaluation of the enthalpy change of the reaction. The procedure adopted for finding the temperature change (ΔT) and the corrected temperature change (ΔT_c) from a typical time - temperature plot of sample dissolution is shown in Fig. 2.7. As seen from Fig. 2.7a, the temperature-time curves, AB and EF were extrapolated to BC and ED, respectively and the initial and final temperatures i.e., T_1 (temperature of commencement of the reaction) and T_2 (temperature at the end of the reaction) were determined. From this, ΔT was calculated as $T_2 - T_1$. Then the mean temperature, T_m was calculated as: $T_m = T_1 + (0.63 \times \Delta T)$. A vertical line is drawn through T_m in such a way that it touches DE and BC and the corrected initial and final temperatures i.e., T_{c1} and T_{c2} were determined as shown in Fig. 2.7 b. The corrected temperature change, ΔT_c is given by $T_{c2} - T_{c1}$.



(a)



(b)

Fig. 2.7 A typical plot showing the method by which temperature change was determined as given in ref. 12. T_1 and T_2 represent the initial and final temperatures, respectively as shown in Fig. 2.7 a. T_{c1} and T_{c2} are the initial and final temperatures, respectively after correction as shown in Fig. 2.7 b. ΔT_c is the corrected temperature change.

In the present work, enthalpy of formation of $\text{Bi}_2\text{Fe}_4\text{O}_9$ and $\text{Bi}_{25}\text{FeO}_{39}$ were determined by acid solution calorimetric technique with 8.38 mol kg^{-1} HCl as the calorimetric solvent.

2.6.2 Differential Scanning Calorimetry (DSC) [13, 17, 18]

DSC is a technique in which the heat flow rate (power) to the sample is monitored against time or temperature. In this technique, sample and reference materials, both enclosed in a specified atmosphere, are heated in a programmed way. Both the sample and reference are maintained at nearly the same temperature throughout the experiment and the difference in the amount of heat required to increase the temperature of the sample and reference are measured. DSC can be used to determine the heat capacity, temperatures of melting and crystallization, phase and magnetic transitions, glass transition temperature etc of a sample.

DSC can be classified into two types, namely heat flux DSC and power compensation DSC.

2.6.2.1 Heat flux DSC

In this type of DSC, the measurement signal is the temperature difference between the sample and the reference which is proportional to heat flow rate. A typical heat flux DSC with disc type measuring system is shown in Fig. 2.8. The characteristic feature of this measuring system is that the major part of the heat flow from the furnace to the sample and reference occurs symmetrically through discs of good thermal conductivity. The sample and reference (along with their crucibles) are positioned on these discs symmetrical to the center of the calorimeter. The temperature sensors cover more or less the area supporting the respective crucibles. When the sample and reference pans that are identical with respect to their mass, material and arrangement are only placed on the discs, heat flow rates would be equal for both and the differential signal, ΔT would be zero. When a sample is placed in the

sample pan, any thermal events in the sample result in a differential signal which would be proportional to the difference between the heat flow rates to the sample and the reference.

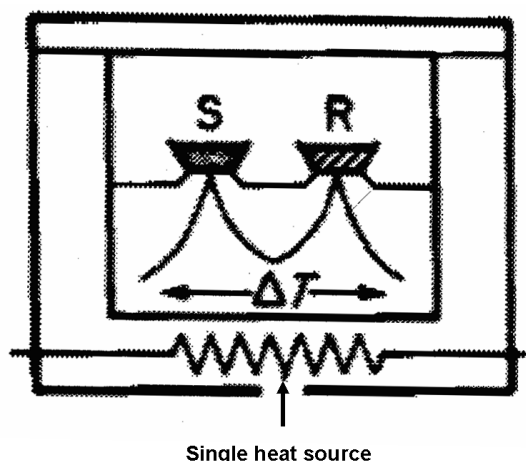


Fig. 2.8 Heat flux DSC

2.6.2.2 Power compensation DSC

In this type of DSC, the temperature difference between the sample and the reference is always maintained zero by decreasing or increasing an adjustable Joule's heat using additional micro heaters i.e., by compensating with electric energy. The measurement signal is the compensating electrical energy supplied to the sample or reference. A typical power compensation DSC is shown in Fig. 2.9. The measuring system consists of two micro furnaces of the same type, each of which contains a temperature sensor (typically Pt-resistance sensor) and a heating resistor (typically made of platinum wire). Both micro furnaces are separated from each other (thermally decoupled) and are positioned in a silver block of constant temperature. During heating up, the same heating power is supplied to both micro furnaces via a control circuit with the preset heating programme. If the thermal symmetry between these micro furnaces is ideal, the temperatures of both the furnaces would always be

the same. When an asymmetry arises as a result of a thermal event in the sample, a temperature difference results between the micro furnaces accommodating the sample and that containing the reference. The temperature difference, in this case, is both the measurement signal as well as the input signal to a feedback circuit. The feedback circuit tries to compensate the reaction heat flow rate by proportional control through increasing or decreasing the additional heating power. The compensating heating power, ΔP is proportional to the ΔT . The time integral over the compensating heating power is proportional to the heat released or consumed in the sample.

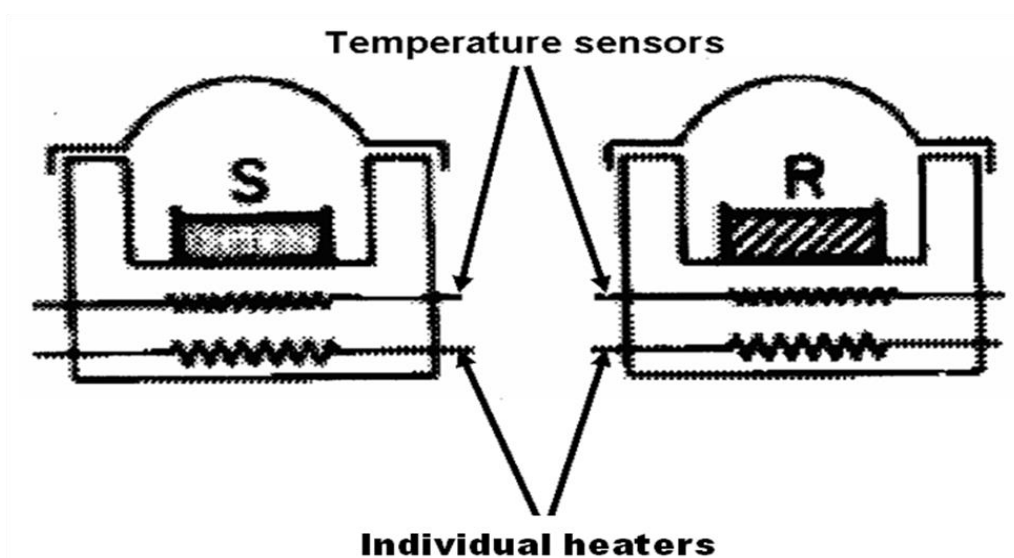


Fig.2.9 Power compensation DSC

2.6.2.3 Calibration of DSC

As DSC is not an absolute heat and temperature measuring device, the relative data obtained must be correlated to absolute values by calibration. The calibration procedure involves:

1. Temperature calibration
2. Heat calibration
3. Heat flow rate calibration

2.6.2.3.1 Temperature calibration

Temperature calibration means the apparent assignment of the temperature indicated by the instrument to the true temperature. Temperature calibration is accomplished by using melting points of high purity metals. The thermodynamically defined transition temperature is always the equilibrium temperature whereas DSC measurements are dynamic. Therefore, DSC calibration results must be extrapolated to equilibrium conditions to ensure a temperature calibration, which is independent of the heating rate used. This is carried out by measuring the melting points of reference materials such as In, Sn, Pb and Zn as a function of heating rate and extrapolating the values to zero heating rate.

2.6.2.3.2 Heat calibration

Heat calibration refers to the unique assignment of the heat measured by the calorimeter to the true heat taken up or released by the sample as a result of a transition. The heat calibration can be carried out by using the enthalpy of melting of NBS standards such as In, Sn, Pb and Zn.

2.6.2.3.3 Heat flow rate calibration

Heat flow rate calibration refers to the unique assignment of the heat flow rate to or released by the sample. The materials used for heat flow rate calibration should not undergo any phase transition in the temperature range of study. Sapphire (α - Al_2O_3) is generally used for heat flow rate calibration.

2.6.2.4 Heat capacity measurement using DSC

The “Classical” three step procedure for measuring heat capacity as a function of temperature by DSC is illustrated in Fig. 2.10 and the plot of typical heat flow

rates are shown in Fig. 2.11. The three steps are (1) blank run, (2) calibration run and (3) sample run.

(1) Blank run: In this run, the heat flow rate of the zero line $\Phi_0(T)$ is determined using empty pans of equal weight in the sample and the reference sides. The zero line reflects the asymmetry of the DSC.

(2) Calibration run: A calibration substance (ref) of known heat capacity C_{ref} is placed into the sample pan (S), whereas the reference side (R) is unchanged. The heat flow rate is measured using the same experimental parameters as for the zero line. The following expression is valid:

$$C_{\text{ref}} m_{\text{ref}} \beta = K_{\phi}(T) (\Phi_{\text{ref}} - \Phi_0) \quad (2.16)$$

where C_{ref} is the heat capacity of the reference material, β is heating rate, m_{ref} is the mass of the reference material, Φ_{ref} and Φ_0 are the heat flow rates for the reference run and the blank run, respectively and $K_{\phi}(T)$ is temperature dependent calibration factor.

(3) Sample run: For the measurement on sample, the calibration substance (reference) in the sample pan is replaced by the sample (S). Similar to the above equation we get:

$$C_s m_s \beta = K_{\phi}(T) (\Phi_s - \Phi_0) \quad (2.17)$$

where C_s is the heat capacity of the sample, m_s is the mass of the sample, Φ_s is the heat flow rate for the sample.

The specific heat capacity, C_s (at a given temperature) can be calculated by a simple comparison of the heat flow rates from the sample and reference substances as illustrated below:

$$C_S = C_{\text{ref}} (\Phi_S - \Phi_o) m_{\text{ref}} / (\Phi_{\text{ref}} - \Phi_o) m_S \quad (2.18)$$

In each of the steps, a typical three segment heating programme is used. The first segment lasting typically for ten minutes is an isothermal segment at the initial temperature; the second segment is a dynamic segment with a defined heating rate and the final segment lasting for ten minutes is another isothermal segment at the final temperature. At isothermal segments, heat flow rate from furnace to the sample is nil whereas as soon as the dynamic heating segment starts in the DSC run, an exponential endothermic effect is observed due to the flow of heat from the furnace to the sample and is proportional to the heat capacity of the samples taken. The slope of the line during the dynamic segment indicates the variation of the heat capacity of the material with temperature. Generally, aluminium sample pans are used for the sample and reference and are hermetically sealed with a pin hole on the lid. This is to ensure that the measurements are done under constant pressure conditions.

The samples for C_p measurements are usually taken in the form of a flat disc similar to the standard material due to the following reasons:

- (i) To get a good thermal contact between the pan and the sample
- (ii) To simulate the geometry of the calibration material and
- (iii) To eliminate any possible errors due to temperature gradient within the sample.

A heat flux type differential scanning calorimeter, of M/s. Mettler Toledo GmbH (model number DSC821e/700), Switzerland was used in this study. The heat capacities of $\text{Bi}_2\text{Fe}_4\text{O}_9$ and $\text{Bi}_{25}\text{FeO}_{39}$ were measured using this instrument.

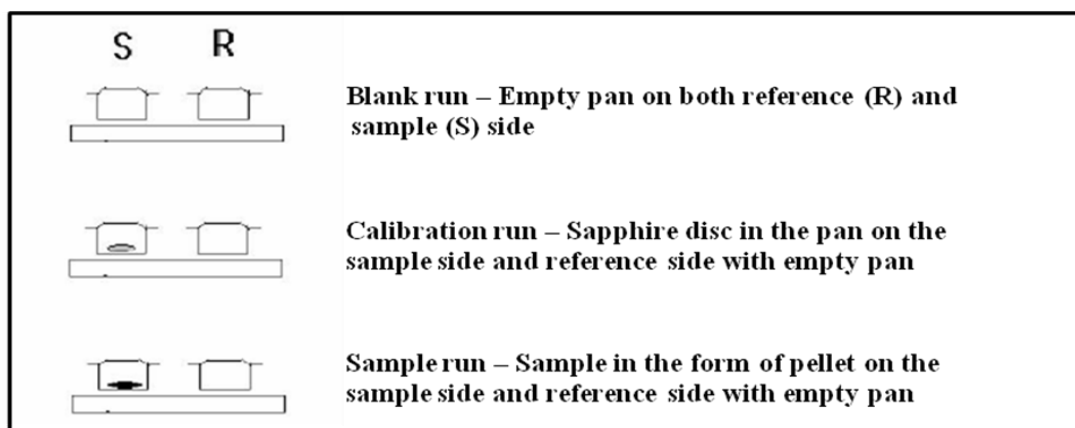


Fig. 2.10 Three step procedure for measuring the heat capacity of a sample

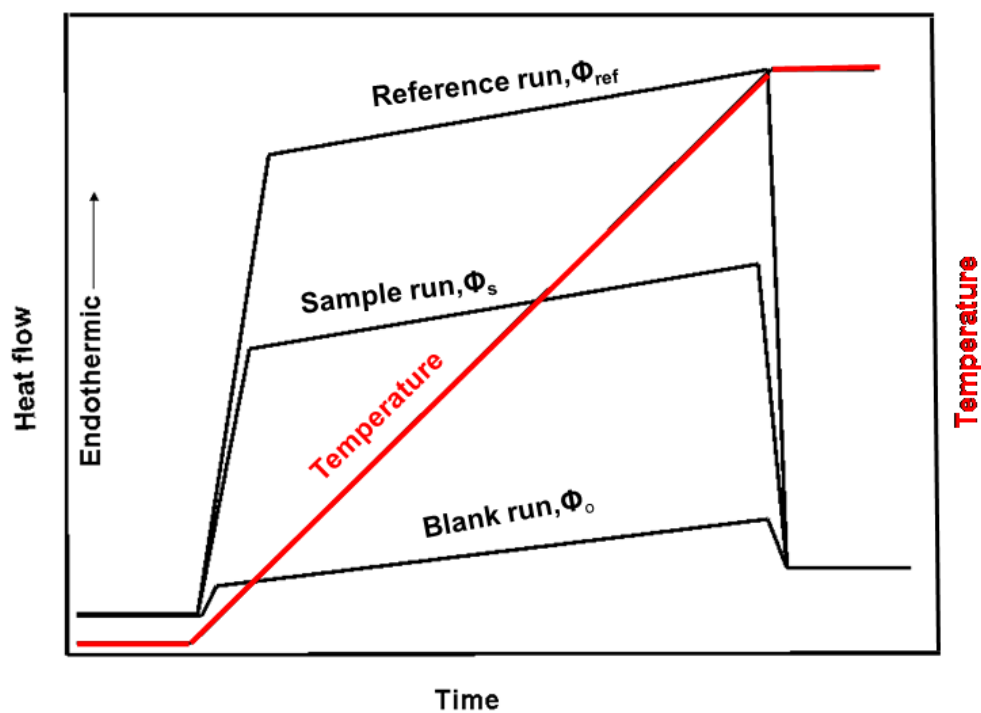


Fig. 2.11 Typical DSC run for blank, sample and reference

2.7 Pseudo-isopiestic equilibrations of samples under controlled oxygen partial pressures [19]

In an isopiestic equilibration experiment, a condensed phase sample is allowed to attain equilibrium with a gas/vapour phase in a closed system. The composition and pressure of the gas/vapour phase are determined by a standard substance for which the equilibrium partial pressure of the gas/vapour is known as a function of temperature. In fact, the isopiestic method had been used in isothermal conditions to determine the vapour pressures of aqueous solutions where the aqueous solution to be investigated was equilibrated with a standard solution whose water vapour pressure was known as a function of temperature and concentration. However, to extend the pressures to lower values, water was tried as the standard solvent whose vapour pressure could be varied easily by changing its temperature. Thus the non-isothermal isopiestic method, also known as pseudo isopiestic method evolved. Currently, the pseudo isopiestic method is widely used for the study of binary metallic systems.

Principle

A sample, A (usually nonvolatile) kept at a particular temperature, T_S , is equilibrated in a closed system with vapour from a reservoir of pure volatile component, B kept at the reservoir temperature, T_R ($T_R < T_S$). The vapour pressures of the pure components, A and B should differ by at least three orders of magnitude. After sufficient equilibration time, the vapours of B would have reacted with the sample in such a way that an alloy is formed with exactly that composition for which the partial pressure of B over the sample at T_S is equal to the vapour pressure of B over pure B at T_R i.e.,

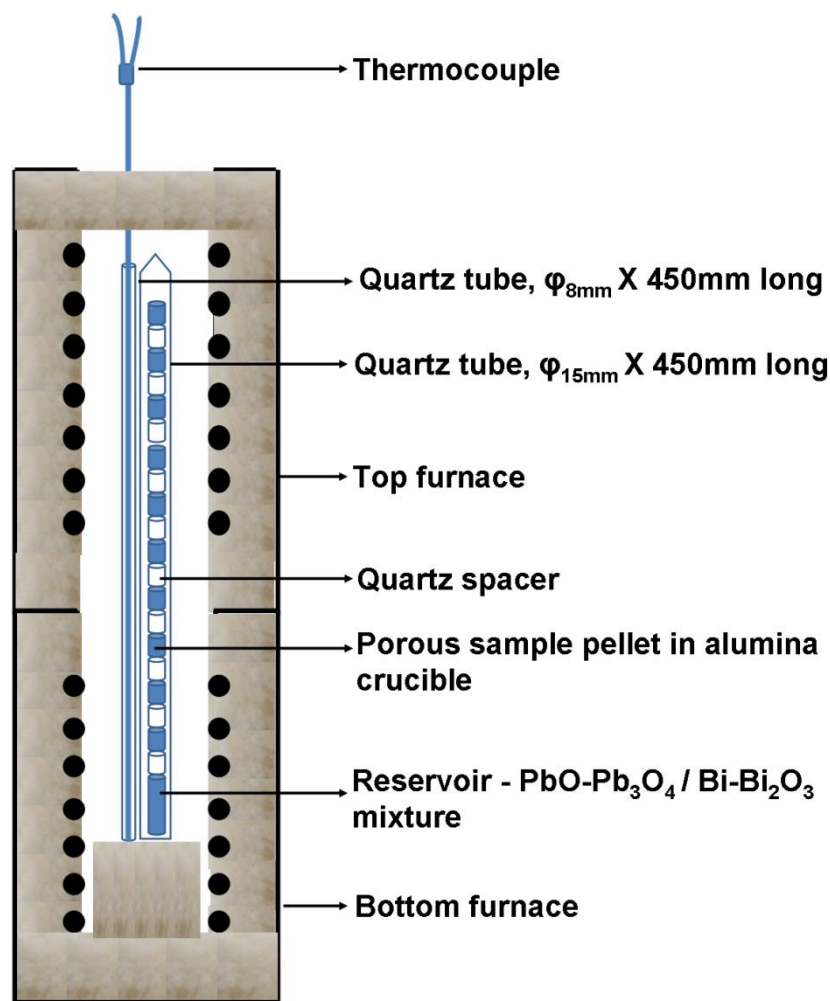
$$p_B(T_S) = p_B^0(T_R) \quad (2.19)$$

The activity of B in the sample can be obtained using the data on the temperature dependence of the vapour pressure of B as given below:

$$a_B(T_S) = \frac{p_B(T_S)}{p_B^0(T_S)} = \frac{p_B^0(T_R)}{p_B^0(T_S)} \quad (2.20)$$

The composition of the sample after the experiment can be determined from the weight change of the sample or by chemical analysis. The isopiestic method has been used over a pressure range of 10^{-10} to 10^{-1} bar. Although the method is generally used for condensable vapours of B, the method can also be used with noncondensable gases.

In the present study, this method was applied for oxide systems i.e., Bi-Cr-O and Bi-Fe-O systems, to identify the phases that coexist at high pressures in Bi-Cr-O system and to determine the temperature range of stability of BiFeO₃. For this, samples were equilibrated under fixed oxygen pressures in a temperature gradient furnace. Oxygen pressure is fixed either by using Bi - Bi₂O₃ and PbO - Pb₃O₄ mixtures as the reservoir (whose equilibrium oxygen pressures are well known as a function of temperature) or by heating the samples in air (where the oxygen pressure is 0.21 atm) and vacuum (where the oxygen pressure is not known). Since oxygen is a noncondensable gas, the Bi-Bi₂O₃ or PbO-Pb₃O₄ reservoirs could be kept at temperatures higher than that of the samples. A schematic diagram of the experimental setup used in this study is shown in Fig. 2.12.



Quartz spacers used are of different heights

Fig. 2.12 Schematic diagram of the pseudo-isopiestic equilibration setup in a gradient furnace

Samples were prepared in the form of pellets. These pellets were taken in small alumina crucibles which were in turn stacked at precisely known heights in a 45 cm long and one end closed 1.5 cm diameter quartz tube using quartz spacers. Around 10 samples were used for each pseudo - isopiestic experiment. For experiments conducted in Bi-Cr-O system, oxygen partial pressure over the samples was fixed by using a mixture of $\text{PbO-Pb}_3\text{O}_4$ in one experiment and $\text{Bi-Bi}_2\text{O}_3$ in the other experiment. $\text{PbO-Pb}_3\text{O}_4$ and $\text{Bi-Bi}_2\text{O}_3$ mixtures were also made in the form of porous pellets. These pellets were placed in alumina crucibles which in turn were kept inside

the same quartz tube where the samples were placed. For experiments with BiFeO_3 , oxygen pressure was maintained by heating the samples in air and vacuum. The quartz tube was then sealed under vacuum (except for samples heated in air) and placed in a two zone furnace which provided a temperature gradient. The sample pellets were maintained at fixed temperatures between 716 and 1089 K. A K-type thermocouple which could move very slowly (0.38 cm min^{-1}) from bottom to top of the furnace and close to the quartz tube with the help of a motor was used to measure the temperatures of the samples. The samples were equilibrated for 480 h, quenched in cold water and the products were characterized by XRD. From the known thermodynamic data on PbO , Pb_3O_4 and Bi_2O_3 , and the temperature at which the reservoir was maintained, the oxygen partial pressures under which the samples were equilibrated could be calculated.

In the present study, this method is applied to identify the coexisting phases in the phase fields that exist above the $\text{Bi}_2\text{O}_3\text{-Cr}_2\text{O}_3$ pseudo binary line where the oxygen pressures are anticipated to be high. This method is also used to determine the temperature range of stability of BiFeO_3 under low and high oxygen partial pressures.

2.8 References

- 1) A.R West, Solid State Chemistry and its Applications, John Wiley & Sons, Singapore, 2008.
- 2) A.M. Alper, Phase Diagrams, Materials Science and Technology, Vol 1 (Theory, Principles and Techniques of Phase Diagram), Academic Press, USA, 1970, 115.

- 3) B.D. Cullity, Elements of X-ray Diffraction, Addison–Wesley Publishing Co., Reading, Massachusetts, 1956.
- 4) C. Whiston, X-ray Methods, Analytical Chemistry by Open Learning, John Wiley & Sons, 1987.
- 5) D.E. Newbury, D.C. Joy, P. Echlin, C.E. Fiori, J.I. Goldstein, Advanced Scanning Electron Microscopy and X-ray Microanalysis, Plenum Press, New York, 1986.
- 6) H.E. Exner in: K. Mills, J.R. Davis and D.A. Dieterich (Eds) Metallography and Microstructure, ASM Handbook Vol. 9, International Soc. ASM., Materials Park, USA, 1998.
- 7) P.F. Kane, G.B. Larrabee, Characterization of Solid Surface, Plenum Press, New York, London, 1978, 107.
- 8) D.B. Williams, C.B. Carter, The transmission electron microscope, Springer, 1996.
- 9) E.C. Subba Rao, Solid Electrolyte and their Applications, Plenum Press, New York, 1980.
- 10) S. Geller, Solid Electrolyte, Springer-Verlag, Berlin Heidelberg New York, 1977.
- 11) O. Kubaschewski, C.B. Alcock, Metallurgical Thermochemistry, fifth ed., Pergamon, Oxford, 1979.
- 12) K.N. Marsh, P.A.G. O'Hare (Ed.), Solution Calorimetry, Experimental Thermodynamics, Vol. IV, Blackwell Scientific Publications, Oxford, 1994.

- 13) M.E. Brown, Handbook of Thermal Analysis and Calorimetry, Vol. I, Principles and Practice, Elsevier Science B.V., The Netherlands, 1998.
- 14) O.J. Kleppa, Thermodynamic analysis of binary liquid alloys of group IIB metals-III, The solutions of zinc, cadmium, indium, tin, thallium, lead and bismuth in mercury, *Acta met.* 8 (1960) 435-445.
- 15) R. Venkatakrishnan, G. Jogeswararao, R. Parthasarathy, S. Premalatha, J.P. Rao, G. Gunasekaran, K. Ananthasivan, Development of semi-adiabatic isoperibol calorimeter, *Rev. Sci. Instrum.* 85 (2014) 124904-1-7.
- 16) S.K. Sahu, R. Ganesan, T.G. Srinivasan, T. Gnanasekaran, The standard molar enthalpies of formation of Pb_2CrO_5 (s) and Pb_5CrO_8 (s) by acid solution calorimetry, *J. Chem. Thermodyn.* 43 (2011) 750-753.
- 17) M. Sorai, Comprehensive Handbook of Calorimetry and Thermal Analysis, John Wiley & Sons, Ltd, England, 2004.
- 18) R.F. Speyer, Thermal Analysis of Materials, Marcel Dekker, New York, 1993.
- 19) H. Ipser, R. Krachler, K.L. Komarek, The isopiestic method and its application to a thermodynamic study of the Au-Zn system, in: H. Brodowsky, H-J. Schaller (Eds.), Thermochemistry of Alloys, Kluwer Academic Publisher, Dordrecht, 1989, 293-306.

Chapter 3

THERMOCHEMICAL STUDIES ON Bi-Fe-O SYSTEM

3.1 Introduction

As discussed in Chapter 1, liquid lead and LBE are highly corrosive towards structural steels due to the solubility of the alloying elements of structural steel in them. This corrosion can be mitigated by proper control of oxygen concentration in the liquid metal thereby forming a protective oxide layer coating over the structural material. To understand the composition of the protective oxide film and its stability, a detailed knowledge of the phase diagrams of Pb-M-O and Bi-M-O systems (M = alloying components of steels) as well as the thermochemical data on ternary oxygen compounds formed in these systems are essential. In this chapter, studies carried out on Bi-Fe-O system are described.

3.2 Literature survey

3.2.1 Fe-O system

Data on Fe-O system has been reviewed by Wriedt [1]. Partial phase diagram of this system at 1 bar pressure is shown in Fig. 3.1. Iron exists in three allotropic forms, viz., α -Fe (bcc, ≤ 1185 K), γ -Fe (fcc, 1185-1667 K), δ -Fe (bcc, 1667-1811 K). The solubility of oxygen in iron is very low (0.58 at% at 1801 K). The three stable oxides present in Fe-O system are FeO_{1+x} , Fe_3O_4 , and Fe_2O_3 . FeO_{1+x} has a broad range of composition from 51.2 at% O at about 1185 K to 54.6 at% O at about 1697 K. It has face centered cubic structure and is stable in the temperature range of 843-1697 K. Below 843 K, it decomposes to Fe and Fe_3O_4 , and above 1697 K, it peritectically decomposes to liquid and Fe_3O_4 . Fe_3O_4 (called as magnetite) is

Weight Percent Oxygen

Temperature °C

Atomic Percent Oxygen

Fe

0 10 20 30 40 50 60 70

0 1000 2000

1538°C 1528°C 1392°C 1371°C 912°C 770°C 570°C 1596°C 1582°C 1457°C 57.94 57.67 59.82 54.57 54.19 51.38 51.26 50.92 50.86 50.47 0.029 0.0098 0.019 0.0094 0.0007 0.0008 57.14 688°C

L_1 L_2 $O_2(G)$ 0.1 MPa (δFe) (γFe) (αFe) Wustite Fe_3O_4 Fe_2O_3

3.2.2 Bi-Fe system

$$\log S \text{ (at\% Fe)} = 2.75 - 3980/T \quad (T: 973\text{-}1173 \text{ K})$$

$$\log S \text{ (at\% Fe)} = 2.75 - 3980/T \quad (T: 973\text{-}1173 \text{ K})$$

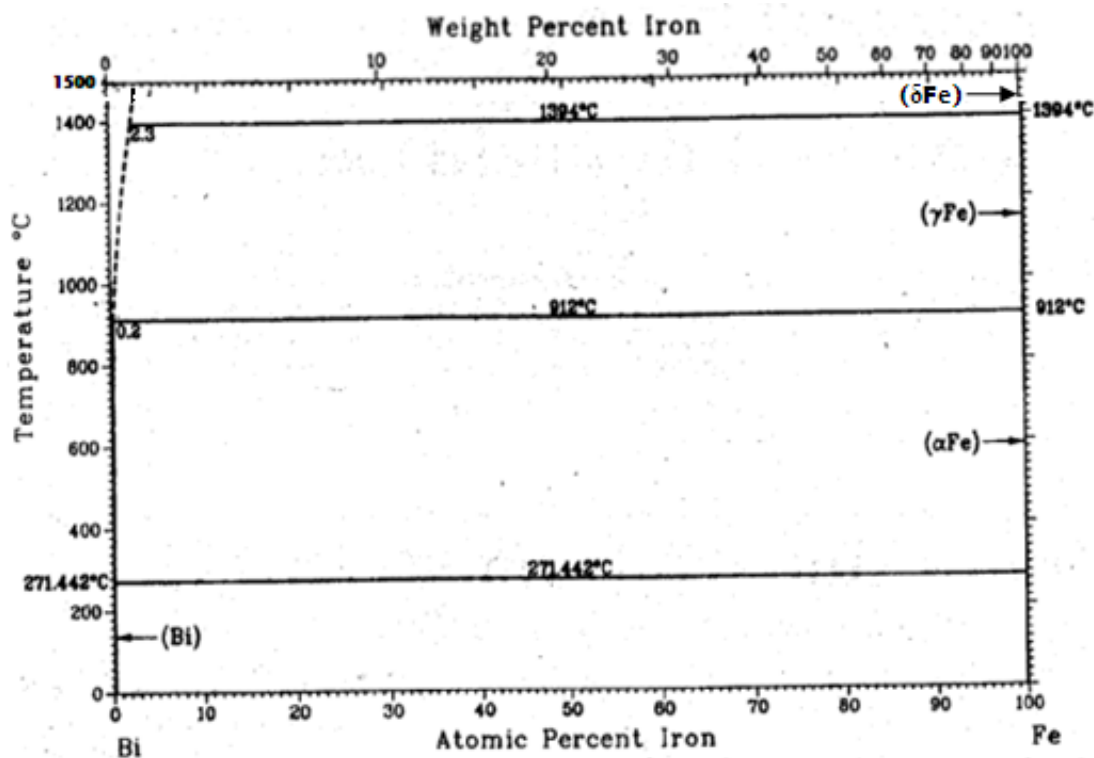


Fig. 3.2 Phase diagram of Bi-Fe system [2]

3.2.3 Bi-O system

Risold et al. [4] reviewed and assessed the data on Bi-O system. The phase diagram of Bi-O system at 1 bar pressure is shown in Fig. 3.3. Bi exists in rhombohedral form and it melts at 544 K. The solubility of oxygen in Bi at 1400 K is around 5 at% and it increases up to 30 at% at around 1650K. The only stable oxide in the Bi-O system is Bi_2O_3 . Bi_2O_3 has four structural modifications - α , β , γ and δ . Among these, α and δ are the stable modifications whereas β and γ are metastable. $\alpha\text{-Bi}_2\text{O}_3$ is monoclinic and stable up to 1002 K where it transforms to $\delta\text{-Bi}_2\text{O}_3$. $\delta\text{-Bi}_2\text{O}_3$ exists in face centered cubic form and melts at 1098 K. $\beta\text{-Bi}_2\text{O}_3$ with a tetragonal symmetry and $\gamma\text{-Bi}_2\text{O}_3$ with base centered cubic structure appear upon cooling $\delta\text{-Bi}_2\text{O}_3$ from high temperature. $\beta\text{-Bi}_2\text{O}_3$ forms at around 920 K and $\gamma\text{-Bi}_2\text{O}_3$ at around 910 K. On further cooling, $\beta\text{-Bi}_2\text{O}_3$ transforms to α -form between 920 and 700 K whereas $\gamma\text{-Bi}_2\text{O}_3$ can be preserved at room temperature.

Miscibility gap exists between Bi and Bi_2O_3 rich phases from 1061 K and complete miscibility in liquid phase occurs above 1650 K.

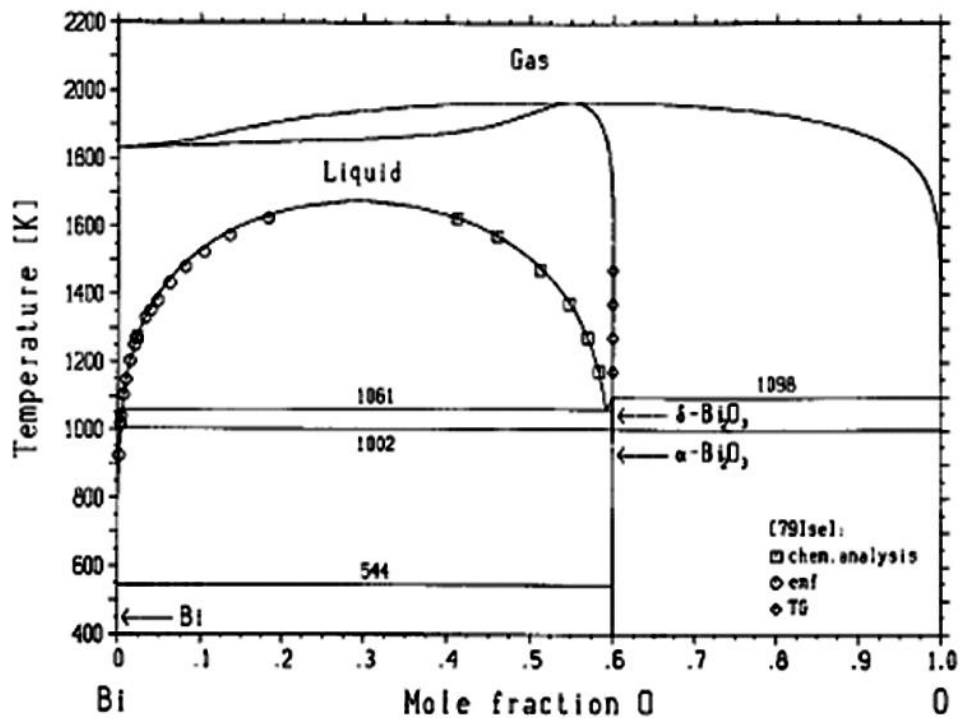


Fig. 3.3 Phase diagram of Bi-O system [4]

3.2.4. $\text{Bi}_2\text{O}_3\text{-Fe}_2\text{O}_3$ system

Pseudo binary $\text{Bi}_2\text{O}_3 - \text{Fe}_2\text{O}_3$ system has been investigated by several authors in the past [5-14]. Salient features of these investigations are listed in Table 3.1. Levin and Roth [5] studied the effect of Fe_2O_3 addition on the polymorphism of Bi_2O_3 and reported a tentative partial phase diagram of $\text{Bi}_2\text{O}_3\text{-Fe}_2\text{O}_3$ system. They reported the existence of a phase rich in Bi_2O_3 and a metastable phase, BiFeO_3 . Koizumi et al. [6] studied this system and reported the existence of two compounds, viz., BiFeO_3 and $\text{Bi}_2\text{Fe}_4\text{O}_9$ along with their decomposition temperatures. Based on DTA and XRD analysis, Speranskaya et al [7] reported the existence of a new compound of composition $\text{Bi}_{40}\text{Fe}_2\text{O}_{63}$, in addition to the previously reported two

Table 3.1 Literature data on Bi₂O₃-Fe₂O₃ system

No:	References	Experimental techniques	Compounds identified and the reported temperature range of stability
1	Levin and Roth [5]	High temperature x-ray diffractometry (HTXRD)	BiFeO ₃ –metastable Bi ₂ O ₃ rich phase in which Bi : Fe > 12:1
2	Koizumi et al. [6]	XRD	Bi ₂ Fe ₄ O ₉ : Peritectic decomposition at 1193 K BiFeO ₃ : Peritectic decomposition at 1053 K
3	Speranskaya et al. [7]	DTA, XRD	Bi ₂ Fe ₄ O ₉ : Peritectic decomposition at 1233 K BiFeO ₃ : α BiFeO ₃ $\xrightarrow{1098K}$ β BiFeO ₃ , peritectic decomposition at 1203 K Bi ₄₀ Fe ₂ O ₆₃ : Peritectic decomposition at 1068 K BiFeO ₃ and Bi ₄₀ Fe ₂ O ₆₃ form eutectic at 1058 K
4	Bruton et al. [8]	DTA and thermo balance technique	Bi ₂ Fe ₄ O ₉ : Stable at least up to 1203 K BiFeO ₃ : Peritectic decomposition at 1203 K Bi ₄₀ Fe ₂ O ₆₃ : Peritectic decomposition at 1058 K BiFeO ₃ -Bi ₄₀ Fe ₂ O ₆₃ eutectic at 1043 K
5	Craig and Stephenson [9]	XRD	Bi ₂₅ FeO ₄₀
6	Ramanan and Gopalakrishnan [10]	XRD, infrared spectroscopy and magnetic susceptibility measurements	Bi ₂₅ FeO ₄₀ Bi _{11.5} Fe _{14.5} O ₃₉ - metastable

Table 3.1 (continued)

No:	References	Experimental techniques	Compounds identified and the reported temperature range of stability
7	Radaev et al. [11]	Neutron diffraction	$\text{Bi}_{25}\text{FeO}_{39}$
8	Maitre et al. [12]	DSC, XRD, SEM, electron probe micro analysis (EPMA)	$\text{Bi}_2\text{Fe}_4\text{O}_9$: Stable at least up to 1248 K BiFeO_3 : α BiFeO_3 $\xrightarrow{1098\text{K}}$ β BiFeO_3 , peritectic decomposition at 1207 K $\text{Bi}_{25}\text{FeO}_{40}^*$: Peritectic decomposition at 1073 K BiFeO_3 - $\text{Bi}_{25}\text{FeO}_{40}^*$ eutectic at 1065 K
9	Palai et al. [13]	DTA, high temperature polarized light microscopy, high temperature and polarized Raman spectroscopy, HTXRD, dc conductivity, optical absorption and reflectivity, domain imaging	$\text{Bi}_2\text{Fe}_4\text{O}_9$: Peritectic decomposition at 1234 K BiFeO_3 : α BiFeO_3 $\xrightarrow{1098\text{K}}$ β BiFeO_3 , peritectic decomposition at 1206 K Reported a cubic γ -phase for BiFeO_3 between 1198 (± 5) and 1206 (± 5) K $\text{Bi}_{25}\text{FeO}_{39}$: Peritectic decomposition at 1066 K BiFeO_3 - $\text{Bi}_{25}\text{FeO}_{39}$ eutectic at 1050 K
10	Lu et al. [14]	XRD, SEM, EDS, inductively coupled plasma-atomic emission spectrometry, DSC	$\text{Bi}_2\text{Fe}_4\text{O}_9$: Peritectic decomposition at 1210 K BiFeO_3 : Peritectic decomposition at 1125 K, ferroelectric transition at 1098 K $\text{Bi}_{25}\text{FeO}_{40}^*$: α $\xrightarrow{1003\text{K}}$ γ , peritectic decomposition at 1063 K BiFeO_3 - $\text{Bi}_{25}\text{FeO}_{40}^*$ eutectic at 1053 K

* Maitre et al. [12] and Liu et al. [14] used the composition, $\text{Bi}_{25}\text{FeO}_{40}$ for the Bi_2O_3 rich sillenite phase.

compounds. They also reported the decomposition temperatures of these compounds.

Bruton et al. [8] reported the partial phase diagram of Bi_2O_3 - Fe_2O_3 pseudo-binary system. Craig and Stephenson [9] studied the crystal structure of Bi_2O_3 rich phase and reported its composition as $\text{Bi}_{25}\text{FeO}_{40}$ ($\text{Bi}_{24}^{3+}\text{Bi}^{5+}\text{Fe}^{3+}\text{O}_{40}$) instead of $\text{Bi}_{40}\text{Fe}_2\text{O}_{63}$ reported earlier. Ramanan and Gopalakrishnan [10] prepared $\text{Bi}_{25}\text{FeO}_{40}$ by a low temperature wet chemical method and deduced its structural parameters which were in good agreement with those reported by Craig and Stephenson [9]. They also reported a metastable iron rich sillenite phase with an approximate composition of $\text{Bi}_{11.5}\text{Fe}_{14.5}\text{O}_{39}$. Later, Radaev et al. [11], based on their neutron diffraction studies showed the absence of Bi^{5+} ion in Bi_2O_3 rich phase and determined its composition as $\text{Bi}_{25}\text{FeO}_{39}$ ($\text{Bi}_{25}^{3+}\text{Fe}^{3+}\text{O}_{39}$) instead of $\text{Bi}_{25}\text{FeO}_{40}$ as reported earlier. Maitre et al [12] studied the partial pseudo - binary phase diagram of Bi_2O_3 - Fe_2O_3 system and reported the decomposition temperatures of all the compounds viz., $\text{Bi}_2\text{Fe}_4\text{O}_9$, BiFeO_3 and $\text{Bi}_{25}\text{FeO}_{40}$. They used the composition, $\text{Bi}_{25}\text{FeO}_{40}$ for the Bi_2O_3 rich sillenite phase. Palai et al. [13] reported a refined Bi_2O_3 - Fe_2O_3 phase diagram and carried out a detailed study on BiFeO_3 . They reported for the first time the existence of a cubic γ -phase of BiFeO_3 between $1198 (\pm 5)$ and $1206 (\pm 5)$ K. Lu et al. [14] studied this system and attributed the discrepancies in the phase diagrams reported in literature to different impurity levels which were present in the starting materials. Based on the experimental results carried out with high purity materials, they reported a pseudo binary phase diagram of Bi_2O_3 - Fe_2O_3 system which is shown in Fig. 3.4. Phapale et al. [15] reported the thermochemical properties of $\text{Bi}_2\text{Fe}_4\text{O}_9$, BiFeO_3 and $\text{Bi}_{25}\text{FeO}_{39}$ based on calorimetric measurements. They also deduced Gibbs energy of formation using the measured heat capacity and the estimated values for the entropy of formation of these compounds. The temperature dependence of the standard Gibbs energy of formation of $\text{Bi}_2\text{Fe}_4\text{O}_9$, BiFeO_3 and $\text{Bi}_{25}\text{FeO}_{39}$ were derived as

$-2459.1 + 0.757 T \text{ kJ mol}^{-1}$, $-773.3 + 0.269 T \text{ kJ mol}^{-1}$ and $-7355.2 + 2.669 T \text{ kJ mol}^{-1}$, respectively in the temperature range of 298.15 to 911 K.

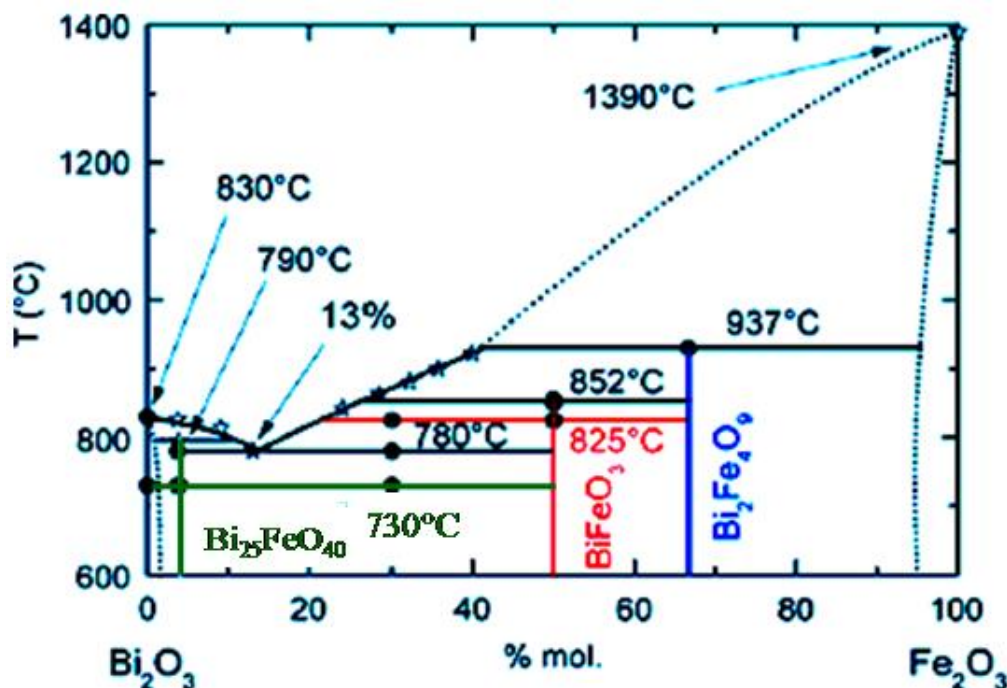
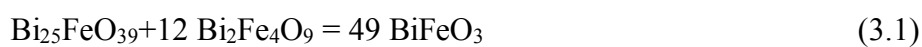


Fig. 3.4 Bi₂O₃-Fe₂O₃ pseudo-binary phase diagram [14]

The reported temperature ranges of stability of BiFeO₃ by different authors are not in agreement. Attempts by Achenbach et al. [16] to prepare phase pure BiFeO₃ by solid state reaction of Bi₂O₃ and Fe₂O₃ at temperatures below 973 K were unsuccessful and they observed the reaction to be incomplete. They also reported BiFeO₃ to be unstable above 1023 K. They reported the formation of Bi₂Fe₄O₉ to be energetically competitive to the formation of BiFeO₃ in the temperature range of 973 to 1023 K. Preparation of BiFeO₃ always yielded a small amount of Bi₂Fe₄O₉ and corresponding amount of residual Bi₂O₃. They could prepare phase pure BiFeO₃ only by taking excess Bi₂O₃ (Bi₂O₃:Fe₂O₃ = 2:1) and heating in air at 1023 K followed by air quenching and removal of the excess Bi₂O₃ by leaching with con. HNO₃. Experiments by De Sitter et al [17] also confirmed these observations. Morozov et al.

[18] studied the characteristics of formation of BiFeO₃ and concluded that BiFeO₃ prepared by heating a mixture of Bi₂O₃ and Fe₂O₃ always contains impurity phases such as the phase with γ -Bi₂O₃ structure and Bi₂Fe₄O₉ presumably due to slow kinetics. Valant et al. [19] reported that phase pure BiFeO₃ could be prepared by heating together 99.9995% pure iron and bismuth oxides. Presence of impurities of the order of 0.1 mol% could produce ~3 vol% Bi₂₅FeO₃₉ and 7.6 vol% of Bi₂Fe₄O₉. Carvalho and Tavares [20] studied the thermodynamic stability of BiFeO₃ and reported that temperature and time were critical in the synthesis of phase pure BiFeO₃. According to them, higher BiFeO₃ content could be obtained by a thermal treatment at 873 K for 1 h. Preparations at temperatures below and above this temperature always yielded secondary phases, Bi₂Fe₄O₉ and Bi₂₅FeO₃₉. Also, heat treatment for longer time at 873 K resulted in the decomposition of BiFeO₃ to the secondary phases. So they concluded that BiFeO₃ to be metastable at 873 K. Selbach et al. [21] studied the thermodynamic stability of BiFeO₃. HTXRD experiments performed on BiFeO₃ prepared by solid state route as well as by a wet chemical route and the analysis of the isothermally heat treated Bi₂O₃-Fe₂O₃ mixtures, showed that BiFeO₃ was metastable in the temperature range of 720 to 1040 K and decomposed to give Bi₂Fe₄O₉ and Bi₂₅FeO₃₉. At higher temperatures, these secondary phases reacted back to form BiFeO₃. Using thermodynamic data reported by Phapale et al. [15], they deduced the standard Gibbs energy change of the following reaction to be positive in the temperature range of 720 to 1040 K and would be negative above 1040 K indicating BiFeO₃ to be stable only above 1040 K:



Lu et al. [14], based on their studies using 99.999% Bi_2O_3 and 99.99% Fe_2O_3 determined the peritectic decomposition temperature of BiFeO_3 as 1125 K and identified a ferroelectric transition for this compound at 1098 K. Maurya et al. [22] studied the reactions in equimolar mixtures of Bi_2O_3 and Fe_2O_3 by heating them at different temperatures for 1 h in air and recording the XRD patterns of the products after cooling them to room temperature. The authors found that $\text{Bi}_{25}\text{FeO}_{39}$ (the authors represented it as $\text{Bi}_{25}\text{FeO}_{40}$) was formed at temperatures above 823 K followed by the appearance of BiFeO_3 phase at 973 K. The impurity phase viz., $\text{Bi}_{25}\text{FeO}_{39}$ was present at all temperatures chosen for heating the samples. Activation of the reactants by ball milling reduced the temperatures by about 100 K but the results obtained were similar. Egorysheva et al. [23] investigated the extent of formation of BiFeO_3 when equimolar mixtures of Bi_2O_3 and Fe_2O_3 were heated in air for 20 minutes at 873 K, 973 K, 1023 K, 1073 K and 1123 K. The experiments showed that BiFeO_3 did not form at 873 K while $\text{Bi}_{25}\text{FeO}_{39}$ was formed as major phase. From 973 K onwards BiFeO_3 was one of the phases formed and its fraction gradually increased with increase in temperature. At 1123 K, BiFeO_3 was the major phase while $\text{Bi}_{25}\text{FeO}_{39}$ was present as a minor phase. The authors reasoned that $\text{Bi}_{25}\text{FeO}_{39}$ was formed (during the initial phase of the reaction) in large fraction because of its wide homogeneity range and high diffusion coefficient of Bi^{3+} in it in comparison with the values in BiFeO_3 , Bi_2O_3 and Fe_2O_3 . The diffusion coefficient of Bi^{3+} in $\text{Bi}_{25}\text{FeO}_{39}$ at 1013 K was found to be $1.5 \times 10^{-8} \text{ m}^2 \text{ s}^{-1}$ while in BiFeO_3 it was found to be $3.2 \times 10^{-16} \text{ m}^2 \text{ s}^{-1}$. The corresponding values in Bi_2O_3 and Fe_2O_3 were found to be $1.3 \times 10^{-17} \text{ m}^2 \text{ s}^{-1}$. Lomanova and Gusarov [24] studied the reactions when samples of coprecipitated bismuth and iron hydroxides were heated in a stepwise manner with isothermal equilibration at 753, 773, 793, 813, 833, 873 and 903 K for 5

to 7 minutes followed by high temperature XRD measurements. Their results showed BiFeO_3 and $\text{Bi}_{25}\text{FeO}_{39}$ form at 753 K. At 773 and 793 K, $\text{Bi}_2\text{Fe}_4\text{O}_9$ appeared along with BiFeO_3 and $\text{Bi}_{25}\text{FeO}_{39}$. At 813 K and above, the fraction of $\text{Bi}_2\text{Fe}_4\text{O}_9$ increased while that of $\text{Bi}_{25}\text{FeO}_{39}$ decreased substantially.

To summarize, the data in the literature indicates that only three ternary compounds exist in the Bi_2O_3 - Fe_2O_3 system viz., $\text{Bi}_2\text{Fe}_4\text{O}_9$, BiFeO_3 and $\text{Bi}_{25}\text{FeO}_{39}$. All of these compounds decompose peritectically. Although the composition of the Bi_2O_3 rich phase was initially reported as $\text{Bi}_{40}\text{Fe}_2\text{O}_{63}$ ($\text{Bi/Fe} = 20$), later it was shown to be $\text{Bi}_{25}\text{FeO}_{39}$ ($\text{Bi/Fe} = 25$) based on XRD and neutron diffraction studies. This compound is known to decompose peritectically and the literature data shows the peritectic temperature lies in the range of 1058 to 1073 K. Peritectic decomposition temperature of $\text{Bi}_2\text{Fe}_4\text{O}_9$ is reported to be in the range of 1193 – 1234 K. The thermodynamic stability of BiFeO_3 has been under disagreement. Even preparation of phase pure BiFeO_3 was difficult which has been attributed to the purity of chemicals used. Obviously, kinetics of the formation/decomposition of phases are sluggish which hinders achievement of equilibrium conditions. Although pseudo-binary phase diagram of Bi_2O_3 - Fe_2O_3 system has been reported, there is disagreement in the peritectic decomposition temperatures of the ternary compounds. No studies have been reported in the literature on the ternary phase diagram of Bi-Fe-O system. The thermochemical data on these ternary compounds are also limited.

3.3 Experimental

3.3.1 Materials

Bi_2O_3 powder (99.99% purity on metals basis, M/s Alfa Aesar, UK), Fe_2O_3 powder (99.99% purity on metals basis, M/s Alfa Aesar, UK) were used as the starting materials for the preparation of the ternary compounds. For phase equilibration studies, Fe powder (99.9+% purity on metals basis, M/s Alfa Aesar, USA), FeO (99.9%, M/s Cerac, USA) and Bi powder (99.5% on metals basis, M/s Alfa Aesar, USA) were also used as the starting materials. Fe_3O_4 was prepared by reducing Fe_2O_3 at 800 K for 6 h under Ar-1% hydrogen gas mixture saturated with water vapour. Bi_2O_3 was calcined at 973 K for 5 h to remove the carbonate impurity and moisture while Fe_2O_3 was calcined at 523 K for 2 h to remove the moisture. Both these oxides were stored in a desiccator before using them in experiments. Commercial Fe_2O_3 powder is usually prepared by steps involving calcination at high temperatures and as a result, its reactivity is anticipated to be low. Because of the low reactivity, its dissolution in HCl during acid solution calorimetric experiments was found to be sluggish. In order to increase the reactivity, finely divided Fe_2O_3 powder was prepared by solution chemistry route. For this, $\text{Fe}(\text{NO}_3)_3 \cdot 9\text{H}_2\text{O}$ (mass fraction purity > 0.9999 on metals basis, M/s Aldrich Chem. Co., USA) was dissolved in distilled water and precipitated out as $\text{Fe}(\text{OH})_3$ by adding excess ammonium hydroxide solution. The precipitate was filtered, dried, heated at 623 K for 12 h in air and Fe_2O_3 formed was characterized using X-ray powder diffractometer (M/s INEL, France) with Cu K_α radiation. Analytical Reagent (AR) grade HCl (aq.) diluted with distilled water to 8.38 mol kg^{-1} was used as the calorimetric solvent. KCl (M/s The National Institute of Standards and Technology (NIST), USA) and tris (hydroxyl

methyl) aminomethane (TRIS) (M/s Merck, UK) were used for chemical calibration of the solution calorimeter.

3.3.2 Preparation of ternary oxides

The ternary compounds were prepared by solid state reaction of appropriate molar ratios of Bi_2O_3 and Fe_2O_3 . The starting materials were ground thoroughly and made in the form of pellets and heated in platinum crucibles for 144 h in air at 973 K for preparing $\text{Bi}_{25}\text{FeO}_{39}$ and $\text{Bi}_2\text{Fe}_4\text{O}_9$, and at 1073 K for preparing BiFeO_3 . All these samples were ground at the end of 50% the total time of heating. They were repelletized followed by heating at the same temperature. The resulting products were characterized by XRD. BiFeO_3 and $\text{Bi}_2\text{Fe}_4\text{O}_9$ were also prepared by a method involving co-precipitation of the hydroxides. For this preparation, stoichiometric amounts of Bi_2O_3 and Fe_2O_3 were first dissolved in a minimum amount of hot 35.2 mol kg^{-1} nitric acid and the resultant nitrate solution was added to excess ammonium hydroxide solution. The precipitate formed was then filtered, washed, dried, and heated in air at 773 K for 24 h while preparing BiFeO_3 and at 823 K while preparing $\text{Bi}_2\text{Fe}_4\text{O}_9$. The products obtained were characterized by XRD.

3.3.3. Equilibration studies

Equilibration of samples with compositions lying on the pseudo - binary line of Bi_2O_3 - Fe_2O_3 system was carried out to unravel the existence of any new ternary compound other than the three reported compounds. Eight samples having different molar ratios of Bi_2O_3 : Fe_2O_3 (7:33, 17:23, 29:11 and 39:1) which corresponded to compositions falling between the reported ternary compounds, were prepared. For this preparation, stoichiometric amounts of Bi_2O_3 and Fe_2O_3 were mixed thoroughly,

made in the form of pellets and equilibrated in platinum crucibles at 1023 K in air for 480 h. All these samples were ground at the end of 50% the total time of heating and characterized by XRD. They were repelletized followed by heating at the same temperature. After equilibration, samples were quenched in ice cold water and the products obtained were characterized by XRD. Similar equilibrations were carried out at 773 K also while increasing the total equilibration time to 960 h. The compositions chosen for equilibration are shown in Fig. 3.5 and the details of the samples are given in Table 3.2.

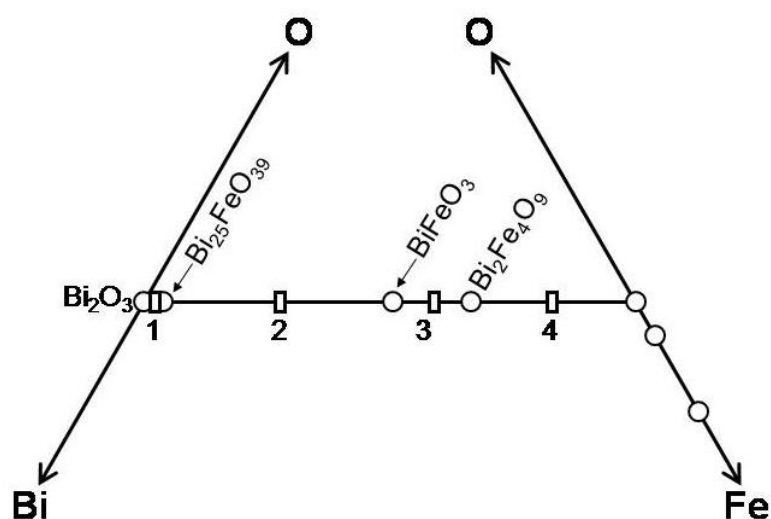


Fig. 3.5 Compositions of samples taken for equilibration (□) in the Bi_2O_3 - Fe_2O_3 pseudo-binary line

Table 3.2 Details of equilibration of samples with composition falling on Bi₂O₃-Fe₂O₃ pseudo-binary line

Sample no.	Phases taken before equilibration (equivalent Bi₂O₃: Fe₂O₃)	Phases obtained after equilibration at 1023 K for 480 h	Phases obtained after equilibration at 773 K for 960 h *
1.a	Bi ₂ O ₃ , Fe ₂ O ₃ (39:1)	Bi ₂ O ₃ , Bi ₂₅ FeO ₃₉	Bi ₂ O ₃ , Bi ₂₅ FeO ₃₉
1.b	Bi ₂ O ₃ , Bi ₂ Fe ₄ O ₉ (39:1)	Bi ₂ O ₃ , Bi ₂₅ FeO ₃₉	Bi ₂ O ₃ , Bi ₂₅ FeO ₃₉
2.a	Bi ₂ O ₃ , Fe ₂ O ₃ (29:11)	Bi ₂₅ FeO ₃₉ , BiFeO ₃	Bi ₂₅ FeO ₃₉
2.b	Bi ₂ O ₃ , Bi ₂ Fe ₄ O ₉ (29:11)	Bi ₂₅ FeO ₃₉ , BiFeO ₃	Bi ₂₅ FeO ₃₉ , Bi ₂ Fe ₄ O ₉
3.a	Bi ₂ O ₃ , Fe ₂ O ₃ (17:23)	BiFeO ₃ , Bi ₂ Fe ₄ O ₉	Bi ₂₅ FeO ₃₉ , Fe ₂ O ₃
3.b	Bi ₂₅ FeO ₃₉ , Fe ₂ O ₃ (17:23)	BiFeO ₃ , Bi ₂ Fe ₄ O ₉	Bi ₂₅ FeO ₃₉ , Fe ₂ O ₃ , BiFeO ₃
4.a	Bi ₂ O ₃ , Fe ₂ O ₃ (7:33)	Bi ₂ Fe ₄ O ₉ , Fe ₂ O ₃	Bi ₂₅ FeO ₃₉ , Fe ₂ O ₃
4.b	BiFeO ₃ , Fe ₂ O ₃ (7:33)	Bi ₂ Fe ₄ O ₉ , Fe ₂ O ₃	BiFeO ₃ , Fe ₂ O ₃

* Results show equilibration time was insufficient.

To determine the phase fields in the ternary Bi-Fe-O system, equilibrations were carried out by taking appropriate mixtures of bismuth and iron metal powders and their oxides. After thorough mixing, the starting materials were made into pellets. The pellets were placed in zirconia crucibles which were hermetically sealed inside copper tubes. The photograph of a copper tube which is sealed with sample inside is shown in Fig. 3.6. The sealing was carried out by pulsed tungsten inert gas welding inside an argon atmosphere glove box containing < 5 ppm of oxygen and moisture. The samples in copper tubes were then equilibrated by placing them in a stainless steel vessel under flowing argon gas. The temperature and total duration of equilibration were 1023 K and 480 h, respectively. Equilibrations were also carried out at 773 K with a total equilibration time of 960 h. All the equilibrations were carried out with one intermediate grinding at the end of 50% total duration of heating, repelletisation and hermetic sealing in copper tubes. This was followed by heating

again at 773 K. Initially these equilibrations were carried out in vacuum sealed quartz tubes with samples contained in alumina crucibles. However, in most of the cases, the quartz tubes were severely attacked. Analysis of the deposits on the quartz tubes showed significant amounts of bismuth indicating attack due to Bi_2O_3 vapour. Since Cu_2O is thermodynamically less stable than Bi_2O_3 (ΔG° for the reaction: $6 \text{ Cu (s)} + \text{Bi}_2\text{O}_3 \text{ (s)} \rightarrow 2 \text{ Bi (l)} + 3 \text{ Cu}_2\text{O (s)}$ is 24.6 kJ mol^{-1} at 773 K and 3.3 kJ mol^{-1} at 1023 K.), copper tubes were used to contain the samples taken in zirconia crucibles. The products obtained after equilibrations were analyzed by XRD. The compositions taken for equilibration are shown in Figs. 3.7 and 3.8. The details of these experiments are given in Tables 3.3 to 3.6.



Fig. 3.6 Cu tube sealed under argon atmosphere with sample inside

To confirm the phases that co-exist with liquid bismuth, samples were equilibrated with excess of liquid bismuth also. Porous pellets of samples containing Bi metal powder as a constituent were prepared and were kept immersed in excess of molten bismuth metal taken in alumina crucibles. The pellets were immersed in liquid Bi with the help of alumina strips. Either two or three alumina crucibles were placed

over the alumina strips so as to keep the pellets immersed in liquid Bi. Bismuth metal was taken as a constituent of the sample pellet to ensure good contact between the solid phases and the excess liquid bismuth in the crucible during equilibrations. The entire sample preparation was carried out inside the argon atmosphere glove box. The samples were then taken outside the glove box, vacuum sealed in quartz ampoules and equilibrated (Since the pellets were immersed in excess liquid Bi, vapourization of Bi_2O_3 was minimum. The samples taken in alumina crucibles could therefore be sealed in quartz ampoules.). The initial compositions of the pellets are shown in Fig. 3.7 and 3.8. The phases and composition of samples taken for equilibration at 1023 K are given in Tables 3.3 and 3.5. The corresponding data on samples equilibrated at 773 K are given in Tables 3.4 and 3.6.

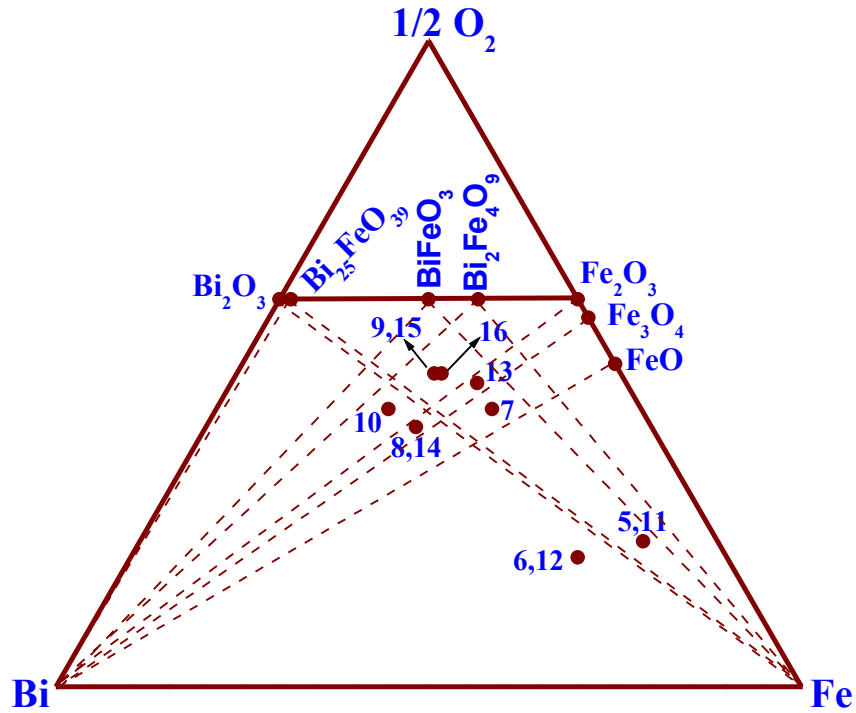


Fig. 3.7 Compositions of samples taken for equilibration (5 to 16) as given in Tables 3.3 and 3.4 and possible phase fields (dotted lines) of Bi-Fe-O system

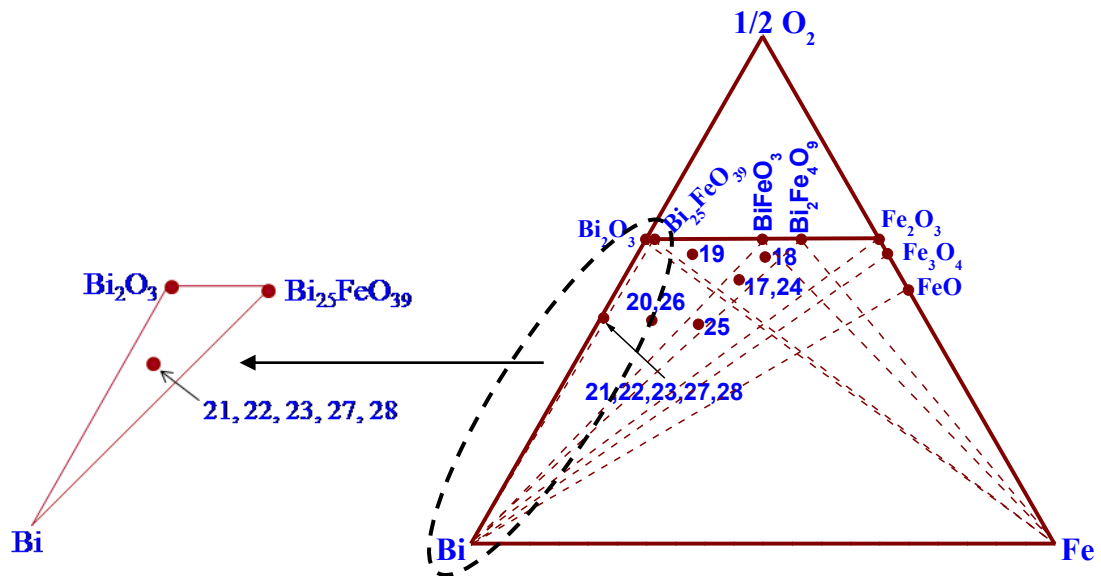


Fig. 3.8 Compositions of samples taken for equilibration (17 to 28) as given in Tables 3.5 and 3.6 and possible phase fields (dotted lines) of Bi-Fe-O system

Table 3.3 Details of equilibration of samples with compositions in the section bound by Bi, Fe and Bi₂Fe₄O₉ at 1023 K

Sample no.	Composition	Phases taken before equilibration	Duration of equilibration (h)	Phases obtained after equilibration
5	Bi _{0.100} Fe _{0.675} O _{0.225}	Fe, Fe ₂ O ₃ , Bi ₂ O ₃	480	Bi, Fe, FeO
6	Bi _{0.200} Fe _{0.600} O _{0.200} *	Bi, Fe, Fe ₂ O ₃ in liq.Bi	390	Bi, Fe, FeO
7	Bi _{0.200} Fe _{0.370} O _{0.430}	Fe, Fe ₂ O ₃ , Bi ₂ O ₃	480	Bi, FeO, Fe ₃ O ₄
8	Bi _{0.316} Fe _{0.282} O _{0.402} *	Bi, Fe, Bi ₂ O ₃ in liq.Bi	390	Bi, Fe ₂ O ₃ , Fe ₃ O ₄
9	Bi _{0.250} Fe _{0.265} O _{0.485}	i)Bi ₂ O ₃ , Fe, FeO	480	Bi, Fe ₂ O ₃ ,
		ii)Bi ₂₅ FeO ₃₉ , Fe, Fe ₃ O ₄	480	Bi ₂ Fe ₄ O ₉ Bi, Fe ₂ O ₃ , Bi ₂ Fe ₄ O ₉
10	Bi _{0.339} Fe _{0.231} O _{0.430} *	Bi, Fe, Bi ₂ O ₃ in liq.Bi	390	Bi, Fe ₂ O ₃ , Bi ₂ Fe ₄ O ₉

* Overall composition of the phase mixture taken in the form of pellet which was equilibrated with excess of liquid Bi. Samples sealed in quartz ampoules.

Table 3.4 Details of equilibration of samples with compositions in the section bound by Bi, Fe and Bi₂Fe₄O₉ at 773 K

Sample no.	Composition	Phases taken before equilibration	Duration of equilibration (h)	Phases obtained after equilibration
11	Bi _{0.100} Fe _{0.675} O _{0.225} *	i) Fe, Fe ₃ O ₄ , Bi ₂₅ FeO ₃₉	960	Bi, Fe, Fe ₃ O ₄
		ii) Bi ₂ O ₃ , Fe, Fe ₂ O ₃ in liq. Bi	960	Bi, Fe, Fe ₃ O ₄
12	Bi _{0.200} Fe _{0.600} O _{0.200} *	Bi, Fe, Fe ₂ O ₃ in liq.Bi	480	Bi, Fe, Fe ₃ O ₄
13	Bi _{0.200} Fe _{0.330} O _{0.470}	Fe, FeO, Bi ₂₅ FeO ₃₉	960	Bi, Fe ₃ O ₄ ,
				Bi ₂ Fe ₄ O ₉ Bi ₂₅ FeO ₃₉
14	Bi _{0.316} Fe _{0.282} O _{0.402} *	Bi, Fe, Bi ₂ O ₃ in liq.Bi	480	Bi, Fe ₂ O ₃ , Fe ₃ O ₄
15	Bi _{0.250} Fe _{0.265} O _{0.485}	Fe, Fe ₃ O ₄ , Bi ₂₅ FeO ₃₉	960	Fe ₃ O ₄ , Bi ₂₅ FeO ₃₉ ,
				Bi, Bi ₂ Fe ₄ O ₉
16	Bi _{0.240} Fe _{0.275} O _{0.485} *	Bi, Bi ₂ Fe ₄ O ₉ , Fe ₂ O ₃ in liq.Bi	480	Bi, Bi ₂ Fe ₄ O ₉ ,
				Fe ₂ O ₃

* Overall composition of the phase mixture taken in the form of pellet which was equilibrated with excess of liquid Bi. Samples sealed in quartz ampoules.

Table 3.5 Details of equilibration of samples with compositions in the section bound by Bi, Bi₂Fe₄O₉ and Bi₂O₃ at 1023 K

Sample no.	Composition	Phases taken before equilibration	Duration of equilibration (h)	Phases obtained after equilibration
17	Bi _{0.280} Fe _{0.200} O _{0.520}	Bi ₂ O ₃ , Fe, Fe ₂ O ₃	480	Bi, Bi ₂ Fe ₄ O ₉ , BiFeO ₃ , Bi ₂₅ FeO ₃₉ (minor)
18	Bi _{0.213} Fe _{0.222} O _{0.565} *	Bi, Fe ₂ O ₃ , Bi ₂ O ₃ in liq. Bi	480	Bi, Bi ₂ Fe ₄ O ₉ , BiFeO ₃ , Bi ₂₅ FeO ₃₉ (minor)
19	Bi _{0.335} Fe _{0.095} O _{0.570}	Bi ₂ O ₃ , Fe, Fe ₂ O ₃	480	Bi, BiFeO ₃ , Bi ₂₅ FeO ₃₉
20	Bi _{0.470} Fe _{0.090} O _{0.440} *	Bi, Fe, Bi ₂ O ₃ in liq. Bi	480	Bi, BiFeO ₃ , Bi ₂₅ FeO ₃₉
21	Bi _{0.550} Fe _{0.005} O _{0.445}	Bi, Bi ₂ Fe ₄ O ₉ , Bi ₂ O ₃	480	Bi, Bi ₂₅ FeO ₃₉ , Bi ₂ O ₃
22	Bi _{0.550} Fe _{0.005} O _{0.445} *	Bi, Fe ₂ O ₃ , BiFeO ₃ in liq. Bi	480	Bi, Bi ₂₅ FeO ₃₉ , Bi ₂ O ₃
23	Bi _{0.550} Fe _{0.005} O _{0.445} *	Bi, Fe, Bi ₂ O ₃ in liq. Bi	480	Bi, Bi ₂₅ FeO ₃₉ , Bi ₂ O ₃

* Overall composition of the phase mixture taken in the form of pellet which was equilibrated with excess of liquid Bi. Samples sealed in quartz ampoules.

Table 3.6 Details of equilibration of samples with compositions in the section bound by Bi, Bi₂Fe₄O₉ and Bi₂O₃ at 773 K

Sample no.	Composition	Phases taken before equilibration	Duration of equilibration (h)	Phases obtained after equilibration
24	Bi _{0.280} Fe _{0.200} O _{0.520} *	Bi ₂ O ₃ , Fe, Fe ₂ O ₃ in liq. Bi	480	Bi, Bi ₂ Fe ₄ O ₉ , BiFeO ₃ , Bi ₂₅ FeO ₃₉ (minor)
25	Bi _{0.394} Fe _{0.174} O _{0.432} *	Bi, Fe, Bi ₂ O ₃ in liq. Bi	480	Bi, Bi ₂ Fe ₄ O ₉ , BiFeO ₃ , Bi ₂₅ FeO ₃₉ (minor)
26	Bi _{0.470} Fe _{0.090} O _{0.440} *	Bi, Fe, Bi ₂ O ₃ in liq. Bi	480	Bi, BiFeO ₃ , Bi ₂₅ FeO ₃₉
27	Bi _{0.550} Fe _{0.005} O _{0.445}	Bi, Bi ₂ Fe ₄ O ₉ , Bi ₂ O ₃	960	Bi, Bi ₂₅ FeO ₃₉ , Bi ₂ O ₃
28	Bi _{0.550} Fe _{0.005} O _{0.445} *	Bi, Fe ₂ O ₃ , BiFeO ₃ in liq. Bi	480	Bi, Bi ₂₅ FeO ₃₉ , Bi ₂ O ₃

* Overall composition of the phase mixture taken in the form of pellet which was equilibrated with excess of liquid Bi. Samples sealed in quartz ampoules.

3.3.4 Oxygen potential measurements using yttria stabilized zirconia solid electrolyte

Oxygen potentials in the relevant phase fields were measured using emf cells based on yttria stabilized zirconia solid electrolyte. The schematic of the experimental assembly of the emf cell and its photograph are shown in Figs. 3.9 and 3.10, respectively. One end closed yttria stabilized zirconia (YSZ) solid electrolyte tube having a flat bottom (13 mm OD, 9 mm ID and 300 mm long) supplied by M/s Nikkato Corporation, Japan was used. Reference electrode of the cell was prepared by applying platinum paste (M/s Eltecks Corporation, India) over the inner bottom surface of the electrolyte tube and heating it at 1373 K for 2 h in air which resulted in a uniform and porous platinum film over the electrolyte surface. A platinum wire attached to platinum mesh, co-fired with the platinum paste was used as the electrical lead. A similar porous platinum electrode was formed on the external surface at the bottom of the electrolyte tube. The solid electrolyte tube was fastened to a stainless steel coupling using a high temperature epoxy seal. The stainless steel coupling had provision for placing a K-type thermocouple very close to electrode-electrolyte assembly so that the cell temperature can be measured accurately. The thermocouple was calibrated prior to actual experiments against a standard calibrated thermocouple supplied by National Physical Laboratory, India. The entire cell assembly was surrounded by a one end closed quartz tube which was also attached to the stainless steel coupling using an O-ring seal. It also had provision for flowing gases through the sample and reference compartments. The performance of the emf cell was tested by measuring the null emf by maintaining identical oxygen pressures on both sides of the electrolyte (air-air and oxygen-oxygen).

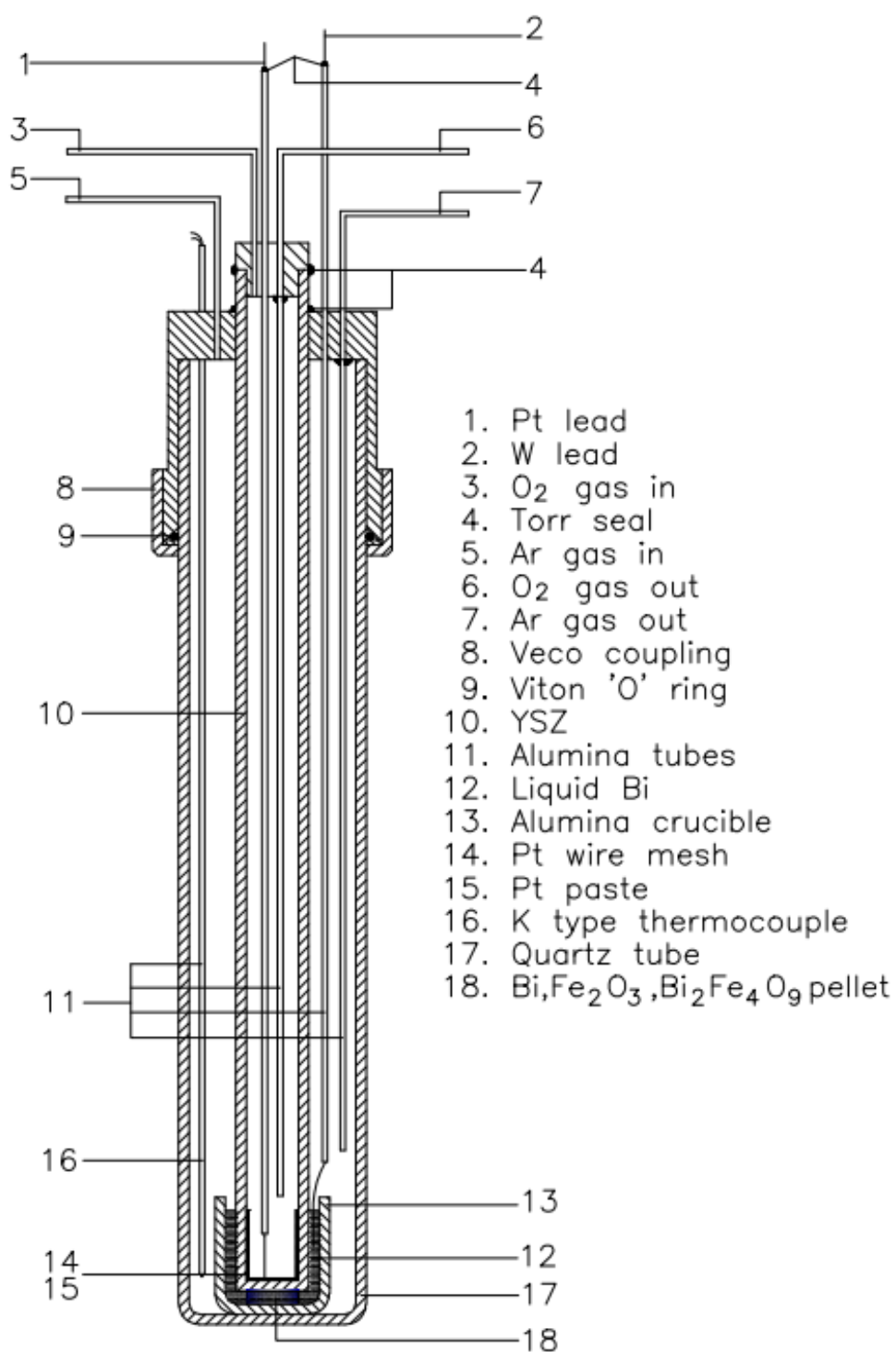


Fig. 3.9 Schematic of the emf cell



Fig. 3.10 Photograph of the emf cell used

Later, the Pt electrode and the Pt lead present on the external surface of the electrolyte tube were removed, thoroughly cleaned and used for measurements with sample electrodes. For sample electrodes, tungsten wire was used as electrical lead instead of platinum because platinum was not compatible with the sample electrode. Sample electrode was prepared by mixing the starting materials in approximately equal volume ratios and by pelletizing it. The entire cell assembly was taken inside an argon atmosphere glove box. Appropriate quantity of Bi metal was melted in an alumina crucible and the sample pellet was then forcibly dipped in liquid bismuth by placing the solid electrolyte tube over it in such a way that the lower end of the tungsten lead was dipped in liquid Bi. After slow cooling, the entire cell assembly was taken outside the glove box. During emf measurements, high purity argon and

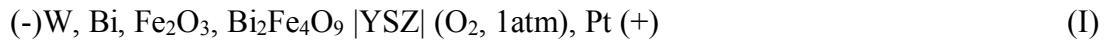
oxygen gases were passed through the sample and reference compartments, respectively. High purity argon was obtained by passing commercial argon through a purification assembly. The purification train consisted of columns of regenerated LINDE 4A molecular sieves and active Cu impregnated MgSiO_3 pellets (popularly known as BASF catalyst) maintained at ambient temperature followed by three columns containing metallic copper turnings held at 773 K, titanium sponge held at 1173 K and calcium metal shots held at 773 K. The gas exiting from the outlet of the emf cell was again passed over another column containing calcium metal shots maintained at 773 K before letting it out to the ambient air. The cell assembly was placed in the constant temperature zone of a furnace. A 50 mm long, hollow cylindrical stainless steel block was also placed in the constant temperature zone of the furnace to further enhance the uniformity of the temperature in the zone. Using this arrangement, the cell temperature could be controlled within ± 0.2 K using a PID temperature controller. The stainless steel block was grounded to avoid any a.c. pickup in the emf signal. The cell emf was measured using a high impedance electrometer (input impedance $>10^{14}\Omega$, M/s Keithley, U.S.A, Model-6514) and the temperature was measured using a multimeter (M/s Agilent Technologies, Malaysia, Model- 34970A Data acquisition/switch unit). Data were recorded using a computer interface. Attainment of equilibrium was tested by shorting the two electrical leads and testing for the restoration of the pre-test emf. The readings were recorded when the cell emf was stable within ± 0.05 mV for at least 6 h.

In the present study, emf measurements were carried out for two purposes:

- (i) To determine the Gibbs energy of formation of $\text{Bi}_2\text{Fe}_4\text{O}_9$, BiFeO_3 and $\text{Bi}_{25}\text{FeO}_{39}$.

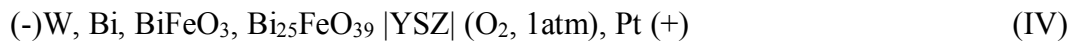
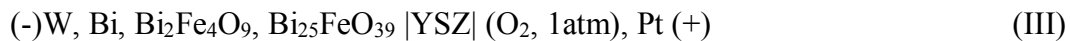
- (ii) To determine the temperature range of stability of BiFeO_3

Gibbs energy of formation of $\text{Bi}_2\text{Fe}_4\text{O}_9$ was determined by measuring the equilibrium oxygen partial pressure in the $\text{Bi-Fe}_2\text{O}_3\text{-Bi}_2\text{Fe}_4\text{O}_9$ phase field employing the emf cell and by using the data on Gibbs energy of formation of Fe_2O_3 from literature. The following galvanic cell was constructed and used for this purpose:



The sample electrode was prepared by mixing Bi, Fe_2O_3 and $\text{Bi}_2\text{Fe}_4\text{O}_9$ powders in approximately equal volume ratios and by pelletizing it. Oxygen gas at 1 atm was used as the reference electrode. Emf was measured in the temperature range of 773 to 1023 K.

The following three emf cells were constructed and operated to determine the Gibbs energy of formation of BiFeO_3 and $\text{Bi}_{25}\text{FeO}_{39}$ and to determine the temperature range of stability of BiFeO_3 :



For cell II, Bi, $\text{Bi}_2\text{Fe}_4\text{O}_9$ and BiFeO_3 (containing small amount of $\text{Bi}_{25}\text{FeO}_{39}$) mixture was used as the sample electrode and for cell III, a mixture of Bi, $\text{Bi}_2\text{Fe}_4\text{O}_9$ and $\text{Bi}_{25}\text{FeO}_{39}$ was used as the sample electrode. Two sample electrodes with different compositions but falling within the section bound by Bi, BiFeO_3 and $\text{Bi}_{25}\text{FeO}_{39}$ were used for measurements with cell IV. As in the case of cell I, 1 atm oxygen gas was used as the reference electrode and emf was measured in the temperature range of 773 to 1023 K.

Before and after completion of the emf measurements (which involved multiple heating and cooling cycles), the sample electrodes were analyzed by XRD.

The thermo emf due to dissimilar electrical leads viz., platinum and tungsten was measured by forming a junction between the two electrical leads followed by the measurement of the thermo emf between them as a function of temperature. The measured data were fitted to a polynomial expression of order two and is given by:

$$E \pm 0.16 / \text{mV} = -1.56 - 7.97 \times 10^{-4} T + 1.84 \times 10^{-5} T^2 (T: 337 - 1076 \text{ K}) \quad (3.2)$$

The error given is the standard deviation of the least squares fitted line. Using the above expression for thermo EMF, the measured cell EMF values were corrected to derive the actual EMF.

3.3.5 Investigations on thermal stability of BiFeO₃

In literature, there is disagreement in the temperature range of stability of BiFeO₃ which has been discussed in section 3.2.4. Hence, various studies involving DTA, DSC, long term equilibrations etc were carried out to determine the temperature range of stability of BiFeO₃.

3.3.5.1 DTA and DSC studies with BiFeO₃

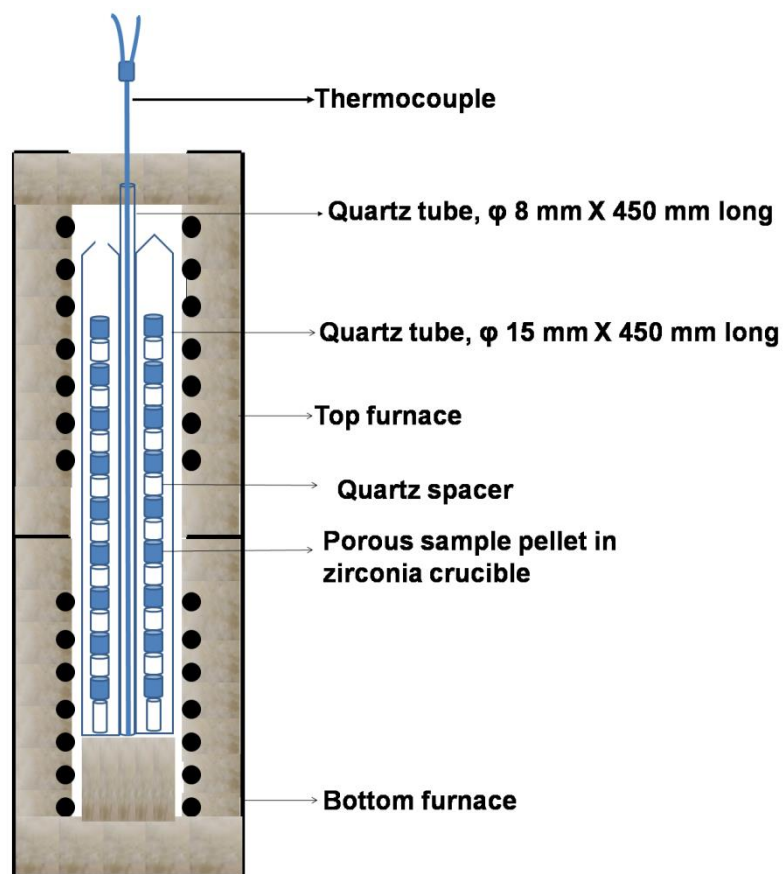
In this experiment, ~50 mg of BiFeO₃ taken in a crucible was heated up to 973 K in argon atmosphere at a heating rate of 10 K min⁻¹ followed by cooling at a rate of 10 K min⁻¹ up to room temperature. After the experiment, the sample was characterized by XRD for identifying any change it might have undergone during DTA experiments. Thermal behaviour of BiFeO₃ was also studied by differential scanning calorimetry. Approximately 150 mg of sample was used and DSC runs were made up to 823 K at a heating rate of 10 K min⁻¹ under argon atmosphere and

maintained at that temperature for 10 minutes. The sample was then cooled to room temperature. Before and after the experiment, the sample was characterized by XRD.

3.3.5.2 Equilibration of BiFeO₃ in vacuum and air at different temperatures

As discussed in section 3.2.4, BiFeO₃ has been reported to be metastable at low temperatures (720 to 1040 K) and attains thermodynamic stability at relatively high temperature (above 1040 K). Hence, experiments involving equilibration of BiFeO₃ in air and under vacuum for prolonged periods were carried out to determine its temperature range of stability. The schematic of the experimental setup used for this study is shown in Fig. 3.11. For this experiment, BiFeO₃ prepared by co-precipitation method described in section 3.3.2 was used. Samples of BiFeO₃ were made in the form of pellets. These pellets were taken in zirconia crucibles and placed in two 450 mm long and 15 mm dia one end closed quartz tubes at different heights using quartz spacers. In each quartz tube, nine samples were loaded. One of the quartz tubes was sealed under vacuum (10^{-6} torr) while the other tube was kept open to air. A K-type thermocouple which can move vertically at a very slow speed (0.38 cm min^{-1}) with the help of a motor was inserted in another quartz tube and which was used to measure the temperature of the samples and the data was logged using data acquisition system. The three quartz tubes were tied together and placed concentrically inside a temperature gradient furnace assembly. The assembly consisted of two furnaces which were stacked one over the other. The temperature of each furnace was maintained at different values and controlled within $\pm 1 \text{ K}$. The actual position of the samples i.e., height in the furnace assembly determined their temperatures. The temperature of the samples varied between 716 and 1089 K.

Samples were equilibrated for 480 h, quenched in ice cold water and the products were characterized by XRD. The temperatures chosen for the equilibrations are given in Tables 3.7 and 3.8.



Quartz spacers used are of different heights

Fig. 3.11 Schematic of the experimental setup used for equilibrating BiFeO_3 at different temperatures

Table 3.7 Phases formed after equilibration of BiFeO₃ (containing small amount of Bi₂₅FeO₃₉) in vacuum for 480 h

Sample no.	Temperature (K)	Phases obtained after equilibration
1	716	BiFeO ₃ (major phase), Bi ₂₅ FeO ₃₉ (minor phase)
2	722	BiFeO ₃ (major phase), Bi ₂₅ FeO ₃₉ (minor phase)
3	726	BiFeO ₃ (major phase), Bi ₂₅ FeO ₃₉ (minor phase)
4	763	BiFeO ₃ , Bi ₂₅ FeO ₃₉ , Bi ₂ Fe ₄ O ₉
5	805	Bi ₂₅ FeO ₃₉ , Bi ₂ Fe ₄ O ₉
6	871	Bi ₂₅ FeO ₃₉ , Bi ₂ Fe ₄ O ₉
7	943	BiFeO ₃ (minor phase), Bi ₂₅ FeO ₃₉ (major phase), Bi ₂ Fe ₄ O ₉ (major phase)
8	1034	BiFeO ₃ (major phase), Bi ₂₅ FeO ₃₉ (minor phase), Bi ₂ Fe ₄ O ₉ (minor phase)
9	1089	BiFeO ₃ (major phase), Bi ₂₅ FeO ₃₉ (minor phase), Bi ₂ Fe ₄ O ₉ (minor phase)

Table 3.8 Phases formed after equilibration of BiFeO₃ (containing small amount of Bi₂₅FeO₃₉) in air for 480 h

Sample no.	Temperature (K)	Phases obtained after equilibration
10	716	BiFeO ₃ (major phase), Bi ₂₅ FeO ₃₉ (minor phase)
11	722	BiFeO ₃ (major phase), Bi ₂₅ FeO ₃₉ (minor phase)
12	725	BiFeO ₃ (major phase), Bi ₂₅ FeO ₃₉ (minor phase)
13	757	BiFeO ₃ (major phase), Bi ₂₅ FeO ₃₉ (minor phase)
14	807	BiFeO ₃ , Bi ₂₅ FeO ₃₉ , Bi ₂ Fe ₄ O ₉
15	853	Bi ₂₅ FeO ₃₉ , Bi ₂ Fe ₄ O ₉
16	941	BiFeO ₃ (minor phase), Bi ₂₅ FeO ₃₉ (major phase), Bi ₂ Fe ₄ O ₉ (major phase)
17	1028	BiFeO ₃ (major phase), Bi ₂₅ FeO ₃₉ (minor phase), Bi ₂ Fe ₄ O ₉ (minor phase)
18	1085	BiFeO ₃ (major phase), Bi ₂₅ FeO ₃₉ (minor phase), Bi ₂ Fe ₄ O ₉ (minor phase)

3.3.5.3 Equilibration of samples containing BiFeO₃ with liquid Bi

Thermal stability of BiFeO₃ was also examined by equilibrating phase mixtures containing BiFeO₃ with liquid Bi. Equilibrations were carried out at 873 and 1023 K. Starting materials were made in the form of porous pellets and kept immersed in liquid Bi taken in alumina crucibles using alumina strips as described in section 3.3.3. The samples were prepared in the inert atmosphere glove box. Then the samples were taken out from the glove box, vacuum sealed in quartz ampoules and equilibrated at the chosen temperatures for 480 h. After equilibration, the ampoules were quenched in ice cold water and the samples were retrieved. They were then characterized by XRD. The compositions chosen for equilibration are given in Table 3.9.

Table 3.9 Results of equilibration of Bi, Bi₂Fe₄O₉, BiFeO₃ and Bi, BiFeO₃, Bi₂₅FeO₃₉ mixtures in liquid Bi

Starting materials and their mole ratio	Temperature (K)	Phases obtained after equilibrating in liq. Bi for 480 h
Bi, Bi ₂ Fe ₄ O ₉ , BiFeO ₃ (1 : 0.6 : 2) (Overall composition within the area bound by Bi, Bi ₂ Fe ₄ O ₉ and BiFeO ₃)	873	Bi, Bi ₂ Fe ₄ O ₉ , BiFeO ₃ (minor phase), Bi ₂₅ FeO ₃₉
	1023	Bi, Bi ₂ Fe ₄ O ₉ , BiFeO ₃ , Bi ₂₅ FeO ₃₉
Bi, BiFeO ₃ , Bi ₂₅ FeO ₃₉ (1 : 1.56 : 0.1) (Overall composition within the area bound by Bi, BiFeO ₃ and Bi ₂₅ FeO ₃₉)	873	Bi, BiFeO ₃ (minor phase), Bi ₂₅ FeO ₃₉ , Bi ₂ Fe ₄ O ₉ (minor phase)
	1023	Bi, BiFeO ₃ , Bi ₂₅ FeO ₃₉

3.3.6 Determination of standard enthalpy of formation of bismuth ferrites by acid solution calorimetry

Standard enthalpy of formation of bismuth ferrites viz., $\text{Bi}_{25}\text{FeO}_{39}$ and $\text{Bi}_2\text{Fe}_4\text{O}_9$ were determined by acid solution calorimetry. Since BiFeO_3 could not be prepared phase pure (it always contained small amount of $\text{Bi}_{25}\text{FeO}_{39}$), its standard enthalpy of formation could not be measured. The details of the experimental setup are given in Chapter 2. Prior to the actual experiments, the calorimeter was calibrated chemically by measuring the heats of dissolution of KCl and TRIS in double distilled water and 0.1 mol kg^{-1} HCl, respectively. The system was electrically calibrated in situ before and after every calibration experiment. The temperature changes (ΔT) observed during the electrical calibration as well as during the chemical calibration were corrected for heat exchange between calorimeter and its surroundings by the method given in reference 25 which is explained in section 2.6.1 of Chapter 2. A similar experimental procedure was adopted during the calorimetric measurements with bismuth ferrites, Fe_2O_3 and Bi_2O_3 . In a typical experiment, about 50 to 100 mg of sample was taken inside a small glass tube provided with a thin walled bulb at the bottom. The glass tube had a glass push rod, which was sealed to the inner wall of the sample tube using a set of O-rings. 300 ml of HCl (8.38 mol kg^{-1}) was used as the calorimetric solvent. The maximum time taken for the dissolution of samples was around 7 min. The temperature changes (ΔT) during the experiment were also corrected for heat exchange between the calorimeter and its surroundings as explained above. Experiments were repeated to confirm reproducibility.

$\text{Bi}_2\text{Fe}_4\text{O}_9$ prepared by solid state method and commercially purchased Fe_2O_3 were found to dissolve slowly in the calorimetric solvent. To enhance their

dissolution rates, Fe_2O_3 and $\text{Bi}_2\text{Fe}_4\text{O}_9$ were prepared by solution route as described in sections 3.3.1 and 3.3.2, respectively and used for the calorimetric measurements. Commercially purchased Fe_2O_3 had a specific surface area of $13 \text{ m}^2 \text{ g}^{-1}$ while that of the Fe_2O_3 prepared through the solution route was $67 \text{ m}^2 \text{ g}^{-1}$. Similarly, the specific surface area of $\text{Bi}_2\text{Fe}_4\text{O}_9$ prepared by solid state reaction route was found to be $4.1 \text{ m}^2 \text{ g}^{-1}$ and that of $\text{Bi}_2\text{Fe}_4\text{O}_9$ prepared by the solution route was $7.1 \text{ m}^2 \text{ g}^{-1}$. Increased specific surface area of the samples resulted in their higher dissolution rate.

3.3.7 Heat capacity measurements using differential scanning calorimetry

Molar heat capacities of $\text{Bi}_{25}\text{FeO}_{39}$ and $\text{Bi}_2\text{Fe}_4\text{O}_9$ were measured using a heat flux type differential scanning calorimeter (Model no. HP DSC827e of M/s. Mettler Toledo GmbH, Switzerland). Temperature calibration of the DSC was carried out by using melting points of high purity metals such as In, Sn and Zn. The heat calibration was carried out using the enthalpy of melting of high purity metals such as In, Sn, Pb and Zn and heat flow rate was calibrated using sapphire. In addition to the heat flow calibration by sapphire, the performance of the DSC was also verified by measuring the heat capacity of Bi_2O_3 . For measuring heat capacity of $\text{Bi}_{25}\text{FeO}_{39}$, about 125 mg of the sample was pelletized, sintered at 973 K in air for 12 h and hermetically sealed in 40 μL aluminium pan. In the case of $\text{Bi}_2\text{Fe}_4\text{O}_9$, nearly same amount of sample was pelletized and sintered at 1073 K in air for 12h. A three-segment temperature programme was used in the heat capacity measurements. The first segment lasting for 10 min was an isothermal segment at the initial temperature; the second segment was a dynamic segment with a heating rate of 10 K min^{-1} and the final segment lasting for 10 minutes was another isothermal segment at the final temperature. Measurements

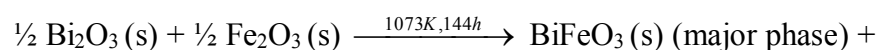
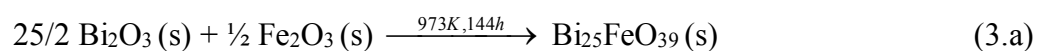
were carried out under ultra high purity argon maintained at a flow rate of 50 ml min⁻¹ in the temperature range of 308 to 823 K. A disc of sapphire was used as the molar heat capacity standard. The molar heat capacity of sapphire given by NIST, USA [26] was used for computing those of the samples. The samples were characterized by XRD before and after the calorimetric experiments.

3.4 Results and discussion

3.4.1 Preparation of ternary compounds

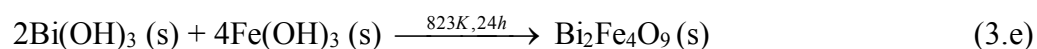
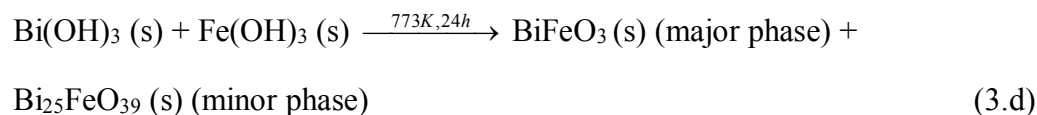
The temperature, duration of heating employed for preparing the compounds and the phases formed by the solid state reaction between the oxides and also through the solution route are given below:

3.4.1.1. Solid state reaction between oxides



3.4.1.2 Reaction between precursors prepared through solution route

In the solution route experiments, stoichiometric ratios of bismuth and iron hydroxides (prepared by the dissolution of a mixture of Bi₂O₃ and Fe₂O₃ powders in nitric acid followed by precipitation by addition of NH₄OH and thorough washing) were heated in air as follows:



The XRD patterns obtained for $\text{Bi}_{25}\text{FeO}_{39}$ and $\text{Bi}_2\text{Fe}_4\text{O}_9$ matched exactly with the patterns reported in JCPDS files 46-0416 and 74-1098, respectively [27]. Phase pure sample of BiFeO_3 could not be prepared. XRD pattern of BiFeO_3 sample showed the presence of a small amount of $\text{Bi}_{25}\text{FeO}_{39}$ also. The XRD patterns of the prepared compounds (by solid state reaction of oxides) are compared with their PCPDF patterns in Fig. 3.12.

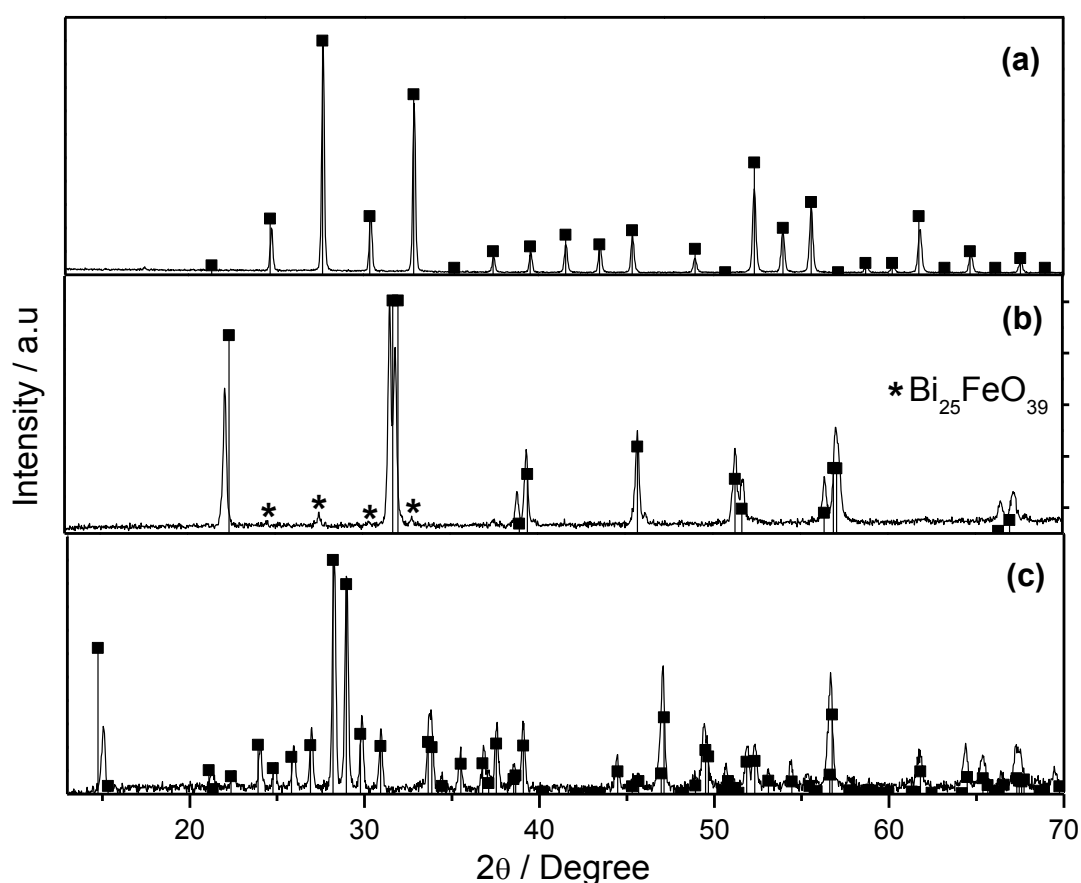


Fig. 3.12 XRD patterns of prepared compounds are overlapped with their PCPDF patterns (■). (a) $\text{Bi}_{25}\text{FeO}_{39}$, (b) BiFeO_3 and (c) $\text{Bi}_2\text{Fe}_4\text{O}_9$. Small shift of XRD pattern from the PCPDF patterns is due to the instrumental shift.

3.4.2 Studies involving equilibration of Bi_2O_3 and Fe_2O_3

The phases obtained after equilibrating the samples containing different molar ratios of Bi_2O_3 and Fe_2O_3 in air at 1023 and 773 K are shown in Table 3.2. These results clearly show that ternary compounds other than $\text{Bi}_2\text{Fe}_4\text{O}_9$, BiFeO_3 and $\text{Bi}_{25}\text{FeO}_{39}$ do not exist in the Bi_2O_3 - Fe_2O_3 system. Results of the equilibrations at 773 K reveal that the kinetics of the reactions is very slow at this temperature and the equilibrium had not reached even after 960 h. For example in sample no. 3b, presence of three phases could be identified, although only two phases could be present after attainment of equilibrium. Similarly in sample 4b, the starting materials, BiFeO_3 and Fe_2O_3 were only obtained after equilibration. As seen from the table, $\text{Bi}_{25}\text{FeO}_{39}$ was found to be formed in all samples (except in 4b) at 773 K. This could be because of the high diffusion coefficient of Bi^{3+} in $\text{Bi}_{25}\text{FeO}_{39}$ than in other relevant phases in this system; a large fraction of it was formed at 773 K. It is, however, to be noted that all expected equilibrium phases were formed at 1023K.

3.4.3 Studies with samples of composition within the section bound by Bi, Fe and $\text{Bi}_2\text{Fe}_4\text{O}_9$

Results of equilibration studies for the samples whose overall composition falling within the section bound by Bi, Fe and $\text{Bi}_2\text{Fe}_4\text{O}_9$ are described below.

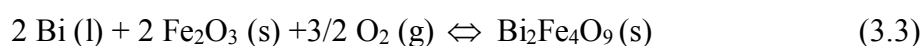
3.4.3.1 Long term equilibration of samples in the temperature range of 773 to 1023 K

Details of the studies involving equilibration of mixtures of bismuth and iron metal powders and their oxides as starting materials are given in Tables 3.3 and 3.4. Table 3.3 gives the details of equilibrations carried out at 1023 K. The attainment of equilibrium is confirmed by the appearance of same phases at the end of first half

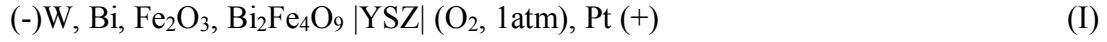
(240 h) and second half (240 h) of the total duration of equilibrations. Additional equilibrations were also carried out in liquid bismuth. From the results obtained, the existence of the following phase fields at 1023 K could be identified: 1) Bi-Fe-FeO, 2) Bi-FeO-Fe₃O₄, 3) Bi-Fe₃O₄-Fe₂O₃ and 4) Bi-Fe₂O₃-Bi₂Fe₄O₉. Equilibration of samples containing only solid state reactants at 773 K revealed that the kinetics of the reaction to be very slow. The presence of four phases in the final product (Sample Nos. 13 and 15 in Table 3.4) indicated that equilibrium was not attained even after a period of 960 h with intermittent grinding of the reactants/intermediates followed by repelletisation and heating at the same temperature. In order to ensure equilibrium, all further equilibrations at 773 K and 1023 K were carried out with liquid Bi as a constituent. The presence of liquid Bi is expected to facilitate the diffusion and reaction of constituent species by their dissolution in the liquid metal. Results of these equilibrations are also given in Tables 3.3 and 3.4. Equilibrations with excess bismuth at 773 K also revealed the existence of same phase fields as in the case of 1023 K, except for the Bi-Fe-FeO phase field. Since FeO is stable only above 853 K, this phase field did not appear at 773 K.

3.4.3.2. Gibbs energy of formation of Bi₂Fe₄O₉ from emf measurements

Based on the long term equilibrations, the existence of Bi-Fe₂O₃-Bi₂Fe₄O₉ phase field in the temperature range of 773 to 1023 K has been confirmed. The chemical equilibrium in the phase field can be represented as below:



To measure the equilibrium oxygen potentials and deduce the Gibbs energy of formation of Bi₂Fe₄O₉, emf cells based on yttria stabilized zirconia solid electrolyte were employed. The cell is represented as:



The total duration of the emf measurement was approximately 4 months. The XRD patterns of the sample before and after emf measurements confirmed the presence of Bi, Fe₂O₃ and Bi₂Fe₄O₉, as constituents before and after the experiment.

The cell emf is given by

$$E = \left(\frac{RT}{4F} \right) \ln \left(\frac{p_{O_2}^{ref}}{p_{O_2}^{sple}} \right), \quad (3.4)$$

where E is electromotive force in volts, R is universal gas constant (8.314 J K⁻¹ mol⁻¹), F is Faraday constant (96485 C mol⁻¹), $p_{O_2}^{ref}$ and $p_{O_2}^{sple}$ are the partial pressures of reference and sample electrodes, respectively. Equation (3.4) can be written as

$$4EF = RT \ln p_{O_2}^{ref} - RT \ln p_{O_2}^{sple} \quad (3.5)$$

$$4FE = \Delta \overline{G}_{O_2}^{ref} - \Delta \overline{G}_{O_2}^{sple}, \quad (3.6)$$

where $\Delta \overline{G}_{O_2}^{ref}$ and $\Delta \overline{G}_{O_2}^{sple}$ are the oxygen potentials at the reference and sample electrodes, respectively.

The emf values measured as a function of temperature are given in the chronological order in Table 3.10 and are shown in Fig. 3.13.

Table 3.10 Emf output of cell - I as a function of temperature

Temperature (K)	Dwell time (h)	Emf (mV)	Temperature (K)	Dwell time (h)	Emf (mV)
972.5	26	542.4	914.6	67	570.7
1022.9	25	518.4	873.8	265	589.6
927.3	72	564.0	823.5	187	612.6
952.5	45	552.7	848.5	138	602.7
998.6	43	530.6	799.2	396	623.5
900.1	90	576.9	885.2	167	586.3
1007.9	24	526.2	858.0	117	597.5
985.9	50	537.7	857.7	122	598.0
968.6	16	545.9	859.4	46	597.6
963.4	45	548.2	838.7	177	606.6
939.9	75	559.8	810.6	287	618.7

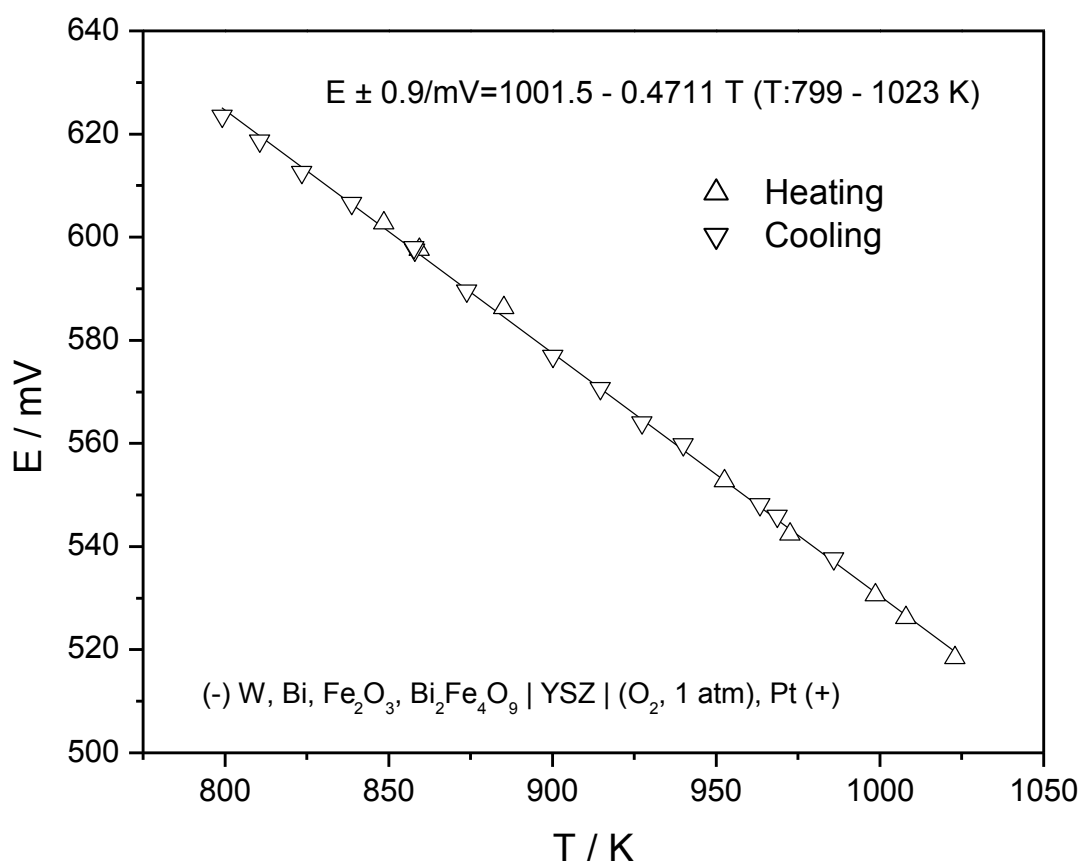


Fig. 3.13 Variation of emf with temperature for cell - I

The variation of emf with temperature can be represented by the following least squares fitted expression:

$$E \pm 0.9 / \text{mV} = 1001.5 - 0.4711 (T / \text{K}) \quad (T: 799 - 1023 \text{ K}) \quad (3.7)$$

The error given is the standard deviation of the least squares fitted line.

Considering the equilibrium (3.3) that occurs at the sample electrode, the Gibbs energy of formation of $\text{Bi}_2\text{Fe}_4\text{O}_9$ can be related to that of Fe_2O_3 and equilibrium oxygen potential.

$$\Delta_f G_m^o <\text{Bi}_2\text{Fe}_4\text{O}_9> = 2 \Delta_f G_m^o <\text{Fe}_2\text{O}_3> + 3/2 \Delta \bar{G}_{\text{O}_2}^{\text{sple}} \quad (3.8)$$

where $\Delta_f G_m^o <\text{Bi}_2\text{Fe}_4\text{O}_9>$ and $\Delta_f G_m^o <\text{Fe}_2\text{O}_3>$ are the standard molar Gibbs energies of formation of $\text{Bi}_2\text{Fe}_4\text{O}_9$ and Fe_2O_3 , respectively.

By substituting the value of $\Delta \bar{G}_{\text{O}_2}^{\text{sple}}$ from eq. (3.6) in eq. (3.8), the $\Delta_f G_m^o <\text{Bi}_2\text{Fe}_4\text{O}_9>$ can be expressed as:

$$\Delta_f G_m^o <\text{Bi}_2\text{Fe}_4\text{O}_9> = 2 \Delta_f G_m^o <\text{Fe}_2\text{O}_3> + 3/2 \Delta \bar{G}_{\text{O}_2}^{\text{ref}} - 6FE \quad (3.9)$$

Since $p_{\text{O}_2}^{\text{ref}} = 1 \text{ atm}$, eq. (3.9) becomes:

$$\Delta_f G_m^o <\text{Bi}_2\text{Fe}_4\text{O}_9> = 2 \Delta_f G_m^o <\text{Fe}_2\text{O}_3> - 6FE \quad (3.10)$$

The maximum atmospheric pressure variation observed during the period of emf measurement was $\pm 0.008 \text{ atm}$ and this deviation can result in an error of maximum $\pm 0.1 \text{ kJ}$ in the measured oxygen potentials.

The Gibbs energy of formation of Fe_2O_3 was obtained from literature data as follows: The Gibbs energy data of Fe_2O_3 , Fe and O_2 were taken from Sundman [28]. After incorporating magnetic contribution for Fe from [29], the Gibbs energy data for

Fe was recalculated. Using these data, Gibbs energy of formation of Fe₂O₃ was calculated for the temperature interval of 750 to 1050 K covering the temperature range of our experimental measurements, namely, 799 to 1023 K and is given in Table 3.11.

Table 3.11 Calculation of Gibbs energy of formation of Fe₂O₃

T / K	$G_{Fe_2O_3} /$ kJ mol ⁻¹ [28]	$G_{Fe} /$ kJ mol ⁻¹ [28]	$G_{mag,Fe} /$ kJ mol ⁻¹ [29]	$G_{Fe} +$ $G_{mag,Fe}$ / kJ mol ⁻¹	$G_{O_2} /$ kJ mol ⁻¹ [28]	$\Delta_f G_m^o <Fe_2O_3> /$ kJ mol ⁻¹
750	-918.574	-24.8198	-2.3057	-27.1255	-161.0729	-622.7136
800	-929.151	-27.9630	-1.9442	-29.9073	-172.8095	-610.1222
850	-940.224	-31.2017	-1.6099	-32.8116	-184.6516	-597.6234
900	-951.786	-34.5318	-1.3073	-35.8391	-196.5940	-585.2170
950	-963.840	-37.9494	-1.0422	-38.9916	-208.6319	-572.9091
1000	-976.355	-41.4513	-0.8218	-42.2731	-220.7610	-560.6673
1050	-989.247	-45.0345	-0.6561	-45.6905	-232.9773	-548.4000

$G_{Fe_2O_3}$, G_{Fe} and G_{O_2} : Gibbs energy data of Fe₂O₃, Fe and O₂, respectively.

$G_{mag,Fe}$: Magnetic contribution to Gibbs energy data of Fe.

$\Delta_f G_m^o <Fe_2O_3>$: Gibbs energy of formation of Fe₂O₃.

These values were fitted to a straight line by the method of least squares regression analysis and is given by:

$$\Delta_f G_m^o <Fe_2O_3> \pm 0.14 \text{ kJ} = -808.2 + 0.2476 (T / K) \quad (T: 750 - 1050 \text{ K}) \quad (3.11)$$

From the emf data given by eq. (3.7) and using the above value of $\Delta_f G_m^o$ of Fe₂O₃, the standard molar Gibbs energy of formation of Bi₂Fe₄O₉ was calculated using eq. (3.10) and is given by:

$$\Delta_f G_m^o <Bi_2Fe_4O_9> \pm 0.6 \text{ kJ} = -2196.2 + 0.7679 (T / K) \quad (T : 799-1023K) \quad (3.12)$$

Fig. 3.14 compares the Gibbs energy of formation of $\text{Bi}_2\text{Fe}_4\text{O}_9$ measured in this work with the data derived by Phapale et al. [15] from their calorimetric measurements. The data obtained in the present work is deduced from the direct measurement of equilibrium oxygen potentials. However, Phapale et al. derived the Gibbs energy data from the measured enthalpy of formation data and the enthalpy increment data from calorimetric experiments, and by using estimated value of $\Delta S_{298.15}^o$ and the value of $\Delta C_{p,298.15}$ obtained from the enthalpy increment data. Although the exact reason for the observed deviation of their data by $\sim 250 \text{ kJ mol}^{-1}$ from the value obtained by extrapolation of the data from the present work is not known, experimental errors in their enthalpy data is a possibility.

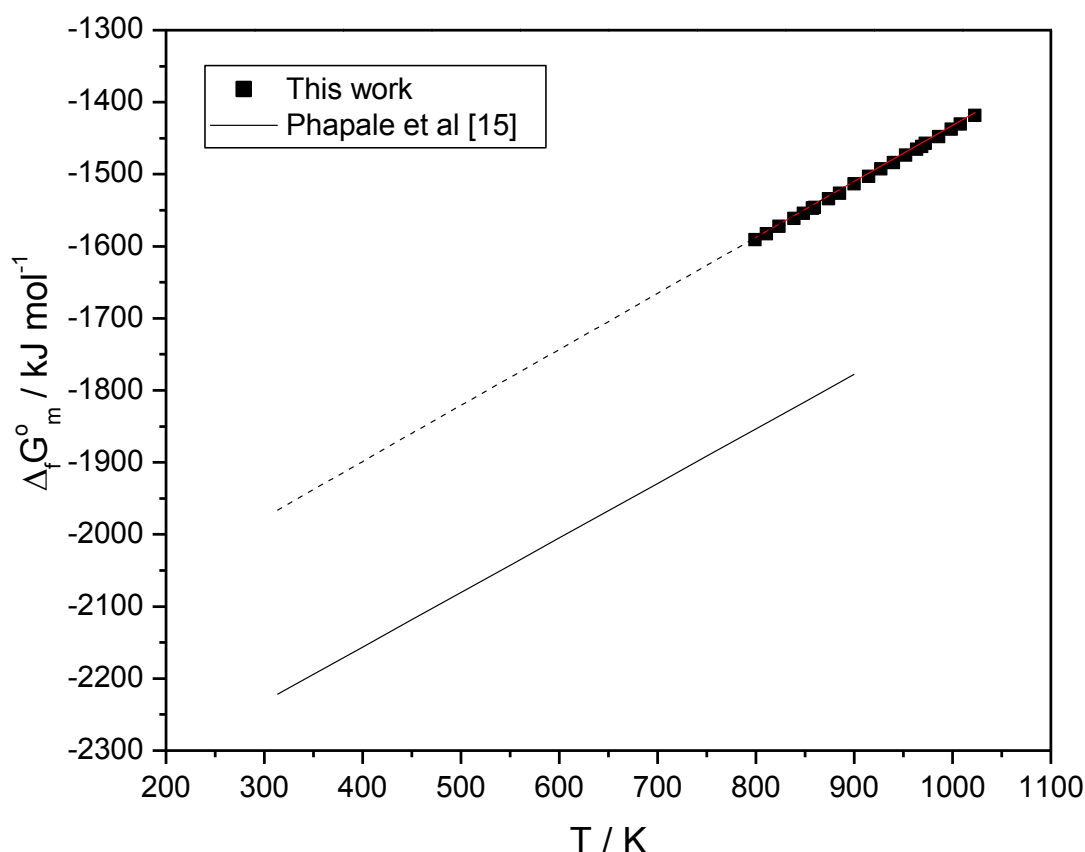


Fig. 3.14 Comparison of the measured $\Delta_f G_m^o$ $\text{Bi}_2\text{Fe}_4\text{O}_9$ in this work with that of the data derived by Phapale et al. [15]

3.4.3.3. Standard enthalpy of formation of $\text{Bi}_2\text{Fe}_4\text{O}_9$ from acid solution calorimetry experiments

The results of the measurements of the molar enthalpy of dissolution of KCl are given in Table 3.12 and a typical plot of dissolution of KCl in double distilled water is shown in Fig.3.15. The molar enthalpy of dissolution of KCl at infinite dilution derived in this study was found to be $17.30 \pm 0.43 \text{ kJ mol}^{-1}$. This value is in good agreement with the value of $17.21 \pm 0.01 \text{ kJ mol}^{-1}$ reported by Venugopal et al. [30] and the certified value quoted by NIST, $17.241 \pm 0.018 \text{ kJ mol}^{-1}$ [31]. The results of the measurements of the molar enthalpy of dissolution of TRIS are given in Table 3.13 and a typical plot of dissolution of TRIS in 0.1 mol kg^{-1} HCl is shown in Fig. 3.16. The value of the molar enthalpy of solution of TRIS measured in the present study was $-29.94 \pm 0.37 \text{ kJ mol}^{-1}$ which is in agreement with the value of $-29.770 \pm 0.032 \text{ kJ mol}^{-1}$ cited in [32]. The results obtained for KCl and TRIS dissolution are endothermic and exothermic, respectively. These results validated the experimental setup and procedure used in this study for calorimetric measurements.

Table 3.12 Experimentally determined values of enthalpies of dissolution (ΔH) and molar enthalpies of dissolution ($\Delta_{\text{sol}}H_{\text{m}}$) of KCl in double distilled water (mass of solvent = 300 ± 0.01 g) at 298.15 K* and 0.1 M Pa pressure.^a

Sample	Weight (w) / g	ΔH / J	$\Delta_{\text{sol}}H_{\text{m}}$ / kJ
KCl	0.2297	54.2833	17.6202
(Molecular mass:	0.3573	82.2140	17.1561
74.56 g mol ⁻¹)	0.2860	65.2583	17.0128
	0.2188	49.2092	16.7689
	0.1003	24.1407	17.9455
			$\bar{X} = 17.30 \pm 0.43^{\text{@}}$

* Temperature stability inside the calorimeter prior to start of experiment was ± 0.001 K.

\bar{X} : Mean value of the measurements.

^aThe standard uncertainties, $u(w) = 0.0001$ g and $u(p) = 0.3$ k Pa.

[@] Uncertainty given is the expanded uncertainty with level of confidence 0.95.

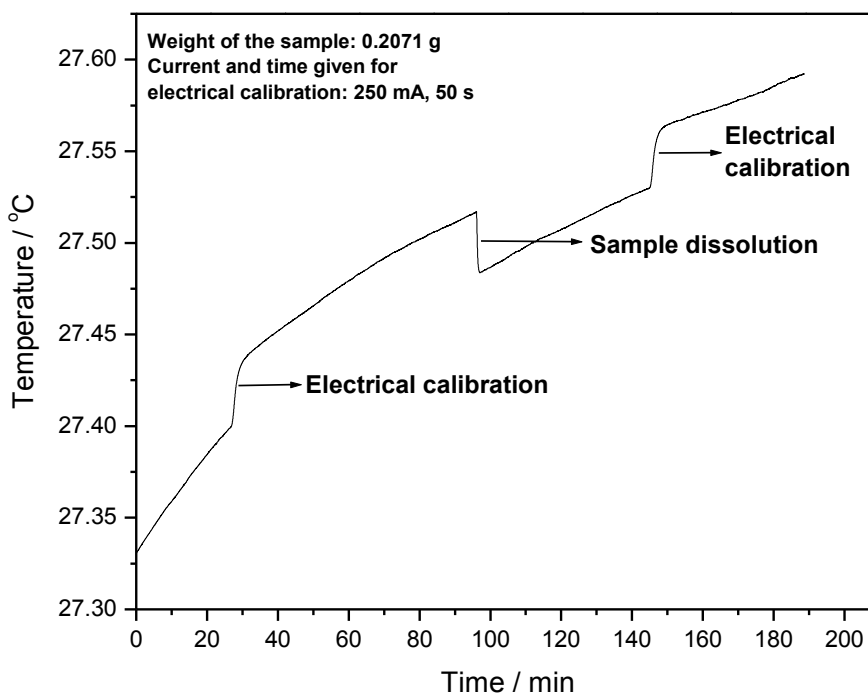


Fig. 3.15 A typical plot of dissolution of KCl in double distilled water

Table 3.13 Experimentally determined values of enthalpies of dissolution (ΔH) and molar enthalpies of dissolution ($\Delta_{\text{sol}}H_{\text{m}}$) of TRIS in 0.1 mol kg⁻¹ HCl (mass of solvent = 298.53 ± 0.01 g) at 298.15 K* and 0.1 M Pa pressure.^a

Sample	Weight (w) / g	ΔH / J	$\Delta_{\text{sol}}H_{\text{m}}$ / kJ
TRIS	0.0728	-17.9644	-29.8930
(Molecular mass:	0.0803	-20.0989	-30.3211
121.14 g mol ⁻¹)	0.0912	-22.7999	-29.5942
	0.1079	-27.0772	-30.3998
	0.1013	-24.6569	-29.4861
			$\bar{X} = -29.94 \pm 0.37^{\text{@}}$

* Temperature stability inside the calorimeter prior to start of experiment was ± 0.001 K.

\bar{X} : Mean value of the measurements.

^aThe standard uncertainties, $u(w) = 0.0001$ g and $u(p) = 0.3$ k Pa.

[@]Uncertainty given is the expanded uncertainty with level of confidence 0.95.

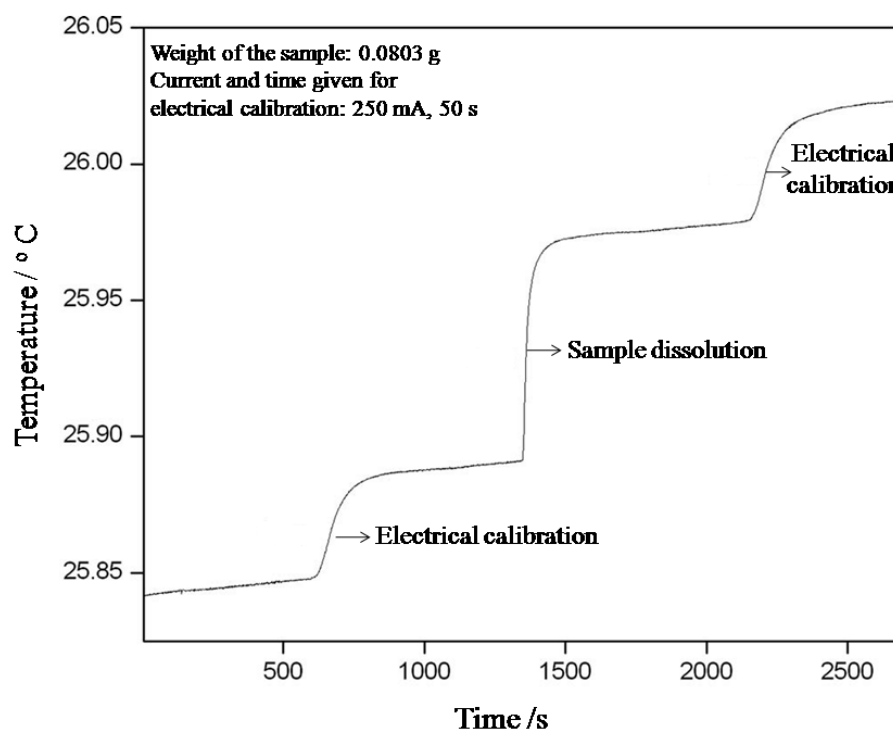


Fig. 3.16 A typical plot of dissolution of TRIS in 0.1 mol kg⁻¹ HCl

The results of the measurements of enthalpy of dissolution for $\text{Bi}_2\text{Fe}_4\text{O}_9$ and for the starting materials Bi_2O_3 and Fe_2O_3 are given in Table 3.14. Typical plots of dissolution of Bi_2O_3 , Fe_2O_3 and $\text{Bi}_2\text{Fe}_4\text{O}_9$ in $8.38 \text{ mol kg}^{-1} \text{ HCl}$ are shown in Fig. 3.17 to 3.19. The molar enthalpies of solution of $\text{Bi}_2\text{Fe}_4\text{O}_9$ and the starting materials Bi_2O_3 and Fe_2O_3 , deduced from the experiments are $-623.3 \pm 14.5 \text{ kJ}$, $-381.6 \pm 14.2 \text{ kJ}$ and $-99.6 \pm 9.4 \text{ kJ}$, respectively. The thermochemical reaction scheme used to derive the standard molar enthalpy of formation of $\text{Bi}_2\text{Fe}_4\text{O}_9$ is given in Table 3.15. By using the values of the standard molar enthalpies of formation of Bi_2O_3 and Fe_2O_3 namely ΔH_4 and ΔH_5 from ref. [33], the standard molar enthalpy of formation of $\text{Bi}_2\text{Fe}_4\text{O}_9$ was determined as $-2170.8 \pm 28.6 \text{ kJ}$.

Table 3.14 Experimentally determined values of enthalpies of dissolution (ΔH) and molar enthalpies of dissolution ($\Delta_{\text{sol}}H_{\text{m}}$) of $\text{Bi}_2\text{Fe}_4\text{O}_9$, Bi_2O_3 and Fe_2O_3 in $8.38 \pm 0.01 \text{ mol kg}^{-1}$ HCl (mass of solvent = $327.15 \pm 0.01 \text{ g}$) at 298.15 K^* and 0.1 M Pa pressure.^a

Sample	Weight (w) / g	ΔH / J	$\Delta_{\text{sol}}H_{\text{m}}$ / kJ mol^{-1}
$\text{Bi}_2\text{Fe}_4\text{O}_9$	0.0677	-52.28	-606.5
	0.0408	-32.71	-629.6
	0.0505	-41.49	-645.2
	0.0304	-24.32	-628.3
	0.0549	-41.77	-597.5
	0.0545	-43.91	-632.7
			$\overline{X} = -623.3 \pm 14.5^{\text{@}}$
Bi_2O_3	0.0573	-46.97	-382.0
	0.0534	-40.65	-354.7
	0.0490	-42.88	-407.8
	0.0487	-38.57	-369.0
	0.0530	-40.64	-357.3
	0.0838	-71.10	-395.3
	0.0722	-59.45	-383.7
	0.1029	-89.02	-403.1
			$\overline{X} = -381.6 \pm 14.2^{\text{@}}$
Fe_2O_3	0.0846	-58.72	-110.8
	0.0536	-33.84	-100.8
	0.0550	-38.91	-113.0
	0.0427	-26.76	-100.1
	0.0483	-25.61	-84.7
	0.0405	-22.31	-88.0
			$\overline{X} = -99.6 \pm 9.4^{\text{@}}$

* Temperature stability inside the calorimeter prior to start of experiment was $\pm 0.001 \text{ K}$.

\overline{X} : Mean value of the measurements.

^aThe standard uncertainties, $u(w) = 0.0001 \text{ g}$ and $u(p) = 0.3 \text{ k Pa}$.

[@]Uncertainty given is the expanded uncertainty with level of confidence 0.95.

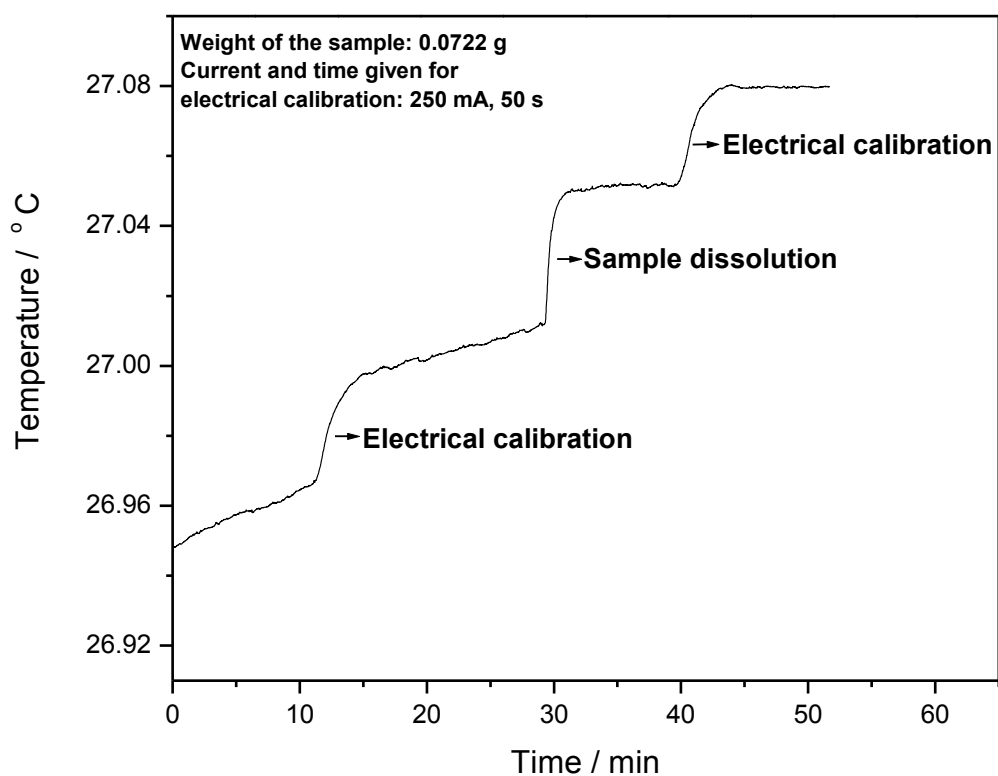


Fig. 3.17 A typical plot of dissolution of Bi_2O_3 in $8.38 \text{ mol kg}^{-1} \text{ HCl}$

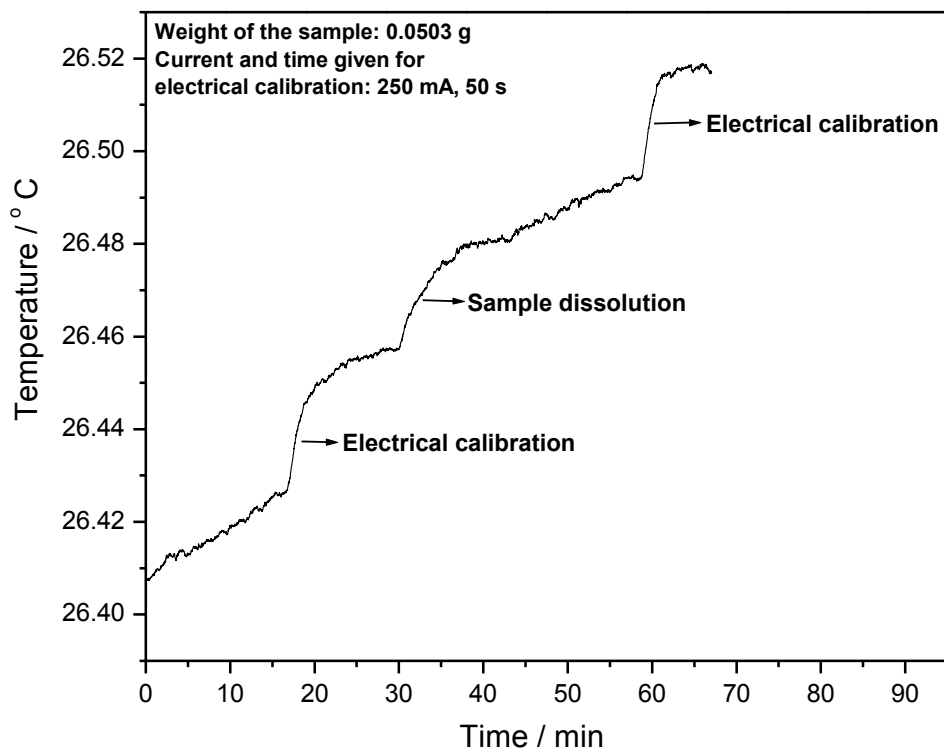


Fig. 3.18 A typical plot of dissolution of Fe_2O_3 in $8.38 \text{ mol kg}^{-1} \text{ HCl}$

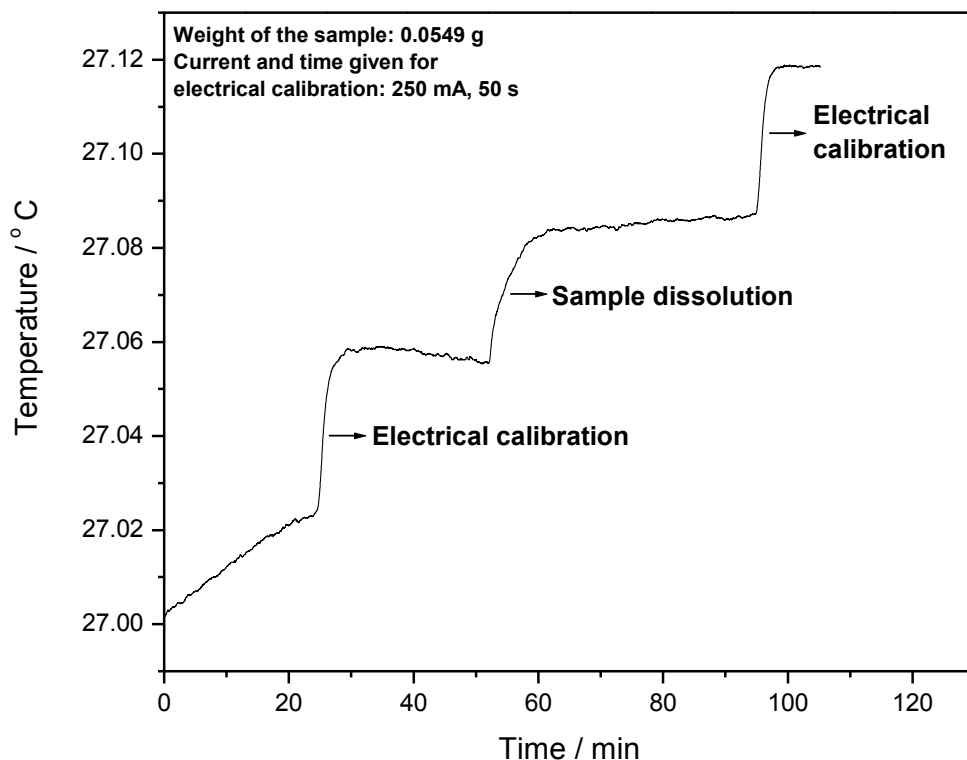


Fig. 3.19. A typical plot of dissolution of $\text{Bi}_2\text{Fe}_4\text{O}_9$ in $8.38 \text{ mol kg}^{-1} \text{ HCl}$

Table. 3.15 Reaction scheme for calculating the standard molar enthalpy of formation of $\text{Bi}_2\text{Fe}_4\text{O}_9$

Reaction	Enthalpy change
$\text{Bi}_2\text{Fe}_4\text{O}_9(\text{s}) + 18 \text{ HCl}(\text{sln})$ $= (2 \text{ BiCl}_3 + 4 \text{ FeCl}_3 + 9 \text{ H}_2\text{O})(\text{sln})$	$\Delta H_1 = -623.3 \pm 14.5 \text{ kJ mol}^{-1} @$
$\text{Bi}_2\text{O}_3(\text{s}) + 6 \text{ HCl}(\text{sln})$ $= (2 \text{ BiCl}_3 + 3 \text{ H}_2\text{O})(\text{sln})$	$\Delta H_2 = -381.6 \pm 14.2 \text{ kJ mol}^{-1} @$
$\text{Fe}_2\text{O}_3(\text{s}) + 6 \text{ HCl}(\text{sln}) = (2 \text{ FeCl}_3 + 3 \text{ H}_2\text{O})(\text{sln})$	$\Delta H_3 = -99.6 \pm 9.4 \text{ kJ mol}^{-1} @$
$2 \text{ Bi}(\text{s}) + 3/2 \text{ O}_2(\text{g}) = \text{Bi}_2\text{O}_3(\text{s})$	$\Delta H_4 = -570.7 \pm 3.3 \text{ kJ mol}^{-1}$ from [33]
$2 \text{ Fe}(\text{s}) + 3/2 \text{ O}_2(\text{g}) = \text{Fe}_2\text{O}_3(\text{s})$	$\Delta H_5 = -821.3 \pm 3.3 \text{ kJ mol}^{-1}$ from [33]
$2 \text{ Bi}(\text{s}) + 4 \text{ Fe}(\text{s}) + 9/2 \text{ O}_2(\text{g}) = \text{Bi}_2\text{Fe}_4\text{O}_9(\text{s})$	$\Delta H_6 = \Delta H_2 + 2 \Delta H_3 + \Delta H_4 + 2 \Delta H_5 - \Delta H_1$ $= -2170.8 \pm 28.6 \text{ kJ mol}^{-1} @$

@ Uncertainty given is the combined expanded uncertainty with level of confidence 0.95.

3.4.3.4 Measurement of heat capacity of Bi₂Fe₄O₉ using differential scanning calorimetry

The performance of the differential scanning calorimeter was verified by measuring the heat capacity of Bi₂O₃ in the temperature range of 333 to 813 K and shown in Fig. 3.20 and the C_p data at selected temperatures are given in Table 3.16. The experimental heat capacity values are compared with the literature data [34] which is also shown in Fig. 3.20 and given in Table 3.16. It is seen that the measured C_p values are in good agreement with the reported C_p values at temperatures between 348 and 443 K. Deviations from the literature data are observed at temperatures below and above this range. The maximum deviation is found to be 2.5 % at 778 K.

The XRD patterns of Bi₂Fe₄O₉ before and after the DSC measurements remained the same indicating that it did not undergo any change during heat capacity measurements. The experimental values of the molar heat capacity of Bi₂Fe₄O₉ are given in Table 3.17 for selected temperatures and are plotted in Fig. 3.21. Three pellets of Bi₂Fe₄O₉ were used for heat capacity measurements and for each pellet seven measurements were carried out. Hence, each measured data is the mean of twenty one measurements and the uncertainty expressed for each value (in Table 3.17) is the expanded uncertainty obtained from these measurements. These data were fitted into the following eq. (3.13) using the least squares regression analysis as,

$$C_p <\text{Bi}_2\text{Fe}_4\text{O}_9> (\text{J K}^{-1} \text{mol}^{-1}) \pm 11.0 = 395.5 - 23.0 \times 10^{-3} T - 7.6 \times 10^{-6} T^2$$

(T / K: 313-773) (3.13)

The error given is the combined expanded uncertainty with a confidence level of 0.95 (see Table 3.17). These fitted values are also shown in the table along with those measured. Molar heat capacity of Bi₂Fe₄O₉ reported by Phapale et al. [15] deduced from the enthalpy increment values measured in the temperature range of

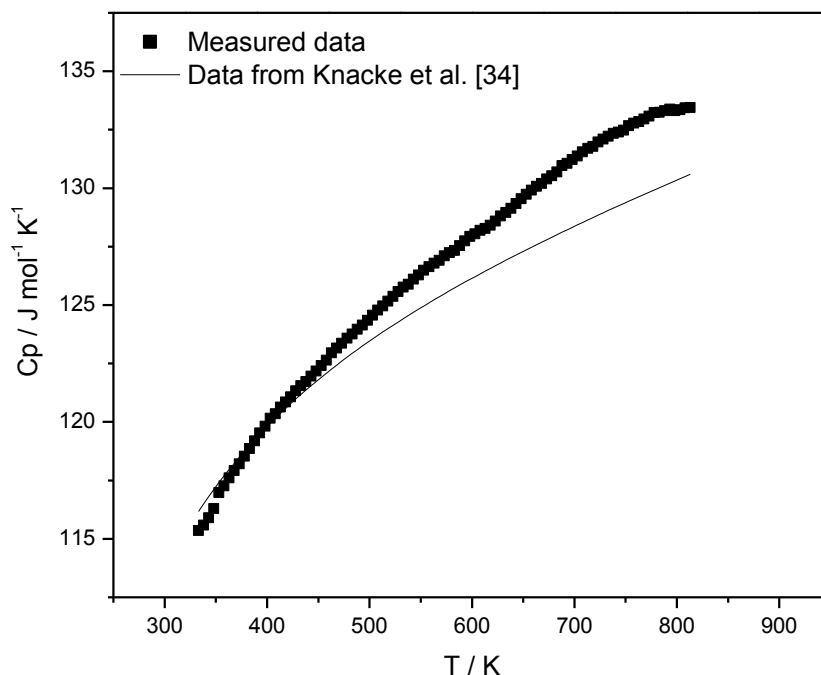


Fig. 3.20 Comparison of molar heat capacity of Bi_2O_3 measured in this work with the data reported by Knacke et al. [34]

Table 3.16 Measured heat capacity (C_p) values of Bi_2O_3 are compared with heat capacity values reported by Knacke et al. [34] at 0.1 M Pa pressure.^a

T / K	C_p / J K ⁻¹ mol ⁻¹		
	Measured data	Data from Knacke et al. [34]*	Deviation of measured data from the data reported by Knacke et al.
333	115.4 ± 0.3	116.2	-0.8
353	117.0 ± 0.2	117.4	-0.4
403	120.1 ± 0.2	119.9	0.2
453	122.4 ± 0.2	121.9	0.5
503	124.6 ± 0.3	123.6	1.0
553	126.5 ± 0.2	125.0	1.5
603	128.0 ± 0.2	126.2	1.8
653	129.7 ± 0.1	127.4	2.4
703	131.4 ± 0.2	128.4	2.9
753	132.7 ± 0.2	129.4	3.2
778	133.2 ± 0.3	129.9	3.3
813	133.5 ± 0.1	130.6	2.9

^aStandard uncertainties, $u(T) = 0.4$ K and $u(p) = 0.3$ k Pa. Measured data is the mean of ten measurements and the uncertainty given for each measured value is the expanded uncertainty with level of confidence 0.95. The relative expanded uncertainty, $U_r(C_p) = 0.03$ with level of confidence 0.95.

*Uncertainty not reported in ref. [34].

Table 3.17 Measured and fitted heat capacity (C_p) values of $\text{Bi}_2\text{Fe}_4\text{O}_9$ are compared with heat capacity values computed through Neumann-Kopp rule using C_p of Fe_2O_3 and Bi_2O_3 from [34] (C_p^{NKR}) and using C_p of Fe_2O_3 from [37] incorporating correction for magnetic contribution and C_p of Bi_2O_3 from [34] ($C_p^{\text{NKR,corr}}$) at 0.1 M Pa pressure.^a

T / K	C_p / J K ⁻¹ mol ⁻¹			
	Measured data	Fitted values	Estimated using Neumann Kopp rule	
			$C_p^{\text{NKR}*}$	$C_p^{\text{NKR,corr}*}$
313	308.3 ± 1.2	310.8	329.7	317.6
353	327.5 ± 1.0	326.4	345.1	329.5
403	340.5 ± 0.8	339.5	361.0	340.5
453	348.8 ± 0.8	348.1	374.5	349.0
503	354.1 ± 1.0	353.9	386.7	355.9
553	356.8 ± 0.6	357.9	397.9	361.7
603	360.3 ± 1.0	360.7	408.5	366.9
653	363.6 ± 1.0	362.7	418.6	371.5
703	363.9 ± 1.2	364.0	428.4	375.8
753	364.7 ± 1.4	364.8	438.0	379.7
773	366.3 ± 1.2	365.0	441.8	381.3

^aStandard uncertainties, $u(T) = 0.4$ K and $u(p) = 0.3$ k Pa. Measured data is the mean of twenty one measurements and the uncertainty given for each measured value is the expanded uncertainty with level of confidence 0.95. The combined expanded uncertainty, $U_c(C_p) = 11.0$ J K⁻¹ mol⁻¹ with level of confidence 0.95[@].

*Uncertainty not reported in references [34] and [37].

[@]The combined expanded uncertainty was calculated by incorporating the relative uncertainties of experimental data and the relative uncertainty attributed to the instrument. The relative uncertainty of the instrument was determined from the measured C_p values of Bi_2O_3 (Table 3.16). The relative uncertainty in the measured heat capacity of $\text{Bi}_2\text{Fe}_4\text{O}_9$ was also calculated as $\Delta x/x$ where Δx is the maximum expanded uncertainty and x is the smallest measured C_p value.

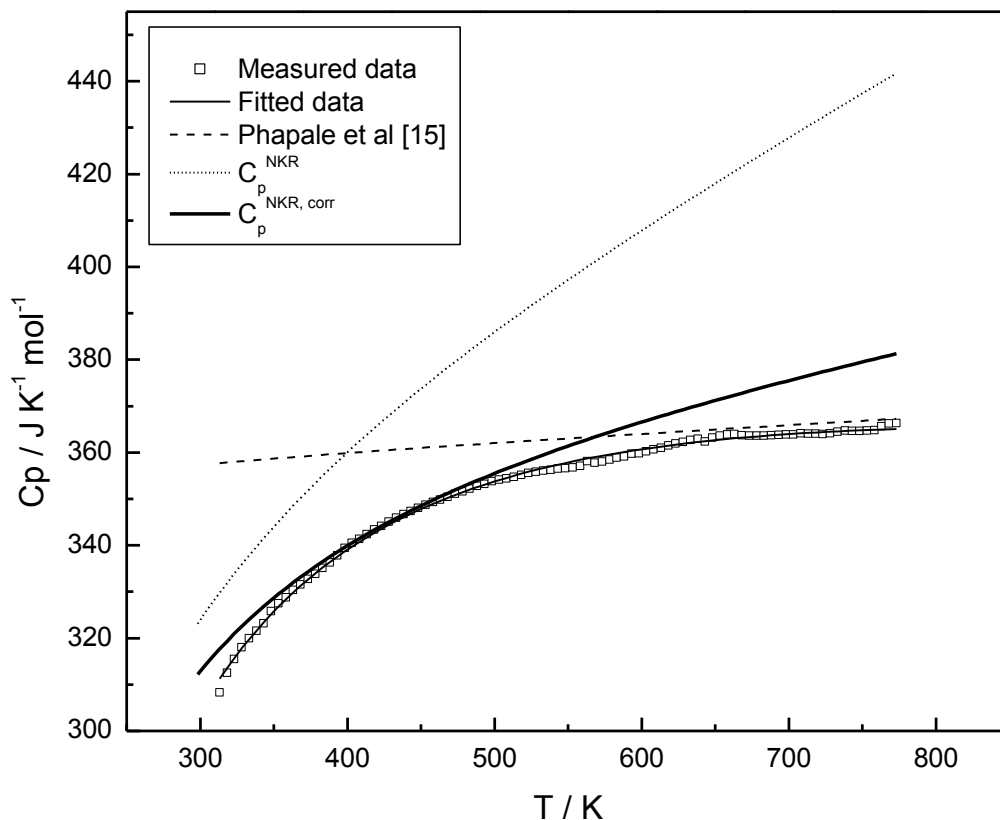


Fig. 3.21 Molar heat capacity of $\text{Bi}_2\text{Fe}_4\text{O}_9$. C_p^{NKR} is the molar heat capacity calculated using Neumann-Kopp rule and $C_p^{\text{NKR,corr}}$ is after correcting for magnetic contribution.

313 to 911 K is also shown in Fig. 3.21. As seen from Fig. 3.21, the data reported by Phapale et al. [15] are significantly higher than the present data at lower temperatures while it is comparable at higher temperatures. It is also to be pointed out that the temperature dependence of the molar heat capacity data reported by Phapale et al. [15] is lower than that of the present data.

The values of the molar heat capacity of $\text{Bi}_2\text{Fe}_4\text{O}_9$ were also computed by Neumann-Kopp rule (NKR) using molar heat capacities of Bi_2O_3 and Fe_2O_3 [34] and are presented in Fig. 3.21.

3.4.3.5. Deviation of measured C_p values from the estimates by the Neumann-Kopp rule (NKR)

Comparison of the experimentally determined heat capacity of $\text{Bi}_2\text{Fe}_4\text{O}_9$ with those estimated by the Neumann-Kopp rule indicates a large deviation. At the mean temperature of the present measurement (543 K), the deviation is -10 %.

The molar heat capacity of a solid at constant pressure, $C_{p,m}$ can be expressed as the sum of several contributions [35, 36]:

$$C_{p,m} = C_{ph} + C_d + C_{others} \quad (3.14)$$

where C_{ph} represents the contribution of lattice vibrations (phonons), C_d stands for lattice dilatation and C_{others} represents other contributions which include those of conduction electrons, excitations of localized electrons, ordering changes upon second order phase transitions, formation of vacancies, magnetic contribution etc. The contribution due to lattice vibrations, C_{ph} can be expressed as $C_{ph} = C_h + C_{anh}$, where C_h corresponds to heat capacity with harmonic crystal approximation and C_{anh} represents the contribution due to anharmonicity of vibrations. When ternary oxides are formed from the constituent binary oxides, modification in both C_{anh} and C_d could occur because of the differences in lattice dynamics between the ternary and the limiting binary oxides. Deviation of the NKR estimated values from the experimental values owing to an-harmonicity term ΔC_{anh} , would depend on the structure and the nature of these oxides.

$\alpha\text{-Fe}_2\text{O}_3$ is antiferromagnetic with Neel's temperature of about 950 K. Gronvold et al. [37] had measured the molar heat capacity of $\alpha\text{-Fe}_2\text{O}_3$ and

theoretically delineated the lattice, dilatational and magnetic contribution to the molar heat capacity of $\alpha\text{-Fe}_2\text{O}_3$. Their work showed the magnetic contribution to the heat capacity of $\alpha\text{-Fe}_2\text{O}_3$ is around 6 to 16 % in the temperature range of 300 to 800 K and shows an increasing trend with increase in temperature. $\text{Bi}_2\text{Fe}_4\text{O}_9$ is reported to be paramagnetic at room temperature and on cooling, it undergoes a transition to an antiferromagnetic state at about 264 K [38]. So the large deviation of the measured heat capacity values of $\text{Bi}_2\text{Fe}_4\text{O}_9$ from NKR estimated values could be due to the contribution of magnetic properties of $\alpha\text{-Fe}_2\text{O}_3$. Therefore, the C_p of $\text{Bi}_2\text{Fe}_4\text{O}_9$ was recalculated by NKR by subtracting the magnetic contribution and considering only the estimated lattice and dilatational contributions of $\alpha\text{-Fe}_2\text{O}_3$ which is also shown in Fig. 3.21. These values are referred to as $C_p^{NKR,corr}$. Fig. 3.21 shows that the deviation of the measured data for $\text{Bi}_2\text{Fe}_4\text{O}_9$ from the $C_p^{NKR,corr}$ is only 0.9 % at the mean temperature, namely 543 K.

Although, the probable main factor for the deviation of measured data from C_p^{NKR} values is the magnetic contribution from Fe_2O_3 , other factors like lattice vibrations, C_{ph} and lattice dilatations, C_d would also have their own contributions. The dilatational term, C_d constitutes the change in $C_p - C_v$ with temperature and is given by,

$$C_p - C_v = T V_m \alpha^2 / \beta \quad (3.15)$$

where V_m is the molar volume of the solid, α is its isobaric volume expansion, and β is the isothermal compressibility. The temperature dependence of the deviation of the measured heat capacity from the NKR predicted values could be due to change in difference in the dilatational properties, ΔC_d with temperature. This would depend

upon the difference in molar volumes of the constituent oxides, their isobaric volume expansions, and isothermal compressibilities.

$$\Delta C_{dil} / T = V_{m, AB} \left(\frac{\alpha_{AB}^2}{\beta_{AB}} \right) - X_A V_{m, A} \left(\frac{\alpha_A^2}{\beta_A} \right) - X_B V_{m, B} \left(\frac{\alpha_B^2}{\beta_B} \right) \quad (3.16)$$

where A and B represent the constituent oxides and AB represents the ternary mixed oxide. Table 3.18 shows the unit cell volumes of Bi₂O₃ and Fe₂O₃ and those of Bi₂Fe₄O₉ [27]. As seen from the Table, the unit cell volume of Bi₂Fe₄O₉ is 8 % higher than the sum of the unit cell volumes of stoichiometric quantities of constituent oxides. If the difference in the molar volume ΔV_m would have contributed to the difference in the C_p values between the measured and that computed, the measured C_p values of Bi₂Fe₄O₉ should have been more than that estimated by using NKR approximation. However, the deviation observed (Fig. 3.21) is much different from what is expected based on the ΔV_m . It is presumed that the α^2/β terms and their temperature dependence for the binary and ternary oxides significantly contribute to this observed difference. However, these values are not available in the open literature.

Table 3.18 Unit cell volumes of Bi₂Fe₄O₉

Unit cell volume/formula unit (Å ³)		$\left(\frac{V_c - V_o}{V_o} \right) \times 100$
Compound, V _c	Constituent oxides, V _o	
201.18	(Bi ₂ O ₃ +2Fe ₂ O ₃), 185.94	8

3.4.3.6 Internal consistency of the measured thermodynamic data

The agreement of the standard enthalpy of formation of $\text{Bi}_2\text{Fe}_4\text{O}_9$ at 298 K obtained from the acid solution calorimetry measurements with the standard enthalpy of its formation at the mid temperature of emf measurements was checked as given below:

Gibbs energy of formation of $\text{Bi}_2\text{Fe}_4\text{O}_9$ is given by eq. (3.12). From eq. (3.12), the enthalpy of formation of $\text{Bi}_2\text{Fe}_4\text{O}_9$ at the mid temperature of emf measurements (911 K), $\Delta_f H_{911\text{K}}^\circ < \text{Bi}_2\text{Fe}_4\text{O}_9 > = -2196.2 \pm 0.6 \text{ kJ mol}^{-1}$ and this can be related to $\Delta_f H_{298\text{K}}^\circ < \text{Bi}_2\text{Fe}_4\text{O}_9 >$ by the following expression:

$$\Delta_f H_{298\text{K}}^\circ < \text{Bi}_2\text{Fe}_4\text{O}_9 > = \Delta_f H_{911\text{K}}^\circ < \text{Bi}_2\text{Fe}_4\text{O}_9 > - \left[\int_{298}^{545} \Delta C_p dT - 2\Delta H_{\text{fus}} \text{Bi} + \int_{545}^{911} \Delta C_p dT \right] \quad (3.17)$$

where, ΔC_p is the difference in the molar heat capacities of $\text{Bi}_2\text{Fe}_4\text{O}_9$ and the constituent elements in their standard states and in the required stoichiometric quantities.

The heat capacity of $\text{Bi}_2\text{Fe}_4\text{O}_9$ was taken from eq. (3.13) and those of Bi (s / l), Fe (s) and O_2 (g) were taken from ref. [34] and are given below:

$$C_p < \text{Bi} > (\text{J K}^{-1} \text{ mol}^{-1}) = 28.033 - 24.267 \times 10^{-3} T + 50.208 \times 10^{-6} T^2 \quad (\text{T / K: 298-545}) \quad (3.18)$$

$$C_p \{ \text{Bi} \} (\text{J K}^{-1} \text{ mol}^{-1}) = 23.359 + 3.138 \times 10^{-3} T + 1.661 \times 10^{-6} T^2 - 0.720 \times 10^{-6} T^3 \quad (\text{T / K: 545-1835}) \quad (3.19)$$

$$C_p <Fe> (J K^{-1} mol^{-1}) = 14.954 + 28.079 \times 10^{-3} T + 0.155 \times 10^{-6} T^2$$

(T / K: 298-800) (3.20)

$$C_p <Fe> (J K^{-1} mol^{-1}) = 26.439 + 20.677 \times 10^{-3} T \quad (T / K: 800-1184) \quad (3.21)$$

$$C_p (O_2) (J K^{-1} mol^{-1}) = 29.154 + 6.477 \times 10^{-3} T - 0.184 \times 10^{-6} T^2 - 1.017 \times 10^{-6} T^2$$

(T / K: 298-3200) (3.22)

Hence,

$$\left[\int_{298}^{545} \Delta C_p dT - 2 \Delta H_{fus} Bi + \int_{545}^{911} \Delta C_p dT \right] = \int_{298}^{545} \left[C_p^{Bi_2Fe_4O_9} - (2C_p^{Bi} + 4C_p^{Fe} + \frac{9}{2} C_p^{O_2}) \right] dT$$

$$- 2 \Delta H_{fus} Bi + \int_{545}^{800} \left[C_p^{Bi_2Fe_4O_9} - (2C_p^{Bi} + 4C_p^{Fe} + \frac{9}{2} C_p^{O_2}) \right] dT$$

$$+ \int_{800}^{911} \left[C_p^{Bi_2Fe_4O_9} - (2C_p^{Bi} + 4C_p^{Fe} + \frac{9}{2} C_p^{O_2}) \right] dT \quad (3.23)$$

$$= -10.1 \text{ kJ mol}^{-1} \quad (3.24)$$

By substituting the values of $\Delta_f H_{911K}^o < Bi_2Fe_4O_9 >$ and

$$\left[\int_{298}^{545} \Delta C_p dT - 2 \Delta H_{fus} Bi + \int_{545}^{911} \Delta C_p dT \right] \text{ in eq. (3.17), we get}$$

$$\Delta_f H_{298K}^o < Bi_2Fe_4O_9 > = -2186.1 \pm 2.8 \text{ kJ mol}^{-1} \quad (3.25)$$

The difference between the values of $\Delta_f H_{298K}^o < Bi_2Fe_4O_9 >$ obtained from acid solution calorimetry ($-2170.8 \pm 28.6 \text{ kJ mol}^{-1}$) and deduced from emf measurements is less than 1%. The agreement between enthalpy data deduced from high temperature Gibbs energy data and the enthalpy data measured at 298 K confirms internal consistency of the measured thermochemical data on $Bi_2Fe_4O_9$.

3.4.4 Studies with samples of composition within the section bound by Bi, Bi₂Fe₄O₉ and Bi₂O₃

3.4.4.1 Long term equilibration of samples in the temperature range of 773 to 1023 K

Results of long term equilibrations of samples with composition falling in this section at 1023 K are given in Table 3.5. Compositions of samples 17 and 18 are in the region bound by Bi, Bi₂Fe₄O₉ and BiFeO₃. Hence, it was expected to obtain Bi, Bi₂Fe₄O₉ and BiFeO₃ as coexisting phases after equilibration of these samples. As expected, a mixture of Bi, Bi₂Fe₄O₉ and BiFeO₃ was obtained after equilibration, but a small amount of Bi₂₅FeO₃₉ also formed along with these three phases. It is to be pointed out that during the preparation of BiFeO₃ (described in section 3.4.1) also, a small amount of Bi₂₅FeO₃₉ was formed along with BiFeO₃. Samples, 19 and 20, whose compositions were in the region bound by Bi, BiFeO₃ and Bi₂₅FeO₃₉, after equilibration gave a mixture of Bi, BiFeO₃ and Bi₂₅FeO₃₉, indicating the coexistence of these phases at 1023 K. Samples 21 to 23, after equilibration, confirmed the presence of the phase field, Bi-Bi₂₅FeO₃₉-Bi₂O₃. Equilibrations at 773 K also showed the same results as in the case of equilibrations at 1023 K. Samples, 24 and 25 (in Table 3.6) whose compositions were in the region bound by Bi, Bi₂Fe₄O₉ and BiFeO₃, gave a mixture of Bi, Bi₂Fe₄O₉, BiFeO₃ and a small amount of Bi₂₅FeO₃₉. Sample 26, whose composition was in the region bound by Bi, BiFeO₃ and Bi₂₅FeO₃₉, after equilibration, gave a mixture of Bi, BiFeO₃ and Bi₂₅FeO₃₉, indicating the coexistence of these phases at 773 K. Samples 27 and 28, confirmed the presence of the phase field: Bi-Bi₂₅FeO₃₉-Bi₂O₃ at 773 K. To summarize, the phase fields identified by the above experiments at 1023 and 773 K are: (a) Bi-BiFeO₃-Bi₂₅FeO₃₉ and (b) Bi-Bi₂₅FeO₃₉-Bi₂O₃. In view of the literature data on the stability of BiFeO₃,

additional experiments were carried out to confirm these results which are described in the following sections.

3.4.4.2 Experiments to determine the temperature range of stability of BiFeO₃

3.4.4.2.1 DTA and DSC experiments with BiFeO₃

The thermogram obtained by differential thermal analysis of BiFeO₃ from 298 to 973 K did not show any thermal event both during heating and cooling. XRD pattern of BiFeO₃ after the DTA experiment also did not show any change from its XRD pattern prior the experiment. The thermogram from DSC experiment in the temperature range of 298 to 823 K also gave the same results. This could mean either BiFeO₃ is thermodynamically stable in the temperature range of study or the kinetics of its decomposition is too slow that it did not decompose within the short dwell time of the sample during DTA and DSC experiments at high temperatures.

3.4.4.2.2 Equilibration of BiFeO₃ in vacuum and air at different temperatures

As described in section 3.3.5.2, nine samples of BiFeO₃ were simultaneously equilibrated for prolonged periods in a temperature gradient furnace in vacuum to determine its temperature range of stability. Similar equilibrations were carried out in air also. The results obtained are given in Tables 3.7 and 3.8. As mentioned in section 3.4.1, phase pure BiFeO₃ could not be prepared and it always contained a small amount of Bi₁₂FeO₃₉. XRD patterns obtained after equilibrating the samples in vacuum and air are shown in Figs. 3.22 and 3.23, respectively. The pattern of the samples equilibrated at temperatures below 763 K in vacuum (samples 1 to 3 in Table 3.7) were identical to that of the starting material i.e., a mixture of BiFeO₃ (major

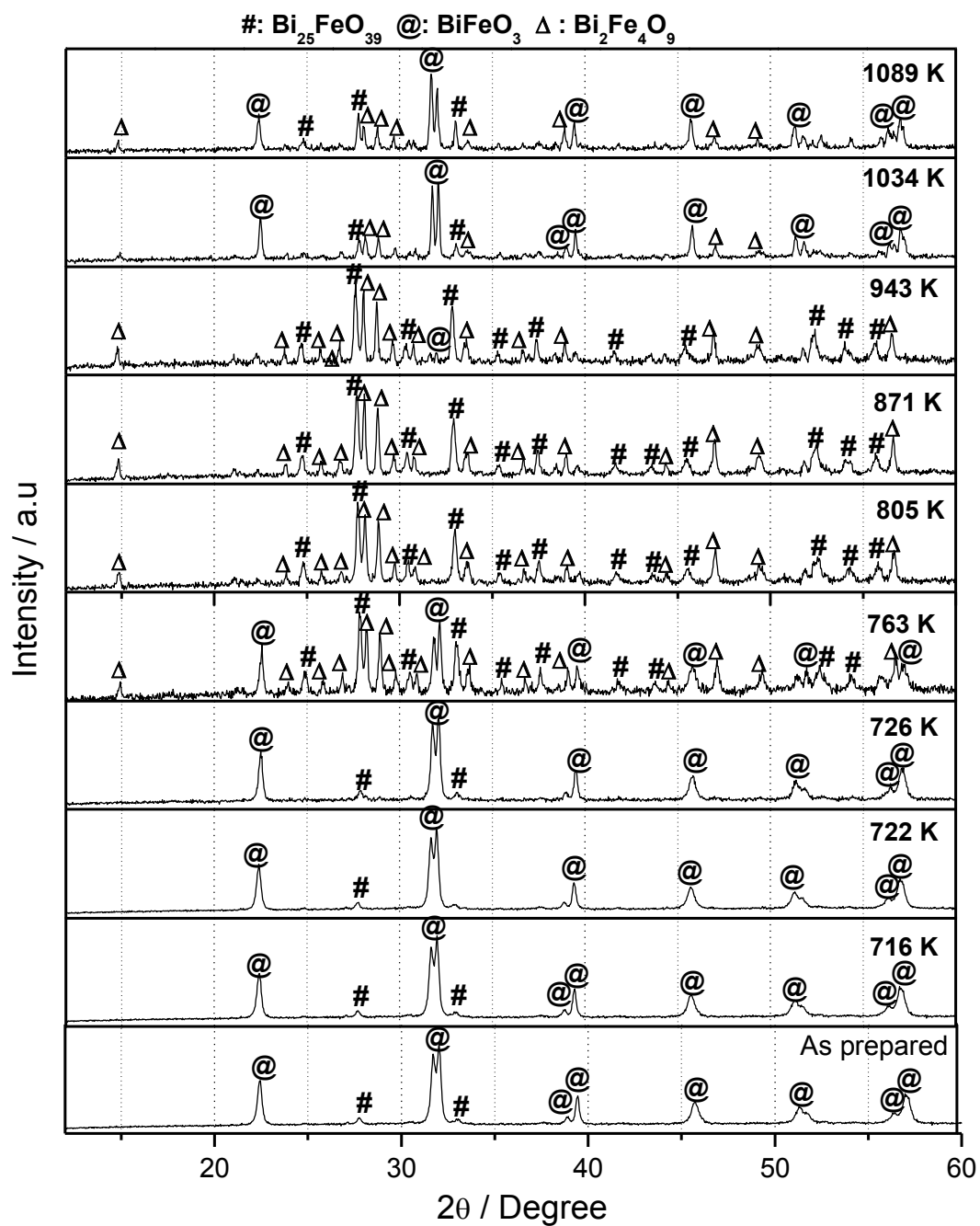


Fig. 3.22 XRD patterns obtained after equilibrating BiFeO_3 at different temperatures in vacuum for 480 h

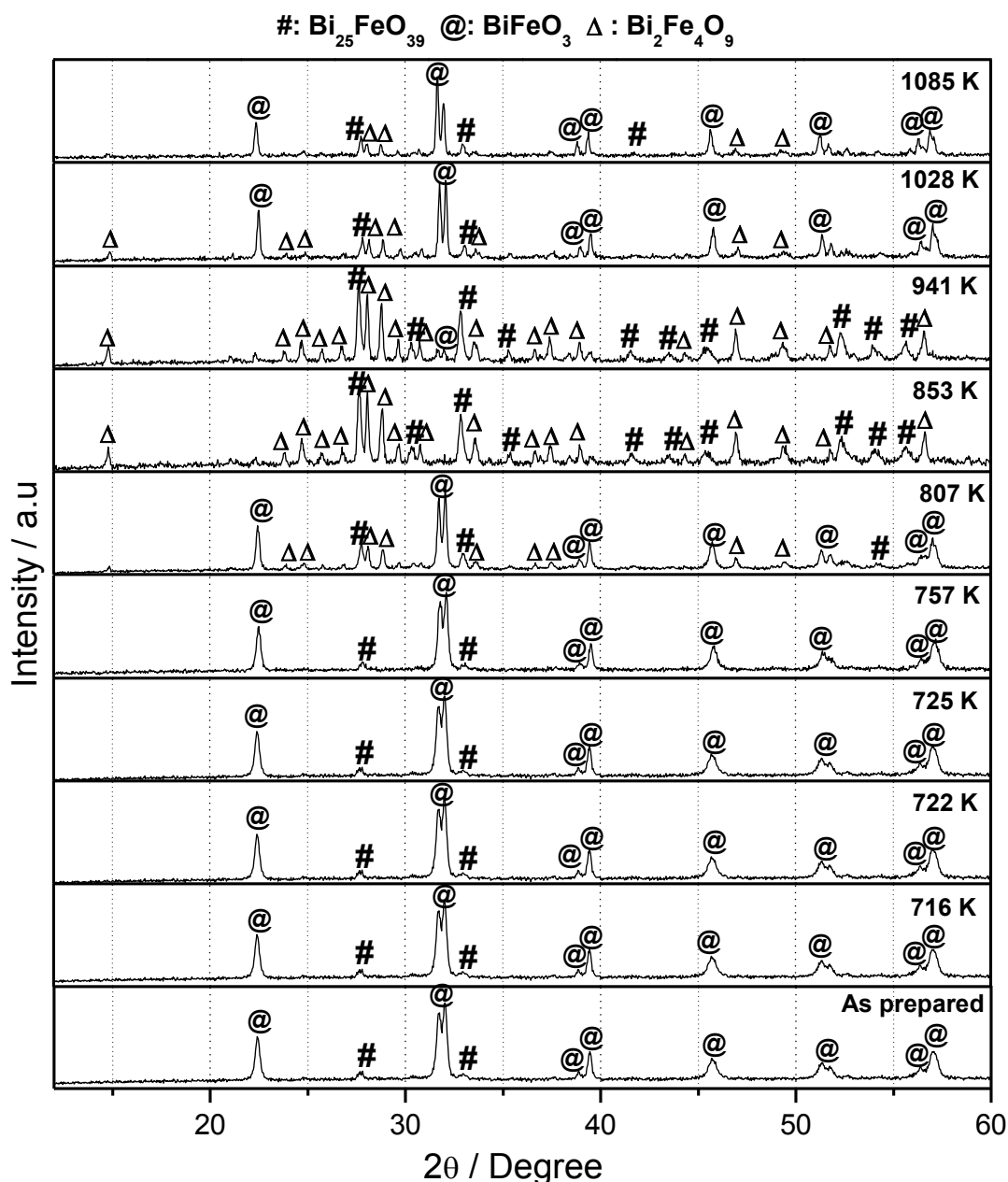


Fig. 3.23 XRD patterns obtained after equilibrating BiFeO_3 at different temperatures in air for 480 h

phase) and $\text{Bi}_{25}\text{FeO}_{39}$ (minor phase). A similar feature is observed for samples equilibrated in air at 757 K and below (samples 10 to 13 in Table 3.8). In the case of the sample which was equilibrated in vacuum at 763 K, the intensity of XRD lines of $\text{Bi}_{25}\text{FeO}_{39}$ increased along with those of $\text{Bi}_2\text{Fe}_4\text{O}_9$. Simultaneously, a reduction in the intensity of the lines corresponding to BiFeO_3 was also observed. This shows the

decomposition of BiFeO_3 to the neighbouring compounds, namely $\text{Bi}_{25}\text{FeO}_{39}$ and Bi_2FeO_9 , but this decomposition was not complete even after 480 h. A similar feature is observed in the sample equilibrated in air at 807 K. In the case of the samples equilibrated at 805 and 871 K in vacuum (853 K in air), BiFeO_3 had decomposed completely to $\text{Bi}_{25}\text{FeO}_{39}$ and Bi_2FeO_9 . In the case of sample equilibrated at 943 K in vacuum (941 K in air), presence of a small amount of BiFeO_3 could be identified although major phases are $\text{Bi}_{25}\text{FeO}_{39}$ and $\text{Bi}_2\text{Fe}_4\text{O}_9$. In the case of samples equilibrated at higher temperatures, BiFeO_3 was the major phase although small quantities of the other two phases could be identified. These results indicate that BiFeO_3 is a metastable compound at low temperatures and would become stable only at temperatures around 940 K. These results are in agreement with those reported by Maurya et al. [22] and Egorysheva et al. [23]. In their works, the authors observed the formation of BiFeO_3 at temperatures between 873 and 973 K. But according to Selbach et al. [21], BiFeO_3 is stable only above 1040 K. They calculated the free energy change for the reaction represented by eq. (3.1) using the data reported by Phapale et al. [15] and found that it would become negative only above 1040 K. The difference in the temperature from this data and that of Selbach et al. could be due to the possible errors in the data reported by Phapale et al. It is to be noted that the Gibbs energy of formation of $\text{Bi}_2\text{Fe}_4\text{O}_9$ derived by Phapale et al. (from the measured enthalpy of formation data and enthalpy increment data from calorimetric experiments and using estimated value of $\Delta S_{298,15}^\circ$ and the value of $\Delta C_{p,298,15}$ obtained from the enthalpy increment data) is lower than the value reported in this work by direct emf measurement. Further experiments are required to determine the exact

temperature above which BiFeO₃ becomes thermodynamically stable. The reaction involving Bi₂₅FeO₃₉, Bi₂Fe₄O₉ and BiFeO₃ can be represented by eq. (3.1):



Although BiFeO₃ could be prepared by heating the hydroxides at 773 K for shorter periods, it is found to decompose, although partially, on prolonged heating at 763 K. This might be the reason for the presence of BiFeO₃ in sample 3b in Table 3.2 and samples 24, 25 and 26 in Table 3.6 equilibrated at 773 K. Presumably because of small Gibbs energy change for the reaction (3.1) and also because of slow kinetics of decomposition, BiFeO₃ is present as metastable phase at low temperatures.

3.4.4.2.3 Equilibration of samples containing BiFeO₃ with liquid Bi

XRD patterns obtained after equilibrating mixtures of Bi, Bi₂Fe₄O₉ and BiFeO₃ in liquid Bi at 873 and 1023 K for 480 h are shown in Fig. 3.24 and the results are summarized in Table 3.9. At 873 K, the intensity of the lines corresponding to BiFeO₃ had drastically reduced and the intensities of the lines of Bi₂Fe₄O₉ and Bi₂₅FeO₃₉ had increased. At 1023 K, the intensity of the lines of Bi₂₅FeO₃₉ had decreased and those of BiFeO₃ had increased. This is in agreement with the observations made during equilibrations of BiFeO₃ in air and vacuum described in section 3.4.4.2.2.

XRD patterns obtained after equilibrating mixtures of Bi, BiFeO₃ and Bi₂₅FeO₃₉ in liquid Bi at 873 and 1023 K are shown in Fig. 3.25 and the results are given in Table 3.9. At 1023 K, BiFeO₃ had not decomposed but at 873 K, it decomposed almost completely and the other two phases i.e., Bi₂Fe₄O₉ and Bi₂₅FeO₃₉ had formed. This is again in agreement with the results of long term equilibration of

BiFeO₃ in air and vacuum described in the earlier section. These results also confirm that BiFeO₃ is metastable at low temperatures and would become stable only at high temperatures.

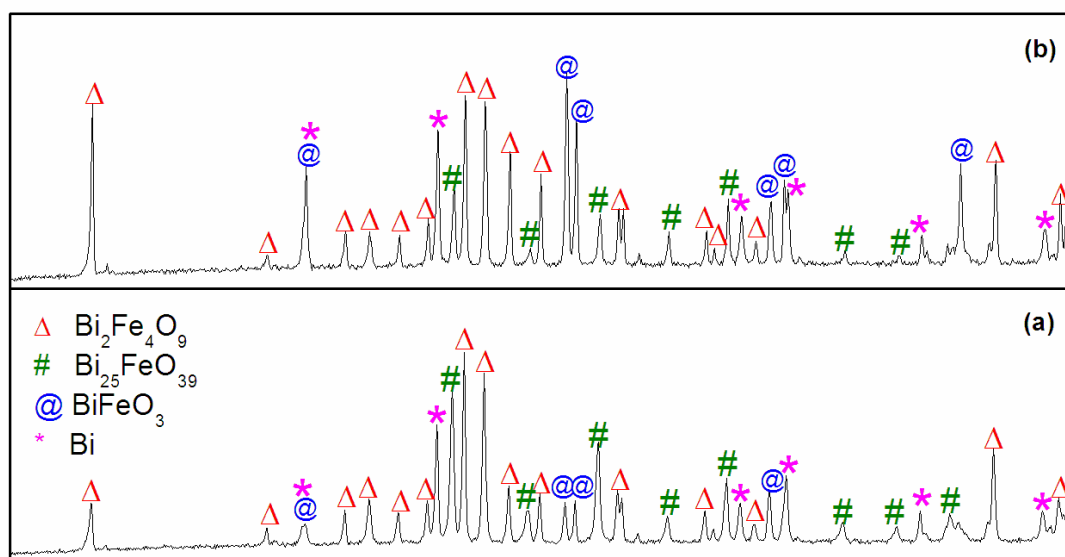


Fig. 3.24 XRD patterns of the products formed after equilibration of Bi, Bi₂Fe₄O₉, BiFeO₃ mixture in liq. Bi (a) at 873 K and (b) at 1023 K for 480 h

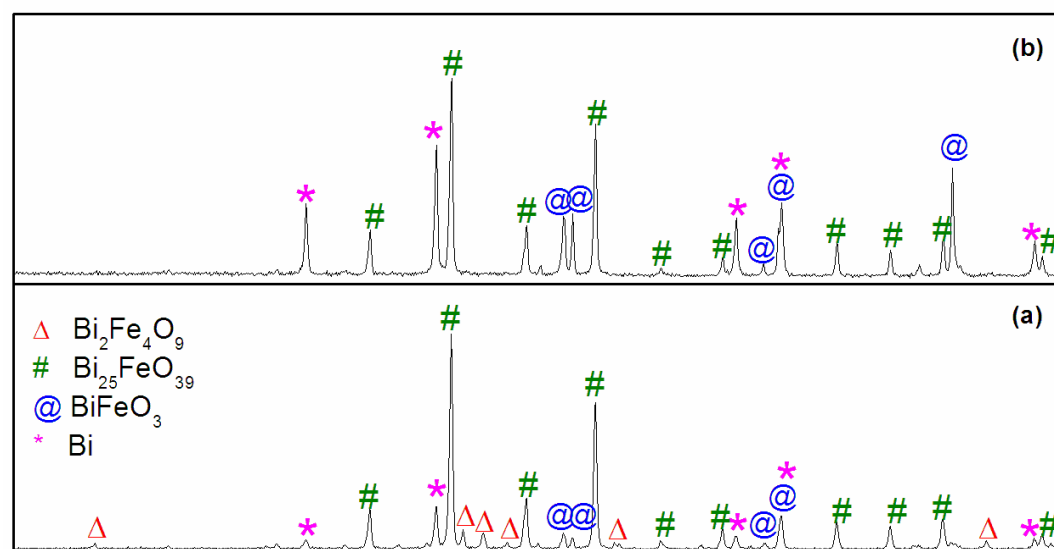


Fig. 3.25 XRD patterns of the products formed after equilibration of Bi, BiFeO₃, Bi₂₅FeO₃₉ mixture in liq. Bi (a) at 873 K and (b) at 1023 K for 480 h

The results of the present experiments in conjunction with the data in literature bring out the following characteristics of BiFeO₃ and the attainment of equilibrium in Bi-Fe-O system:

BiFeO₃ is thermodynamically unstable at low temperatures. The rate of its decomposition is very slow at temperatures as high as ~750 K. At temperatures above 750 K, the decomposition rate increases. On prolonged heating at ~850 K, BiFeO₃ decomposes completely to form Bi₂₅FeO₃₉ and Bi₂Fe₄O₉ (eq. 3.1). At a temperature around 940 K, BiFeO₃ appears as thermodynamically stable phase and remains as a stable phase above that temperature. This would explain the presence of a small amount of BiFeO₃ in samples equilibrated in vacuum at 943 K and in air at 941 K while it had decomposed completely at 805 and 871 K in vacuum and 853 K in air. This is also evident from the presence of BiFeO₃ as the major phase in the samples equilibrated at 1034 and 1089 K in vacuum and in the samples equilibrated in air at 1028 K and 1085 K. Since BiFeO₃ is only metastable at 773 K, the phase fields that exist in the region bound by Bi, Bi₂Fe₄O₉ and Bi₂O₃ at 773 K are: 1) Bi-Bi₂Fe₄O₉-Bi₂₅FeO₃₉ and 2) Bi-Bi₂₅FeO₃₉-Bi₂O₃. None of the equilibrations proved the existence of Bi-Bi₂Fe₄O₉-Bi₂₅FeO₃₉ phase field at 773 K and this was because of the metastable nature of BiFeO₃. However, the existence of Bi-Bi₂Fe₄O₉-Fe₂O₃ and Bi-Bi₂₅FeO₃₉-Bi₂O₃ phase fields has been established by the long term equilibration studies. Further, the equilibration of different molar ratios of Bi₂O₃ and Fe₂O₃ in air (discussed in section 3.4.2) indicated that no other ternary compounds with their composition falling in between Bi₂Fe₄O₉ and Bi₂₅FeO₃₉ are present at 773 K. All these observations lead to the confirmation of the existence of Bi-Bi₂Fe₄O₉-Bi₂₅FeO₃₉ phase field at 773 K.

The phase fields identified in the region bound by Bi, Bi₂Fe₄O₉ and Bi₂O₃ at 1023 K are: 1) Bi-BiFeO₃-Bi₂₅FeO₃₉ and 2) Bi-Bi₂₅FeO₃₉-Bi₂O₃. Present experiments have also established the thermodynamic stability of BiFeO₃ at this temperature. It is to be noted that the existence of Bi-Bi₂Fe₄O₉-BiFeO₃ phase field was not evidenced in any of the equilibration studies at 1023 K. However, its existence can be deduced

since (i) the existence of Bi-Bi₂Fe₄O₉-Fe₂O₃ and Bi-BiFeO₃-Bi₂₅FeO₃₉ phase fields has been confirmed by the long term equilibrations and (ii) the coexistence of Bi₂Fe₄O₉ and BiFeO₃, and BiFeO₃ and Bi₂₅FeO₃₉ has been established by long term equilibration of different molar ratios of Bi₂O₃ and Fe₂O₃ in air (discussed in section 3.4.2). Based on all the above results, the ternary phase diagram of Bi-Fe-O system at 773 and 1023 K have been constructed and are shown in Figs. 3.26 and 3.27. The results of the experiments showed that on increasing the oxygen content of bismuth metal in equilibrium with iron metal, iron oxides would first appear as the coexisting phases. With further increase in oxygen content in bismuth, Bi₂Fe₄O₉ would appear as the coexisting phase.

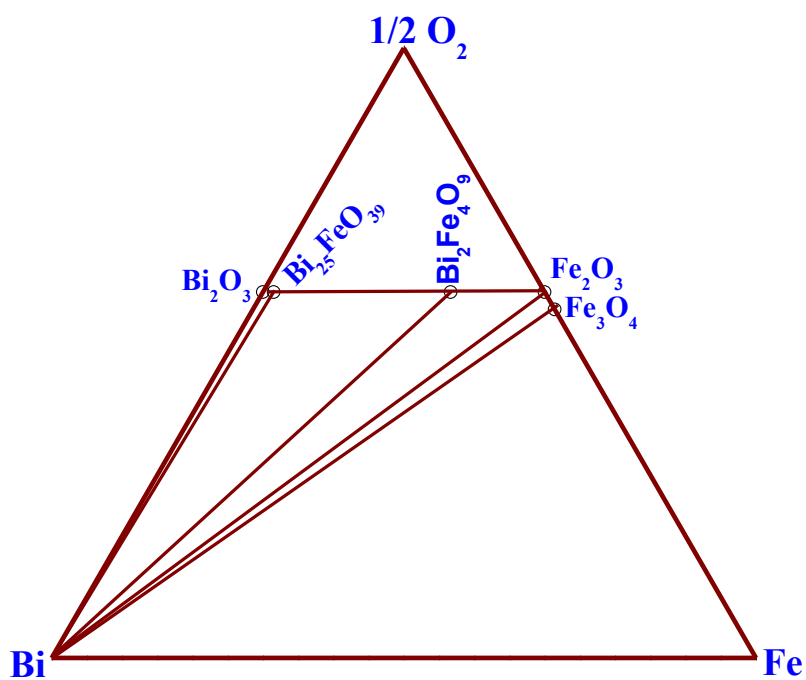


Fig. 3.26 Isothermal cross section of the ternary phase diagram of Bi-Fe-O system at 773 K

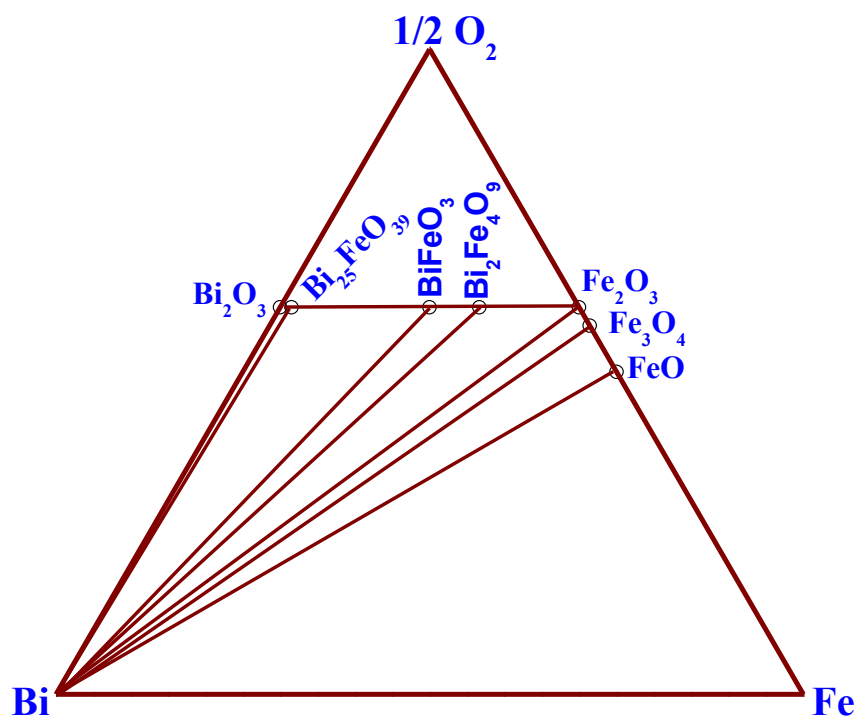


Fig. 3.27 Isothermal cross section of the ternary phase diagram of Bi-Fe-O system at 1023 K

3.4.4.3 Emf measurements

To determine the temperature above which BiFeO_3 appear as a thermodynamically stable phase in liquid Bi and also to determine the Gibbs energy of formation of BiFeO_3 and $\text{Bi}_{25}\text{FeO}_{39}$, oxygen potentials in liquid Bi in equilibrium with different phases were measured. The details of the emf measurements are given in Table 3.19 and the output of the emf cells, namely II, III, IV- a and IV- b in the chronological order of measurements along with the dwell time at each temperature are given in Tables 3.20 to 3.23. The variation of emf output of these cells with temperature is shown in Fig. 3.28. As seen in Tables 3.20 to 3.23, all the cells were first operated at temperatures above 1000 K where BiFeO_3 would be thermodynamically stable. The values of emf and its temperature dependence in all the cells were nearly same, as seen from Fig. 3.28. As seen from Table 3.19, overall compositions of the samples for the cells were chosen such that in cell - II and III, they would lie in the region bound by Bi, $\text{Bi}_2\text{Fe}_4\text{O}_9$ and BiFeO_3 . In cells IV-a and b, the overall compositions would lie in the region bound by Bi, BiFeO_3 and $\text{Bi}_{25}\text{FeO}_{39}$.

From the results of the experiments discussed in the earlier section, it is known that BiFeO_3 would appear as stable phase around 940 K. Hence, when equilibrium is established at temperatures below about 940 K, samples in all the four cells are expected to belong to Bi- $\text{Bi}_2\text{Fe}_4\text{O}_9$ - $\text{Bi}_{25}\text{FeO}_{39}$ phase field. At temperatures above about 940 K, cell II and III are expected to belong to Bi- $\text{Bi}_2\text{Fe}_4\text{O}_9$ - BiFeO_3 phase field, while the samples of cells IV-a and b are expected to belong to the Bi- BiFeO_3 - $\text{Bi}_{25}\text{FeO}_{39}$ phase field. Since the temperature dependence of oxygen potentials in all

Table 3.19 Details of emf measurements

Cell No.	Starting materials	Region in which overall composition would lie	Duration	Phases obtained after emf measurement
Cell II	Bi, Bi ₂ Fe ₄ O ₉ , BiFeO ₃ (containing small amount of Bi ₂₅ FeO ₃₉)	Bi- Bi ₂ Fe ₄ O ₉ -BiFeO ₃	22 days (17 data points)	Bi, Bi ₂ Fe ₄ O ₉ , BiFeO ₃ , Bi ₂₅ FeO ₃₉ (minor phase)
Cell III	Bi, Bi ₂ Fe ₄ O ₉ , Bi ₂₅ FeO ₃₉	Bi- Bi ₂ Fe ₄ O ₉ -BiFeO ₃	3 months (33 data points)	Bi, Bi ₂ Fe ₄ O ₉ (major phase), BiFeO ₃ (minor phase) Bi ₂₅ FeO ₃₉ (minor phase)
Cell IV-a	Bi, BiFeO ₃ (containing small amount of Bi ₂₅ FeO ₃₉), Bi ₂₅ FeO ₃₉	Bi- BiFeO ₃ -Bi ₂₅ FeO ₃₉	2 months (20 data points)	Bi, BiFeO ₃ , Bi ₂₅ FeO ₃₉
Cell IV-b	Bi, BiFeO ₃ (containing small amount of Bi ₂₅ FeO ₃₉), Bi ₂₅ FeO ₃₉	Bi- BiFeO ₃ -Bi ₂₅ FeO ₃₉	17 days (12 data points)	Bi, BiFeO ₃ , Bi ₂₅ FeO ₃₉

Table 3.20 Output of cell II as a function of temperature

No.	Temperature (K)	Dwell time (h)	Emf (mV)
1	1013.3	37	504.5
2	930.0	23	541.2
3	822.3	40	594.4
4	780.0	25	615.0
5	868.0	24	572.0
6	969.5	18	522.0
7	998.8	46	510.8
8	955.7	25	529.3
9	897.8	63	557.4
10	852.4	27	579.9
11	803.5	27	603.4
12	777.9	21	615.5
13	837.4	22	586.7
14	882.3	39	564.8
15	913.6	22	549.6
16	943.4	12	535.0
17	985.5	14	515.2

Table 3.21 Output of cell III as a function of temperature

No.	Temperature (K)	Dwell time (h)	Emf (mV)	No.	Temperature (K)	Dwell time (h)	Emf (mV)
1	1023.7	179	501.8	18	773.1	28	616.7
2	1000.0	84	511.4	19	798.2	33	604.4
3	981.9	26	517.4	20	810.2	29	598.4
4	956.5	26	528.3	21	836.2	18	587.1
5	930.9	60	540.8	22	861.2	20	577.0
6	903.6	46	554.5	23	888.2	64	562.5
7	923.2	28.5	545.1	24	785.1	22	606.2
8	965.6	24	524.3	25	1018.1	48	500.2
9	939.8	48	536.0	26	998.1	49	508.6
10	1012.5	117	506.1	27	781.7	64	610.4
11	992.2	141	515.1	28	924.3	26	544.0
12	955.5	28	528.6	29	826.3	15	589.8
13	948.7	22	532.0	30	876.6	23	568.4
14	918.0	26	547.2	31	797.1	20	602.9
15	873.5	28	567.4	32	973.4	50	520.0
16	848.2	20	577.5	33	1024.6	26	498.7
17	823.2	164	589.1				

Table 3.22 Output of cell IV – a as a function of temperature

No.	Temperature (K)	Dwell time (h)	Emf (mV)	No.	Temperature (K)	Dwell time (h)	Emf (mV)
1	1014.3	14	498.8	11	790.5	46	611.2
2	915.4	54	547.7	12	778.8	73	617.7
3	818.4	46	597.1	13	952.9	26	529.7
4	766.0	120	623.5	14	927.8	22	542.3
5	865.5	7	573.0	15	996.0	40	509.0
6	965.3	20	523.4	16	902.6	71	555.1
7	806.8	42	602.4	17	877.8	20	567.2
8	980.5	20	516.4	18	852.0	67	580.7
9	939.9	93	536.4	19	829.4	50	592.6
10	889.6	39	561.0	20	801.4	42	606.2

Table 3.23 Output of cell IV – b as a function of temperature

No.	Temperature (K)	Dwell time (h)	Emf (mV)
1	1020.6	17	497.0
2	921.5	22	545.5
3	828.1	19	590.0
4	783.8	47	611.5
5	874.6	55	568.5
6	969.1	18	522.0
7	998.4	42	507.3
8	950.8	6	530.9
9	945.4	12	533.8
10	804.2	24	601.4
11	896.0	21	557.9
12	859.6	24	576.2

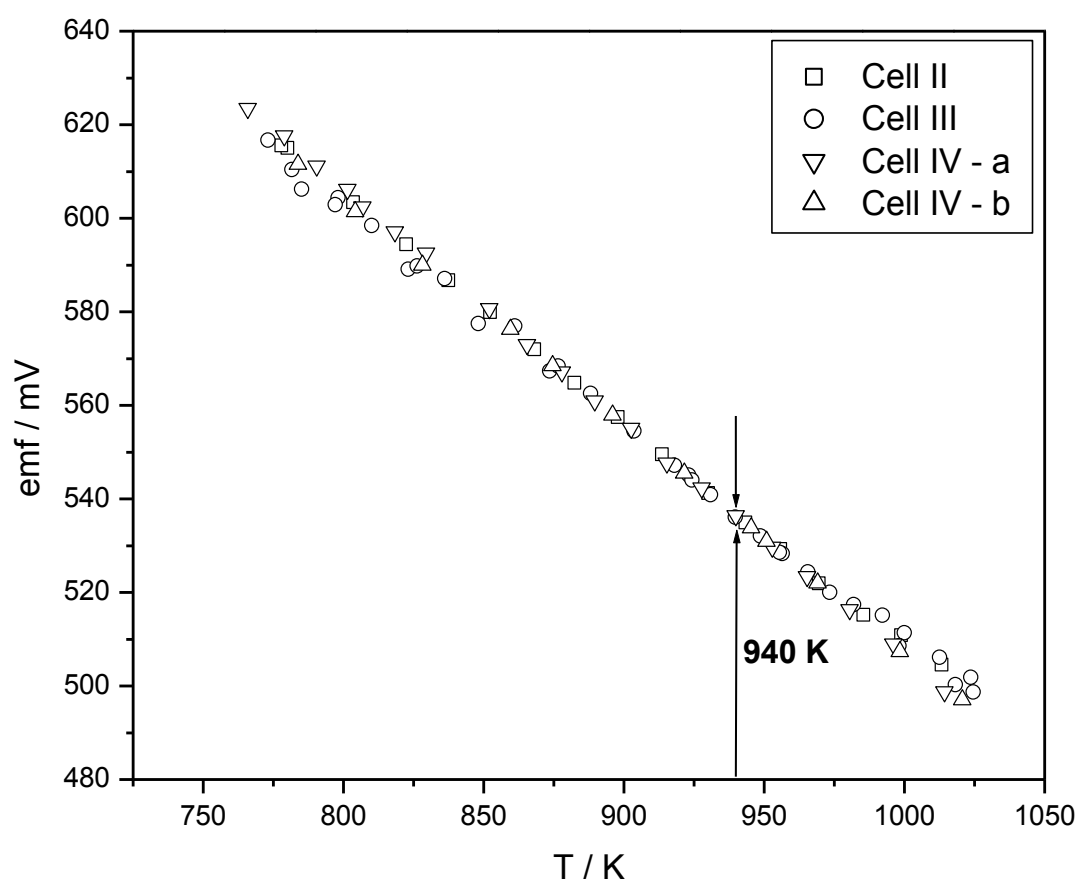


Fig. 3.28 Variation of emf with temperature for cells II, III, IV – a and IV – b

the three phase fields are expected to be different, a slope change at the temperature of appearance of BiFeO_3 as stable phase is expected. However, as seen from Fig. 3.28, no significant change in slope has been observed.

It is seen from Table 3.20 and 3.21, the final temperature of operation of cell II and III were 985.5 and 1024.6 K, respectively. At these temperatures, BiFeO_3 is expected to be present as a stable phase. When the cells IV-a and b were cooled to room temperature from 801.4 and 859.6 K, respectively, BiFeO_3 is not expected to be present. However, XRD patterns of the samples retrieved from all the four cells showed the presence of Bi, BiFeO_3 and $\text{Bi}_{25}\text{FeO}_{39}$ in them. Cells II and III contained additionally $\text{Bi}_2\text{Fe}_4\text{O}_9$ as seen from Table 3.19. It is seen that metastable phases were present in the samples. This could be due to insufficient dwell time at low operating temperatures of the cell for the metastable phases to decompose completely, although emf values were stable due to the ‘equilibrium’ established with these phases. Due to the identical ‘equilibrium’ conditions in all the four cells, emf values and their temperature dependence were same. Obviously, these data could not be used to deduce the Gibbs energy of formation of BiFeO_3 and $\text{Bi}_{25}\text{FeO}_{39}$.

3.4.4.4 Standard enthalpy of formation of $\text{Bi}_{25}\text{FeO}_{39}$

The chemical calibration of the calorimeter using KCl and TRIS were discussed in section 3.4.3.3. The results of the measurements of enthalpy of dissolution of $\text{Bi}_{25}\text{FeO}_{39}$ is given in Table 3.24 and the results of the measurements of enthalpy of dissolution for the starting materials, Bi_2O_3 and Fe_2O_3 are given in Table 3.14. A typical plot of dissolution of $\text{Bi}_{25}\text{FeO}_{39}$ in 8.38 mol kg⁻¹ HCl is shown in

Fig. 3.29. The molar enthalpy of solution of $\text{Bi}_{25}\text{FeO}_{39}$ deduced from the experiments is -4823.5 ± 180.7 kJ. The thermochemical reaction scheme used to derive the standard molar enthalpy of formation of $\text{Bi}_{25}\text{FeO}_{39}$ is given in Table 3.25. By using the values of the standard molar enthalpies of formation of Bi_2O_3 and Fe_2O_3 , namely ΔH_4 and ΔH_5 from ref. [33], the standard molar enthalpy of formation of $\text{Bi}_{25}\text{FeO}_{39}$ was determined as -7540.7 ± 256.7 kJ.

Table 3.24 Experimentally determined values of enthalpies of dissolution (ΔH) and molar enthalpies of dissolution ($\Delta_{\text{sol}}H_{\text{m}}$) of $\text{Bi}_{25}\text{FeO}_{39}$ in 8.38 ± 0.01 mol kg^{-1} HCl (mass of solvent = 327.15 ± 0.01 g) at 298.15 K* and 0.1 M Pa pressure.^a

Sample	Weight (w) / g	ΔH / J	$\Delta_{\text{sol}}H_{\text{m}}$ / (kJ mol^{-1})
$\text{Bi}_{25}\text{FeO}_{39}$	0.0588	-47.22	-4741.4
(Molecular mass:	0.0706	-54.01	-4516.5
5904.306 g mol^{-1})	0.0742	-61.73	-4912.1
	0.0665	-56.79	-5041.9
	0.0545	-45.28	-4905.6

$$\overline{X} = -4823.5 \pm 180.7^{\textcircled{a}}$$

*Temperature stability inside the calorimeter prior to start of experiment was ± 0.001 K.

\overline{X} : Mean value of the measurements.

^aThe standard uncertainties, $u(w) = 0.0001$ g and $u(p) = 0.3$ k Pa.

[@]Uncertainty given is the expanded uncertainty with level of confidence 0.95.

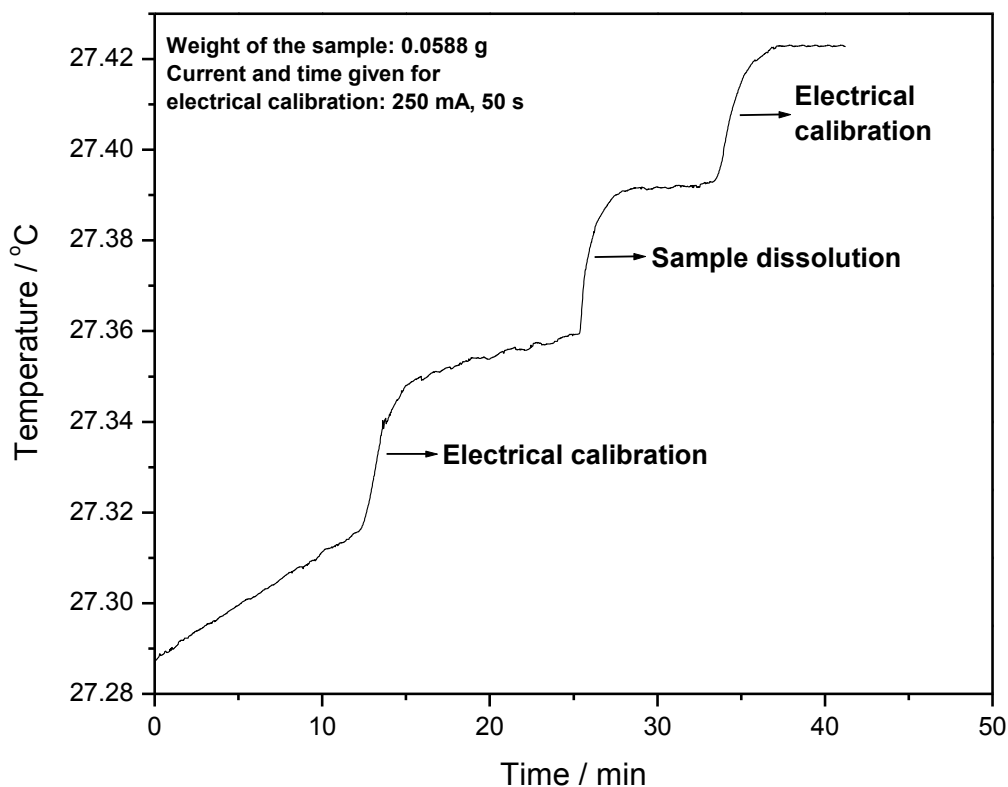


Fig. 3.29 A typical plot of dissolution of $\text{Bi}_{25}\text{FeO}_{39}$ in $8.38 \text{ mol kg}^{-1} \text{ HCl}$

Table. 3.25 Reaction scheme for calculating the standard molar enthalpy of formation of $\text{Bi}_{25}\text{FeO}_{39}$

Reaction	Enthalpy change
$\text{Bi}_{25}\text{FeO}_{39} (\text{s}) + 78 \text{ HCl} (\text{sln})$ $= (25 \text{ BiCl}_3 + \text{FeCl}_3 + 39 \text{ H}_2\text{O}) (\text{sln})$	$\Delta H_1 = -4823.5 \pm 180.7 \text{ kJ mol}^{-1} @$
$\text{Bi}_2\text{O}_3 (\text{s}) + 6 \text{ HCl} (\text{sln})$ $= (2 \text{ BiCl}_3 + 3 \text{ H}_2\text{O}) (\text{sln})$	$\Delta H_2 = -381.6 \pm 14.2 \text{ kJ mol}^{-1} @$
$\text{Fe}_2\text{O}_3 (\text{s}) + 6 \text{ HCl} (\text{sln})$ $= (2 \text{ FeCl}_3 + 3 \text{ H}_2\text{O}) (\text{sln})$	$\Delta H_3 = -99.6 \pm 9.4 \text{ kJ mol}^{-1} @$
$2 \text{ Bi} (\text{s}) + 3/2 \text{ O}_2 (\text{g}) = \text{Bi}_2\text{O}_3 (\text{s})$	$\Delta H_4 = -570.7 \pm 3.3 \text{ kJ mol}^{-1}$ from [33]
$2 \text{ Fe} (\text{s}) + 3/2 \text{ O}_2 (\text{g}) = \text{Fe}_2\text{O}_3 (\text{s})$	$\Delta H_5 = -821.3 \pm 3.3 \text{ kJ mol}^{-1}$ from [33]
$25 \text{ Bi} (\text{s}) + \text{Fe} (\text{s}) + 39/2 \text{ O}_2 (\text{g})$ $= \text{Bi}_{25}\text{FeO}_{39} (\text{s})$	$\Delta H_6 = 25/2 \Delta H_2 + 1/2 \Delta H_3 + 25/2 \Delta H_4 + 1/2 \Delta H_5 - \Delta H_1$ $= -7540.7 \pm 256.7 \text{ kJ mol}^{-1} @$

@ Uncertainty given is the combined expanded uncertainty with level of confidence 0.95.

3.4.4.5 Heat capacity measurement of Bi₂₅FeO₃₉ using differential scanning calorimetry

The XRD patterns of Bi₂₅FeO₃₉ before and after the DSC measurements remained the same indicating that it did not undergo any change during heat capacity measurements. The measured values of the molar heat capacity of Bi₂₅FeO₃₉ are given in Table 3.26 for selected temperatures and shown in Fig. 3.30. Three pellets of Bi₂₅FeO₃₉ were used for heat capacity measurements and for each pellet seven measurements were carried out. Hence, each measured data is the mean of twenty one measurements and the uncertainty expressed for each value (in Table 3.26) is the expanded uncertainty obtained from these measurements. These mean values were fitted to the following equation by using the least squares regression analysis as,

$$C_p <\text{Bi}_{25}\text{FeO}_{39}> (\text{J K}^{-1} \text{mol}^{-1}) \pm 49.9 = 1529.9 + 200.6 \times 10^{-3} T - 21.6 \times 10^6 T^{-2} \\ (T / \text{K}: 308\text{-}818) \quad (3.26)$$

The error given is the combined expanded uncertainty with a confidence level of 0.95 (see Table 3.26). These fitted values are shown along with the measured values in the Table. Phapale et al. [15] measured the enthalpy increment of Bi₂₅FeO₃₉ in the temperature range of 324 to 834 K and deduced its molar heat capacity. The data reported by them are also shown in Fig. 3.30. As seen from Fig. 3.30, the data reported by Phapale et al. [15] are significantly lower than the values from the present work over the entire temperature range of investigation. It is also to be pointed out that the temperature dependence of the C_p reported by Phapale et al. [15] is lower than that of the present data.

Molar heat capacity of Bi₂₅FeO₃₉ was also estimated by using Neumann-Kopp rule (NKR) by using the values of molar heat capacity for Bi₂O₃ and Fe₂O₃ [34].

These values, represented as C_p^{NKR} , are also shown in Fig. 3.30. At the mean temperature (563 K) of the present measurement, the experimental value of the molar heat capacity is about 4 % lower than that estimated by NKR.

Table 3.26 Measured and fitted heat capacity (C_p) values of $\text{Bi}_{25}\text{FeO}_{39}$ are compared with heat capacity values computed through Neumann-Kopp rule using C_p of Fe_2O_3 and Bi_2O_3 from [34] (C_p^{NKR}) and using C_p of Fe_2O_3 from [37] incorporating correction for magnetic contribution and C_p of Bi_2O_3 from [34] ($C_p^{NKR,corr}$) at 0.1 M Pa pressure.^a

T / K	C_p / J K ⁻¹ mol ⁻¹			
	Measured data	Fitted values	Estimated using Neumann Kopp rule	
			C_p^{NKR} *	$C_p^{NKR,corr}$ *
308	1355.9 ± 13.0	1364.0	1482.7	1479.8
353	1430.1 ± 13.0	1427.4	1524.6	1520.7
403	1482.3 ± 16.2	1477.7	1559.6	1554.4
453	1520.3 ± 16.6	1515.5	1587.2	1580.8
503	1543.9 ± 14.4	1545.4	1610.2	1602.5
553	1563.9 ± 13.8	1570.2	1630.3	1621.2
603	1587.1 ± 17.2	1591.5	1648.3	1637.9
653	1610.4 ± 14.4	1610.2	1664.9	1653.1
703	1628.1 ± 11.0	1627.2	1680.4	1667.3
753	1644.7 ± 11.4	1642.9	1695.2	1680.6
803	1658.4 ± 16.2	1657.5	1709.4	1693.4
818	1662.7 ± 18.0	1661.7	1713.5	1697.1

^aStandard uncertainties, $u(T) = 0.4$ K and $u(p) = 0.3$ k Pa. Measured data is the mean of twenty one measurements and the uncertainty given for each measured value is the expanded uncertainty with level of confidence 0.95. The combined expanded uncertainty, $U_c(C_p) = 49.9$ J K⁻¹ mol⁻¹ with level of confidence 0.95[@].

*Uncertainty not reported in references [34] and [37].

[@]The combined expanded uncertainty was calculated as in the case of $\text{Bi}_2\text{Fe}_4\text{O}_9$ (see Table 3.17).

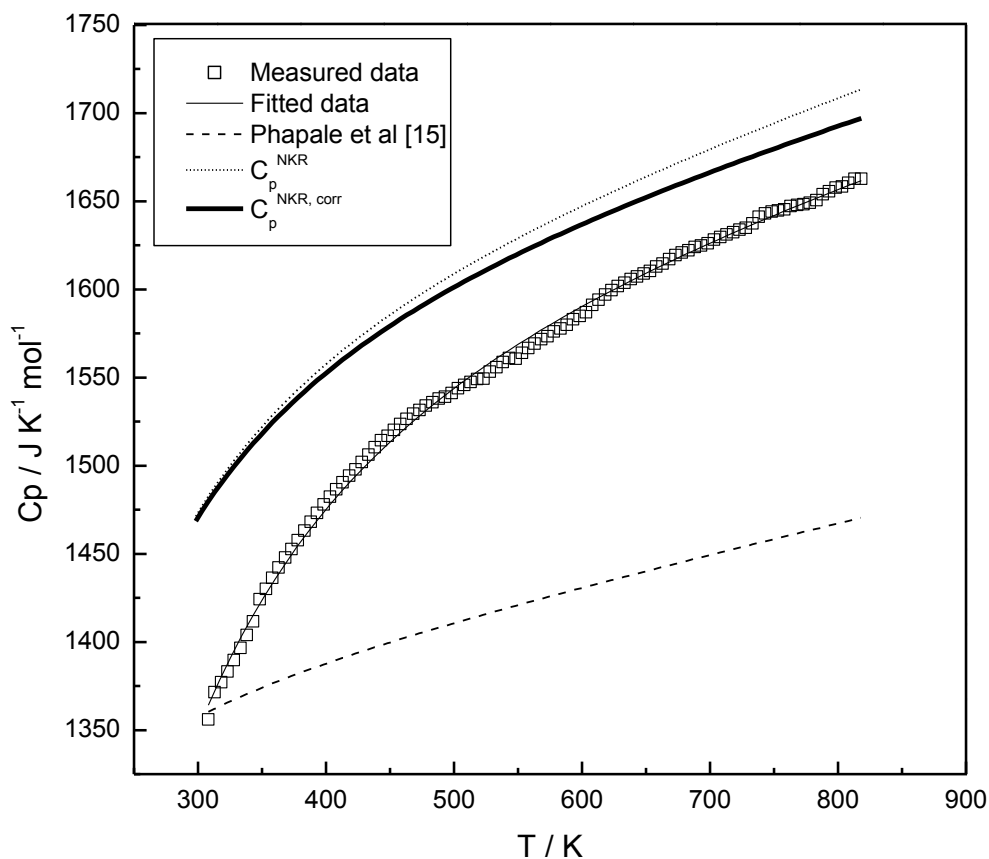


Fig. 3.30 Molar heat capacity of $\text{Bi}_{25}\text{FeO}_{39}$. C_p^{NKR} is the molar heat capacity calculated using Neumann-Kopp rule and $C_p^{\text{NKR,corr}}$ is after correcting for magnetic contribution.

3.4.4.6. Deviation of measured C_p values from the estimates by the Neumann-Kopp rule (NKR)

Comparison of the experimentally determined heat capacity of $\text{Bi}_{25}\text{FeO}_{39}$ with those estimated by the Neumann-Kopp rule indicates a large deviation. At the mean temperature of the present measurement, the deviation is -4 %. The reasons for this deviation were discussed in section 3.4.3.5. Large deviation of the measured heat capacity values of $\text{Bi}_{25}\text{FeO}_{39}$ from NKR estimated values could be due to the contribution of magnetic properties of $\alpha\text{-Fe}_2\text{O}_3$ because $\text{Bi}_{25}\text{FeO}_{39}$ is reported to be paramagnetic up to the temperature range of 5 to 950 K [39]. Therefore, the C_p of

$\text{Bi}_{25}\text{FeO}_{39}$ was recalculated by NKR by subtracting the magnetic contribution and considering only the estimated lattice and dilatational contributions of $\alpha\text{-Fe}_2\text{O}_3$ which are also shown in Fig. 3.30. These values are referred to as $C_p^{NKR,corr}$. Fig. 3.30 shows that in the case of $\text{Bi}_{25}\text{FeO}_{39}$, the deviation of the measured data from the $C_p^{NKR,corr}$ did not change significantly, compared to $\text{Bi}_2\text{Fe}_4\text{O}_9$ i.e., it reduced from 4 % to 3% only. This is probably due to the difference in the fraction of Fe_2O_3 present in $\text{Bi}_{25}\text{FeO}_{39}$ (3%) and in $\text{Bi}_2\text{Fe}_4\text{O}_9$ (66%).

In addition to magnetic contribution from Fe_2O_3 , other factors such as lattice vibrations, C_{ph} and lattice dilatations, C_d would also have their own contributions for the deviation of C_p^{NKR} from the measured value. The temperature dependence of the deviation of the measured heat capacity from the NKR predicted values could be due to change in difference in the dilatational properties, ΔC_d with temperature and which would depend upon the difference in molar volumes of the constituent oxides, their isobaric volume expansions and isothermal compressibilities. Table 3.27 shows the unit cell volumes of Bi_2O_3 and Fe_2O_3 and those of $\text{Bi}_{25}\text{FeO}_{39}$ [27].

Table 3.27 Unit cell volumes of $\text{Bi}_{25}\text{FeO}_{39}$

Unit cell volume/formula unit (\AA^3)		$\left(\frac{V_c - V_o}{V_o} \right) \times 100$
Compound, V_c	Constituent oxides, V_o	
1055.35	(25/2 Bi_2O_3 + 1/2 Fe_2O_3), 1058.70	-0.3

As seen from Table 3.27, the unit cell volume of $\text{Bi}_{25}\text{FeO}_{39}$ is 0.3% lower than the value obtained by the linear combination of the values of the unit cell volumes of the two binary oxides, taken in the appropriate stoichiometric ratio. If the difference in the molar volume ΔV_m would have contributed to the difference between the

measured and computed C_p values, then the measured C_p values of $\text{Bi}_{25}\text{FeO}_{39}$ should have been very close to that of the computed one. However, the deviation observed (Fig. 3.30) is much different from what is expected based on the ΔV_m . Hence, the α^2/β terms and their temperature dependence for the binary and ternary oxides might be the contributing factors for this observed difference and these values are not available in the open literature.

3.5 References

1. H.A. Wriedt, Bull. Alloy Phase Diagr. 9 (1988) 106. (reported in: T.B. Massalski (Ed.), Binary Alloys Phase Diagrams, 2nd Ed., ASM International (1990) 1739.
2. H. Okamoto, “Bi-Fe (Bismuth-Iron)” reported in: T.B. Massalski (Ed.), Binary Alloys Phase Diagrams, 2nd Ed., ASM International (1990) 1749.
3. J.R. Weeks, Trans. ASM, 58 (1965) 426-428.
4. D. Risold, B. Hallstedt, L.J. Gauckler, The Bismuth-Oxygen System, J. Phase Equilib. 16 (1995) 223-234.
5. E.M. Levin, R.S. Roth, Polymorphism of bismuth sesquioxide. II. Effect of Oxide additions on the polymorphism of Bi_2O_3 , J. Res. Nat. Bur. Std. US 68A (1964) 197-206.
6. H. Koizumi, N. Niizeki, T. Ikeda, An X-ray study on $\text{Bi}_2\text{O}_3\text{-Fe}_2\text{O}_3$ system, Jpn. J. Appl. Phys. 3 (1964) 495-496.
7. E.I. Speranskaya, V.M. Skorikov, Y.E. Rode, V.A. Terekhova, The phase diagram of the system bismuth oxide-ferric oxide, Bull. Acad. Sci. USSR, Div. Chem. Sci. (Engl. Transl.) 5 (1965) 905-906.

8. T.M. Bruton, J.C. Brice, O.F. Hill, P.A.C. Whiffin, The flux growth of some γ - Bi_2O_3 crystals by the top seeded technique, *J. Cryst. Growth* 23 (1974) 21-24.
9. D.C. Craig, N.C. Stephenson, Structural studies of some body-centered cubic phases of mixed oxides involving Bi_2O_3 : The structures of $\text{Bi}_{25}\text{FeO}_{40}$ and $\text{Bi}_{38}\text{ZnO}_{60}$, *J. Solid State Chem.* 15 (1975) 1-8.
10. A. Ramanan, J. Gopalakrishnan, Low-temperature preparation of sillenite phases in Bi-M-O (M = Mn, Fe, Co) systems, *Ind. J. Chem.* 24A (1985) 594-596.
11. S.F. Radaev, L.A. Muradyan, V.I. Simonov, Atomic structure and crystal chemistry of sillenites: $\text{Bi}_{12}(\text{Bi}_{0.67}^{3+}\text{Zn}_{0.33}^{2+})\text{O}_{19.50}$ and $\text{Bi}_{12}(\text{Bi}_{0.67}^{3+}\text{Zn}_{0.33}^{2+})\text{O}_{19.50}$ and $\text{Bi}_{12}(\text{Bi}_{0.50}^{3+}\text{Fe}_{0.50}^{3+})\text{O}_{19.33}$, *Acta Cryst.* B47 (1991) 1-6.
12. A. Maitre, M. Francois, J.C. Gachon, Experimental study of the Bi_2O_3 - Fe_2O_3 pseudo-binary system, *J. Phase Equilib. Diff.* 25 (2004) 59-67.
13. R. Palai, R.S. Katiyar, H. Schmid, P. Tissot, S.J. Clark, J. Robertson, S.A.T. Redfern, G. Catalan, J.F. Scott, β phase and γ - β metal-insulator transition in multiferroic BiFeO_3 , *Phys. Rev. B* 77 (2008) 014110-1-11.
14. J. Lu, L.J. Qiao, P.Z. Fu, Y.C. Wu, Phase equilibrium of Bi_2O_3 - Fe_2O_3 pseudo-binary system and growth of BiFeO_3 single crystal, *J. Cryst. Growth* 318 (2011) 936-941.
15. S. Phapale, R. Mishra, D. Das, Standard enthalpy of formation and heat capacity of compounds in the pseudo-binary Bi_2O_3 - Fe_2O_3 system, *J. Nucl. Mater.* 373 (2008) 137-141.

16. G.D. Achenbach, W.J. James, R. Gerson, Preparation of single-phase polycrystalline BiFeO_3 , *J. Am. Ceram. Soc.* 50 (1967) 437.
17. J. De Sitter, C. Dauwe, E. De Grave, A. Govaert, G. Robbrecht, On the magnetic properties of the basic compounds in the Fe_2O_3 - Bi_2O_3 system, *Physica* 86-88 B (1977) 919 - 920.
18. M.I. Morozov, N.A. Lomanova, V.V. Gusarov, Specific features of BiFeO_3 formation in a mixture of bismuth (III) and iron (III) oxides, *Russ. J. Gen. Chem.* 73 (2003) 1676-1680.
19. M. Valant, A.K. Axelsson, N. Alford, Peculiarities of a solid state synthesis of multiferroic polycrystalline BiFeO_3 , *Chem. Mater.* 19 (2007) 5431 – 5436.
20. T.T. Carvalho, P.B. Tavares, Synthesis and thermodynamic stability of multiferroic BiFeO_3 , *Mater. Lett.* 62 (2008) 3984 - 3986.
21. S.M. Selbach, M.A. Einarsrud, T. Grande, On the thermodynamic stability of BiFeO_3 , *Chem. Mater.* 21 (2009) 169-173.
22. D. Maurya, H. Thota, K.S. Nalwa, A. Garg, BiFeO_3 ceramics synthesized by mechanical activation assisted versus conventional solid-state reaction process: A comparative study, *J. Alloy. Comp.* 477 (2009) 780 - 784.
23. A.V. Egorysheva, V.D. Volodin, O.G. Ellert, N.N. Efimov, V.M. Skorikov, A.E. Baranchikov, V.M. Novotortsev, Mechanochemical activation of starting oxide mixtures for solid - state synthesis of BiFeO_3 , *Inorg. Mater.* 49 (2013) 303 – 309.

24. N.A. Lemonova, V.V. Gusarov, Influence of synthesis temperature on BiFeO₃ nanoparticles formation, *Nanosystems: Phys. Chem. Math.* 4 (2013) 696–705.
25. K.N. Marsh, P.A.G. O'Hare (Ed.), *Solution calorimetry, Experimental thermodynamics*, Vol. IV, Blackwell scientific publications, Oxford, 1994.
26. D.G. Archer, Thermodynamic properties of synthetic sapphire (α -Al₂O₃), standard reference material 720 and the effect of temperature-scale differences on thermodynamic properties, *J. Phys. Chem. Ref. Data* 22 (1993) 1441-1453.
27. PDF-4+ database, International Centre for Diffraction Data, 2015.
28. B. Sundman, An assessment of the Fe-O system, *J. Phase Equilib.* 12 (1991) 127-140.
29. A.F. Guillermet, P. Gustafson, An assessment of the thermodynamic properties and the (p, T) phase diagram of iron, *High Temp. – High Press.* 16 (1985) 591 – 610.
30. V. Venugopal, N.K. Shukla, V. Sundaresh, K.N. Roy, R. Prasad, D.D. Sood, Thermochemistry of cesium iodide and cesium chromate, *J. Chem. Thermodyn.* 18 (1986) 735–738.
31. Nat. Bur. Stand. Certificate for SRM 1655 (KCl), US Dept. of Commerce, Washington, March 1981.
32. Model 1455 Solution Calorimeter Operating Instruction Manual, No. 281MM, PARR Instrument Company, USA.
33. O. Kubaschewski, C.B. Alcock, *Metallurgical Thermochemistry*, fifth ed., Pergamon, Oxford, 1979.

34. O. Knacke, O. Kubaschewski, K. Hesselmann, Thermo-chemical properties of inorganic substances, Vol. 1, second ed., Springer, Berlin, 1991.
35. G. Grimvall, Thermophysical properties of materials, Enlarged and revised ed., Elsevier, North-Holland, 1999.
36. J. Leitner, P. Vonka, D. Sedmidubsky, P. Svoboda, Application of Neumann–Kopp rule for the estimation of heat capacity of mixed oxides, *Thermochim Acta* 497 (2010) 7-13.
37. F. Gronvold, E.J. Samuelsen, Heat capacity and thermodynamic properties of α -Fe₂O₃ in the region 300-1050 K. Antiferromagnetic transition, *J. Phys. Chem. Solids* 36 (1975) 249-256.
38. N. Shamir, E. Gurewitz, H. Shaked, The Magnetic structure of Bi₂Fe₄O₉ – analysis of neutron diffraction measurements, *Acta Cryst.* A34 (1978) 662-666.
39. A.A. Zatsiupa, L.A. Bashkirov, I.O. Troyanchuk, G.S. Petrov, A.I. Galyas, L.S. Lobanovsky, S.V. Truhanov, Magnetization, magnetic susceptibility, effective magnetic moment of Fe³⁺ ions in Bi₂₅FeO₃₉ ferrite, *J. Solid State Chem.* 212 (2014) 147-150.

Chapter 4

THERMOCHEMICAL STUDIES ON Bi-Cr-O SYSTEM

4.1 Introduction

Use of lead and lead-bismuth eutectic alloy as coolants in nuclear reactors and in ADS has received greater attention in recent years. Various aspects of corrosion of structural materials in these coolant systems are discussed in Chapter 1. Formation of a protective oxide layer by controlling the oxygen concentration in the coolant can reduce the corrosion of structural material in these heavy liquid metal cooled systems. To understand the nature of this protective oxide film, the data on phase diagram and thermochemical properties of the ternary compounds formed in the Pb-M-O and Bi-M-O (M = alloying elements of steel) systems are essential. In this chapter, studies carried out on Bi-Cr-O system are described.

4.2 Literature survey

4.2.1 Cr-O system

Fig. 4.1 shows the partial phase diagram of Cr-O system [1]. Among the several oxides reported in Cr-O system, Cr_2O_3 and CrO_3 are the stable oxides under atmospheric pressure. CrO_3 is extremely hygroscopic and melts at 470 K. Cr_2O_3 is obtained as the end product on dissociation of CrO_3 at elevated temperatures in air. All other oxides reported in this system, namely CrO , Cr_3O_4 , Cr_3O_8 , Cr_2O_5 , Cr_6O_{15} , Cr_5O_{12} and CrO_2 are stable either at high temperatures or under high oxygen pressures only [2, 3].

Gibbs energy of formation of Cr_2O_3 has been measured by using gas equilibration techniques and solid oxide electrolyte based emf cells [3-12]. The literature data on Gibbs energy of formation of Cr_2O_3 are listed in Table 4.1 including the experimental details. They are also shown in Fig. 4.2. Ziemniak et al. [12] carried out a detailed review on the Gibbs energy of formation of Cr_2O_3 . Ramsey et al. [4] determined the Gibbs energy of formation of Cr_2O_3 by a microbalance technique in which oxidized chromium sheet heated in prepared $\text{H}_2/\text{H}_2\text{O}$ atmospheres and the dissociation pressure of Cr_2O_3 was determined. Toker et al. [3] and Jeannin et al. [5] determined the equilibrium oxygen pressure over $\text{Cr}/\text{Cr}_2\text{O}_3$ by gas equilibration using H_2/CO_2 and $\text{H}_2/\text{H}_2\text{O}$ mixtures, respectively.

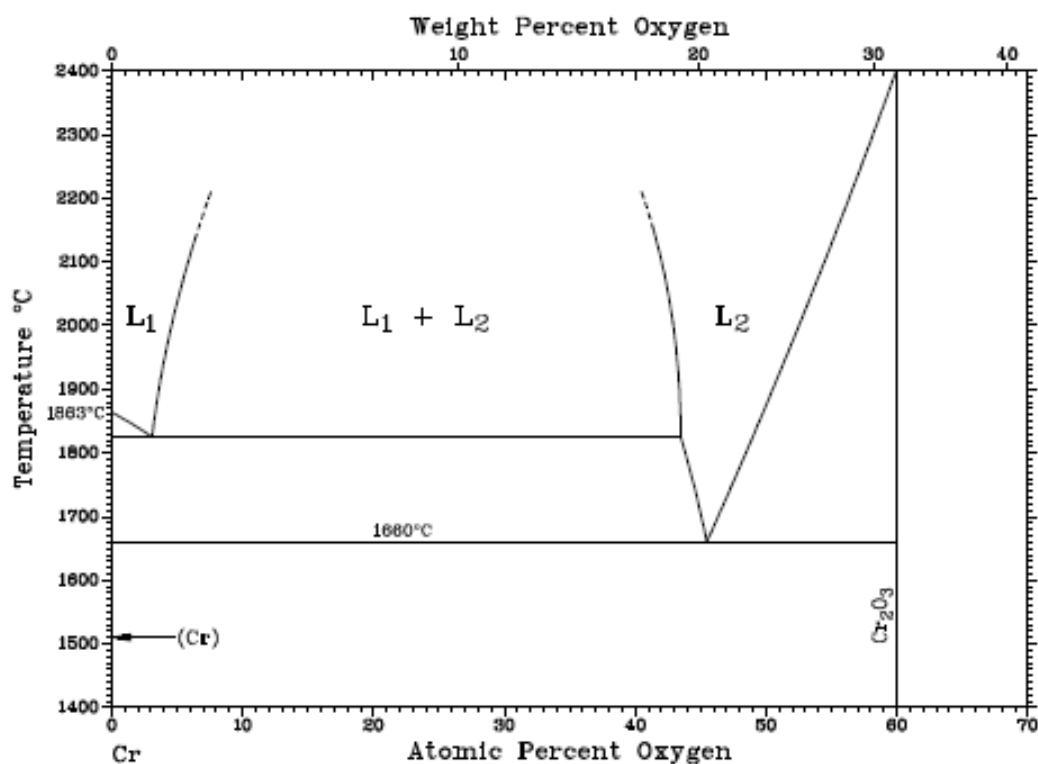


Fig. 4.1 Partial phase diagram of Cr-O system [1]

Tretjakow and Schmalzried [6], Pugliese and Fitterer [7] and Davies and Smeltzer [8] determined Gibbs energy of formation of Cr_2O_3 using zirconia based emf cells. Fig. 4.3 shows the electrolytic domain boundaries of CSZ along with the data reported by these authors. It can be seen that the measurements were carried out outside the electrolytic boundaries of CSZ. Mazandarany and Pehlke [9], Jacob [10] and Holzheid and O'Neill [11], determined the Gibbs energy of formation Cr_2O_3 using thoria based emf cells. Fig. 4.3 shows the electrolytic domain boundaries of YDT also and the data reported by these authors. The entire data sets fall within the domain boundaries of YDT. Fig. 4.2, which compares the data on Gibbs energy of formation of Cr_2O_3 reported by different authors clearly revealed the deviation among them. Generally, gas equilibration techniques are employed at high temperatures (>1000 K) and the error associated with this method are higher than those encountered in emf methods. It is to be pointed out that the data derived using zirconia cells are associated with error due to the contribution of electronic conduction. However, close agreement is observed among the data derived from YDT based emf cells viz., by Mazandarany and Pehlke [9], Jacob [10] and Holzheid and O'Neil [11].

Table 4.1 Literature data on the Gibbs energy of formation of Cr₂O₃

Reference	Experimental techniques	Temperature / K	$\Delta_f G_m^\circ \text{Cr}_2\text{O}_3 / \text{kJ}$
Toker et al. [3]	Gas equilibration with H ₂ /CO ₂ mixture	1773 - 1923	$-1092.4 + 0.2379 T (\pm 0.5)$
Ramsey et al. [4]	Gas equilibration with H ₂ /H ₂ O mixture	871 - 1427	$-1125.6 + 0.2658 T^*$
Jeannin et al. [5]	Gas equilibration with H ₂ /H ₂ O mixture	1313 - 1573	$-1115.9 + 0.2508 T^*$
Tretjakow and Schmalzried [6]	CSZ based emf cell with air reference	1000 - 1500	$-1082.0 + 0.2310 T (\pm 1.3)$
Pugliese and Fitterer [7]	CSZ based emf cell with air reference	1073 - 1448	$-1134.4 + 0.2766 T (\pm 1.5)$
Davies and Smeltzer [8]	CSZ based emf cell with Fe + FeO reference	1173 - 1373	$-1101.9 + 0.2475 T (\pm 2.6)$
Mazandarany and Pehlke [9]	YDT based emf cell with Co + CoO and Mn + MnO reference	1150 - 1540	$-1115.5 + 0.2501 T (\pm 1.5)$
Jacob [10]	YDT based emf cell with Co + CoO reference	1073 - 1473	$-1115.9 + 0.2504 T (\pm 0.9)$
Holzheid and O'Neill [11]	YDT based emf cell with Fe + FeO reference	600 - 1800	$-1113.9 + 0.2497 T (\pm 0.3)$

*Error has not been reported in the publications.

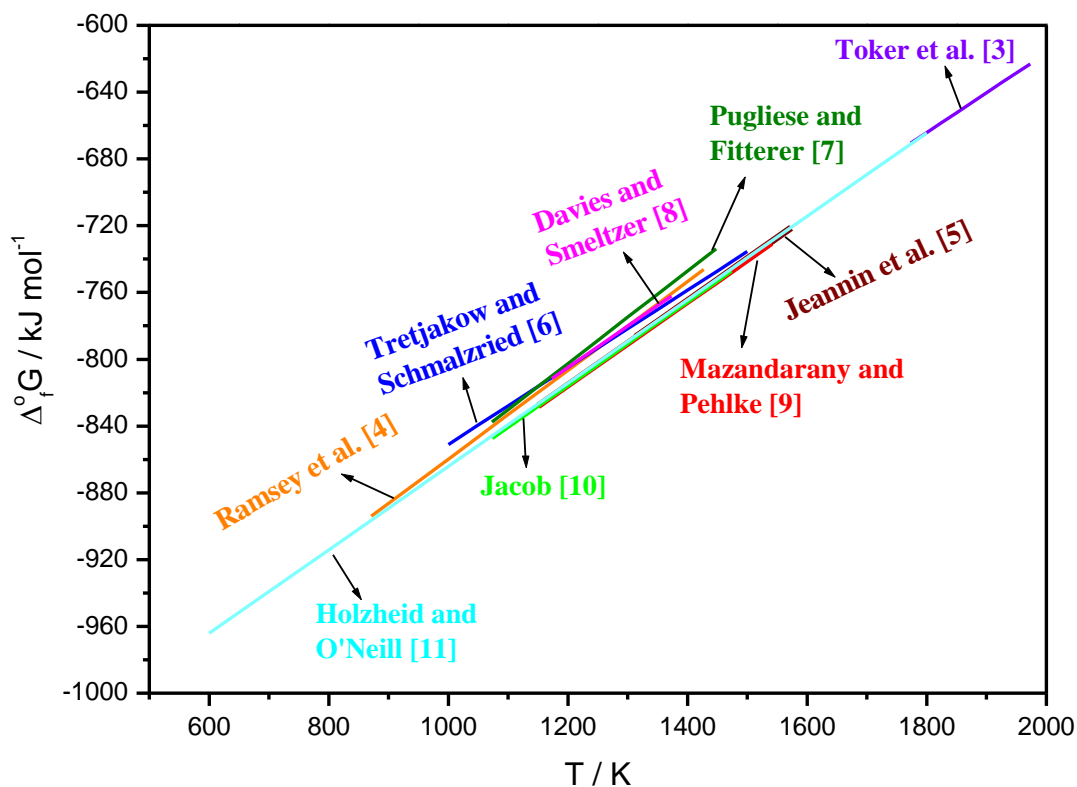


Fig. 4.2 Literature data on the Gibbs energy of formation of Cr₂O₃

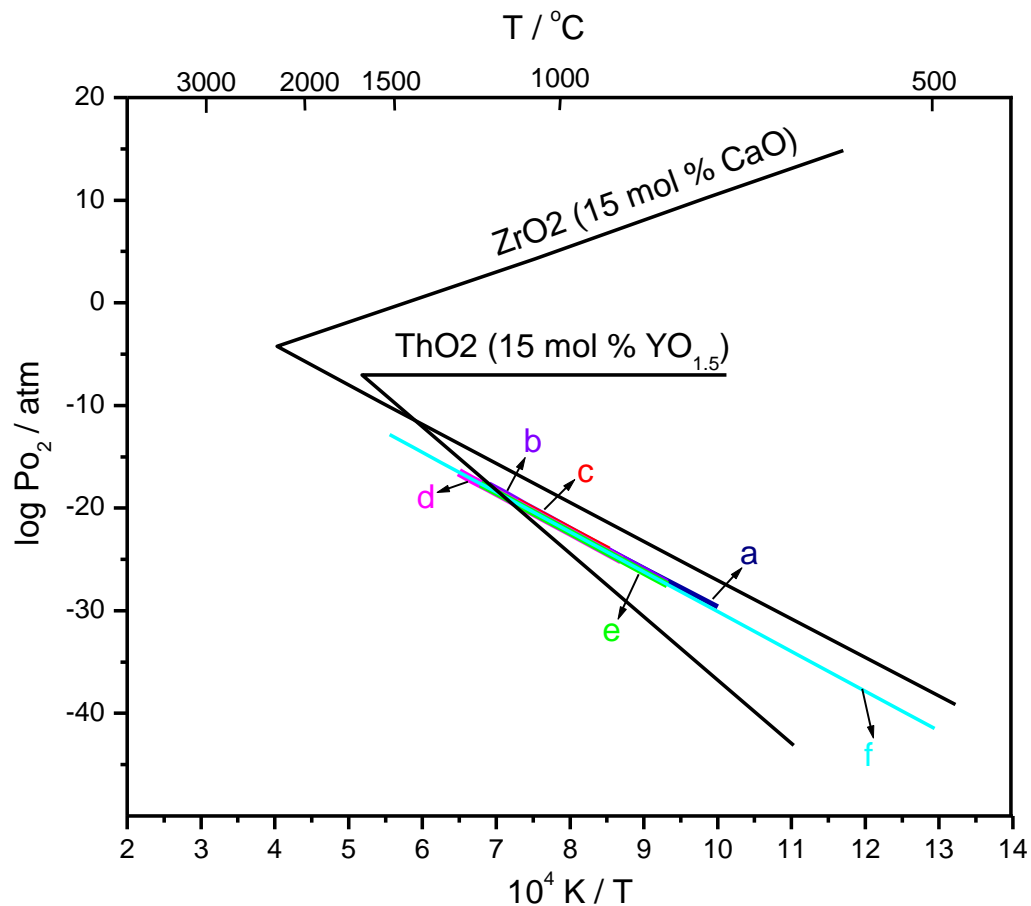


Fig. 4.3 Measured equilibrium oxygen pressures of $\text{Cr}/\text{Cr}_2\text{O}_3$ system and the electrolytic domain boundaries of calcia stabilized zirconia and yttria-doped thoria solid electrolytes

i) Measurements using CSZ based cells

- (a) Tretjakow and Schmalzried [6]
- (b) Pugliese and Fitterer [7]
- (c) Davies and Smeltzer [8]

ii) Measurements using YDT based cells

- (d) Mazandarany and Pehlke [9]
- (e) Jacob [10]
- (f) Holzheid and O'Neill [11]

4.2.2 Bi-Cr system

Venkatraman and Neumann [13] reviewed and assessed the data on Bi-Cr system. Data available in the literature on this system is very limited. No intermetallic compounds exist in Bi-Cr system. Extensive miscibility occurs in the liquid state while the metals are essentially immiscible in the solid state.

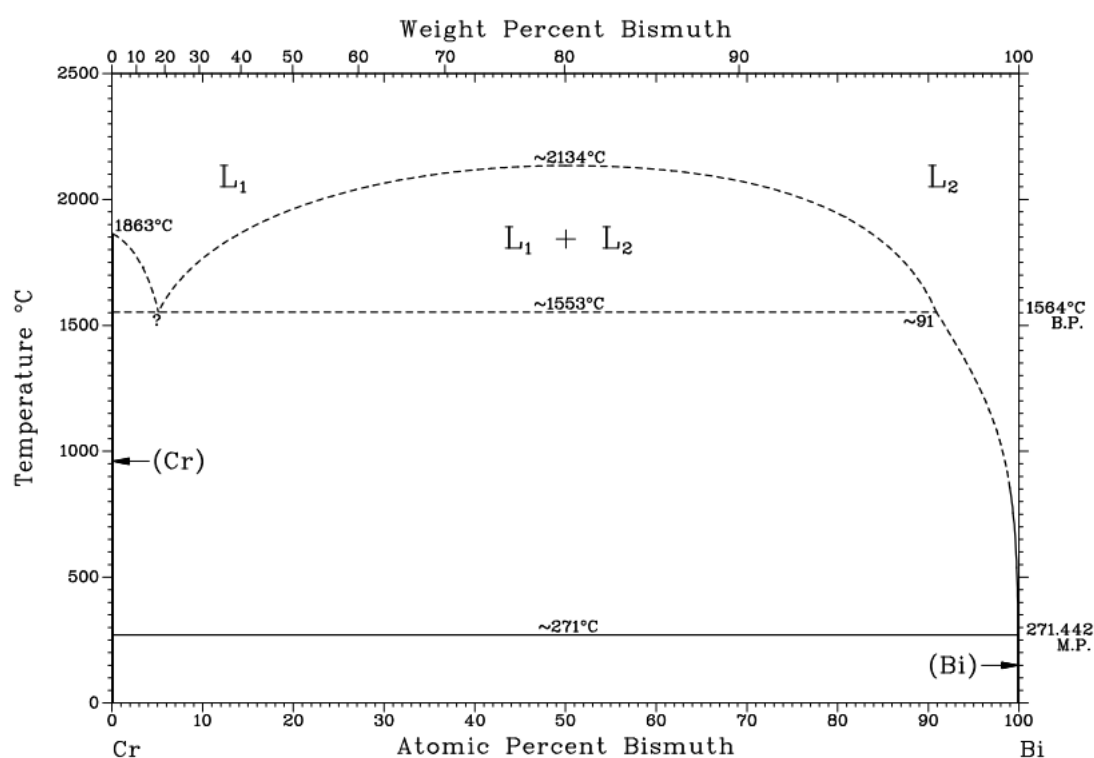


Fig. 4.4 Phase diagram of Bi-Cr system [13]

4.2.3 Studies on Bi₂O₃-CrO₃ pseudo-binary system

Pseudo-binary system of Bi₂O₃-CrO₃ has been studied by several authors in the past [14-23]. In all these studies, the experiments involved equilibrating a mixture of Bi₂O₃ and Cr₂O₃ in air at elevated temperatures. Upon heating in air, Cr (III) gets oxidized to Cr (VI) and the resulting compounds lie on Bi₂O₃-CrO₃ line. However, all the authors had presented their results as pertaining to Bi₂O₃-Cr₂O₃ phase diagram. Salient results from these studies on Bi₂O₃-CrO₃ system are given in Table 4.2.

Table 4.2 Literature data on $\text{Bi}_2\text{O}_3\text{-CrO}_3$ and $\text{Bi}_2\text{O}_3\text{-Cr}_2\text{O}_3$ pseudo-binary systems

Sl. No.	Reference	Details of preparation and characterization	Salient features reported
<i>Studies on $\text{Bi}_2\text{O}_3\text{-CrO}_3$ pseudo binary system:</i>			
1	Masuno [14]	Different molar ratios of Bi_2O_3 and Cr_2O_3 were heated at 1003-1153 K in air. Characterization by XRD, DTA and potentiometric titrations	$\text{Bi}_{18}\text{CrO}_{30}$ (tetragonal) Bi/Cr: 14.87 to 17.87 (all Cr in +6 state) $\text{Bi}_6\text{Cr}_2\text{O}_{15}$ (orthorhombic) Bi/Cr: 3 to 9.99 (fraction of Cr in +6 state was low) *BiCrO_3 (orthorhombic) Bi/Cr=1 (fraction of Cr in +6 state was 20%)
2	Cudennec et al. [15]	A new compound prepared from saturated solution of CrO_3 and bismuth nitrate at 293 K. Characterization by XRD and TG-DTA- up to 473 K	A new compound- $\text{Bi}_2\text{Cr}_4\text{O}_{15}$ (triclinic)
3	Zhitomirskii et al. [16]	Different molar ratios of Bi_2O_3 and Cr_2O_3 were heated in air at 973 K (3 h) and 1023 K (1 h) Single crystals of $\text{Bi}_{16}\text{CrO}_{27}$ and $\text{Bi}_{38}\text{CrO}_{60}$ were prepared by hydrothermal method Characterization by XRD, IR spectroscopy, dielectric studies	A new compound - $\text{Bi}_{38}\text{CrO}_{60}$ (sillenite type structure) – reported to be metastable $\text{Bi}_{16}\text{CrO}_{27}$ (tetragonal) Bi/Cr: 11.99 to 17.87 $\text{Bi}_6\text{Cr}_2\text{O}_{15}$ (orthorhombic) Bi/Cr: 3 to 6.69 *BiCrO_3 (orthorhombic) Bi/Cr = 1
4	Warda et al. [17]	Stoichiometric amounts of Bi_2O_3 and Cr_2O_3 were heated at 1023 K in air for 2 days with intermediate grinding Single crystals of $\text{Bi}_{14}\text{CrO}_{24}$ were prepared by cooling the oxide melt from 1133 to 873 K at a rate of 4.8 K / h Single crystal XRD, UV-Vis spectroscopy, X-ray absorption near-edge structure (XANES) spectroscopy and electron paramagnetic resonance (EPR) spectroscopy were the characterization tools used.	Based on single crystal studies, the actual composition of the tetragonal phase was reported as $\text{Bi}_{14}\text{CrO}_{24}$ (earlier reported as $\text{Bi}_{18}\text{CrO}_{30}$ and also as $\text{Bi}_{16}\text{CrO}_{27}$) $\text{Bi}_{10}\text{Cr}_2\text{O}_{21}$ – structure not elucidated

Table 4.2 (continued)

Sl. No.	Reference	Details of preparation and characterization	Salient features reported
5	Esmaeizadeh et al. [18]	Different molar ratios of Bi ₂ O ₃ and Cr ₂ O ₃ were heated in air upto 1123-1223 K for 5 min followed by quenching to room temperature XRD, SEM, TG, optical spectroscopy, IR spectroscopy and magnetic measurements were the characterization tools	Metastable solid solution Bi _{1-x} Cr _x O _{1.5+1.5x} where $0.05 \leq x \leq 0.15$ Bi/Cr: 5.67 to 19
6	Grins et al. [19]	Stoichiometric amounts of Bi ₂ O ₃ and Cr ₂ O ₃ were heated in air at 923 K for 72h with three intermediate grindings Characterization by XRD, time of flight neutron powder diffraction (TOF-NPD)	Determined the structure of Bi ₆ Cr ₂ O ₁₅ as orthorhombic
7	Crumpton et al. [20]	Stoichiometric amounts of Bi ₂ O ₃ and Cr ₂ O ₃ were heated at 1023 K for 12 h with several intermediate grindings DSC, inductively coupled plasma emission spectroscopy, variable temperature X-ray powder diffraction and neutron powder diffraction were the characterization tools.	Bi ₁₄ CrO ₂₄ structure reported On cooling, undergoes phase transition from tetragonal to monoclinic form below room temp.
8	Kumada et al. [21]	Single crystals of Bi ₈ CrO ₁₅ were prepared by hydrothermal reaction using NaBiO ₃ .nH ₂ O and K ₂ CrO ₄ at 453 K for 4 days Single crystal XRD and TG-DTA were the characterization tools used	A new compound-Bi ₈ CrO ₁₅ (monoclinic) Decomposes at 1069 K to Bi ₁₄ CrO ₂₄ and an unknown phase (in air)

Table 4.2 (continued)

Sl. No.	Reference	Details of preparation and characterization	Salient features reported
9	Liu et al. [22]	Different molar ratios of Bi_2O_3 and Cr_2O_3 were heated in air at different temperatures (from 863 to 1264 K) for 48-72 h XRD and DTA were the characterization tools used	Considered $\text{Bi}_{38}\text{CrO}_{60}$ as γ -modification of Bi_2O_3 Reported $\text{Bi}_{14}\text{CrO}_{24}$ (tetragonal) as a solid solution with Bi/Cr: 13.3 to 6.1. When the starting composition had $14 < \text{Bi/Cr} < 6$, the authors found peak splitting which was attributed to solid solution formation and distortion of lattice $\text{Bi}_{10}\text{Cr}_2\text{O}_{21}$ based high temperature solid solution (orthorhombic) $\text{Bi}_6\text{Cr}_2\text{O}_{15}$ (orthorhombic) New compound- Bi_2CrO_6 (monoclinic)
10	Colmont et al. [23]	Stoichiometric amounts of Bi_2O_3 and Cr_2O_3 were heated in air at 773 K for 12h and 1073 K for 24h Single crystals were prepared by heating 3.1:1 mixture of Bi_2O_3 and Cr_2O_3 upto 1123 K in air and slow cooling of the melt at the rate of 5 K / h TGA, EDS, single crystal XRD, high temperature x-ray diffraction (HTXRD), magnetic measurements were the characterization tools.	A new compound- $\text{Bi}_{31}\text{Cr}_5\text{O}_{61.5}$ and its structural details reported (monoclinic) Cr oxidation state found to be +6.

Table 4.2 (continued)

Sl. No.	Reference	Details of preparation and characterization	Salient features reported
<i>Studies on Bi₂O₃-Cr₂O₃ pseudo binary system:</i>			
11	Sugawara et al. [24]	High pressure and high temperature synthesis of BiCrO ₃ (3.5-5.5 GPa, 973-1073 K). Characterized by XRD.	BiCrO ₃ (perovskite) Bi/Cr: 1 Decomposed at 673 K under ambient pressure Transforms from pseudo-triclinic to pseudo-monoclinic at 410 K
12	Niitaka et al. [25]	High pressure and high temperature synthesis (4GPa and 993 K). Characterized by synchrotron X-ray diffraction. Refined the structural parameters by Rietveld analysis. Carried out dielectric permittivity measurements and magnetic measurements.	BiCrO ₃ Transforms from monoclinic to orthorhombic at 440 K
13	Belik et al. [26]	High pressure and high temperature synthesis (6GPa and 1653 K). Determined the crystal and magnetic structures by the Rietveld method from neutron diffraction data.	BiCrO ₃ Transforms from monoclinic to orthorhombic at 420 K
14	Goujon et al. [27]	Synthesized BiCrO ₃ in a wide range of pressures (1 to 6GPa) and temperatures (963 to 1138 K) and optimized the conditions for the preparation Characterization tools used were XRD, DTA, SEM, TEM.	BiCrO ₃ Transforms from monoclinic to orthorhombic at 440 K Decomposed at 923 K under oxygen BiCrO ₃ stable upto 1123 K under argon and melted at 1313 K

*Later Liu et al. [22] proved that it is not actually BiCrO₃ and it is a mixture of Bi₆Cr₂O₁₅ and Cr₂O₃.

Masuno [14] reported the presence of two compounds with nominal compositions $\text{Bi}_{18}\text{CrO}_{30}$ (tetragonal phase) and $\text{Bi}_6\text{Cr}_2\text{O}_{15}$ (orthorhombic phase). They reported that the Bi to Cr ratio in the tetragonal phase varied between 14.87 and 17.86 and in the orthorhombic phase, it varied between 3 and 9.99. Masuno [14] also reported that all chromium ions in $\text{Bi}_{18}\text{CrO}_{30}$ were present in +6 oxidation state while in $\text{Bi}_6\text{Cr}_2\text{O}_{15}$, the fraction of the chromium ions present in +6 oxidation state was low. The author also reported the pseudo-binary phase diagram. Cudennec et al. [15] synthesized a new compound of composition $\text{Bi}_2\text{Cr}_4\text{O}_{15}$ from a saturated solution of CrO_3 and bismuth nitrate and characterized it by XRD and thermal analysis. Zhitomirskii et al. [16] studied the Bi_2O_3 - CrO_3 system and reported a new compound $\text{Bi}_{38}\text{CrO}_{60}$ with sillenite structure in addition to the two compounds reported by Masuno [14]. They prepared the single crystals of $\text{Bi}_{38}\text{CrO}_{60}$ by hydrothermal method. According to the authors, this compound is metastable under normal pressure and reported this as the reason for the earlier investigators not observing it when prepared by the usual solid state method. The authors refined the homogeneity regions of $\text{Bi}_{18}\text{CrO}_{30}$ and $\text{Bi}_6\text{Cr}_2\text{O}_{15}$ reported by Masuno [14]. Their studies showed the tetragonal $\text{Bi}_{18}\text{CrO}_{30}$ phase had Bi to Cr ratio varying between 11.99 and 17.87.

In fact, the authors used the composition $\text{Bi}_{16}\text{CrO}_{27}$ to represent the tetragonal phase instead of $\text{Bi}_{18}\text{CrO}_{30}$. They also reported the Bi to Cr ratio in $\text{Bi}_6\text{Cr}_2\text{O}_{15}$ ranged from 3 to 6.69. Later, based on single crystal X-ray studies, Warda et al. [17] reported the actual composition of the tetragonal phase to be $\text{Bi}_{14}\text{CrO}_{24}$. Based on powder X-ray investigations and from single crystal studies, they also reported the presence of a new compound with approximate composition $\text{Bi}_{10}\text{Cr}_2\text{O}_{21}$ in the composition range where Bi to Cr ratio varied between 3 and 6.69. However, they

couldn't elucidate its structure. Esmaeizadeh et al. [18] synthesized a new metastable solid solution, $Bi_{1-x}Cr_xO_{1.5+1.5x}$ with Bi to Cr ratio of 5.67 to 19. They prepared the solid solution by quenching Bi-Cr-O melts from high temperature (1123-1223 K) and carried out structural investigation using electron microscopy and X-ray diffraction. The oxidation state of chromium in this solid solution was determined to be +6. Grins et al. [19] prepared the compound $Bi_6Cr_2O_{15}$ by solid state reaction between Bi_2O_3 and Cr_2O_3 in air at 923 K and confirmed the structure of this compound as orthorhombic. Crumpton et al. [20] studied the structure of $Bi_{14}CrO_{24}$ and reported a phase transition from tetragonal to monoclinic form between 200 K and 275 K. Kumada et al. [21] prepared a new bismuth chromate - $Bi_8(CrO_4)O_{11}$ by hydrothermal method using $NaBiO_3 \cdot nH_2O$ and K_2CrO_4 at lower temperatures (453 K). The structure of this compound was investigated by single crystal XRD and its thermal stability was studied by thermal analysis. Results showed the compound to be decomposing to $Bi_{14}CrO_{24}$ and an unknown phase at 1069 K but the authors couldn't identify the unknown phase. Later Liu et al. [22] studied the system using XRD and DTA and reconstructed the phase diagram. The compounds reported by them are $Bi_{14}CrO_{24}$, $Bi_{10}Cr_2O_{21}$, $Bi_6Cr_2O_{15}$ and a new compound, Bi_2CrO_6 . They didn't report the compound, $Bi_{38}CrO_{60}$ and they considered it as the γ -modification of Bi_2O_3 . They reported that the compounds, $Bi_{14}CrO_{24}$ and $Bi_{10}Cr_2O_{21}$ had wide non-stoichiometry range and $Bi_{10}Cr_2O_{21}$ was stable only from 1003 K. The compound, Bi_2CrO_6 was prepared by equilibrating a mixture of Bi_2O_3 and Cr_2O_3 (33.3%) at 1063 K for 48 to 72 h in air followed by quenching it to room temperature. Liu et al. [22] also characterized the compounds, $Bi_{10}Cr_2O_{21}$ and Bi_2CrO_6 and reported their XRD patterns. They also reported that the compounds ' $Bi_6Cr_2O_{15}$ ' and ' $BiCrO_3$ ' reported by Masuno [14] were actually $Bi_{10}Cr_2O_{21}$ and a mixture of $Bi_6Cr_2O_{15}$ and Cr_2O_3 , respectively according to their XRD patterns. Colmont et al. [23] synthesized and

characterized a new compound $\text{Bi}_{31}\text{Cr}_5\text{O}_{61.5}$. They have also determined the oxidation state of Cr in this compound as +6 by thermogravimetric and magnetic measurements.

4.2.4 Studies on Bi_2O_3 - Cr_2O_3 pseudo-binary system

Studies on Bi_2O_3 - Cr_2O_3 system, has shown the existence of only one compound, namely BiCrO_3 . BiCrO_3 is reported as a high pressure compound in literature [24-32]. Although, Masuno [14] and Zhitomirskii et al. [16] reported the preparation of BiCrO_3 in air, later, Liu et al. [22] reported that the BiCrO_3 which Masuno [14] prepared was actually not BiCrO_3 and it was a mixture of $\text{Bi}_6\text{Cr}_2\text{O}_{15}$ and Cr_2O_3 according to their XRD patterns. BiCrO_3 has been a subject of interest as a multiferroic material since 1960s and many works have been carried out on the synthesis and structure of this compound [24-32]. For example, Sugawara et al. [24] synthesized BiCrO_3 by adopting a high temperature and high pressure synthesis method (3.5-5.5 GPa and 973-1073 K) and they showed it to be having perovskite structure. The authors observed that this high pressure phase decomposed on heating at 673 K at ambient pressure. Niitaka et al. [25] also prepared BiCrO_3 under similar conditions i.e., at 4 GPa and 993 K. Belik et al. [26] used higher pressure (6 GPa) and temperature (1653 K) for the preparation of BiCrO_3 . Goujon et al. [27] optimized the conditions for the preparation of BiCrO_3 and studied its thermal stability. Their studies showed it to be stable under inert gas but it decomposed under oxygen at 923 K. They determined the melting point of this compound using differential thermal analysis (DTA) as 1313 K under argon atmosphere.

It is to be pointed out that $\text{Bi}_{38}\text{CrO}_{60}$, $\text{Bi}_8\text{CrO}_{15}$ and $\text{Bi}_2\text{Cr}_4\text{O}_{15}$ were synthesized by hydrothermal methods at low temperatures while investigation of all other compounds was at high temperatures. Although $\text{Bi}_{14}\text{CrO}_{24}$ was reported to have a wide non-stoichiometry range by Liu et al. [22], later work by Colmont et al. [23] in

the relevant composition range showed the presence of another compound ($\text{Bi}_{31}\text{Cr}_5\text{O}_{61.5}$) in this composition range. This indicates the non-stoichiometry range of $\text{Bi}_{14}\text{CrO}_{24}$, if any, would not be very wide. $\text{Bi}_{10}\text{Cr}_2\text{O}_{21}$ is shown to be stable only above 1003 K and is also shown to have a wide composition range [22]. Though, the compound, $\text{Bi}_6\text{Cr}_2\text{O}_{15}$ was reported to have a wide non-stoichiometry range by Masuno [14] and Zhitomirskii et al. [16], later works by Liu et al. [22] and Colmont et al. [23] in the relevant composition range showed the presence of two compounds ie, $\text{Bi}_{10}\text{Cr}_2\text{O}_{21}$ and $\text{Bi}_{31}\text{Cr}_5\text{O}_{61.5}$ in this composition range. Liu et al. [22] and Grins et al. [19] reported it as a stoichiometric compound with Bi to Cr ratio equal to 3:1. Similarly, the compound, BiCrO_3 has been reported to be a high pressure compound in the literature [24-32] but the studies on the thermal stability of this compound by Goujon et al. [27] using DTA indicates it to be stable up to its melting temperature, 1313 K under argon atmosphere.

To summarize, nine ternary compounds have been reported so far in Bi-Cr-O system: eight in Bi_2O_3 - CrO_3 pseudo-binary line, viz., $\text{Bi}_{38}\text{CrO}_{60}$, $\text{Bi}_{14}\text{CrO}_{24}$, $\text{Bi}_8\text{CrO}_{15}$, $\text{Bi}_{31}\text{Cr}_5\text{O}_{61.5}$, $\text{Bi}_{10}\text{Cr}_2\text{O}_{21}$, $\text{Bi}_6\text{Cr}_2\text{O}_{15}$, Bi_2CrO_6 , and $\text{Bi}_2\text{Cr}_4\text{O}_{15}$ and one in Bi_2O_3 - Cr_2O_3 pseudo-binary line, viz., BiCrO_3 .

4.3 Experimental

4.3.1 Materials

Bi_2O_3 powder (99.99% purity on metals basis, M/s. Alfa Aesar, UK) and Cr_2O_3 powder (99.99% purity on metals basis, M/s. Alfa Aesar, UK) were used for the preparation of the ternary compounds. For phase equilibration studies, Cr powder (99.9+ % purity on metals basis, M/s. Alfa Aesar, UK) and Bi powder (99.5% purity on metals basis, M/s. Alfa Aesar, UK) along with ternary compounds were also used as the starting materials.

4.3.2 Preparation of ternary compounds

For preparing the eight ternary compounds reported in the Bi_2O_3 - CrO_3 pseudo-binary line, viz., $\text{Bi}_{38}\text{CrO}_{60}$, $\text{Bi}_{14}\text{CrO}_{24}$, $\text{Bi}_8\text{CrO}_{15}$, $\text{Bi}_{31}\text{Cr}_5\text{O}_{61.5}$, $\text{Bi}_{10}\text{Cr}_2\text{O}_{21}$, $\text{Bi}_6\text{Cr}_2\text{O}_{15}$, Bi_2CrO_6 and $\text{Bi}_2\text{Cr}_4\text{O}_{15}$, appropriate molar ratios of Bi_2O_3 and Cr_2O_3 were mixed and ground thoroughly. They were made into pellets and heated in platinum crucibles in air at different temperatures for 144 h with one intermittent grinding and pelletizing followed by heating at the same temperature. The experimental details are given in Table 4.3. Experiments were also made in an attempt to prepare BiCrO_3 , which was reported to be a high pressure compound, by heating 1:1 mole ratio of Bi_2O_3 and Cr_2O_3 in vacuum at 1023 K. The resulting products were characterised by XRD using X-ray powder diffractometer (M/s. Inel, France) with $\text{Cu K}\alpha$ radiation.

Table 4.3 Experimental details adopted for the preparation of the ternary compounds

Sample No.	Compound	Starting materials	Conditions of preparation	Products obtained based on XRD analysis
1	$\text{Bi}_{38}\text{CrO}_{60}$	$\text{Bi}_2\text{O}_3, \text{Cr}_2\text{O}_3$ (38:1)	1023 K, 144 h in air	Mixture of $\text{Bi}_{38}\text{CrO}_{60}$ and $\text{Bi}_{14}\text{CrO}_{24}$
2	$\text{Bi}_{14}\text{CrO}_{24}$	$\text{Bi}_2\text{O}_3, \text{Cr}_2\text{O}_3$ (14:1)	1023 K, 144 h in air	Matched with the JCPDS pattern 04-011-3851
3	$\text{Bi}_8\text{CrO}_{15}$	$\text{Bi}_2\text{O}_3, \text{Cr}_2\text{O}_3$ (8:1)	1023 K, 144 h in air	Mixture of $\text{Bi}_{14}\text{CrO}_{24}$ and $\text{Bi}_{31}\text{Cr}_5\text{O}_{61.5}$. XRD pattern of $\text{Bi}_{31}\text{Cr}_5\text{O}_{61.5}$ matched with the pattern reported in ref. [23].
4	$\text{Bi}_{31}\text{Cr}_5\text{O}_{61.5}$	$\text{Bi}_2\text{O}_3, \text{Cr}_2\text{O}_3$ (6.2:1)	1023 K, 144 h in air	Matched with the pattern for $\text{Bi}_{31}\text{Cr}_5\text{O}_{61.5}$.
5	$\text{Bi}_{10}\text{Cr}_2\text{O}_{21}$	$\text{Bi}_2\text{O}_3, \text{Cr}_2\text{O}_3$ (5:1)	1023 K, 144 h in air	Matched with pattern for $\text{Bi}_{10}\text{Cr}_2\text{O}_{21}$ reported in ref. [22]
6	$\text{Bi}_6\text{Cr}_2\text{O}_{15}$	$\text{Bi}_2\text{O}_3, \text{Cr}_2\text{O}_3$ (3:1)	1023 K, 144 h in air	Matched with the JCPDS pattern 04-010-4501
7	Bi_2CrO_6	$\text{Bi}_2\text{O}_3, \text{Cr}_2\text{O}_3$ (2:1)	1063 K, 144 h in air	Matched with the pattern reported in ref. [22]
8	$\text{Bi}_2\text{Cr}_4\text{O}_{15}$	$\text{Bi}_2\text{O}_3, \text{Cr}_2\text{O}_3$ (1:2)	1023 K, 144 h in air	Mixture of $\text{Bi}_6\text{Cr}_2\text{O}_{15}$ and Cr_2O_3
9	BiCrO_3	$\text{Bi}_2\text{O}_3, \text{Cr}_2\text{O}_3$ (1:1)	1023 K, 144 h in vacuum	Mixture of an unknown phase and Cr_2O_3

4.3.3. Phase equilibration studies

4.3.3.1 Equilibrations of mixtures of Bi_2O_3 and Cr_2O_3 in air

Equilibration of mixtures of Bi_2O_3 and Cr_2O_3 were carried out in air at 1023 K to unravel the existence of any new ternary compounds on the pseudo-binary line of Bi_2O_3 - CrO_3 other than those reported in the literature. For this, 12 compositions that fall between those of the ternary compounds in the pseudo-binary line of Bi_2O_3 - CrO_3

were chosen. Corresponding stoichiometric amounts of Bi_2O_3 and Cr_2O_3 were mixed thoroughly, made in the form of pellets, placed in platinum crucibles and equilibrated at 1023 K in air for 480 h with one intermittent grinding and pelletizing followed by heating at the same temperature. After equilibrations, the samples were quenched in ice cold water. The products obtained were characterized by XRD. Details of the equilibrations are given in Table 4.4.

Table 4.4 Results of equilibrations of mixtures of Bi_2O_3 and Cr_2O_3 in air

Sample No.	Molar ratios of Bi_2O_3 : Cr_2O_3	Phases observed after equilibration at 1023 K for 480 h in air*
1	22.6:1	' $\text{Bi}_{38}\text{CrO}_{60}$ ', $\text{Bi}_{14}\text{CrO}_{24}$
2	18.4:1	' $\text{Bi}_{38}\text{CrO}_{60}$ ', $\text{Bi}_{14}\text{CrO}_{24}$
3	17.9:1	' $\text{Bi}_{38}\text{CrO}_{60}$ ', $\text{Bi}_{14}\text{CrO}_{24}$
4	8.7:1	$\text{Bi}_{14}\text{CrO}_{24}$, $\text{Bi}_{31}\text{Cr}_5\text{O}_{61.5}$
5	5.5:1	$\text{Bi}_{31}\text{Cr}_5\text{O}_{61.5}$, $\text{Bi}_{10}\text{Cr}_2\text{O}_{21}$
6	3.8:1	$\text{Bi}_{10}\text{Cr}_2\text{O}_{21}$, $\text{Bi}_6\text{Cr}_2\text{O}_{15}$
7	1.67:1	Bi_2CrO_6 , Cr_2O_3
8	1.58:1	Bi_2CrO_6 , Cr_2O_3
9	1:1	Bi_2CrO_6 , Cr_2O_3
10	0.60:1	Bi_2CrO_6 , Cr_2O_3
11	0.33:1	Bi_2CrO_6 , Cr_2O_3
12	0.14:1	Bi_2CrO_6 , Cr_2O_3

* After 240 h, samples were ground, repelletized and equilibrated.

4.3.3.2. Equilibrations of mixtures of Bi_2O_3 and Cr_2O_3 in vacuum

Samples with compositions lying on Bi_2O_3 - Cr_2O_3 pseudo-binary system were also equilibrated to check the existence of any new ternary compound other than BiCrO_3 . Initially, three samples with Bi_2O_3 and Cr_2O_3 taken in molar ratios of 1:3, 1:1 and 3:1 were prepared by mixing the oxides thoroughly. They were made in the form of pellets, placed in alumina crucibles which were then vacuum sealed in quartz

ampoules and equilibrated at 773 K for a total period of 960 h with one intermediate grinding. Similar equilibrations were carried out at 1023 K for a total period of 480 h. After equilibration, samples were quenched in ice cold water and the products were characterized by XRD. Details of the equilibrations are given in Table 4.5.

Additional equilibrations were carried out with four samples having compositions close to 1:1 molar ratio of Bi_2O_3 and Cr_2O_3 at 1023 K in vacuum sealed quartz tubes as described earlier. The ratios employed were 1.9:1, 1.5:1, 1.2:1 and 1:1.5. The products obtained after equilibrations were characterized by XRD. Details of these equilibration studies are given in Table 4.5. Selected samples were characterized by SEM and EDS using XL 30, Philips, Netherlands.

Table.4.5 Results of equilibrations of mixtures of Bi_2O_3 and Cr_2O_3 in vacuum

Sample No.	Molar ratios of Bi_2O_3 and Cr_2O_3	Phases obtained after equilibration at 1023 K for 480 h*	Phases obtained after equilibration at 773 K for 960 h**
1	1:3	Cr_2O_3 , ' $\text{Bi}_{22}\text{Cr}_{18}\text{O}_{60}$ '	Bi_2O_3 , Cr_2O_3
2	1:1	Cr_2O_3 , ' $\text{Bi}_{22}\text{Cr}_{18}\text{O}_{60}$ '	Bi_2O_3 , Cr_2O_3
3	3:1	' $\text{Bi}_{38}\text{CrO}_{60}$ ', ' $\text{Bi}_{22}\text{Cr}_{18}\text{O}_{60}$ '	Bi_2O_3 , Cr_2O_3
4	1.9:1	' $\text{Bi}_{38}\text{CrO}_{60}$ ', ' $\text{Bi}_{22}\text{Cr}_{18}\text{O}_{60}$ '	--
5	1.5:1	' $\text{Bi}_{38}\text{CrO}_{60}$ ', ' $\text{Bi}_{22}\text{Cr}_{18}\text{O}_{60}$ '	--
6	1.2:1	' $\text{Bi}_{22}\text{Cr}_{18}\text{O}_{60}$ '	--
7	1:1.5	' $\text{Bi}_{22}\text{Cr}_{18}\text{O}_{60}$ ', Cr_2O_3	--

*Samples were ground, repelletized and equilibrated again after 240 h.

**Samples were ground, repelletized and equilibrated again after 480 h.

4.3.3.2.1 Characterization by Transmission Electron Microscopy (TEM)

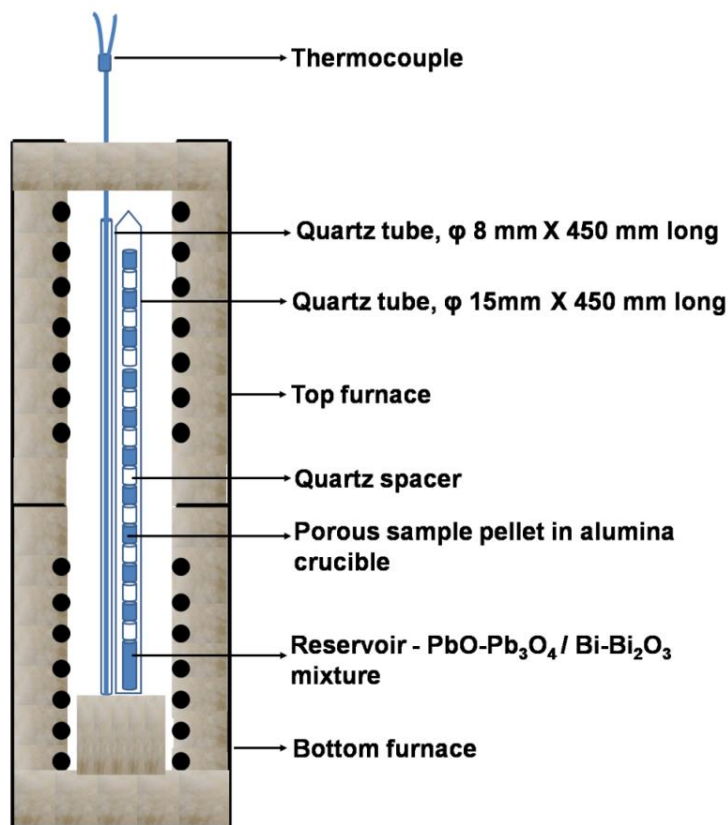
Sample with 1.2:1 molar ratio of Bi_2O_3 and Cr_2O_3 was characterized by transmission electron microscopy by direct imaging and diffraction. Electron transparent sample was prepared by thoroughly grinding the powder followed by

dispersing the ground powder in ethanol. The suspension was ultrasonicated for ~30 minutes and few drops of the solution were dropped onto an amorphous carbon coated copper grid. The grid was dried in air at room temperature for ~6 hours before it was inserted into the microscope. The powder was characterized by transmission electron microscope (Tecnai G2 F30) operated at 300 kV. The particles were systematically tilted through different major zone axes. Electron diffraction patterns and images were recorded at every major zone axes. The electron diffraction patterns were quantified by Digital Micrograph.

4.3.3.3. Pseudo-isopiestic equilibrations of samples under controlled oxygen partial pressures

Equilibrium oxygen pressures in the phase fields with the ternary compounds in the Bi_2O_3 - CrO_3 pseudo-binary as co-existing phases are anticipated to be high. Hence, two pseudo-isopiestic equilibrations under fixed oxygen partial pressures were carried out to identify the coexisting phases in the phase fields that exist above Bi_2O_3 - Cr_2O_3 pseudo-binary line. A schematic diagram of the experimental setup used for this equilibration is shown in Fig. 4.5. Samples containing a mixture of Bi_2O_3 and Cr_2O_3 in 1:1 mole ratio were prepared in the form of pellets. These pellets were taken in small alumina crucibles which were in turn stacked at different heights in a 45 cm long and one end closed 1.5 cm diameter quartz tube using quartz spacers. To maintain the fixed oxygen pressure over the samples, a mixture of PbO - Pb_3O_4 was used as the reservoir in the first experiment. In the second experiment, a mixture of Bi - Bi_2O_3 was used. PbO - Pb_3O_4 and Bi - Bi_2O_3 mixtures were also made in the form of porous pellets. These pellets were placed in alumina crucibles which in turn were kept at the bottom of the same quartz tube where the samples were placed. The quartz tube was then sealed under vacuum and placed in a two zone furnace which provided a

temperature gradient. When PbO-Pb₃O₄ mixture was used as the reservoir, the temperature of the furnace was adjusted in such a way that the reservoir is at 773 K and the samples were at temperatures above 773 K. When Bi-Bi₂O₃ mixture was used as reservoir, temperature of the furnace was adjusted so that the reservoir was at 1023 K and the samples were at temperatures below 1023 K. The sample pellets were maintained at fixed temperatures between 816 K and 1051 K. A K-type thermocouple which could move very slowly (0.38cm/min) from bottom to top of the furnace and closer to the quartz tube with the help of a motor was used to measure the temperatures of the samples. Maintaining the PbO-Pb₃O₄ mixture at 773 K prevails a fixed oxygen partial pressure over the samples by the following equilibrium: $\text{Pb}_3\text{O}_4(\text{s}) \rightleftharpoons 3\text{PbO}(\text{s}) + \frac{1}{2} \text{O}_2(\text{g})$. The equilibrium partial pressure at 773 K is 0.09 atm. The experiment with the Bi-Bi₂O₃ mixture is expected to maintain an oxygen partial pressure of $\sim 2 \times 10^{-10}$ atm over the samples. At such low pressures, molecular flow regime exists and hence P_{O_2} prevailing over the sample would vary with square root of the temperature of the sample [33]. However, this variation would be within the same order (i.e., 10^{-10} atm) only, since the temperature range of the samples was low (847 to 1014 K). In both experiments, the samples were equilibrated for 480 h, quenched in cold water and the products were characterized by XRD. Details of the experiments are given in Table 4.6.



Quartz spacers used are of different heights

Fig. 4.5 Schematic diagram of the pseudo-isopiestic equilibration setup in a gradient furnace

Table 4.6 Results of pseudo-isopiestic experiments

Sample temperature / K	Products obtained after equilibration with PbO-Pb ₃ O ₄ reservoir maintained at 773 K (i.e., $P_{O_2} = 0.09\text{atm}$)	Sample temperature / K	Products obtained after equilibration with Bi-Bi ₂ O ₃ reservoir maintained at 1023 K (i.e., $P_{O_2} \sim 10^{-10}\text{atm}$)
816	Bi ₆ Cr ₂ O ₁₅ , Cr ₂ O ₃	847	Bi ₂ O ₃ , Cr ₂ O ₃
874	Bi ₆ Cr ₂ O ₁₅ , Cr ₂ O ₃	859	Bi ₂ O ₃ , Cr ₂ O ₃
941	Bi ₆ Cr ₂ O ₁₅ , Cr ₂ O ₃	870	Bi ₂ O ₃ , Cr ₂ O ₃
992	Bi ₆ Cr ₂ O ₁₅ , Cr ₂ O ₃	880	Bi ₂ O ₃ , Cr ₂ O ₃
1028	Bi ₆ Cr ₂ O ₁₅ , Cr ₂ O ₃	891	Bi ₂ O ₃ , Cr ₂ O ₃
1051	Bi ₁₀ Cr ₂ O ₂₁ , Cr ₂ O ₃	956	'Bi ₂₂ Cr ₁₈ O ₆₀ ', Cr ₂ O ₃
1041	Bi ₁₀ Cr ₂ O ₂₁ , Cr ₂ O ₃	983	'Bi ₂₂ Cr ₁₈ O ₆₀ ', Cr ₂ O ₃
1028	Bi ₁₀ Cr ₂ O ₂₁ , Cr ₂ O ₃	1003	'Bi ₂₂ Cr ₁₈ O ₆₀ ', Cr ₂ O ₃
		1014	'Bi ₂₂ Cr ₁₈ O ₆₀ ', Cr ₂ O ₃

4.3.3.4. Additional equilibration studies

To establish the different phase fields in this ternary system, additional equilibrations were carried out by placing pellets of appropriate mixtures of oxides of bismuth and chromium and either chromium metal powder or the ternary compounds. These samples were equilibrated in a similar way as described in section 4.3.3.2. After equilibrations, the quartz ampoules were quenched in ice cold water and the products were characterized by XRD. The compositions chosen for equilibration at 773 and 1023 K are shown in Figs. 4.6 and 4.7, respectively.

In order to find the phases that co-exist with liquid Bi, samples of different compositions were equilibrated with excess liquid Bi. For this, molten Bi was taken in an alumina crucible and the sample in the form of a pellet was kept immersed in it by forcing it in with a thin alumina strip. Either two or three alumina crucibles were placed over the alumina strip so as to keep the pellet immersed in liquid Bi. The preparation of the sample was carried out in an argon atmosphere glove box which is used for handling liquid sodium. After cooling, the samples were taken out of the glove box and vacuum sealed in quartz ampoules. They were then equilibrated at 1023 K for 384 h. After equilibration, the ampoules were quenched in ice cold water and the pellets retrieved from liquid Bi were analyzed by XRD. The details of the equilibrations at 773 and 1023 K are given in Tables 4.7 and 4.8, respectively.

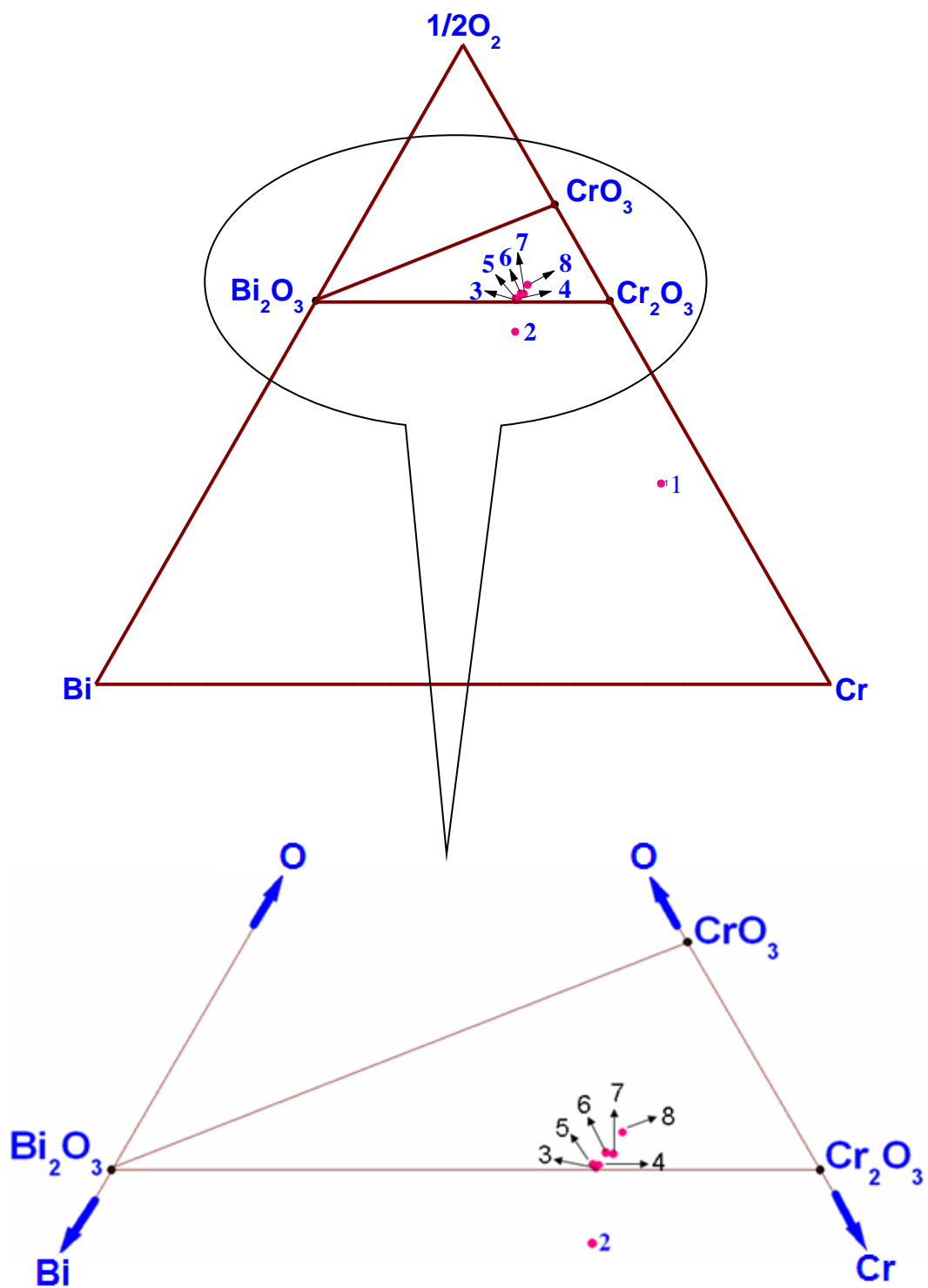


Fig. 4.6. Compositions chosen for equilibration at 773 K as given in Table 4.7

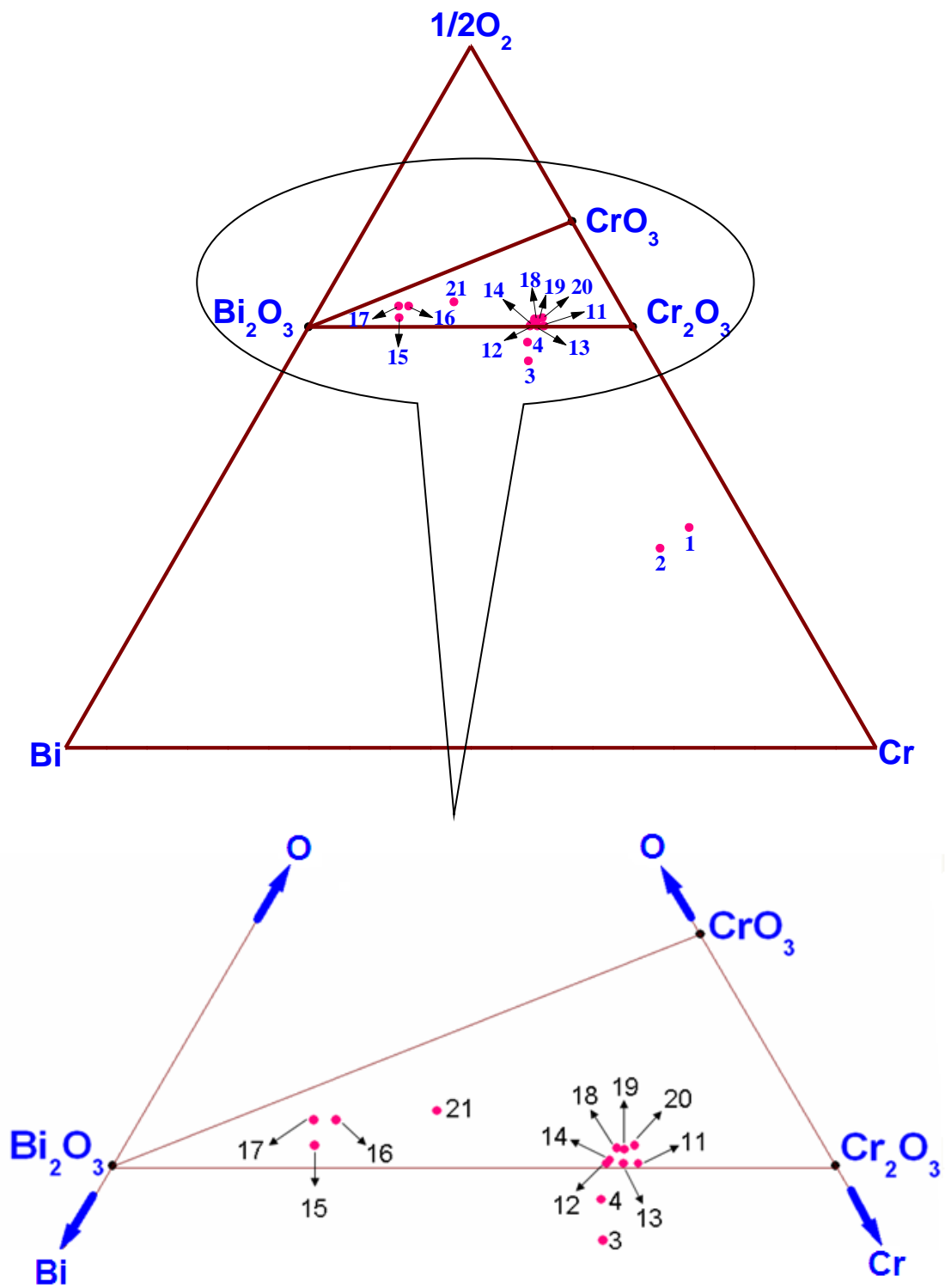


Fig. 4.7 Compositions chosen for equilibration at 1023 K as given in Table 4.8

Table 4.7 Results of the equilibration experiments carried out at 773 K

Sample No.	Phases taken before equilibration (mole ratio)	Phases after equilibration at 773 K for 960 h under vacuum*
1	Bi ₂ O ₃ , Cr, Cr ₂ O ₃ (1:12.99:1.85)	Bi, Cr, Cr ₂ O ₃
2	Bi ₂ O ₃ , Cr, Cr ₂ O ₃ (1:1.06:1.40)	Bi, Bi ₂ O ₃ , Cr ₂ O ₃
3	Bi ₂ O ₃ , Cr ₂ O ₃ , Bi ₁₄ CrO ₂₄ (1:2.61:0.03)	Bi ₂ O ₃ , 'Bi ₃₈ CrO ₆₀ ', Cr ₂ O ₃
4	Bi ₂ O ₃ , Cr ₂ O ₃ , Bi ₆ Cr ₂ O ₁₅ (1:2.45:0.04)	'Bi ₃₈ CrO ₆₀ ', Cr ₂ O ₃
5	Bi ₂ O ₃ , Cr ₂ O ₃ , Bi ₁₀ Cr ₂ O ₂₁ (1:2.74:0.06)	'Bi ₃₈ CrO ₆₀ ', Cr ₂ O ₃ , Bi ₁₄ CrO ₂₄
6	Bi ₂ O ₃ , Cr ₂ O ₃ , Bi ₆ Cr ₂ O ₁₅ (1:4.26:0.31)	Bi ₃₁ Cr ₅ O _{61.5} , Cr ₂ O ₃
7	Bi ₂ O ₃ , Cr ₂ O ₃ , Bi ₂ CrO ₆ (1:3.39:0.46)	Bi ₃₁ Cr ₅ O _{61.5} , Cr ₂ O ₃
8	Bi ₂ O ₃ , Cr ₂ O ₃ , Bi ₂ CrO ₆ (1:13.81:4.85)	Bi ₆ Cr ₂ O ₁₅ , Cr ₂ O ₃

*Samples were ground, repelletized and equilibrated again after 480 h.

Table 4.8 Results of the equilibration experiments carried out at 1023 K

Sample No.	Phases before equilibration (mole ratio)	Phases after equilibration at 1023 K
1	Bi ₂ O ₃ , Cr, Cr ₂ O ₃ (1:12.99:1.85) ^a	Bi, Cr, Cr ₂ O ₃
2	Bi, Cr, 'Bi ₂₂ Cr ₁₈ O ₆₀ ' (1:25.50:0.24) in excess Bi ^b	Bi, Cr, Cr ₂ O ₃
3	Bi ₂ O ₃ , Cr, Cr ₂ O ₃ (1:1.06:1.40) ^a	Bi, 'Bi ₂₂ Cr ₁₈ O ₆₀ ', Cr ₂ O ₃
4	Bi, Bi ₂ O ₃ , Cr ₂ O ₃ (1:1.43:3.84) in excess Bi ^b	Bi, 'Bi ₂₂ Cr ₁₈ O ₆₀ ', Cr ₂ O ₃
5	'Bi ₃₈ CrO ₆₀ '* in excess Bi ^b	Bi, 'Bi ₃₈ CrO ₆₀ ', 'Bi ₂₂ Cr ₁₈ O ₆₀ '
6	Bi ₃₁ Cr ₅ O _{61.5} in excess Bi ^b	Bi, 'Bi ₃₈ CrO ₆₀ ', 'Bi ₂₂ Cr ₁₈ O ₆₀ '
7	Bi ₁₀ Cr ₂ O ₂₁ in excess Bi ^b	Bi, 'Bi ₃₈ CrO ₆₀ ', 'Bi ₂₂ Cr ₁₈ O ₆₀ '
8	Bi ₆ Cr ₂ O ₁₅ in excess Bi ^b	Bi, 'Bi ₃₈ CrO ₆₀ ', 'Bi ₂₂ Cr ₁₈ O ₆₀ '
9	Bi ₂ CrO ₆ in excess Bi ^b	Bi, 'Bi ₃₈ CrO ₆₀ ', 'Bi ₂₂ Cr ₁₈ O ₆₀ '
10	'Bi ₂₂ Cr ₁₈ O ₆₀ ' in excess Bi ^b	Bi, 'Bi ₂₂ Cr ₁₈ O ₆₀ '
11	Bi ₂ O ₃ , Cr ₂ O ₃ , Bi ₁₄ CrO ₂₄ (1:3.30:0.03) ^a	'Bi ₃₈ CrO ₆₀ ', 'Bi ₂₂ Cr ₁₈ O ₆₀ ', Cr ₂ O ₃
12	Bi ₂ O ₃ , Cr ₂ O ₃ , Bi ₁₄ CrO ₂₄ (1:2.61:0.03) ^a	'Bi ₃₈ CrO ₆₀ ', 'Bi ₂₂ Cr ₁₈ O ₆₀ ', Cr ₂ O ₃
13	Bi ₂ O ₃ , Cr ₂ O ₃ , Bi ₆ Cr ₂ O ₁₅ (1:2.50:0.014) ^a	'Bi ₃₈ CrO ₆₀ ', 'Bi ₂₂ Cr ₁₈ O ₆₀ ', Cr ₂ O ₃
14	Bi ₂ O ₃ , Cr ₂ O ₃ , Bi ₆ Cr ₂ O ₁₅ (1:2.55:0.06) ^a	'Bi ₃₈ CrO ₆₀ ', Bi ₁₄ CrO ₂₄ , Cr ₂ O ₃
15	Bi ₂ O ₃ , Cr ₂ O ₃ , Bi ₁₀ Cr ₂ O ₂₁ (1:0.48:0.12) ^a	Bi ₁₄ CrO ₂₄ , Cr ₂ O ₃
16	Bi ₂ O ₃ , Cr ₂ O ₃ , Bi ₆ Cr ₂ O ₁₅ (1:0.52:0.44) ^a	Bi ₃₁ Cr ₅ O _{61.5} , Bi ₁₀ Cr ₂ O ₂₁ , Cr ₂ O ₃
17	Bi ₂ O ₃ , Cr ₂ O ₃ , Bi ₆ Cr ₂ O ₁₅ (1:0.38:0.39) ^a	Bi ₃₁ Cr ₅ O _{61.5} , Bi ₁₀ Cr ₂ O ₂₁ , Cr ₂ O ₃
18	Bi ₂ O ₃ , Cr ₂ O ₃ , Bi ₆ Cr ₂ O ₁₅ (1:4.26:0.31) ^a	Bi ₃₁ Cr ₅ O _{61.5} , Cr ₂ O ₃
19	Bi ₂ O ₃ , Cr ₂ O ₃ , Bi ₂ CrO ₆ (1:3.39:0.46) ^a	Bi ₃₁ Cr ₅ O _{61.5} , Cr ₂ O ₃
20	Bi ₂ O ₃ , Cr ₂ O ₃ , Bi ₂ CrO ₆ (1:4.22:0.70) ^a	Bi ₁₀ Cr ₂ O ₂₁ , Cr ₂ O ₃
21	Bi ₂ O ₃ , Cr ₂ O ₃ , Bi ₆ Cr ₂ O ₁₅ (1:3.98:2.29) ^a	Bi ₁₀ Cr ₂ O ₂₁ , Cr ₂ O ₃ , Bi ₆ Cr ₂ O ₁₅

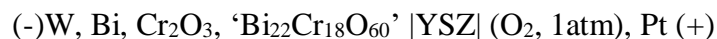
^a Equilibrated for 480 h, samples were ground, repelletized and equilibrated again after 240 h.

^b Equilibrated for 384 h, samples were ground, repelletized and equilibrated again after 192 h.

*'Bi₃₈CrO₆₀' contained small amount of Bi₁₄CrO₂₄ also.

4.3.4 Emf measurements

The following galvanic cell was constructed and used for determination of the Gibbs energy of formation ' $\text{Bi}_{22}\text{Cr}_{18}\text{O}_{60}$ ':



The schematic of the experimental assembly of the galvanic cell is shown in Fig. 3.9 of Chapter 3. One end closed yttria stabilized zirconia (YSZ) solid electrolyte tube having a flat bottom (13 mm OD, 9 mm ID and 300 mm long), supplied by M/s Nikkato Corporation, Japan was used for constructing the galvanic cell. Procedures for preparation of the reference electrode of the emf cell and the test of performance of the emf cell using gases with identical oxygen partial pressures on both sides were similar to those described in section 3.3.3 of Chapter 3. High purity oxygen gas was used as the reference.

Sample electrode was prepared by mixing Bi, Cr_2O_3 and ' $\text{Bi}_{22}\text{Cr}_{18}\text{O}_{60}$ ' powders in approximately equal volume ratios and by pelletizing it. Pellet had a diameter of 12.5 mm and thickness of 5 mm. The entire cell assembly was taken inside an argon atmosphere glove box. Appropriate quantity of Bi metal was melted in an alumina crucible and the sample pellet was then forcibly dipped in liquid bismuth by placing the solid electrolyte tube over it in such a way that the lower end of the tungsten electrical lead dipped in liquid Bi. The volume around the electrolyte tube inside the alumina crucible was filled with the powder of the phase field mixture. This is to ensure good contact between all the three phases and avoid segregation of the oxide phases from liquid Bi due to the large differences in their densities.

The experimental details for measurement of EMF and the procedure adopted to test the attainment of equilibrium were similar to those described in the study of Bi-Fe-O system in Chapter 3. The thermo emf due to dissimilar electrical leads viz., platinum and tungsten was measured separately (described in section 3.4.3.2 of Chapter 3) and was used for correcting the cell emf. Before and after completion of the emf measurements, the sample electrodes were analyzed by XRD.

4.4 Results and discussion

4.4.1 Preparation of ternary compounds

The XRD patterns of the compounds $\text{Bi}_{14}\text{CrO}_{24}$ and $\text{Bi}_6\text{Cr}_2\text{O}_{15}$ matched exactly with the JCPDS patterns 04-011-3851 and 04-010-4501, respectively while the patterns of $\text{Bi}_{10}\text{Cr}_2\text{O}_{21}$ and $\text{Bi}_{31}\text{Cr}_5\text{O}_{61.5}$ matched exactly with the patterns reported in references [22] and [23], respectively. Experiments to prepare $\text{Bi}_{38}\text{CrO}_{60}$ always ended up in a mixture of two phases i.e., $\text{Bi}_{38}\text{CrO}_{60}$ and the neighbouring compound $\text{Bi}_{14}\text{CrO}_{24}$. This could either be due to change from the starting composition by loss of Bi_2O_3 or because Bi to Cr ratio in $\text{Bi}_{38}\text{CrO}_{60}$ may not be exactly 38 but less than that. Later, equilibration studies in liquid Bi also showed the Bi to Cr ratio in $\text{Bi}_{38}\text{CrO}_{60}$ to be less than 38 (discussed in section 4.4.2.4). However, in the present study, the composition of this compound is assumed to be ' $\text{Bi}_{38}\text{CrO}_{60}$ '. XRD pattern of Bi_2CrO_6 matched exactly with the pattern reported by Liu et al. [22]. Attempts to prepare $\text{Bi}_8\text{CrO}_{15}$ yielded a mixture of $\text{Bi}_{14}\text{CrO}_{24}$ and $\text{Bi}_{31}\text{Cr}_5\text{O}_{61.5}$ whereas the experiments to prepare $\text{Bi}_2\text{Cr}_4\text{O}_{15}$ yielded a mixture of $\text{Bi}_6\text{Cr}_2\text{O}_{15}$ and Cr_2O_3 . As mentioned earlier, these compounds had been synthesized by hydrothermal methods at low temperatures [15, 21]. Our experiments show that these compounds are not stable at 1023 K. Goujon et al. prepared BiCrO_3 at high pressure and high

temperature and they reported it stable up to its melting point (1313 K) under argon atmosphere [27]. However, we couldn't prepare BiCrO_3 under vacuum. Our experiments to prepare BiCrO_3 resulted in the formation of a mixture of Cr_2O_3 and an unknown phase whose XRD pattern did not match with any of the compounds reported in Bi-Cr-O system in the literature. If the Bi to Cr ratio in any of the ternary compounds varies and has Cr in different oxidation states, non-stoichiometry in the compound would be wide. However, in the present work, the stoichiometry of the compounds falling on the Bi_2O_3 - CrO_3 pseudo-binary line and identified to be stable within the temperature range of 773 to 1023 K are assumed to be stoichiometric.

4.4.2. Phase equilibration results

4.4.2.1 Equilibrations of mixtures of Bi_2O_3 and Cr_2O_3 in air

The results of the equilibrations are given in Table 4.4. These data show the existence of only six compounds at 1023 K, namely ' $\text{Bi}_{38}\text{CrO}_{60}$ ', $\text{Bi}_{14}\text{CrO}_{24}$, $\text{Bi}_{31}\text{Cr}_5\text{O}_{61.5}$, $\text{Bi}_{10}\text{Cr}_2\text{O}_{21}$, $\text{Bi}_6\text{Cr}_2\text{O}_{15}$ and Bi_2CrO_6 . Even though the compound $\text{Bi}_{38}\text{CrO}_{60}$ was not included in the phase diagram reported by Liu et al. [22], results of our experiments show that $\text{Bi}_{38}\text{CrO}_{60}$ is a stable compound. Though the compounds, $\text{Bi}_8\text{CrO}_{15}$ and $\text{Bi}_2\text{Cr}_4\text{O}_{15}$ were reported to be present in Bi_2O_3 - CrO_3 pseudo-binary, the present experiments involving long term equilibrations show that they are not stable at 1023 K. Esmaeizadeh et al. [18] reported a metastable solid solution $\text{Bi}_{1-x}\text{Cr}_x\text{O}_{1.5+1.5x}$ with Bi to Cr ratio of 5.67, 9 and 19 in the temperature range of 1123 to 1223 K. Our equilibration studies show that this metastable solid solution is not present at 1023 K. Instead, the compounds $\text{Bi}_{10}\text{Cr}_2\text{O}_{21}$, $\text{Bi}_{31}\text{Cr}_5\text{O}_{61.5}$, $\text{Bi}_{14}\text{CrO}_{24}$ and $\text{Bi}_{38}\text{CrO}_{60}$ are present on the Bi_2O_3 - CrO_3 pseudo-binary line within Bi to Cr ratio of 5.67 to 19 at this temperature.

4.4.2.2. Equilibrations of mixtures of Bi_2O_3 and Cr_2O_3 in vacuum

Results of equilibration of samples with different molar ratios of Bi_2O_3 and Cr_2O_3 in vacuum are given in Table 4.5. XRD analysis of the samples equilibrated at 773 K show the coexistence of Bi_2O_3 and Cr_2O_3 . No ternary compound exists in the Bi_2O_3 - Cr_2O_3 pseudo-binary at this temperature. XRD pattern of the product after equilibration of 3:1 mixture of Bi_2O_3 : Cr_2O_3 at 1023 K showed the coexistence of ' $\text{Bi}_{38}\text{CrO}_{60}$ ' and a new phase. XRD analysis of the products obtained after equilibration of the samples with 1:1 and 1:3 mixtures of Bi_2O_3 : Cr_2O_3 at 1023 K under vacuum showed the coexistence of this new phase and Cr_2O_3 . The same unknown phase was obtained during the preparation of BiCrO_3 at 1023 K (discussed under section 4.3.2). The XRD pattern of the new phase did not match with that of any of the compounds reported in the Bi-Cr-O system.

Fig. 4.8 shows the XRD patterns of the products obtained after equilibrating the samples of Bi_2O_3 and Cr_2O_3 mixtures having molar ratios of 1.9:1, 1.5:1, 1.2:1 and 1:1.5 at 1023 K. Analysis of these patterns shows that the new phase is obtained as a single phase at 1.2:1 ratio of Bi_2O_3 and Cr_2O_3 . Further, this sample was analyzed by SEM-EDS (Fig. 4.9). EDS done on different regions of the sample revealed the composition of the sample was homogeneous throughout and the Bi to Cr ratio was nearly equal to 1.2:1. Hence the composition of the new phase is assumed as $1.2\text{Bi}_2\text{O}_3$: Cr_2O_3 i.e., ' $\text{Bi}_{22}\text{Cr}_{18}\text{O}_{60}$ '. XRD pattern of this new phase is shown in Fig. 4.10 and the peak positions and relative intensity of the lines in the pattern are given in Table 4.9.

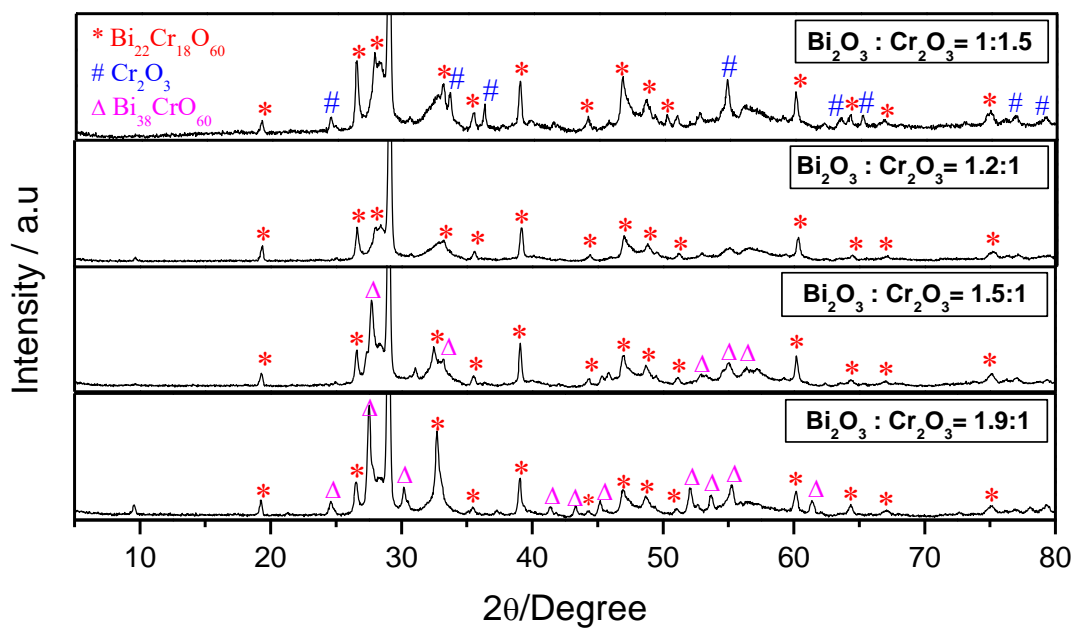


Fig. 4.8 XRD patterns of the samples of compositions with Bi₂O₃:Cr₂O₃ molar ratios of 1.9:1, 1.5:1, 1.2:1 and 1:1.5 after equilibration at 1023 K. Cu K_α λ = 1.54184 Å.

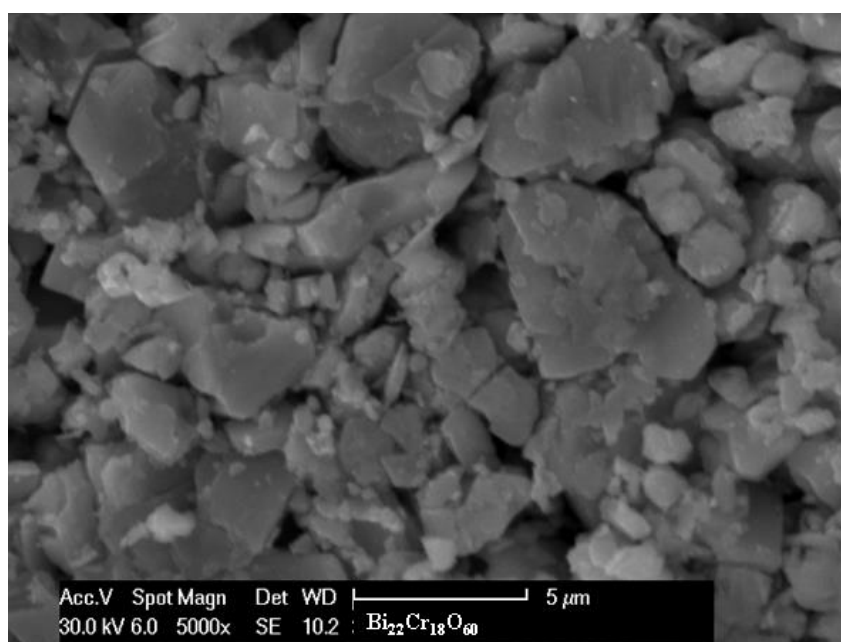


Fig. 4.9 SEM image of 'Bi₂₂Cr₁₈O₆₀'

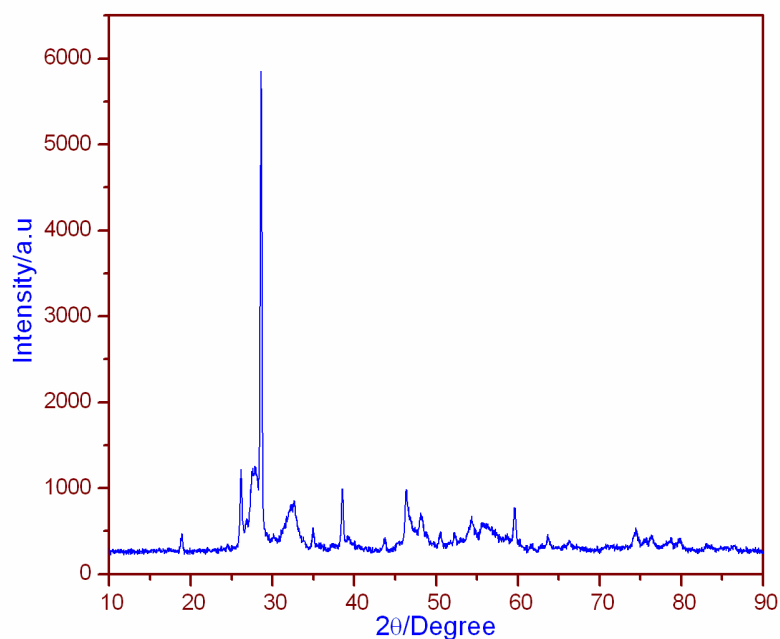


Fig. 4.10 XRD pattern of ‘Bi₂₂Cr₁₈O₆₀’; Cu K_α λ = 1.54184 Å

Table 4.9 Peak positions and relative intensity of the lines of the XRD pattern of ‘Bi₂₂Cr₁₈O₆₀’

2θ / Degree	Relative intensity / %	Experimental d-spacing / Å
19.20	4.0	4.6218
26.50	12.9	3.3635
28.35	11.0	3.1479
29.00	100.0	3.0788
33.00	7.8	2.7145
35.35	3.6	2.5393
39.00	11.2	2.3095
44.15	3.4	2.0514
46.80	9.7	1.9414
48.60	5.8	1.8734
50.95	4.6	1.7924
52.85	3.5	1.7324
54.55	5.8	1.6821
56.45	6.3	1.6302
60.10	9.4	1.5394
64.35	3.2	1.4477
66.70	3.2	1.4022
74.90	4.4	1.2665

Cu K_α λ = 1.54184 Å

4.4.2.2.1 TEM analysis

Low magnification and high resolution phase contrast image of the compound particle are given in Figs. 4.11 a and b. It is observed from the Fig. 4.11a that the particles are quite large and faceted. High resolution phase contrast images indicate that the particles are completely crystalline and regularly spaced lattice fringes could be observed. The spacing between the fringes as measured from the image stands out to be 0.25 nm. This indicates that it could be high lattice parameter phase. In the particle, linear or planar defects could not be observed. Sometimes, presence of a large number of defects in a regular fashion may modulate the actual lattice parameter which may manifest itself in X-ray diffraction pattern as a large lattice parameter phase. Vacancy ordered phase is a typical example of such type. This observation sometimes may extend misleading information. It is worth mentioning at this point that existence of quasiperiodicity was debated for quite some time because of this reason. However, in the present case, such type of high concentration of defects could not be observed which rules out the possibility of having an ambiguous X-ray diffraction pattern.

In order to understand the crystallography of this phase, electron diffraction was carried out from different zone axes. Kinematical diffraction condition was created by converging the electron beam and the Kikuchi pattern of the crystal. The crystal was tilted along the Kikuchi lines and the intersection of many Kikuchi lines was used to reach to the zone axis. The electron diffraction patterns are given in Figs. 4.12 a and c. The analysis of the patterns has been overlaid. In both the diffraction patterns a large number of spots with systematic variation of intensity could be observed. A careful look into the diffraction pattern in Fig. 4.12a and its analysis in 4.12b indicate that there is a basic hexagonal unit in the pattern with almost uniform distribution of intensity. It is a perfect hexagon with inter-arm angle as 60 degree and

length of each arm being the same. This definitely indicates that the crystal structure of this phase has a 3-fold rotational symmetry. This indicates that the structure belongs to either cubic or hexagonal or rhombohedral phase. This basic hexagonal unit extends in the two dimensional reciprocal space. On closer observation, it is found that in every seventh repetition of the smaller unit the diffraction spot becomes intense. The geometry and distribution of the intense spots are also perfectly hexagonal with inter-arm angle as 60 degrees and equal arm length. The arm length for the smaller unit is 0.25 nm and that of the larger unit is 1.75 nm which is exactly seven times of 0.25. This 0.25 nm spacing was observed in the high-resolution image also. The relationship and the modulation in intensity distribution definitely represent a case of commensurately modulated structure. There is a smaller unit and the smaller unit repeats itself after every seventh smaller unit. Each smaller unit is different in terms of chemistry and its defects, that is how modulation is built up. In this system, Cr can exist in different oxidation states, its presence in different oxidation states leads to point defect formation in order to maintain charge neutrality which in turn can alter the state of ordering in the lattice. A combined influence of some or all the above mentioned effects leads to commensurate modulation. However, the smaller unit, as well as the larger unit, could either be cubic or hexagonal as three-fold rotational axis of symmetry is common to both of them. It is worth mentioning at this point that rhombohedral lattice also has a three-fold rotational axis of symmetry. However, the rhombohedral lattice can be represented as a hexagonal lattice by simple axial transformation. So the discussion is being restricted to cubic or hexagonal system. The presence of four-fold symmetry proves beyond ambiguity that the phase is cubic. In this diffraction pattern, there is no direct evidence of four-fold symmetry.

In order to understand the crystallography better, the crystal was systematically tilted to another zone axis. The Diffraction pattern and its overlaid analysis are given in Figs. 4.12 c and d, respectively. In this diffraction pattern also the basic hexagonal unit is observed with 1.75 nm arm length and 60 degree inter-arm spacing. However, new twofold symmetry and distorted fourfold symmetry comes out. The angles and inter-arm spacings of the twofold symmetries as marked in the figure matches with cubic and four-fold symmetry are slightly distorted. This definitely proves that the smaller unit which is defect and chemically modulated has an underlying cubic symmetry. However, for the bigger unit no such evenly distorted fourfold symmetry could be observed.

It is imperative to say from the above analysis that there is a basic cubic unit which has undergone extensive defect and chemical modulation which has led to the manifestation of the pseudo-cubic symmetry. Because of the extensive defect and chemical modulation, the basic unit repeats itself after every seventh layer. That is why the large lattice parameter is observed. As no four-fold symmetry was observed in the large commensurately modulated crystal, it is concluded that the large commensurately modulated crystal is either hexagonal or rhombohedral. Such type of distortion from cubic to hexagonal or rhombohedral phase due to chemical and defect modulation has been observed before in bismuth containing ferrites and manganites, lithium containing nickel oxide etc. It is possible to model such distortions and find out lattice relationships. However, such type of modulation in Bi-Cr-O system in the vicinity of BiCrO_3 perovskite phase over such a large length scale has not been observed before. A more detailed structural investigation on this compound needs to be carried out to elucidate its structure.

Although characterization of the new phase by XRD and SEM-EDS showed that its composition is $\text{Bi}_{22}\text{Cr}_{18}\text{O}_{60}$, structural analysis of this phase by TEM indicates that Cr could be present in different oxidation states in this phase. This could lead to oxygen nonstoichiometry in it. However, in the absence of quantitative data for this non-stoichiometry, the composition of the new phase is assumed to be ' $\text{Bi}_{22}\text{Cr}_{18}\text{O}_{60}$ ' only.

4.4.2.3 Pseudo-isopiestic equilibrations of samples under controlled oxygen partial pressures

The results of the isopiestic equilibration experiments are given in Table 4.6. When equal molar ratios of Bi_2O_3 and Cr_2O_3 were equilibrated under an oxygen partial pressure of 0.09 atm, the products formed were $\text{Bi}_6\text{Cr}_2\text{O}_{15}$ and Cr_2O_3 at temperatures between 816 and 1028 K. This shows that these two phases coexist in this temperature range. At temperatures above 1028 K, $\text{Bi}_{10}\text{Cr}_2\text{O}_{21}$ and Cr_2O_3 were obtained indicating their coexistence. When the oxygen partial pressure was $\sim 10^{-10}$ atm, the ternary compound formed was ' $\text{Bi}_{22}\text{Cr}_{18}\text{O}_{60}$ ' along with Cr_2O_3 in the temperature range of 956 to 1014 K. In samples with temperatures in the range of 847 to 920 K, only Bi_2O_3 and Cr_2O_3 were present showing the coexistence of these two oxides in this temperature range. This is in agreement with the other equilibration experiments discussed in section 4.3.3.4. The data obtained from these equilibrations also show that ' $\text{Bi}_{22}\text{Cr}_{18}\text{O}_{60}$ ' would appear as a stable phase in liquid Bi at a temperature between 891 and 956 K.

4.4.2.4 Additional equilibration studies

The results of the equilibration of samples with compositions falling within the Bi_2O_3 - Cr_2O_3 - CrO_3 region and Bi_2O_3 -Cr- Cr_2O_3 region at 773 K and 1023 K are shown

in Tables 4.7 and 4.8, respectively. Results of the equilibrations of samples with excess of liquid Bi at 1023 K are also given in Table 4.8.

Equilibrations at 773 K show that the ternary compounds, $\text{Bi}_{10}\text{Cr}_2\text{O}_{21}$ and Bi_2CrO_6 are not stable at this temperature. This is in agreement with the results of Liu et al. [22]. Since Bi_2CrO_6 is not stable at 773 K, equilibration of sample 8 in Table 4.7 (initial composition lying in the area bound between $\text{Bi}_6\text{Cr}_2\text{O}_{15}$, Bi_2CrO_6 and Cr_2O_3) yielded products lying on $\text{Bi}_6\text{Cr}_2\text{O}_{15}$ - Cr_2O_3 line. Based on the results of all the equilibration studies, presence of the following phase fields and lines could be identified at 773 K: 1) Bi-Cr- Cr_2O_3 , 2) Bi- Bi_2O_3 - Cr_2O_3 , 3) Bi_2O_3 -‘ $\text{Bi}_{38}\text{CrO}_{60}$ ’- Cr_2O_3 , 4) ‘ $\text{Bi}_{38}\text{CrO}_{60}$ ’- Cr_2O_3 - $\text{Bi}_{14}\text{CrO}_{24}$, 5) ‘ $\text{Bi}_{38}\text{CrO}_{60}$ ’- Cr_2O_3 , 6) $\text{Bi}_{31}\text{Cr}_5\text{O}_{61.5}$ - Cr_2O_3 , 7) $\text{Bi}_6\text{Cr}_2\text{O}_{15}$ - Cr_2O_3 . From these results, the ternary phase diagram of Bi-Cr-O system at 773 K has been drawn and is shown in Fig. 4.13. The phase diagram at 773 K shows that on increasing the dissolved oxygen concentration in liquid bismuth in equilibrium with chromium, Cr_2O_3 would precipitate first as the coexisting phase. With further increase in oxygen concentration, Bi would co-exist with Cr_2O_3 and Bi_2O_3 . No ternary compounds would be stable in liquid Bi at 773 K.

Samples 5 to 9 in Table 4.8 which were equilibrated in liquid Bi at 1023 K show that only two ternary compounds i.e., ‘ $\text{Bi}_{22}\text{Cr}_{18}\text{O}_{60}$ ’ and ‘ $\text{Bi}_{38}\text{CrO}_{60}$ ’ can coexist with liquid Bi at this temperature and no other ternary compound would be stable in liquid Bi. ‘ $\text{Bi}_{38}\text{CrO}_{60}$ ’ (sample no. 5 in Table 4.8) after equilibration in liquid Bi yielded Bi, ‘ $\text{Bi}_{38}\text{CrO}_{60}$ ’ and ‘ $\text{Bi}_{22}\text{Cr}_{18}\text{O}_{60}$ ’. But according to the above equilibration experiments, ‘ $\text{Bi}_{22}\text{Cr}_{18}\text{O}_{60}$ ’ was not expected to form if the starting material, ‘ $\text{Bi}_{38}\text{CrO}_{60}$ ’ is single phase. Since ‘ $\text{Bi}_{38}\text{CrO}_{60}$ ’ contained small amount of $\text{Bi}_{14}\text{CrO}_{24}$, it decomposed in liquid Bi and gave ‘ $\text{Bi}_{22}\text{Cr}_{18}\text{O}_{60}$ ’. It is to be pointed out that the

equilibrations of samples 3, 4 and 5 in Table 4.5 discussed in section 4.3.3.2, yielded ‘Bi₃₈CrO₆₀’ and ‘Bi₂₂Cr₁₈O₆₀’ only where Bi was also expected to form according to the above equilibration studies. Since the amount of Bi expected to be formed for these compositions is very low, Bi might not have been detected during XRD analysis. The phase fields and lines identified at 1023 K are 1) Bi-Cr-Cr₂O₃, 2) Bi-‘Bi₂₂Cr₁₈O₆₀’-Cr₂O₃, 3) Bi-‘Bi₂₂Cr₁₈O₆₀’-‘Bi₃₈CrO₆₀’, 4) ‘Bi₃₈CrO₆₀’-‘Bi₂₂Cr₁₈O₆₀’-Cr₂O₃, 5) ‘Bi₃₈CrO₆₀’-Bi₁₄CrO₂₄-Cr₂O₃, 6) Bi₃₁Cr₅O_{61.5}-Bi₁₀Cr₂O₂₁-Cr₂O₃, 7) Bi₁₀Cr₂O₂₁-Cr₂O₃-Bi₆Cr₂O₁₅, 8) Bi₁₄CrO₂₄-Cr₂O₃, 9) Bi₃₁Cr₅O_{61.5}-Cr₂O₃, 10) Bi₁₀Cr₂O₂₁-Cr₂O₃.

Based on these results, the ternary phase diagram of Bi-Cr-O system at 1023 K has been drawn and shown in Fig. 4.14. Similar to the case at 773 K, on increasing the dissolved oxygen concentration at 1023 K, the first phase which would appear in liquid bismuth which is in equilibrium with chromium metal would be Cr₂O₃. With further increase in oxygen concentration, ‘Bi₂₂Cr₁₈O₆₀’ would appear as the ternary compound that would be stable in liquid bismuth. When the oxygen concentration increases further, ‘Bi₃₈CrO₆₀’ would appear (when Bi/Cr >1, in the system). Further increase of dissolved oxygen would lead to the disappearance of ‘Bi₂₂Cr₁₈O₆₀’ and appearance of Bi₂O₃.

It is to be pointed out that ‘Bi₂₂Cr₁₈O₆₀’ and ‘Bi₃₈CrO₆₀’ appear as equilibrium phases in liquid Bi at two distinct temperatures between 773 and 1023 K. These temperatures were deduced from the emf measurements using solid oxide electrolyte based emf cell (discussed in next section).

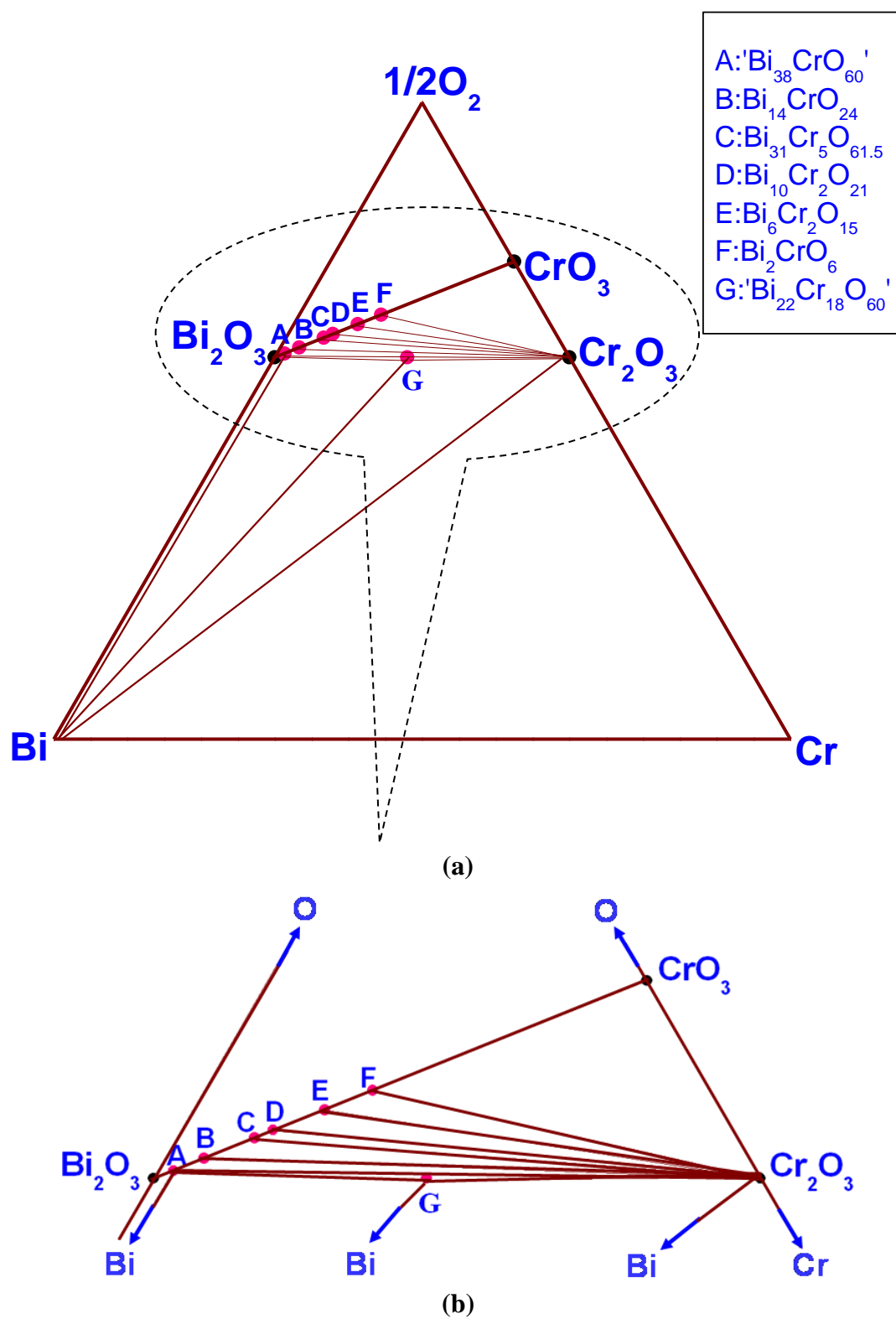


Fig. 4.14 (a) Ternary phase diagram of Bi-Cr-O system at 1023 K (b) enlarged portion of phase diagram

4.4.3. Oxygen potential measurements in liquid Bi

Based on the long term equilibrations, the existence of Bi-Cr₂O₃-‘Bi₂₂Cr₁₈O₆₀’ phase field has been confirmed at 1023 K. Hence, Gibbs energy of formation of ‘Bi₂₂Cr₁₈O₆₀’ can be determined by measuring the equilibrium oxygen potentials in the Bi-Cr₂O₃-‘Bi₂₂Cr₁₈O₆₀’ phase field and by incorporating the data on the Gibbs energy of formation of Cr₂O₃. Equilibrium oxygen potentials in this phase field were measured by employing solid oxide electrolyte based emf cell. A mixture of Bi, Cr₂O₃ and ‘Bi₂₂Cr₁₈O₆₀’ in the form of pellet was used as the sample electrode. Emf was measured in the temperature range of 764 to 1025 K. After the emf measurements, the cell was cooled from 1012 K (where ‘Bi₂₂Cr₁₈O₆₀’ coexists with liquid Bi) and the sample electrode was analyzed by XRD. XRD patterns of the samples before and after emf measurements confirmed the presence of Bi, Cr₂O₃ and ‘Bi₂₂Cr₁₈O₆₀’, as constituents before and after the experiment. The total duration of the emf measurement was approximately two months.

The emf values measured at various temperatures in chronological order are given in Table 4.10. From the emf values, equilibrium oxygen potentials were calculated as described in section 3.4.3.2 of Chapter 3 using eq. (3.6). These values are also given in Table 4.10 and the variation of oxygen potential as a function of temperature is shown in Fig. 4.15. For comparison, Bi-Bi₂O₃ oxygen potentials were also plotted as a function of temperature in the same Figure. It is seen that the oxygen potential versus temperature plot shows slope changes at two temperatures, one at 907 K and the other at 826 K. As discussed in earlier section, ‘Bi₂₂Cr₁₈O₆₀’ and ‘Bi₃₈CrO₆₀’ would appear as equilibrium phases at two distinct temperatures between 773 and 1023 K. Isopiestic experiments described in section 4.4.2.3 have indicated

that 'Bi₂₂Cr₁₈O₆₀' appears as thermodynamically stable phase at a temperature between 891 and 956 K and it is not stable below this temperature. Hence, the slope change at 907 K is attributed to the disappearance of 'Bi₂₂Cr₁₈O₆₀' on cooling (or appearance of Bi₂₂Cr₁₈O₆₀' on heating).

Table 4.10 Output of emf cell as a function of temperature

No.	Temperature (K)	Dwell time (h)	Emf (mV)	Equilibrium oxygen potential, $\overline{\Delta G}_{O_2}^{sple}$ @ (kJ mol ⁻¹)
1	763.7	42	620.7	-239.6
2	889.5	177	561.6	-216.7
3	885.2	197	564.2	-217.7
4	851.3	77	578.3	-223.2
5	833.1	11	585.1	-225.8
6	790.8	46	606.5	-234.1
7	870.2	75	570.0	-220.0
8	896.6	41	558.5	-215.5
9	929.2	45	545.8	-210.6
10	929.3	121	547.7	-211.4
11	801.6	90	601.1	-232.0
12	954.2	77	540.9	-208.8
13	974.2	41	535.5	-206.7
14	999.5	26	527.6	-203.6
15	1024.6	27	517.1	-199.6
16	1011.9	48	521.9	-201.4

$${}^{\circ} \overline{\Delta G}_{O_2}^{sple} = RT \ln p_{O_2}^{sple}$$

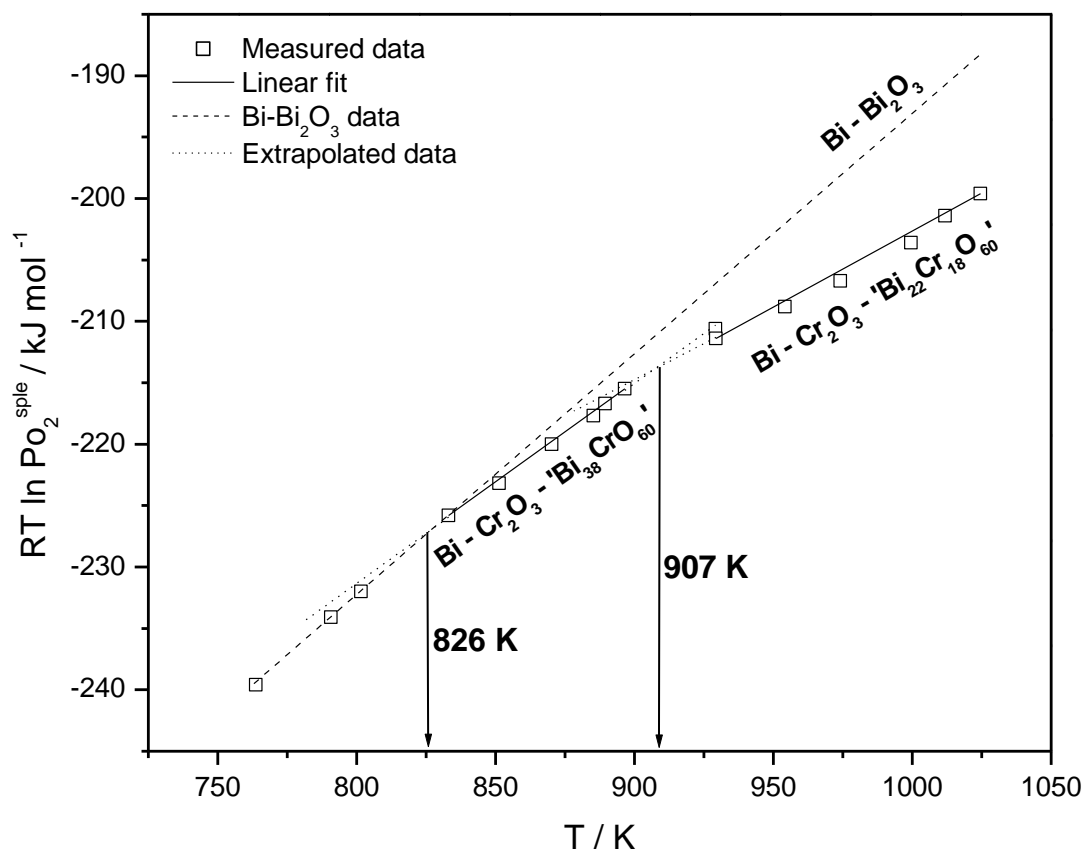


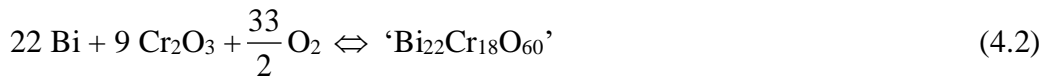
Fig. 4.15 Variation of measured oxygen potential with temperature

Based on the composition of the sample electrode taken in the cell, oxygen potentials measured at temperatures above 907 K can be attributed to those in Bi-Cr₂O₃-‘Bi₂₂Cr₁₈O₆₀’ phase field. The slope change in oxygen potentials at 826 K on cooling the system corresponds to the appearance of ‘Bi₃₈CrO₆₀’. The oxygen potentials between 826 and 907 K would correspond to the Bi-Cr₂O₃-‘Bi₃₈CrO₆₀’ phase field. At temperatures below 826 K, ‘Bi₃₈CrO₆₀’ would be thermodynamically unstable and decompose. The coexisting phases at temperatures below 826 K would be Bi-Cr₂O₃-Bi₂O₃ and measured oxygen potentials would correspond to that of Bi-Bi₂O₃ equilibrium. This is seen from Fig. 4.15 that oxygen potentials measured below 826 K agreed with the oxygen potentials of Bi-Bi₂O₃ couple.

The variation of emf with temperature in the temperature interval 929 to 1025 K can be described by the following least squares fitted expression:

$$E \pm 1.48 / \text{mV} = 830.6 - 0.3045 (T / \text{K}) \quad (T: 929 - 1025 \text{ K}) \quad (4.1)$$

The error given is the standard deviation of the least squares fitted line. The chemical equilibrium existing in this temperature range at the sample electrode can be represented as:



The Gibbs energy of formation of 'Bi₂₂Cr₁₈O₆₀' can be written as

$$\Delta_f G_m^o < \text{'Bi}_{22}\text{Cr}_{18}\text{O}_{60}\text{'}} > = 9 \Delta_f G_m^o < \text{Cr}_2\text{O}_3 > - 66 \text{FE} \quad (4.3)$$

By substituting the emf data given by eq. (4.1) and by using the value of $\Delta_f G_m^o$ of Cr₂O₃ from ref. [11], the standard molar Gibbs energy of formation of 'Bi₂₂Cr₁₈O₆₀' was calculated using eq. (4.3) and is given by:

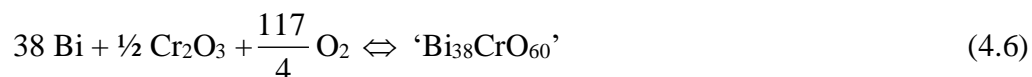
$$\Delta_f G_m^o < \text{'Bi}_{22}\text{Cr}_{18}\text{O}_{60}\text{'}} > \pm 9.8 \text{ kJ} = -15314.4 + 4.1864 (T / \text{K}) \quad (T: 929 - 1025 \text{ K}) \quad (4.4)$$

Data on $\Delta_f G_m^o$ of Cr₂O₃ reported by Holzheid and O'Neil [11] was used since it covered the temperature range of the present emf measurements.

Similarly, the variation of emf with temperature in the temperature interval 833 to 890 K can be described by the following least squares fitted expression:

$$E \pm 0.46 / \text{mV} = 934.8 - 0.4193 (T / \text{K}) \quad (T: 833 - 890 \text{ K}) \quad (4.5)$$

The error given is the standard deviation of the least squares fitted line. The chemical equilibrium existing in this temperature range at the sample electrode can be represented as:



The Gibbs energy of formation of 'Bi₃₈CrO₆₀' can be written as

$$\Delta_f G_m^o <\text{'Bi}_{38}\text{CrO}_{60}\text{'> = } \frac{1}{2} \Delta_f G_m^o <\text{Cr}_2\text{O}_3> - 117 \text{ FE}$$
 (4.7)

From the emf data given by eq. (4.5) and using the value of $\Delta_f G_m^o$ of Cr₂O₃ from ref. [11], the standard molar Gibbs energy of formation of 'Bi₃₈CrO₆₀' was calculated using eq. (4.7) and is given by:

$$\Delta_f G_m^o <\text{'Bi}_{38}\text{CrO}_{60}\text{'> } \pm 5.2 \text{ kJ} = -11109.7 + 4.8582 (\text{T} / \text{K}) \text{ (T: 833 - 890 K)} \text{ (4.8)}$$

Although both the compounds could incorporate oxygen non-stoichiometry, their Gibbs energy of formation was calculated by assuming their compositions as 'Bi₂₂Cr₁₈O₆₀' and 'Bi₃₈CrO₆₀'.

4.5 References

- 1) T.B. Massalski, H. Okamoto, Binary alloy phase diagram, 2nd Ed., ASM International, 1990.
- 2) W.B. White, R. Roy, The system chromium-oxygen at high oxygen pressures, Geochim. Cosmochim. Acta 39 (1975) 803-817.
- 3) N.Y. Toker, L.S. Darken, A. Muan, Equilibrium phase relations and thermodynamics of the Cr-O system in the temperature range of 1500°C to 1825°C, Metall. Trans. B 22 (2) (1991) 225-232.
- 4) J.N. Ramsey, D. Caplan, A.A. Burr, Thermodynamics of the oxidation of chromium, J. Electrochem. Soc. 103 (1956) 135-138.

- 5) Y. Jeannin, C. Mannerskantz, F.D. Richardson, Trans. Met. Soc. AIME 227 (1963) 300, as cited in ref. 9.
- 6) J.D. Tretjakow, H. Schmalzried: B. Bunsengesellschaft, Phys. Chem., 69 (1965) 396 - 402, as cited in ref. 7.
- 7) A. Pugliese, G.R. Fitterer, Activities and phase boundaries in the Cr-Ni system using a solid electrolyte technique, Metall. Trans. 1 (1970) 1997-2002.
- 8) H. Davies, W.W. Smeltzer, Oxygen and metal activities of the chromium–nickel–oxygen system between 900° and 1100°C, J. Electrochem. Soc.: Solid State Sci. Technol. 121 (1974) 543-549.
- 9) F.N. Mazandarany, R.D. Pehlke, Standard free energy of formation of Cr₂O₃ J. Electrochem. Soc.: Solid State Sci. Technol. 121 (1974) 711-714.
- 10) K.T. Jacob, Potentiometric determination of the Gibbs free energy of formation of cadmium and magnesium chromites, J. Electrochem. Soc. 124 (1977) 1827-1831.
- 11) A. Holzheid, H. St.C. O'Neill, The Cr – Cr₂O₃ oxygen buffer and the free energy of formation of Cr₂O₃ from high–temperature electrochemical measurements, Geochim. Cosmochim. Acta 59 (1995) 475-479.
- 12) S.E. Ziemniak, L.M. Anovitz, R.A. Castelli, W.D. Porter, J. Chem. Thermodyn. 39 (2007) 1474-1492.
- 13) M. Venkatraman, J.P. Neumann, The Bi-Cr (bismuth- chromium) system, Bull. Alloy Phase Diagr. 9 (1988) 271-273.

- 14) K. Masuno, Crystal chemical investigation of bismuth (III) oxide–chromium (III) oxide system, J. Chem. Soc. Jpn. 90 (1969) 1122-1127.
- 15) Y. Cudennec, A. Lecerf, A. Riou, Y. Gerault, Synthesis and study of three new chromates dichromates of bismuth: $\text{Bi}_2(\text{CrO}_4)_2\text{Cr}_2\text{O}_7$, $\text{MBiCrO}_4\text{Cr}_2\text{O}_7 \cdot \text{H}_2\text{O}$ ($\text{M} = \text{K}^+, \text{NH}_4^+$), C.R. Acad. Sc. Paris 293 (1981) 369-371.
- 16) D. Zhitomirskii, S.V. Fedotov, N.E. Skorokodv, A.A. Bush, A.A. Marin, Y.N. Benevtsev, Synthesis and properties of phases in the Bi_2O_3 - Cr_2O_3 system, Russ. J. Inorg. Chem. 28 (1983) 570-573.
- 17) S.A. Warda, W. Pietzuch, W. Massa, U. Kesper, D. Reinen, Colour and constitution of Cr^{VI} - doped Bi_2O_3 phases: The structure of $\text{Bi}_{14}\text{CrO}_{24}$, J. Solid State Chem. 149 (2000) 209-217.
- 18) S. Esmailzadeh, S. Lundgren, U. Halenius, J. Grins, $\text{Bi}_{1-x}\text{Cr}_x\text{O}_{1.5+1.5x}$, $0.05 \leq x \leq 0.15$: A New high-temperature solid solution with a three-dimensional incommensurate modulation, J. Solid State Chem. 156 (2001) 168-180.
- 19) J. Grins, S. Esmailzadeh, S. Hull, Structure and ionic conductivity of $\text{Bi}_6\text{Cr}_2\text{O}_{15}$, a new structure type containing $(\text{Bi}_{12}\text{O}_{14})_n^{8n+}$ columns and CrO_4^{2-} tetrahedra, J. Solid State Chem. 163 (2002) 144-150.
- 20) T.E. Crumpton, M.G. Francesconi, C. Greaves, The structural chemistry of $\text{Bi}_{14}\text{MO}_{24}$ ($\text{M} = \text{Cr}, \text{Mo}, \text{W}$) phases: bismuth oxides containing discrete MO_4 tetrahedra, J. Solid State Chem. 175 (2003) 197-206.
- 21) N. Kumada, T. Takei, N. Kinomura, G. Wallez, Preparation and crystal structure of a new bismuth chromate: $\text{Bi}_8(\text{CrO}_4)\text{O}_{11}$, J. Solid State Chem. 179 (2006) 793-799.

- 22) Y.H. Liu, J.B. Li, J.K. Liang, J. Luo, L.N. Ji, J.Y. Zhang, G.H. Rao, Phase diagram of the $\text{Bi}_2\text{O}_3\text{-Cr}_2\text{O}_3$ system, *Mater. Chem. Phys.* 112 (2008) 239-243.
- 23) M. Colmont, M. Drache, P. Roussel, Synthesis and characterization of $\text{Bi}_{31}\text{Cr}_5\text{O}_{61.5}$, a new bismuth chromium oxide, potential mixed-ionic-electronic conductor for solid oxide fuel cells, *J. Power Sources* 195 (2010) 7207-7212.
- 24) F. Sugawara, S. Iida, Y. Syono, S. Akimoto, Magnetic properties and crystal distortions of BiMnO_3 and BiCrO_3 , *J. Phys. Soc. Jpn.* 25 (1968) 1553-1557.
- 25) S. Niitaka, M. Azuma, M. Takano, E. Nishibori, M. Takata, M. Sakata, Crystal structure and dielectric and magnetic properties of BiCrO_3 as a ferroelectromagnet, *Solid State Ionics* 172 (2004) 557-559.
- 26) A.A. Belik, S. Iikubo, K. Kodama, N. Igawa, S. Shamoto, E.T. Muromachi, Neutron powder diffraction study on the crystal and magnetic structures of BiCrO_3 , *Chem. Mater.* 20 (2008) 3765-3769.
- 27) C. Goujon, C. Darie, M. Bacia, H. Klein, L. Ortega, P. Bordet, High pressure synthesis of BiCrO_3 , a candidate for multiferroism, *J. Phys.: Conf. Ser.* 121 (2008) 022009 1-6.
- 28) C. Darie, C. Goujon, M. Bacia, H. Klein, P. Toulemonde, P. Bordet, E. Suard, Magnetic and crystal structures of BiCrO_3 , *Solid-State Sci.* 12 (2010) 660-664.
- 29) C. Himcinschi, I. Vrejoiu, T. Weißbach, K. Vijayanandhini, A. Talkenberger, C. Roder, S. Bahmann, D.R.T. Zahn, A.A. Belik, D. Rafaja, J.

- Kortus, Raman spectra and dielectric function of BiCrO₃: Experimental and first principles studies, J. Appl. Phys. 110 (2011) 073501-1-8.
- 30) A. David, Ph. Boullay, R.V.K. Mangalam, N. Barrier, W. Prellier, Microstructure of epitaxial strained BiCrO₃ thin films, Appl. Phys. Lett. 96 (2010) 221904-1-3.
- 31) V. Kannan, M. Arredondo, F. Johann, D. Hesse, C. Labrugere, M. Maglione, I. Vrejoiu, Thickness dependent microstructural modifications of BiCrO₃ epitaxial thin films, Thin Solid Films 545 (2013) 130-139.
- 32) J. Ding, L. Wen, X. Kang, H. Li, J. Zhang, Polar and nonpolar structures of BiCrO₃ from first principles calculations, Comput. Mater. Sci. 96 (2015) 219-222.
- 33) H. Ipser, R. Krachler, K.L. Komarek, The isopiestic method and its application to a thermodynamic study of the Au-Zn system, in: H. Brodowsky, H.-J. Schaller (Eds.), Thermochemistry of Alloys, Kluwer Academic Publishers, Dordrecht, 1989, 293-306.

Chapter 5

SUMMARY AND CONCLUSIONS

The results reported in the thesis can be summarized as follows:

1) Ternary phase diagram of Bi-Fe-O system has been established by phase equilibration studies at 773 and 1023 K. Phase fields in the section bound by Bi, Fe and $\text{Bi}_2\text{Fe}_4\text{O}_9$ have been determined in the temperature range of 773 to 1023 K. Phase fields identified in the temperature range of 773 to 853 K are: (1) Bi-Fe- Fe_3O_4 , (2) Bi- Fe_3O_4 - Fe_2O_3 and (3) Bi- Fe_2O_3 - $\text{Bi}_2\text{Fe}_4\text{O}_9$. Phase fields identified in the temperature range of 853 to 1023 K are: (1) Bi-Fe-FeO, (2) Bi-FeO- Fe_3O_4 , (3) Bi- Fe_3O_4 - Fe_2O_3 and (4) Bi- Fe_2O_3 - $\text{Bi}_2\text{Fe}_4\text{O}_9$.

Experiments were also carried out to establish the phase fields in the composition region bound by Bi, $\text{Bi}_2\text{Fe}_4\text{O}_9$ and Bi_2O_3 . Results of these equilibrations clearly showed the existence of the phase field, Bi- $\text{Bi}_{25}\text{FeO}_{39}$ - Bi_2O_3 in the temperature range 773 to 1023 K. In order to determine the temperature range over which BiFeO_3 is stable, experiments were carried out by equilibrating BiFeO_3 at different temperatures and by equilibrating phase mixtures containing BiFeO_3 in liquid Bi. The results of these experiments showed that BiFeO_3 is metastable at low temperatures and becomes thermodynamically stable only around 940 K. Based on these results, the partial phase diagrams of Bi-Fe-O system valid at 773 and 1023 K have been constructed. The phase diagrams show that on increasing the dissolved oxygen concentration in liquid bismuth in equilibrium with iron metal, iron oxides would precipitate first as the coexisting phases. With further increase in oxygen

concentration, $\text{Bi}_2\text{Fe}_4\text{O}_9$ would appear as the first ternary compound stable in liquid bismuth.

Standard molar Gibbs energy of formation of $\text{Bi}_2\text{Fe}_4\text{O}_9$ was determined by measuring equilibrium oxygen partial pressures in $\text{Bi-Fe}_2\text{O}_3\text{-Bi}_2\text{Fe}_4\text{O}_9$ phase field using solid oxide electrolyte based emf cell and is given below:

$$\Delta_f G_m^\circ <\text{Bi}_2\text{Fe}_4\text{O}_9> \pm 0.6 \text{ kJ} = -2196.2 + 0.7679 (T / \text{K}) \quad (T : 799\text{-}1023 \text{ K}) \quad (5.1)$$

The heat capacities of $\text{Bi}_{25}\text{FeO}_{39}$ and $\text{Bi}_2\text{Fe}_4\text{O}_9$ measured by differential scanning calorimetry are given below:

$$C_p <\text{Bi}_{25}\text{FeO}_{39}> (\text{J K}^{-1} \text{ mol}^{-1}) \pm 49.9 = 1529.9 + 200.6 \times 10^{-3} T - 21.6 \times 10^6 T^{-2} \\ (T / \text{K}: 308\text{-}818) \quad (5.2)$$

$$C_p <\text{Bi}_2\text{Fe}_4\text{O}_9> (\text{J K}^{-1} \text{ mol}^{-1}) \pm 11.0 = 395.5 - 23.0 \times 10^{-3} T - 7.6 \times 10^6 T^{-2} \\ (T / \text{K}: 313\text{-}773) \quad (5.3)$$

Deviation of measured C_p values from the estimates by the Neumann-Kopp Rule (NKR) has been analyzed.

The standard molar enthalpies of formation, $\Delta_f H_{m298 \text{ K}}^\circ$ of $\text{Bi}_{25}\text{FeO}_{39}$ and $\text{Bi}_2\text{Fe}_4\text{O}_9$ were also determined using an isoperibol calorimeter. The enthalpies of solution of pure compounds, viz., $\text{Bi}_{25}\text{FeO}_{39}$ and $\text{Bi}_2\text{Fe}_4\text{O}_9$ as well as the starting materials, viz., Bi_2O_3 and Fe_2O_3 in HCl (8.38 mol kg^{-1}) at 298.15 K were measured. By using the values of the standard molar enthalpies of formation of Bi_2O_3 and Fe_2O_3 from ref. [1], the standard molar enthalpies of formation of $\text{Bi}_{25}\text{FeO}_{39}$ and $\text{Bi}_2\text{Fe}_4\text{O}_9$ were determined as $-7540.7 \pm 256.7 \text{ kJ}$ and $-2170.8 \pm 28.6 \text{ kJ}$, respectively.

The internal consistency of the experimentally determined thermochemical properties viz., Gibbs energy, enthalpy of formation and heat capacity was also evaluated. The experimental data are consistent within the experimental uncertainty.

2) Ternary phase diagram of Bi-Cr-O system has been established by phase equilibration studies at 773 and 1023 K. The existence of a new compound of composition, 'Bi₂₂Cr₁₈O₆₀' in this system was identified. This compound has been characterized by XRD, SEM and TEM. Presence of the following phase fields and lines were identified at 773 K: 1) Bi-Cr-Cr₂O₃, 2) Bi-Bi₂O₃-Cr₂O₃, 3) Bi₂O₃- 'Bi₃₈CrO₆₀'-Cr₂O₃, 4) 'Bi₃₈CrO₆₀'-Cr₂O₃-Bi₁₄CrO₂₄, 5) 'Bi₃₈CrO₆₀'-Cr₂O₃, 6) Bi₃₁Cr₅O_{61.5}-Cr₂O₃, 7) Bi₆Cr₂O₁₅-Cr₂O₃. The phase fields and lines identified at 1023 K are 1) Bi-Cr-Cr₂O₃, 2) Bi-'Bi₂₂Cr₁₈O₆₀'-Cr₂O₃, 3) Bi-'Bi₂₂Cr₁₈O₆₀'-'Bi₃₈CrO₆₀', 4) 'Bi₃₈CrO₆₀'-'Bi₂₂Cr₁₈O₆₀'-Cr₂O₃, 5) 'Bi₃₈CrO₆₀'-Bi₁₄CrO₂₄-Cr₂O₃, 6) Bi₃₁Cr₅O_{61.5}-Bi₁₀Cr₂O₂₁-Cr₂O₃, 7) Bi₁₀Cr₂O₂₁-Cr₂O₃-Bi₆Cr₂O₁₅, 8) Bi₁₄CrO₂₄-Cr₂O₃, 9) Bi₃₁Cr₅O_{61.5}-Cr₂O₃, 10) Bi₁₀Cr₂O₂₁-Cr₂O₃.

Pseudo-isopiestic equilibrations carried out under different oxygen partial pressures revealed that 'Bi₂₂Cr₁₈O₆₀' appear as a stable phase in liquid Bi at a temperature between 891 and 956 K. Oxygen potential measurements carried out in the Bi-Cr₂O₃- 'Bi₂₂Cr₁₈O₆₀' phase field by employing solid oxide electrolyte based emf cell delineated the temperature of formation of 'Bi₂₂Cr₁₈O₆₀' and 'Bi₃₈CrO₆₀' to be 907 and 826 K, respectively. From the measured oxygen potentials, the Gibbs energies of formation of 'Bi₂₂Cr₁₈O₆₀' and 'Bi₃₈CrO₆₀' have been determined and are given below:

$$\Delta_f G_m^o < \text{'Bi}_{22}\text{Cr}_{18}\text{O}_{60}\text{'>} \pm 9.8 \text{ kJ} = -15314.4 + 4.1864 (T / \text{K})$$

$$(T: 929 - 1025 \text{ K}) \quad (5.4)$$

$$\Delta_f G_m^o < \text{'Bi}_{38}\text{CrO}_{60}\text{'>} \pm 5.2 \text{ kJ} = -11109.7 + 4.8582 (T / \text{K})$$

$$(T: 833 - 890 \text{ K}) \quad (5.5)$$

The phase diagram at 773 K shows that on increasing the dissolved oxygen concentration in liquid bismuth in equilibrium with chromium, Cr_2O_3 would precipitate first as the coexisting phase. With further increase in oxygen concentration, Bi would co-exist with Cr_2O_3 and Bi_2O_3 . No ternary compounds would be stable in liquid Bi at 773 K. Similar to the case at 773 K, on increasing the dissolved oxygen concentration at 1023 K, the first phase which would appear in liquid bismuth which is in equilibrium with chromium metal would be Cr_2O_3 . With further increase in oxygen concentration, ' $\text{Bi}_{22}\text{Cr}_{18}\text{O}_{60}$ ' would appear as the ternary compound that would be stable in liquid bismuth. When the oxygen concentration increases further, ' $\text{Bi}_{38}\text{CrO}_{60}$ ' would appear (when $\text{Bi/Cr} > 1$, in the system). Further increase of dissolved oxygen would lead to disappearance of ' $\text{Bi}_{22}\text{Cr}_{18}\text{O}_{60}$ ' and appearance of Bi_2O_3 .

5.1 Prediction of the nature of passive oxide layer on steel-liquid Bi interface

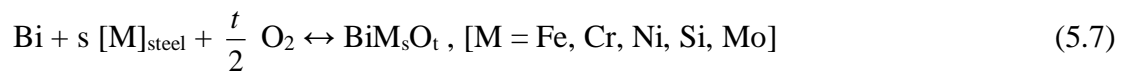
Based on the results of this thesis work on Bi-Fe-O and Bi-Cr-O systems and the data on solubility of oxygen in liquid bismuth, the oxide layer that can form at the steel-liquid Bi interface can be predicted. The threshold concentration of the oxygen in the molten bismuth above which a ternary compound appears in the liquid metal system is determined by the thermodynamic stability of the compound, chemical activity of the alloying elements of the structural material and the activity and solubility of oxygen in the coolant. Sahu et al. [2-4] carried out a detailed study on Pb-Fe-O and Pb-Cr-O systems and predicted the nature of the passive oxide layer

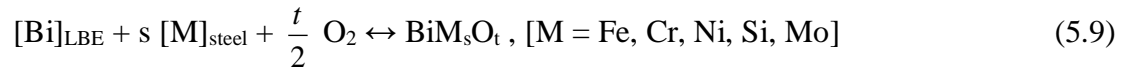
formed on steel–liquid Pb interface. Using the data reported in this work and the data reported by Sahu et al., the nature of the passive oxide layer formed on the steel–LBE interface also can be predicted.

To understand the nature of the ternary compound formed on Bi-stainless steel system, equilibrium oxygen potentials of various equilibria that would exist in this system were computed. The following conclusions (mentioned earlier) from the present work were taken into account for this computation:

- (a) At low levels of dissolved oxygen, iron oxides only would coexist with liquid bismuth in equilibrium with iron metal. Ternary compounds appear only at high oxygen concentrations.
- (b) At 773 K, no bismuth chromates would coexist with liquid Bi in equilibrium with chromium metal. At low oxygen concentrations, only Cr_2O_3 would coexist with them. If the oxygen concentration is increased further, Bi_2O_3 will precipitate with disappearance of chromium metal. At 1023 K, at low oxygen concentrations, Cr_2O_3 would coexist with chromium metal and liquid Bi. With increase in oxygen concentration, ' $\text{Bi}_{22}\text{Cr}_{18}\text{O}_{60}$ ' would become stable in liquid Bi. With further increase in oxygen concentration, ' $\text{Bi}_{22}\text{Cr}_{18}\text{O}_{60}$ ' would disappear and ' $\text{Bi}_{38}\text{CrO}_{60}$ ' would coexist with liquid Bi.

The following equilibria were considered for computation of oxygen potentials:





In equilibria 5.7 and 5.9, the s and t can have different values for different elements, viz., Fe, Cr, Ni, Si, Mo etc. In LBE, PbO is more stable than Bi₂O₃. Hence, the equilibrium considered for computing oxygen potential with different levels of dissolved oxygen concentration in LBE is:



For these computations, data on Gibbs energy of formation of bismuth ferrate and chromates from the present work were used. Data on lead ferrates and chromates were from references 2 to 4. For oxides of Ni, Si and Mo, the data from reference 1, for oxides of iron, data from references 5 and 6, and for chromium sesquioxide, data from 7 were used. Oxygen potentials of the above mentioned equilibria were calculated for two different types of steels, namely SS-304 and 9Cr-1Mo steel whose compositions are given in Table 5.1.

Table 5.1 Composition of SS-304 and 9Cr-1Mo steel

Steel	Composition / wt. %								
	Cr	Ni	Mo	Si	Mn	P	S	C	Fe
SS-304	18	8	-	1	2	0.045	0.030	0.08	70.85
9Cr-1Mo steel	9	-	1	0.625	0.45	0.025	0.025	0.15	88.75

The chemical activity of the alloying elements in steel was obtained by assuming the steel to be an ideal solid solution obeying Raoult's law. Activity of Bi in LBE was calculated from the excess Gibbs energy of Bi in LBE, reported by Gokcen [8]:

$$G_{Bi}^{ex}(L) = RT \ln \gamma_{Bi} = (650 - 2.302 T) (\chi_{Pb}^{LBE})^2 - (16200 - 5.264 T) (\chi_{Pb}^{LBE})^3 + (12150 - 4.215 T) (\chi_{Pb}^{LBE})^4 \text{ J g} - \text{atom}^{-1} \quad (5.11)$$

where G_{Bi}^{ex} is the excess Gibbs energy of Bi, R is the universal gas constant, T is the temperature, γ_{Bi} is the activity coefficient of Bi and χ_{Pb}^{LBE} is the mole fraction of Pb in LBE.

$$\text{Activity of Bi in LBE is given by, } a_{Bi} = \gamma_{Bi} * \chi_{Bi}^{LBE} \quad (5.12)$$

where χ_{Bi}^{LBE} is the mole fraction of Bi in LBE.

Similarly, activity of Pb in LBE was calculated from the excess Gibbs energy of Pb in LBE, reported in reference 8:

$$G_{pb}^{ex}(L) = RT \ln \gamma_{Pb} = (650 - 2.863 T) (\chi_{Bi}^{LBE})^2 - (16200 - 5.994 T) (\chi_{Bi}^{LBE})^3 + (12150 - 4.215 T) (\chi_{Bi}^{LBE})^4 \text{ J g} - \text{atom}^{-1} \quad (5.13)$$

where G_{pb}^{ex} is the excess Gibbs energy of Pb, γ_{Pb} is the activity coefficient of Pb and

χ_{Bi}^{LBE} is the mole fraction of Bi in LBE.

$$\text{Activity of Pb in LBE is given by, } a_{Pb} = \gamma_{Pb} * \chi_{Pb}^{LBE} \quad (5.14)$$

where χ_{Pb}^{LBE} is the mole fraction of Pb in LBE.

Oxygen potentials of pure liquid bismuth containing different levels (say, 1, 5 and 20 ppm) of dissolved oxygen were computed using eq. (5.8) and are given below:

$$\Delta_f G_m^o < \text{Bi}_2\text{O}_3 > = -RT \ln \left(\frac{a_{\text{Bi}_2\text{O}_3}}{a_{Bi} \times P_{O_2}^{3/2}} \right) \quad (5.15)$$

where $\Delta_f G_m^o < \text{Bi}_2\text{O}_3 >$ is the molar Gibbs energy of formation of Bi_2O_3 , a_{Bi} and $a_{\text{Bi}_2\text{O}_3}$ are the activities of Bi and Bi_2O_3 and P_{O_2} is the equilibrium oxygen pressure.

Since the activity of Bi is unity, eq. (5.15) can be written as:

$$RT \ln P_{\text{O}_2} = \frac{2}{3} \Delta_f G_m^o < \text{Bi}_2\text{O}_3 > + \frac{2}{3} RT \ln a_{\text{Bi}_2\text{O}_3} \quad (5.16)$$

Assuming Henry's law, $a_{\text{Bi}_2\text{O}_3}$ = concentration of oxygen in liquid Bi / solubility of oxygen in liquid Bi at the chosen temperature T.

The solubility of oxygen in liquid Bi is given by equations (5.17) and (5.18) [9]:

$$\log (S / \text{ppm O}) (\pm 0.05) = - 4480 / T \text{ K}^{-1} + 6.94 \quad (\text{T: } 753 - 988 \text{ K}) \quad (5.17)$$

$$\log (S / \text{ppm O}) (\pm 0.04) = - 3800 / T \text{ K}^{-1} + 6.26 \quad (\text{T: } 988 - 1020 \text{ K}) \quad (5.18)$$

Oxygen potentials in LBE were calculated using eq. (5.10) as given below:

$$\Delta_f G_m^o < \text{PbO} > = - RT \ln \left(\frac{a_{\text{PbO}}}{a_{\text{Pb}} \times P_{\text{O}_2}^{1/2}} \right) \quad (5.19)$$

where $\Delta_f G_m^o < \text{PbO} >$ is the molar Gibbs energy of formation of PbO, a_{Pb} and a_{PbO} are the activities of Pb and PbO and P_{O_2} is the equilibrium oxygen pressure.

By rearranging eq. (5.19),

$$RT \ln P_{\text{O}_2} = 2 \Delta_f G_m^o < \text{PbO} > + 2RT \ln a_{\text{PbO}} - 2 \ln a_{\text{Pb}} \quad (5.20)$$

where a_{PbO} = concentration of oxygen in LBE / solubility of oxygen in LBE at the chosen temperature T, according to Henry's law.

The solubility of oxygen in LBE is given by eq. (5.21) [10]:

$$\log (S / \text{ppm O}) (\pm 0.06) = - 4290 / T \text{ K}^{-1} + 6.42 \quad (\text{T: } 812 - 1012 \text{ K}) \quad (5.21)$$

The oxygen potentials of the different equilibria in Bi and LBE are shown in Figs. 5.1 and 5.2, respectively. Fig. 5.1a shows the oxygen potentials of different chemical equilibria in liquid Bi - SS 304 system. The oxygen potentials in liquid Bi containing different levels of dissolved oxygen concentrations are also shown in the same figure. It can be seen from the figure that at low oxygen concentrations, SiO_2 and Cr_2O_3 layers would be formed on the steel surface depending upon the amount of Si and Cr present in the steel. With increase in oxygen concentration, iron oxides would be formed at the steel – liquid Bi interface. If the oxygen concentration in the molten bismuth is further increased, $\text{Bi}_2\text{Fe}_4\text{O}_9$ would appear. Although the figure shows that NiO could be one of the products, nickel would be leached away from steel surface since its solubility is very high and hence this reaction need not be considered.

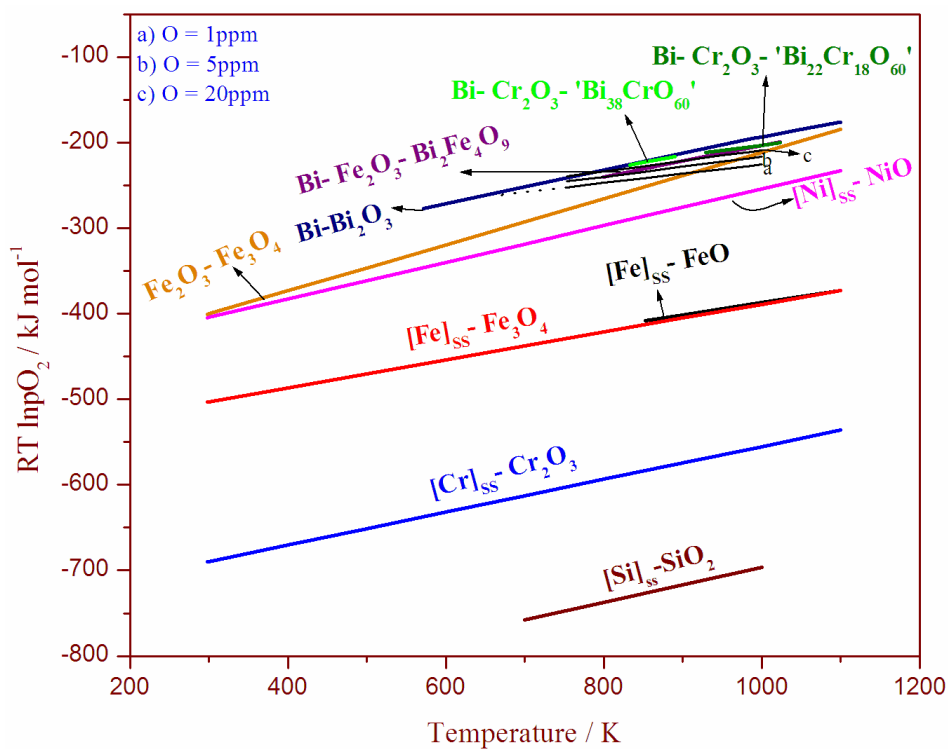


Fig. 5.1 a Oxygen potentials in liquid Bi containing different oxygen concentrations and with different chemical equilibria for SS 304

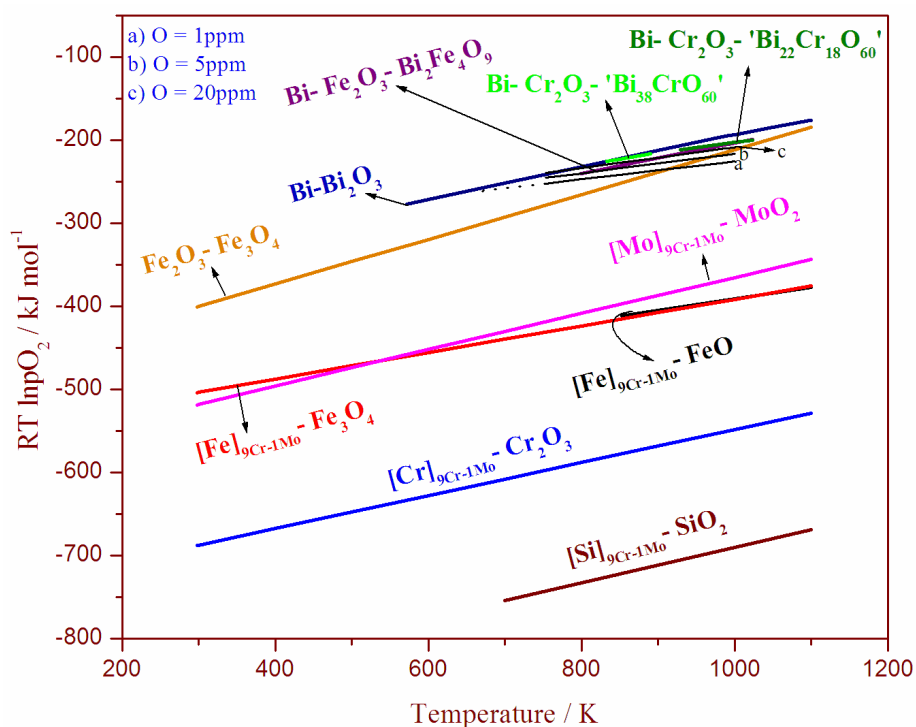


Fig. 5.1 b Oxygen potentials in liquid Bi containing different oxygen concentrations and with different chemical equilibria for 9Cr-1Mo steel

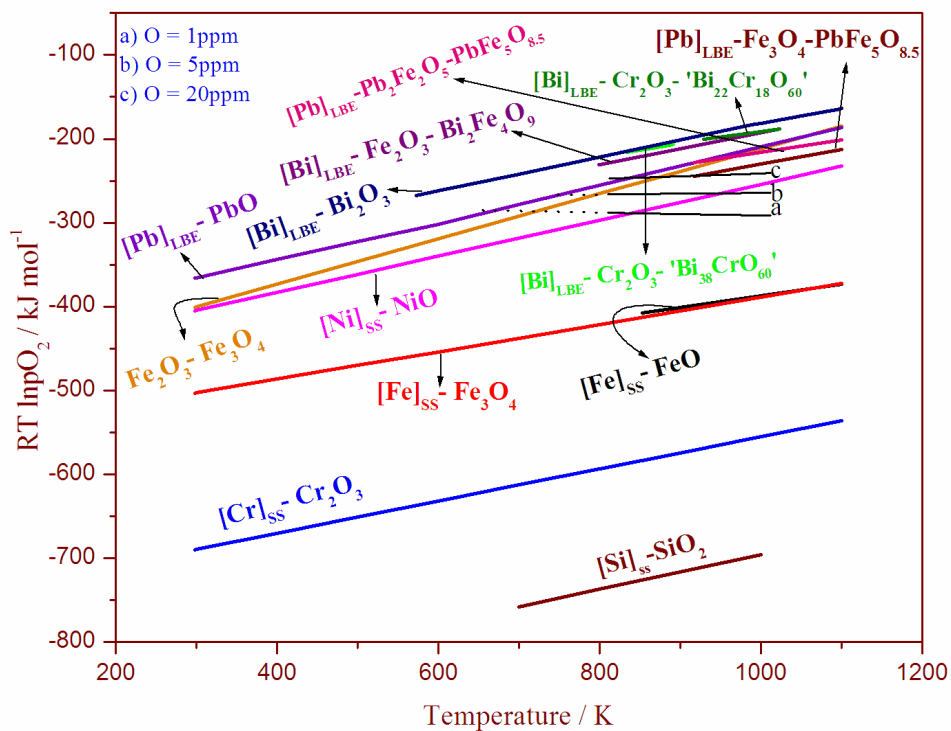


Fig. 5.2 a Oxygen potentials in LBE containing different oxygen concentrations and with different chemical equilibria for SS 304

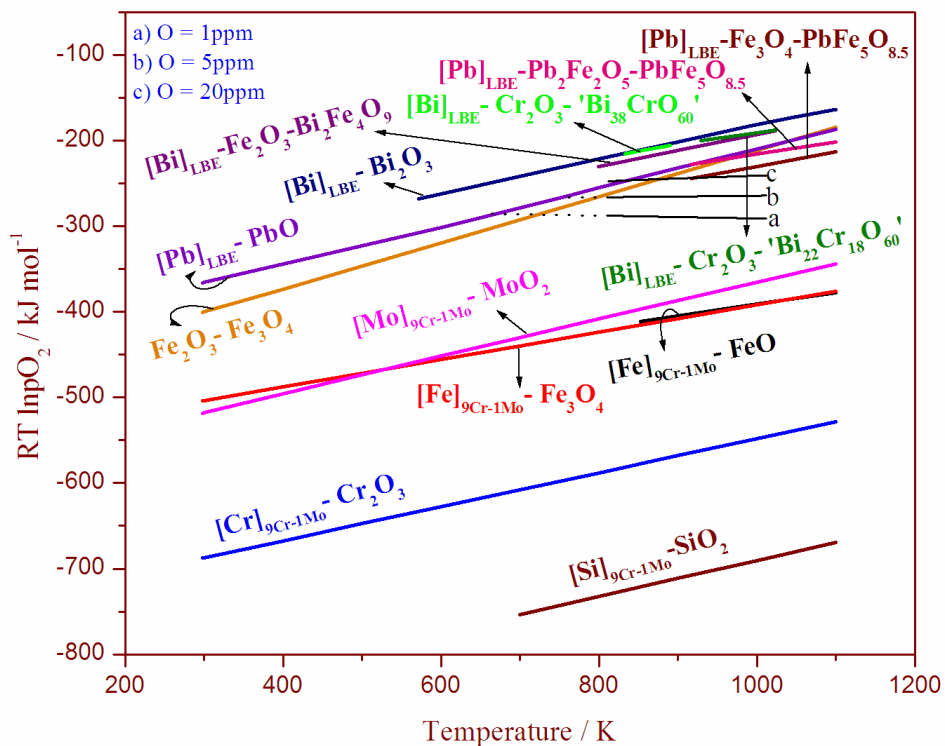


Fig. 5.2 b Oxygen potentials in LBE containing different oxygen concentrations and with different chemical equilibria for 9Cr-1Mo steel

Fig. 5.1b shows the oxygen potentials in liquid Bi containing different dissolved oxygen concentrations and chemical equilibria computed for 9 Cr – 1Mo steel. In the case of this steel, MoO₂ layer also could be formed on the steel along with Cr₂O₃ layer at low oxygen concentrations depending upon the amount of Mo present in the steel. Figs. 5.2 a and b show the oxygen potentials of different chemical equilibria in LBE and the oxygen potentials in LBE containing different oxygen concentrations for SS 304 and 9 Cr - 1 Mo steel, respectively. In LBE also, at lower oxygen concentrations, SiO₂, Cr₂O₃ and MoO₂ layers could be formed depending upon the steel. With increase in oxygen concentration, iron oxides would be formed at the steel–LBE interface. At higher oxygen concentrations, the first ternary compound formed would be PbFe₅O_{8.5}.

5.2 References

- 1) O. Kubaschewski, C.B. Alcock, Metallurgical Thermochemistry, fifth ed., Pergamon, Oxford, 1979.
- 2) S.K. Sahu, R. Ganesan, T. Gnanasekaran, Studies on phase diagram of Pb–Cr–O system, J. Nucl. Mater. 376 (2008) 366-370.
- 3) S.K. Sahu, R. Ganesan, T. Gnanasekaran, Standard molar Gibbs free energy of formation of Pb₅CrO₈ (s), Pb₂CrO₅ (s), and PbCrO₄ (s), J. Chem. Thermodyn. 42 (2010) 1 – 7.
- 4) S.K. Sahu, R. Ganesan, T. Gnanasekaran, Studies on the phase diagram of Pb–Fe–O system and standard molar Gibbs energy of formation of ‘PbFe₅O_{8.5}’ and Pb₂Fe₂O₅, J. Nucl. Mater. 426 (2012) 214-222.

- 5) B. Sundman, An assessment of the Fe-O system, *J. Phase Equilibria*, 12 (1991) 127-140.
- 6) A.F. Guillermet, P. Gustafson, An assessment of the thermodynamic properties and the (p, T) phase diagram of iron, *High Temp. – High Press.*, 16 (1985) 591 – 610.
- 7) A. Holzheid, H. St.C. O'Neill, The Cr-Cr₂O₃ oxygen buffer and the free energy of formation of Cr₂O₃ from high-temperature electrochemical measurements, *Geochim. Cosmochim. Acta* 59 (1995) 475-479.
- 8) N.A. Gokcen, The Bi – Pb (bismuth – lead) system, *J. Phase Equilib.* 13 (1992) 21 - 32.
- 9) R. Ganesan, T. Gnanasekaran, R.S. Srinivasa, Electrochemical study on determination of diffusivity, activity and solubility of oxygen in liquid bismuth, *J. Chem. Thermodyn.* 38 (2006) 739-747.
- 10) R. Ganesan, T. Gnanasekaran, R.S. Srinivasa, Diffusivity, activity and solubility of oxygen in liquid lead and lead-bismuth eutectic alloy by electrochemical methods, *J. Nucl. Mater.* 349 (2006) 133-149.

Chapter 6

SCOPE FOR FUTURE STUDIES

As corrosion in the LBE-steel systems can be mitigated effectively by the formation of an adherent oxide layer on the structural steels, a detailed knowledge on the composition and the thermochemical data of this oxide layer is needed to exploit this process. Understanding of thermochemistry of ternary compounds of the Pb-M-O and Bi-M-O (M: Fe, Cr) systems is of considerable interest in this regard. A detailed study on Bi-M-O (M: Fe, Cr) system has been carried out in this thesis work. Sahu et al. [1-6] carried out the studies on Pb-M-O (M: Fe, Cr) systems.

In Bi-Fe-O ternary system, the Gibbs energy of formation of $\text{Bi}_2\text{Fe}_4\text{O}_9$ has been determined in the present work. Gibbs energies of formation of BiFeO_3 and $\text{Bi}_{25}\text{FeO}_{39}$ need to be determined. In Bi-Cr-O system, Gibbs energies of formation of two compounds, namely ' $\text{Bi}_{22}\text{Cr}_{18}\text{O}_{60}$ ' and ' $\text{Bi}_{38}\text{CrO}_{60}$ ' which coexist with liquid Bi have been determined in the present work. Gibbs energies of formation of other ternary compounds, namely $\text{Bi}_{14}\text{CrO}_{24}$, $\text{Bi}_{31}\text{Cr}_5\text{O}_{61.5}$, $\text{Bi}_{10}\text{Cr}_2\text{O}_{21}$, $\text{Bi}_6\text{Cr}_2\text{O}_{15}$, Bi_2CrO_6 and their enthalpies of formation and heat capacities also need to be measured.

Mo containing steels such as 9Cr-1Mo steel has been considered as the structural material for LBE. Hence, the interaction of Mo in the structural steel with LBE in the presence of oxygen needs to be studied. In this aspect, studies on Pb (Bi) –Mo-O systems deserve greater importance. Studies have shown that surface alloying of steel with Si and Al is a promising option to reduce corrosion. It was observed that the alumina or SiO_2 film formed on the surface of steel is very effective in preventing the dissolution of alloying components without influencing the mechanical properties

of the base material [7, 8]. Hence, studies on Pb (Bi) –Si-O systems and Pb (Bi) –Al-O systems also need to be carried out to understand and exploit the corrosion protection phenomena in lead and LBE circuits.

6.1 References

- 1) S.K. Sahu, R. Ganesan, T. Gnanasekaran, Studies on phase diagram of Pb–Cr–O system, *J. Nucl. Mater.* 376 (2008) 366-370.
- 2) S.K. Sahu, R. Ganesan, T. Gnanasekaran, Standard molar Gibbs free energy of formation of Pb_5CrO_8 (s), Pb_2CrO_5 (s), and PbCrO_4 (s), *J. Chem. Thermodyn.* 42 (2010) 1 – 7.
- 3) S.K. Sahu, R. Ganesan, T.G. Srinivasan, T. Gnanasekaran, The standard molar enthalpies of formation of Pb_2CrO_5 (s) and Pb_5CrO_8 (s) by acid solution calorimetry, *J. Chem. Thermodyn.* 43 (2011) 750-753.
- 4) S.K. Sahu, R. Ganesan, T. Gnanasekaran, Studies on the phase diagram of Pb–Fe–O system and standard molar Gibbs energy of formation of ‘ $\text{PbFe}_5\text{O}_{8.5}$ ’ and $\text{Pb}_2\text{Fe}_2\text{O}_5$, *J. Nucl. Mater.* 426 (2012) 214-222.
- 5) S.K. Sahu, M. Sahu, R.S. Srinivasa, T. Gnanasekaran, Determination of heat capacities of PbCrO_4 (s), Pb_2CrO_5 (s), and Pb_5CrO_8 (s), *Monatsh. Chem.* 143 (2012) 1207–1214.
- 6) S.K. Sahu, R. Ganesan, T. Gnanasekaran, The standard molar enthalpies of formation of $\text{Pb}_2\text{Fe}_2\text{O}_5$ (s) and $\text{PbFe}_5\text{O}_{8.5}$ (s) by acid solution calorimetry, *J. Chem. Thermodyn.* 56 (2013) 57–59.

- 7) L. Ruiguo, F. Jun, F. Zhongchao, Microstructure and properties of laser surface alloying 304 stainless steel with Si, Chin. J. Met.Sci. Technol., 8 (1992) 335-338.
- 8) G. Muller, V. Engelko, A. Weisenburger, A. Heinzl, Surface alloying by pulsed intense electron beams, Vacuum 77 (2005) 469-474.